UNIVERSITY of CALIFORNIA
Santa Barbara

Rare exclusive semileptonic decays at CLEO

A dissertation submitted in partial satisfaction of the
requirements for the degree of

Doctor of Philosophy

in

Physics

by

David J. Lange

Committee in charge:

Professor Jeffrey Richman, Chair
Professor Rollin Morrison
Professor Joseph Polchinski

August 1999

The dissertation of David J. Lange is approved:

Chair

August 1999

Rare exclusive semileptonic decays at CLEO

To my parents

Acknowledgements

I must begin by acknowledging Jeff Richman for everything he has done over the past 5 years. He has taught me much about high-energy physics as well as that there is much still to be learned. Without his constant support this thesis would not be possible.

One of the best experiences of my education was working as part of the CLEO II.V SVX hardware group while at Cornell. I thank Tony Hill, Mark Palmer, Jeff Gronberg, Harry Nelson, and David Asner for bearing with me while I learned the discinction between analysis and the responsiblities of day to day data collection.

Also instrumental in my education are my friends and colleagues from UCSB, especially Anders Ryd, Tony, Jeff G., David A., Harry, Claudio Campagnari, Rollie Morrison, Mike Witherell, Tim Nelson, Dave Flynt, Lap Leung, and Anton Eppich.

Any phyiscs result from an experiment in high-energy physics is the result of work of many people. I acknowledge the efforts of all of my CLEO colleagues. In particular, Lawrence Gibbons, Yuichi Kubota, Dave Cinabro, and Kay Kinoshita have contributed significantly to this thesis work.

Finally, I acknowledge the support and encouragement from my family. My parents always have supported whatever ambitions I have pursued. The Santa Barbara part of my family, Carol, Fred and Gordon, have helped keep me sane during graduate school.

Curriculum Vitæ

David J. Lange

Personal

Born	June 3, 1972. Portland, Oregon.

Education

1993–1999	Ph.D., University of California, Santa Barbara. Experimental high-energy physics.
1990-1993	B.A., College of William and Mary. Physics with high honors.

Research experience

1994-1999	Study of Semileptonic B Meson Decays
1997-1999	Operation of Silicon Vertex Detector for CLEO-II.V
1995-1999	Implementation of Monte Carlo Event Generator (EvtGen)

Presentations

1996	"Study of $B \to \rho\ell\nu$ decay at CLEO", April meeting of American Physical Society. Indianapolis, 1996.
1999	"Recent results on semileptonic decay from CLEO", 11th Rencontres de Blois. Blois, 1999.

Publications

1997	"A New Measurement of the $b \to u$ Semileptonic Decays $B \to \rho\ell\nu$ and $B \to \omega\ell\nu$," CLEO Collaboration (EPS 343). Presented at the International Europhysics Conference on High-Energy Physics. Jerusalem, 1997.

1998	"Measurement of $\mathcal{B}(B \to \rho\ell\nu)$, $\|V_{ub}\|$, and the Form Factor Slope in $B \to \rho\ell\nu$ Decay," CLEO Collaboration (ICHEP 98-855). Presented at the 29th International Conference on High Energy Physics. Vancouver, 1998.
1998	"The EvtGen Event Generator Package," David Lange and Anders Ryd. Presented at the International Conference on Computing in High-Energy Physics. Chicago, 1998.
1999	"Measurement of $B \to \rho\ell\nu$ decay and $\|V_{ub}\|$," CLEO Collaboration (B. H. Behrens *et al.*) , Submitted to Phys. Rev. D.

Rare exclusive semileptonic decays at CLEO

Abstract

by

David J. Lange

Using a sample of 3.3×10^6 $\Upsilon(4S) \rightarrow B\bar{B}$ events collected with the CLEO II detector at the Cornell Electron Storage Ring (CESR), we measure the branching fraction for $B \rightarrow \rho\ell\nu$, the Cabibbo-Kobayashi-Maskawa matrix element $|V_{ub}|$, and the partial rate $(\Delta\Gamma)$ in three bins of $q^2 \equiv (p_B - p_\rho)^2$. We find $\mathcal{B}(B^0 \rightarrow \rho^-\ell^+\nu) = (2.69 \pm 0.41^{+0.35}_{-0.40} \pm 0.50) \times 10^{-4}$, $|V_{ub}| = (3.23 \pm 0.24^{+0.23}_{-0.26} \pm 0.58) \times 10^{-3}$, $\Delta\Gamma(0 < q^2 < 7\ \mathrm{GeV}^2/c^4) = (7.6 \pm 3.0^{+0.9}_{-1.2} \pm 3.0) \times 10^{-2}\ \mathrm{ns}^{-1}$, $\Delta\Gamma(7 < q^2 < 14\ \mathrm{GeV}^2/c^4) = (4.8 \pm 2.9^{+0.7}_{-0.8} \pm 0.7) \times 10^{-2}\ \mathrm{ns}^{-1}$, and $\Delta\Gamma(14 < q^2 < 21\ \mathrm{GeV}^2/c^4) = (7.1 \pm 2.1^{+0.9}_{-1.1} \pm 0.6) \times 10^{-2}\ \mathrm{ns}^{-1}$. Here, $\ell = e$ or μ, but not both, and the quoted errors are statistical, systematic, and theoretical. The method is sensitive primarily to $B \rightarrow \rho\ell\nu$ decays with leptons in the energy range above 2.3 GeV. Averaging with the previously published CLEO results for $B \rightarrow \rho\ell\nu$, we obtain $\mathcal{B}(B^0 \rightarrow \rho^-\ell^+\nu) = (2.57 \pm 0.29^{+0.33}_{-0.46} \pm 0.41) \times 10^{-4}$ and $|V_{ub}| = (3.25 \pm 0.14^{+0.21}_{-0.29} \pm 0.55) \times 10^{-3}$.

Contents

List of Figures

List of Tables

Chapter 1

Introduction

We present a measurement of the branching fractions for $B^0 \to \rho^- \ell^+ \nu$ and $B^+ \to \rho^0 \ell^+ \nu$, where $\ell = e$ or μ. Unlike the dominant B decay modes, which involve $b \to c$ transitions, these rare decays result from a $b \to u$ transition. This process involves two quark generation changes and is therefore highly suppressed. We identify these decays by reconstructing a high-energy lepton that is close to the lepton-energy endpoint for $b \to c\ell\nu$ processes. We find 216 ± 32 $\rho \to \pi\pi$ signal events with $E_\ell > 2.3$ GeV. The extrapolation of measured yields to the full lepton-energy range relies on form-factor models and introdues a theoretical uncertainty in the branching frations.

The branching fractions for these decays are proportional to $|V_{ub}|^2$. V_{ub} is one of the smallest and least well understood elements of the Cabibbo-Kobayashi-Maskawa (CKM) quark-mixing matrix [1]. The CKM matrix contains 4 of 18 free parameters of the standard model of particle physics. Measurements of $|V_{ub}|$ provide one constraint on these 4 parameters. Measurements of $|V_{ub}|$ have been performed using inclusive $b \to u\ell\nu$ decay as well as the exclusive modes $B \to \pi\ell\nu$ and $B \to \rho\ell\nu$. Here, we use measurements of $B \to \rho\ell\nu$ decay to make a new measurement of $|V_{ub}|$. Exclusive $b \to u\ell\nu$ modes from CLEO now provide the most precise determination of this CKM matrix element.

The study of B-meson decay is interesting for many reasons. In particular, understanding the origin of CP violation, first discovered in the $K^0 - \bar{K}^0$ system [2], is currently one of the most exciting problems in particle physics.

Measurements of CP-violation in a system other than $K^0 - \bar{K}^0$ should provide information on the origins of this effect. The B-meson system is an excellent place to look, as there is reason to expect large CP-violating effects, unlike the $K^0 - \bar{K}^0$ system. Beyond CP violation the B-meson and its decays are interesting for other many reasons, as shown in Fig. 1.1.

The discovery of the b quark and subsequently the B meson were not completely unexpected. In the mid 1970s, it seemed natural that a third generation of quarks, beyond the already discovered u, d, s, and c quarks, should be discovered to go along with the third lepton, the newly discovered τ. The b quark was first observed in 1977 in the $\mu^-\mu^+$ spectrum produced from 400 GeV protons at Fermilab [3]. Two resonances, to be called the Υ and Υ' (or $\Upsilon(1S)$ and $\Upsilon(2S)$), were observed. Soon thereafter, this discovery was confirmed at DESY in two experiments [4, 5] using the e^+e^- DORIS storage ring. Measurements of $R \equiv \sigma(e^+e^- \rightarrow \text{hadrons})/\sigma(e^+e^- \rightarrow \mu^+\mu-)$ and the width of these resonances determined that the Υ was made up of quarks with charge magnitude 1/3 and not 2/3.

Later, the CUSB and CLEO experiments at the Cornell Electron Storage Ring (CESR) observed higher resonances [6, 7] in the Υ system. In particular, the fourth such resonance was discovered in 1980. The width of this resonance was larger than the preceeding three, an indication that this resonance, now known as the $\Upsilon(4S)$, was above threshold for $B\bar{B}$ production. Exclusive decay modes of the B meson were observed [8] shortly thereafter, albeit with measured branching fractions an order of magnitude too large. The $\Upsilon(4S)$ resonance has become one of the most interesting ways to study the properties of B mesons.

This thesis presents data collected on the $\Upsilon(4S)$ resonance by the CLEO II detector, which is located at CESR. As with the set of experiments described in the preceeding paragraphs, the b quark is now studied in e^+e^- collisions and in hadronic machines. Along with the $\Upsilon(4S)$ experiments CLEO and ARGUS (at DESY in Hamburg), investigations at LEP (ALEPH, DELPHI, OPAL, and L3 experiments), the SLC (SLD experiment), and at the Fermilab Tevatron $p\bar{p}$ collider (CDF and D0 experiments) have led to a broad and varied program

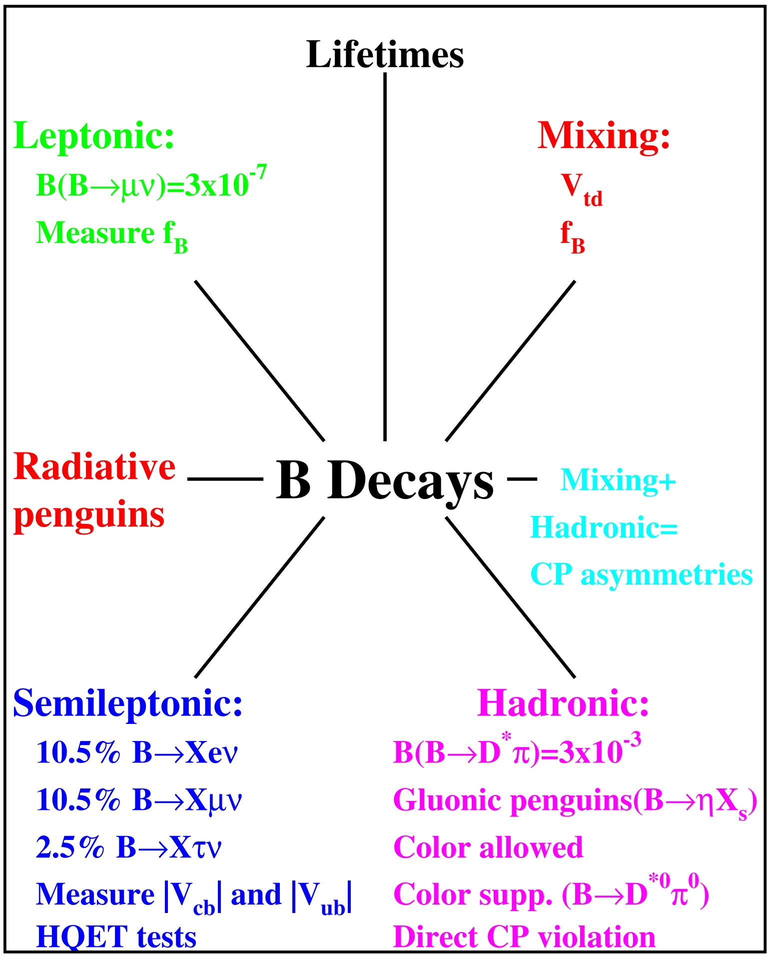

Figure 1.1: Areas of research in B physics.

for the study of the b quark. At LEP and the SLC, measurements of the b lifetime, mixing, as well as of semileptonic decays have been performed. At CDF and D0, perhaps the most significant contribution has been the use of b-quark jets to search for other processes, in particular the top quark and the higgs boson. One reason that so many b-physics programs exist is that none of these experiments is limited to the study of b physics. At CLEO, there are large programs for the study of the charm quark and τ lepton. In particular, CLEO has been very competitive with dedicated charm fixed target experiments in the study of the D and D_s mesons.

The number of b-physics experiments continues to grow. Indeed, at least six experiments are currently in the final construction or commisioning phases that are expected to contribute. The BABAR experiment at SLAC is taking its first data as this thesis is being written. This third generation of experiments has more than simply the capability of taking larger and larger data samples. For example the BABAR and BELLE experiments are located at asymmetric rings that operate at the $\Upsilon(4S)$ resonance. The moving center of mass allows for the measurement of asymmetries as a function of decay time, not currently possible with the CLEO II detector.

The B-meson is also interesting for its variety of possible decay processes, as shown in Figure 1.2. Exclusive semileptonic $b \to u\ell\nu$ decays are an active area of experimental and theoretical study [9, 10, 11, 12, 13, 14, 15, 16, 17, 18, 19, 20, 21, 22, 23, 24, 25, 26, 27, 28, 29, 30, 31]. These rare processes can be used to extract the magnitude of V_{ub}, one of the smallest and least well known elements of the CKM matrix. Because $|V_{ub}/V_{cb}| \approx 0.08$, the branching fractions for exclusive $b \to u\ell\nu$ processes are small, of order 10^{-4}, and they have only recently become experimentally accessible. The present analysis confirms the initial CLEO observation [9] of $B \to \rho\ell\nu$, improves the precision on the branching fraction and $|V_{ub}|$, and provides the first information on the q^2 dependence for this decay.

Extracting $|V_{ub}|$ from a measured decay rate requires significant theoretical input because the matrix elements for such processes involve complex strong-

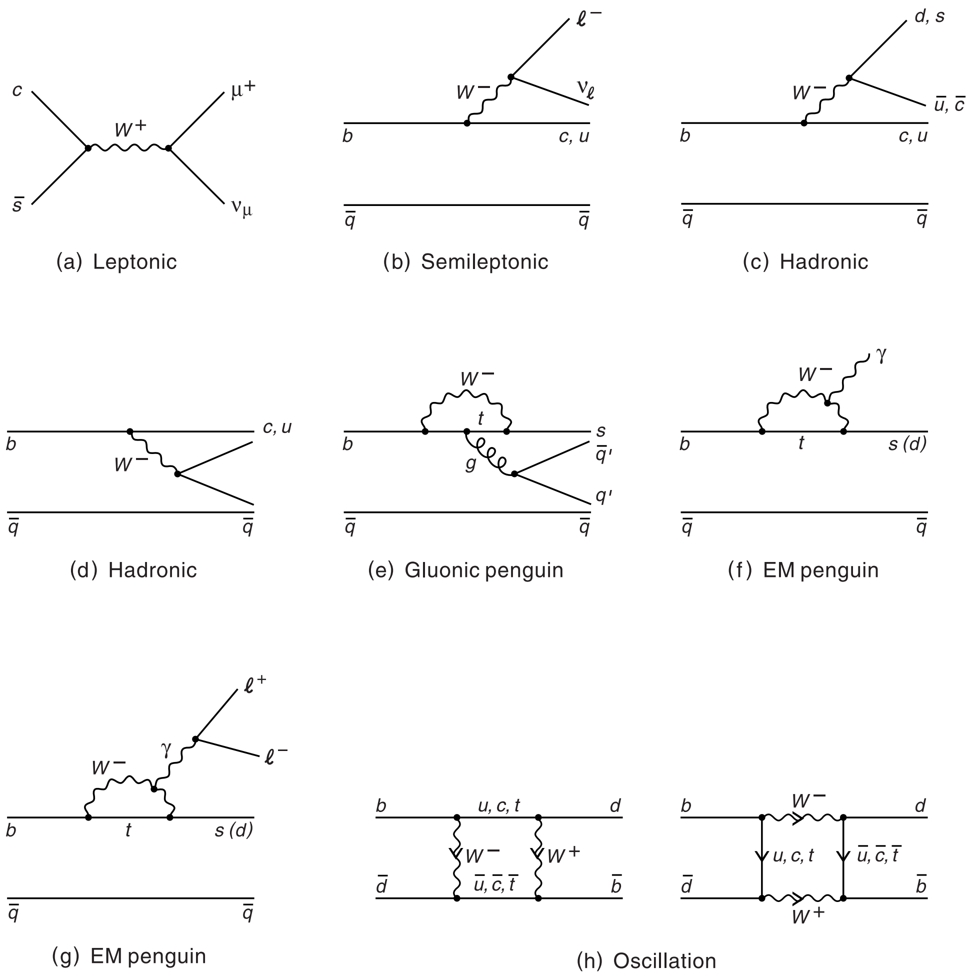

Figure 1.2: Decay processes of the B meson: (a) leptonic decay, (b) semileptonic decay, (c) hadronic decay via an external spectator, (d) hadronic decay via an internal spectator, (e) gluonic pengiun, (f) and (g) radiative penguin, and (h) $B^0 - \bar{B}^0$ mixing. From Ref. [49].

interaction dynamics. Although the underlying $b \to u\ell\nu$ decay is a relatively simple weak process, it is difficult to calculate the strong-interaction effects involved in the transition from the heavy B meson to the light daughter meson. Because of these theoretical uncertainties, even a perfectly measured $B \to \rho\ell\nu$ branching fraction would not at present lead to a precise value of $|V_{ub}|$.

The dynamics in $B \to \rho\ell\nu$ decay are in contrast with $b \to c\ell\nu$ decays, such as $B \to D^*\ell\nu$, where a heavy quark is present both in initial and final states. In this case, techniques based on Heavy Quark Effective Theory (HQET) can be used to calculate the decay amplitude with good precision, particularly for the kinematic configuration in which the charm hadron has zero recoil velocity. The zero-recoil point in $B \to \rho\ell\nu$ cannot be treated with similar techniques, however, because the daughter u quark is not heavy compared to the scale of hadronic energy transfers. Nevertheless, substantial progress has been made using a variety of theoretical methods, including quark models [14, 15, 16, 17, 18, 19, 20], lattice QCD [21, 22, 23], QCD sum rules [24, 25, 26], and models relating form factors measured in $D \to K^*\ell\nu$ decay [27] to those in $B \to \rho\ell\nu$ decay.

Experimentally, the main difficulty in observing signals from $b \to u\ell\nu$ processes is the very large background due to $b \to c\ell\nu$. Because a significant fraction of $B \to \rho\ell\nu$ events have lepton energy beyond the endpoint for $b \to c\ell\nu$ decay, lepton-energy requirements provide a powerful tool for background suppression. However, extrapolation of the decay rate measured in this portion of phase space to the full rate again requires the use of theoretical models, and it introduces model dependence beyond that associated with simply extracting the value of $|V_{ub}|$ from the branching fraction. In this study, we begin to explore the decay dynamics of $B \to \rho\ell\nu$ by measuring the distribution of q^2, the square of the mass of the virtual W. The distribution of q^2 is reflected in the ρ momentum spectrum. Eventually, studies of the q^2 distribution, as well as of the angular distributions of the decay products, should reduce the model dependence on $|V_{ub}|$ by constraining theoretical models for the decay form factors.

CLEO has previously observed [9] the decays $B^0 \to \rho^- \ell^+ \nu$, $B^+ \to \rho^0 \ell^+ \nu$, $B^0 \to \pi^- \ell^+ \nu$, and $B^+ \to \pi^0 \ell^+ \nu$ by measuring both the missing energy and momentum in an event to infer the momentum of the neutrino. Using 2.84×10^6 $\Upsilon(4S) \to B\bar{B}$ events, this study obtained

$$\begin{aligned} \mathcal{B}(B^0 \to \rho^- \ell^+ \nu) &= (2.5 \pm 0.4^{+0.5}_{-0.7} \pm 0.5) \times 10^{-4}, \\ \mathcal{B}(B^0 \to \pi^- \ell^+ \nu) &= (1.8 \pm 0.4 \pm 0.3 \pm 0.2) \times 10^{-4}, \\ |V_{ub}| &= (3.3 \pm 0.2^{+0.3}_{-0.4} \pm 0.7) \times 10^{-3}, \end{aligned} \tag{1.0.1}$$

where the errors are statistical, systematic, and theoretical. A large contribution to the $B \to \rho \ell \nu$ systematic error is associated with a possible nonresonant $B \to \pi\pi\ell\nu$ rate. In the analysis described below this uncertainty is reduced.

We report on a measurement of $\mathcal{B}(B \to \rho \ell \nu)$ and $|V_{ub}|$ as well as the first measurement of the partial rate for $B \to \rho \ell \nu$ in bins of q^2. We study five signal modes: $B^0 \to \rho^- \ell^+ \nu$, $B^+ \to \rho^0 \ell^+ \nu$, $B^+ \to \omega \ell^+ \nu$, $B^0 \to \pi^- \ell^+ \nu$, and $B^+ \to \pi^0 \ell^+ \nu$. Our method is sensitive primarily to leptons with energies above the $b \to c \ell \nu$ lepton-energy endpoint ($E_\ell > 2.3$ GeV). The resulting event sample is essentially statistically independent of that from the previous analysis since it contains much larger signal and background yields, even though the data samples are similar.

1.1 Plan of thesis

In performing a measurement of $B \to \rho \ell \nu$ decay, there are several significant problems to overcome:

- Identifying semileptonic decay. The clearest signature of semileptonic decay is the lepton, either an electron or muon, which can be identified with good efficiency and with low background. The undetected neutrino, however, complicates the detection of semileptonic decays significantly. The solution used in this thesis is to use each of the particles detected in the $\Upsilon(4S) \to B\bar{B}$ event in order to obtain a measure of the momentum of the undetected neutrino. In order to maintain a relatively high efficiency, however, we do not make scrict requirements that would improve the resolution on this measurement. This crude measure of the neutrino momentum is nevertheless enough to separate signal events from various background sources.

- Small signal size. In a data sample of more than three million $\Upsilon(4S) \to B\bar{B}$ decays, there are 1200 $B^0 \to \rho^- \ell^+ \nu$ decays ($\ell = e$ or μ) if the branching fraction for $B^0 \to \rho^- \ell^+ \nu$ is 2×10^{-4}. For this mode, our signal efficiency is about 4%, resulting in about 50 expected signal events. Because of the relatively small number of events expected, we combine the three $B \to X_u \ell \nu$ modes in which X_u is a vector meson ($\rho^\pm$, ρ^0, and ω) using isospin and quark model constraints. Using these constraints, we measure the branching fraction for $B \to \rho \ell \nu$ with approximately a 6σ significance.

- Large $B \to X_c \ell \nu$ background. The branching fraction for $B \to X_u \ell \nu$ is approximately 2% of that for $B \to X_c \ell \nu$. Thus, measurements of $b \to u \ell \nu$ processes, such as $B \to \rho \ell \nu$, are most sensitive at high lepton energies, near the endpoint for leptons from $b \to c \ell \nu$ decays. This restriction leads to an additional error due to extrapolating the results in this small part of phase space to a full branching fraction result.

- Large continuum background. At a center-of-mass energy corresponding to the $\Upsilon(4S)$ resonance, the cross section for continuum ($e^+e^- \to q\bar{q}$, $q\bar{q} = u\bar{u}$, $d\bar{d}$, $s\bar{s}$, and $c\bar{c}$) is three times that for $\Upsilon(4S) \to B\bar{B}$. At high lepton energies, this background is dominant. We will explain how signal decays can be distinguished from this background. Nevertheless, the continuum background is the largest background in the region where we are most sensitive to $B \to \rho \ell \nu$ decay.

- Experimentally unstudied $b \to u \ell \nu$ background. Only the exclusive modes $B \to \rho \ell \nu$ and $B \to \pi \ell \nu$ have been experimentally measured. The makeup of the rest of the $b \to u \ell \nu$ inclusive rate is nontrivial in size and is experimentally unstudied. We make use of a theoretical model to predict a mix of resonant $b \to u\ell\nu$ modes that form a significant part of our background. However, this background is also constrained by our data.

We discuss the solution to each of these problems in this thesis.

We use the notation $b \to u(c)\ell\nu$ to denote inclusive $B \to X_{u(c)}\ell\nu$ decay, where X_u is a hadronic system with no charm quarks, and X_c is a hadronic system with a charm quark. When discussing backgrounds, we will often refer to $b \to u\ell\nu$ inclusive decays excluding one or more signal modes. In this case, we will use the notation $b \to u\ell\nu$ and explicitly list the modes not to be included. When no charge state is given, $B \to \rho\ell\nu$ refers generically to $B \to \rho^{\pm}\ell\nu$, and $B \to \rho^0\ell\nu$ decays. When specifying a particular decay mode, we implicitly include its charge-conjugate decay.

We begin Chapter 2 by introducing the phenomenology of the CKM matrix. We present the theoretical framework, as well as the experimental status of each element in the matrix. We will see that semileptonic decays of B-mesons are the best way to constrain $|V_{cb}|$ and $|V_{ub}|$. Alternatives to semileptonic decays are either theoretically difficult to interpret (hadronic decays) or have a small branching fraction (leptonic decays). We also introduce the unitarity triangle that describes the unitarity constraint between the first and third columns of the CKM matrix. We show the experimental constraints on this triangle, including that from $|V_{ub}|$. Finally, we discuss the role that the CKM matrix and unitarity triangle play in CP-violation.

Chapter 3 introduces the phenomenology of semileptonic decay. The full differential decay rate is expressed in terms of helicity amplitudes, which in turn depend on form factors, Lorentz-invariant functions of q^2 that parametrize the hadronic current. The prediction of these form factors is an extremely active area of research. Several distinct methods are used to make predictions. In order to evaluate our dependence on these form-factor results, we extract results from our data using the predictions of five form-factor models. For the branching fraction measurement, the largest source of model dependence is due to the efficiency of our lepton-energy requirement. In particular, models predict that between 24% and 35% of $B \to \rho\ell\nu$ events will have a lepton that satisfies our requirement. Additionally for the measurement of $|V_{ub}|$, we rely on theoretical predictions to provide the normalization factor that relates the measured branching fraction to $|V_{ub}|$. We discuss these five models and give the parametrizations of their form factors.

Chapter 4 presents the current status of experimental semileptonic measurements of B-meson decays. Both inclusive and exclusive results are summarized. For measurements of $b \to u\ell\nu$ decay it is important to realize that there is much still unknown about $b \to c\ell\nu$ decay. Although the exclusive modes $B \to D\ell\nu$ and $B \to D^*\ell\nu$ are well measured, including their kinematic distributions, the other hadronic final states are largely unmeasured. This uncertainty must be properly accounted for in any measurement of $b \to u\ell\nu$ decay. In this thesis we allow the data to determine the overall normalization as well as the lepton-energy distribution of the $b \to c\ell\nu$ background. Thus, our final results are relatively insensitive to this uncertainty.

Chapter 5 describes the features of the CLEO II detector crucial in the analysis of $B \to \rho\ell\nu$ decay. In particular, the nearly full angular coverage for both charged and neutral particles is crucial for the measurements presented here. In semileptonic decay, this coverage allows for the measurement of the missing neutrino by computing the missing momentum and energy in the event. Additionally, we describe techniques for high-momentum lepton identification.

We detail the Monte Carlo predictions used in this analysis in Chapter 6. We briefly discuss the generation of these samples and then list the makeup of each sample. These predictions play an important role in this thesis, as they are necessary to predict not only the background contributions but also the kinematics of the signal contribution. In particular, we describe a tool for the generation of sequential decay chains, which are basic to semileptonic decays.

Chapter 7 describes the requirements used to distinguish signal events from backgrounds, which are due primarily to continuum events, $b \to c\ell\nu$, and $b \to u\ell\nu$ (non ρ/ω) events. As described above, $b \to c\ell\nu$ backgrounds are primarily suppressed by requiring a lepton near the $b \to c$ lepton-energy endpoint region. In this region, $e^+e^- \to c\bar{c}$ events are the largest source of leptons. We separate signal events from this background source by examining how jet-like the event is. Because the B-meson is produced nearly at rest at CLEO, the decay particles in $B\bar{B}$ events tend to be distributed over the full solid angle. On the other hand, particles in $e^+e^- \to c\bar{c}$ events tend to aligned along a jet axis.

Chapter 8 describes the binned maximum-likelihood fit used to extract the $B \to \rho\ell\nu$ signal. Such a fit is needed due to the relatively small number of signal events in the presence of several sources of background. Simple counting methods would not provide the desired sensitivity to signal events. Although we must rely on Monte Carlo predictions to model the shapes of distributions for the $b \to c(u)\ell\nu$ backgrounds, the normalization and lepton-energy spectrum of each background component are determined by the data. In addition, the assumed background shapes are extensively tested using sideband regions where the contribution from signal events is small. The continuum background contribution is measured directly using data.

Chapter 9 presents the yields extracted from the fit as well as the model-dependent detection efficiencies used to obtain values for $\mathcal{B}(B \to \rho\ell\nu)$ and $|V_{ub}|$. In our most sensitive region we observe 216 ± 32 $B \to \rho\ell\nu$ events. For the branching fraction measurement, the uncertainty associated with the detection efficiency is similar to the experimental errors. Additionally, we show fit results (projections) in both signal and background dominated regions of the data. We observe good agreement between the data and the results of the fit.

Chapter 10 describes the contributions to our systematic error. Apart from model dependence, these are due primarily to uncertainties in the $b \to u\ell\nu$ backgrounds and to uncertainties in the detector simulation. In the high lepton-energy region, where sensitivity to the signal is greatest, the background from other $b \to u\ell\nu$ processes is comparable to that from $b \to c\ell\nu$ decays, but its kinematic properties are less well understood. In addition, we show that the expected contamination from $B \to \pi\pi\ell\nu$ nonresonant events is small.

Chapter 11 presents our measured values of $\mathcal{B}(B \to \rho\ell\nu)$ and $|V_{ub}|$, as well as the average with the previous CLEO result. This average takes into account the correlation in the systematic errors as well as the variation in results for different form-factor models. In the average each result is given approximately equal weight. For the measurement of $|V_{ub}|$, the uncertainty in the theoretical normalization ($\pm 15\%$) needed to extract results from the measurement of the $B \to \rho\ell\nu$ branching fraction is larger than the experimental uncertainties ($\pm 10\%$). We also describe the measurement of the partial rate for $B \to \rho\ell\nu$ in three bins of q^2. Although these measurements are currently statistically limited, future measurements with larger data samples may be able to use the high q^2 region to extract $|V_{ub}|$ with a relatively small theoretical uncertainty.

In Chapter 12 we present our conclusions and an outlook for future measurements. We discuss how the measurements presented compare with other measurements of $|V_{ub}|$. The CLEO average presented in Chapter 11 represents the most precise determination of $|V_{ub}|$.

Chapter 2

The CKM matrix

The Cabibbo-Kobayashi-Maskawa (CKM) matrix [1] relates the charged-current quark eigenstates to the quark mass eigenstates. In this chapter we introduce the role of the CKM matrix in the standard model of particle interactions. This model describes all of the currently known fundamental particles as well as their interactions. Nevertheless there is much left to be understood within the framework of this model. One such example is whether the CP-violation observed in the K^0 system [2] arises from the framework of this model, or is a sign of new physics beyond this model. Precise measurements of the elements of the CKM matrix are one way to understand this. In this chapter, we describe the currently known particles that make up the standard model, discuss the current experimental status of the CKM matrix, and show that this matrix is fundamentally tied to CP violation within the framework of the standard model.

In Sec. 2.1 we introduce the standard model. Section 2.2 details the current experimental status of the elements of the CKM matrix. In particular we describe the decay modes used to measure each element and the limiting uncertainties.

Assuming three generations of quarks and leptons there are four nontrivial parameters of the CKM matrix. Section 2.3 presents a convenient parametrization of this matrix. We show that measurements of B-meson decays can be used to probe three of these four parameters.

Section 2.4 introduces relations between elements of the CKM matrix because it is unitary. These constraints can experimentally tested. We discuss these constraints and describe their current experimental status.

Section 2.5 describes CP asymmetries due to interference between mixing and decay. We illustrate the role played by the CKM matrix elements in these asymmetries.

We discuss the use of B-meson decays to measure elements of the CKM matrix in Sec. 2.6. We show we semileptonic decays are an especially good choice for measuring $|V_{cb}|$ and $|V_{ub}|$.

2.1 Quarks, leptons, and the CKM matrix

There are thought to be 6 quarks and 6 leptons, which are each divided into three generations:

$$\begin{pmatrix} u \\ d \end{pmatrix} \begin{pmatrix} c \\ s \end{pmatrix} \begin{pmatrix} t \\ b \end{pmatrix} \tag{2.1.1}$$

$$\begin{pmatrix} \nu_e \\ e^- \end{pmatrix} \begin{pmatrix} \nu_\mu \\ \mu^- \end{pmatrix} \begin{pmatrix} \nu_\tau \\ \tau^- \end{pmatrix} \tag{2.1.2}$$

For each quark doublet, the upper member has a charge of $(+2/3)e$ and the lower member $(-1/3)e$, where $-e$ is the electron charge. All six quarks have been experimentally observed, most recently the top quark (t) by the CDF and D0 experiments [33]. As we will describe below, W-boson-mediated interactions between quarks of different generations are allowed and described by the CKM matrix.

This is in contrast to leptons, where interactions between generations are not allowed in the standard model. The three neutrinos (ν) have no electric charge and only upper-limits have been placed on their masses (although neutrino oscillation results [34] from the Super Kamiokande experiment indicate that there is a mass difference ($\Delta m^2 \approx 10^{-3}\text{eV}^2$) between the ν_μ and ν_τ). The τ-neutrino has not been directly observed; however, its presence is inferred from energy and momentum conservation in τ decays.

The lower member of each lepton doublet has a charge of $-e$. As is the case in the quark sector, the masses of the lower members of the lepton doublets increase from the 1st to 3rd generations. The electron mass is only 0.511×10^{-3} GeV/c^2, while the τ-lepton has a mass of 1.78 GeV/c^2. The top quark mass is 174 GeV/c^2. The reason for the absolute mass scale or the progression towards higher masses between generations is not known.

Those quarks and leptons that have an electrical charge undergo electromagnetic interactions, which are mediated by the photon. The strength of this interaction is proportional to the electrical charge. Quark flavor is conserved in these interactions, so that $q_i \to q_j\gamma$ and $q_i\bar{q}_j \to \gamma$ are allowed decays only if $i = j$. In addition, $W^- \to \ell^-\bar{\nu}$ decays are allowed, and governed by a universal coupling constant, g.

All quarks and leptons interact via the charged and neutral weak currents, which are mediated by the $W^\pm$ and Z^0 bosons, respectively. As is the case for the electromagnetic interaction, weak neutral-current interactions conserve quark flavor. Thus, $Z^0 \to q_i\bar{q}_j$ is allowed only if $i = j$. In charged-current interactions, on the other hand, processes such as $b \to W^{*-}u$ are allowed. (We use the notation W^{*-} to denote a virtual W^-.)

The CKM matrix, V_{CKM}, describes the relative size of the charged-current weak amplitudes between quarks. For leptons, there is one universal coupling strength, usually denoted as g. For the decay $q \to W^{*-}Q$, where q is a $-1/3$ charged quark and Q has a charge of $+2/3$, the coupling is gV_{Qq}, where V_{Qq} can in general be complex. For the decay $Q \to W^{*+}q$, the coupling is gV^*_{Qq}. With three generations, V_{CKM} is a 3×3 matrix:

$$\begin{pmatrix} V_{ud} & V_{us} & V_{ub} \\ V_{cd} & V_{cs} & V_{cb} \\ V_{td} & V_{ts} & V_{tb} \end{pmatrix}. \tag{2.1.3}$$

V_{CKM} is the relation between quark mass eigenstates ($q = (d, s, b)$) and weak current eigenstates ($q' = (d', s', b')$), so that $q' = V_{\mathrm{CKM}} q$. In this way, V_{CKM}, as written in Eq. 2.1.3, is unitary, assuming that there exist exactly three generations of quarks. Additional generations would be denoted as extra columns and rows in Eq. 2.1.3. If a fourth generation of quarks and leptons exists, measurements of the Z-boson width at LEP indicate that the neutrinos of that generation must have a mass greater than $M_Z/2$. In Sec. 2.2 we discuss the status of experimental measurements of V_{Qq}.

2.2 Experimental status of V_{CKM}

V_{ud} is the most precisely determined element of the CKM matrix and is determined using decays involving a $d \to u e^- \bar{\nu}$ transition. In particular, measurements of super-allowed nuclear beta decays give [32]

$$|V_{ud}| = 0.9740 \pm 0.0010. \tag{2.2.1}$$

Super-allowed nuclear beta decays currently provide a significantly more precise value of $|V_{ud}|$ than other methods, in part because the decay proceeds purely via a vector current. However, measurements are limited not by experimental statistics, but rather by uncertainties due to nuclear structure corrections and isospin symmetry-breaking corrections. Current experimental errors lead to an uncertainty of approximately 0.0001 on $|V_{ud}|$.

Beta decays of free neutrons and charge pions are other decays that are used to extract $|V_{ud}|$. Unlike super-allowed nuclear decays, values of $|V_{ud}|$ from these processes are currently experimentally limited. In the case of free neutron decay, there are no nuclear structure related corrections, however the decay proceeds via a mixed vector and axial-vector current. Current best values of $|V_{ud}|$ from neutron decay have an uncertainty of ± 0.0021 [35].

As with super-allowed beta decay, pion beta decay is a purely vector current process. Like free neutron decay, it is free of corrections related to the structure of the nucleus. Current best values of $|V_{ud}|$ from pion beta decay have an uncertainty of ± 0.016 [35], limited by the small (10^{-8}) branching fraction of this decay.

The most precise value of $|V_{us}|$ comes from measurements of the decays

$$K^+ \rightarrow \pi^0 \ell^+ \nu, \tag{2.2.2}$$

$$K_L^0 \rightarrow \pi^- \ell^+ \nu, \tag{2.2.3}$$

and is determined to be [36]

$$|V_{us}| = 0.2196 \pm 0.0023 \tag{2.2.4}$$

After isospin breaking corrections (approximately 4% correction on the rates) are taken into account, the values for $|V_{us}|$ found using K^+ and K_L^0 decays are in good agreement.

Decays of Λ, Σ^-, and Ξ^- baryons are also used to determine $|V_{us}|$ [36]. The current best values for $|V_{us}|$ determined by these decays have uncertainties of approximately ± 0.01 and are limited by uncertainties due to $SU(3)$ breaking, primarily in the axial-vector current.

Measurements of the differential cross section for the process $\nu_\mu N \rightarrow \mu^- c X$ give the current best value [32] of

$$|V_{cd}| = 0.224 \pm 0.016. \tag{2.2.5}$$

This cross section is made up contributions from both the valence and sea quarks in the initial nucleon. There is a larger theoretical uncertainty in predicting cross section due to the sea quarks, in part due to the s quark contribution. There are two ways to reduce these uncertainties. Measurements can be performed at large x where the sea quark contributions are small. x is defined as $2E_c/Q$, where Q is the total center-of-mass energy. Alternatively, the cross section for $\bar{\nu}_\mu N \rightarrow \mu^+ \bar{c} X$, which only has a sea quark contribution, can be subtracted from the $\nu_\mu N \rightarrow \mu^- c X$ measured cross section. The dominant uncertainties in $|V_{cd}|$ are experimental. Measurements from new experiments such as NuTeV, NOMAD, CHORUS, COSMOS, and TOSCA will reduce this uncertainty.

By examining the sea quark contribution in the $\nu_\mu N$ cross section one can extract a measurement of $|V_{cs}|$. The uncertainty on doing this is large and is dominated by the uncertainty on the strange quark contribution to the parton sea. Conservative estimates give [32]

$$|V_{cs}| > 0.59 \tag{2.2.6}$$

Alternatively, decays such as $D \to \bar{K}\ell^+\nu$ can be used to determine [32]

$$|V_{cs}| = 1.04 \pm 0.16, \tag{2.2.7}$$

where the dominant errors are again theoretical. In this case, a form-factor normalization is needed to extract $|V_{cs}|$ from the experimental branching fraction. Finally, $W^\pm \to$ hadrons decay can be used. The DELPHI collaboration has recently reported [37]

$$|V_{cs}| = 0.94^{+0.32}_{-0.26} \pm 0.13, \tag{2.2.8}$$

where unitarity and three generations of quarks has been assumed.

The measurement of $|V_{cb}|$ has been a very active area of experimental and theoretical research. Experimentally, semileptonic B-meson decays are the most precise probe of $|V_{cb}|$. In particular, the decays $B \to D^*\ell\nu$ and $B \to D\ell\nu$, as well as the inclusive $b \to c\ell\nu$ branching fraction have been used to measure $|V_{cb}|$. We describe these experimental results further in Chapter 4. As is the case with other elements of the CKM matrix, a theoretical normalization factor is needed to convert the experimental measurement into a measurement of $|V_{cb}|$. Because both the parent (b) and daughter (c) quarks in the $b \to c\ell\nu$ transition are heavy compared to Λ_{QCD}, heavy quark effective theory (HQET) can be used to normalize theoretical predictions at the kinematic point where the c quark is produced at rest in the b quark rest frame. The current average for $|V_{cb}|$ is [32]

$$|V_{cb}| = 0.0395 \pm 0.0017. \tag{2.2.9}$$

This thesis presents a new measurement of $|V_{ub}|$, using the exclusive semileptonic decay mode $B \to \rho\ell\nu$. Theoretical predictions of $b \to u\ell\nu$ decays are more difficult to normalize than those of $b \to c\ell\nu$ decays because HQET cannot be used. Additionally, experimental measurements have thus far been limited to only part of the allowed decay phase space. Thus, theoretical models must also be used to predict kinematic distributions for the measurement of a branching fraction. Besides the decay $B \to \rho\ell\nu$, measurements of inclusive $b \to u\ell\nu$ decays [38, 39, 40, 11, 12] and of the decay $B \to \pi\ell\nu$ [9] have been used to extract $|V_{ub}|$. Measurements of inclusive decays at the $\Upsilon(4S)$ give [32]

$$|V_{ub}/V_{cb}| = 0.08 \pm 0.02. \tag{2.2.10}$$

$|V_{tb}|$ is expected to be quite close to unity. A measurement of this CKM element has been performed by the CDF and D0 collaborations using tagged and untagged $t\bar{t}$ events, where the tagg is on a jet due to the presence of a b-quark in the t-quark decay. If unitarity of V_{CKM} in three quark generations is assumed, $|V_{tb}|$ is found to be

$$|V_{tb}| = 0.99 \pm 0.15, \tag{2.2.11}$$

where the dominant error is statistical. From measurements of $|V_{td}|$ and $|V_{ts}|$ as described below, $|V_{tb}|$ is expected to be greater than 0.99. As such, considerable experimental work is needed to confirm this expectation with precision enough to look for additional quark generations. Data collected by CDF and D0 in the coming years, as well as potential $t \to W^+d$ and $t \to W^+s$ searches will dramatically improve the constraint in Eq. 2.2.11.

$|V_{td}|$ and $|V_{ts}|$ are constrained by measurements of B_d and B_s mixing. B-meson mixing in the standard model proceeds primarily via a box diagram made up of top quarks and W bosons, as shown in Fig. 1.2. Thus, measurements of ΔM are sensitive to $|V_{tb}^*V_{td}|$ and $|V_{tb}^*V_{ts}|$. In the case of the B_d system, current measurements give $\Delta M_d = 0.472 \pm 0.018$ ps^{-1}, which implies [32]

$$|V_{tb}^*V_{td}| = 0.0084 \pm 0.0018. \tag{2.2.12}$$

The large theoretical uncertainty in the extraction of $|V_{tb}^* V_{td}|$ can be reduced by considering the ratio of ΔM_d to ΔM_s. In this case no absolute normalization is needed, only ratios of theoretical predictions are needed to then extract [32]

$$|V_{td}|/|V_{ts}| < 0.27 \tag{2.2.13}$$

As measurements of B_s mixing are improved (currently, only limits have been set) this ratio will become more precise.

2.3 Parametrizations of V_{CKM}

In general, the CKM matrix is an $n \times n$ complex matrix, where n is the number of quark generations. Thus, there are $2n^2$ real variables. Unitarity means that $V^\dagger V = 1$ and provides n^2 constraints. Also $2n-1$ arbitrary phases can be absorbed into the $(d,\ s,\ b)$ and $(d',\ s',\ b')$ quark states. This leaves $2n^2 - n^2 - (2n-1) = (n-1)^2$ free parameters.

From this point on we consider the case $n = 3$, where there are 4 free parameters in the CKM matrix. Three of these parameters can be thought of as rotation angles, and the last a complex phase. A standard parametrization for this case is [32]

$$V = \begin{pmatrix} c_{12}c_{13} & s_{12}c_{13} & s_{13}e^{-i\delta_{13}} \\ -s_{12}c_{23} - c_{12}s_{23}s_{13}e^{i\delta_{13}} & c_{12}c_{23} - s_{12}s_{23}s_{13}e^{i\delta_{13}} & s_{23}c_{13} \\ s_{12}s_{23} - c_{12}c_{23}s_{13}e^{i\delta_{13}} & -c_{12}s_{23} - s_{12}c_{23}s_{13}e^{i\delta_{13}} & c_{23}c_{13} \end{pmatrix} \tag{2.3.1}$$

where $c_{ij} = \cos\theta_{ij}$ and $s_{ij} = \sin\theta_{ij}$. We simplify this form by using the experimental knowledge of this matrix. In particular, we know that $|V_{ub}| \approx 0.003$, so that $c_{13} \approx 1$ and terms that are proportional to s_{13} are small. Thus, Eq. 2.3.1 becomes

$$V = \begin{pmatrix} c_{12}c_{13} & s_{12}c_{13} & s_{13}e^{-i\delta_{13}} \\ -s_{12}c_{23} & c_{12}c_{23} & s_{23}c_{13} \\ s_{12}s_{23} - c_{12}c_{23}s_{13}e^{i\delta_{13}} & -c_{12}s_{23} & c_{23}c_{13} \end{pmatrix} \tag{2.3.2}$$

to a very good approximation. A parametrization due to Wolfenstein [45] takes further advantage of the measured values of the CKM matrix to establish a hierarchy (in magnetudes) between columns. An expansion is performed in $\lambda \equiv \sin\theta_{12}$ is performed to give

$$V \approx \begin{pmatrix} 1-\lambda^2/2 & \lambda & A\lambda^3(\rho - i\eta) \\ -\lambda & 1-\lambda^2/2 & A\lambda^2 \\ A\lambda^3(1-\rho-i\eta) & -A\lambda^2 & 1 \end{pmatrix} + \mathcal{O}(\lambda^4) \tag{2.3.3}$$

We can use the results of the previous section to determine the values of the four parameters:

$$\lambda = 0.2196 \pm 0.0023 \tag{2.3.4}$$

$$A = 0.819 \pm 0.035 \tag{2.3.5}$$

$$\sqrt{\rho^2+\eta^2} = 0.36 \pm 0.09 \tag{2.3.6}$$

Three of these four parameters (A, ρ, and η) can be probed using B-meson decays. In particular, A is constrained by measurements of $|V_{cb}|$ using $b \to c$ semileptonic decays. Similarly, $b \to u$ semileptonic decays can be used to measure $|V_{ub}|$, and thus $\sqrt{\rho^2+\eta^2}$. Measurements of CP asymmetries in hadronic B-meson decays, such as $B \to J/\psi K_s$, $B \to \pi\pi$, and $B \to D^* D^*$, should provide measurements of the angles of the unitarity triangle, described below, and will constrain ρ and η individually.

2.4 The unitarity triangle

Tests of unitarity in a CKM matrix consisting of three generations provide ways to search for new physics. Of particular interest is the orthogonality of the first and third columns:

$$V_{ud}V_{ub}^* + V_{cd}V_{cb}^* + V_{td}V_{tb}^* = 0 \tag{2.4.1}$$

To simplify this, realize that $V_{ud} \approx 1$ and $V_{tb} \approx 1$. Thus,

$$\frac{-V_{ub}^*}{V_{cd}V_{cb}^*} + \frac{-V_{td}}{V_{cd}V_{cb}^*} = 1 \tag{2.4.2}$$

We can additionally use Eq. 2.3.3 and realize that $V_{cd} < 0$ and that both V_{cd} and V_{cb} are real. Then

$$\frac{V_{ub}^*}{|V_{cd}V_{cb}|} + \frac{V_{td}}{|V_{cd}V_{cb}|} = 1 \tag{2.4.3}$$

This constraint is illustrated in Fig. 2.1, and is commonly refered to as the "unitarity triangle". It is important to note that the lengths of all three sides as written in Eq. 2.4.3 are proportional to λ^0. There are actually six such triangles, corresponding to the orthogonality between pairs of columns and of rows in the CKM matrix. Four of the other triangles have sides with lengths proportional to different powers of λ.

We will discuss the relationship between CP violation and the CKM matrix below. Here we simply state a few conclusions. First, for CP violation to occur within the framework of the standard model and the CKM matrix, η must be nonzero. The apex of the unitarity triangle is (ρ, η) in the complex plane, thus $\eta \neq 0$ implies that the unitarity triangle is not degenerate. CP-violating amplitudes are fundamentally related to the area of the unitarity triangle.

Constraining the apex of the unitarity triangle is the subject of considerable experimental work. In particular, measurements of $|V_{ub}|$, B_d and B_s mixing, and ϵ_K from the neutral K system provide constraints. Figure 2.6 shows the current status of these constraints.

As $|V_{ub}| = A\lambda^3\sqrt{\rho^2 + \eta^2}$, measurements of $|V_{ub}|$ constrain the (ρ, η) apex to lie somewhere on a circle centered at $(0, 0)$. This constraint is shown in Fig. 2.2.

As described above, B_d mixing amplitudes are proportional to $|V_{tb}^* V_{td}|$ and thus constrain $|V_{td}| = A\lambda^3\sqrt{(1-\rho)^2 + \eta^2}$, a circle centered around $(1, 0)$. In particular [47],

$$\Delta M_d = 0.50 \text{ ps}^{-1} \left[\frac{\sqrt{B_{B_d}} f_{B_d}}{200MeV}\right]^2 \left[\frac{\bar{m}_t}{170GeV}\right]^{1.52} \left[\frac{|V_{td}|}{8.8 \times 10^{-3}}\right]^2 \left[\frac{\eta_B}{0.55}\right]. \tag{2.4.4}$$

The LEP B Oscillations Working Group has computed an average for $\Delta M_d = (0.472 \pm 0.018)$ ps^{-1} [32]. The dominant uncertainty in Eq. 2.4.4 is due to f_{B_d},

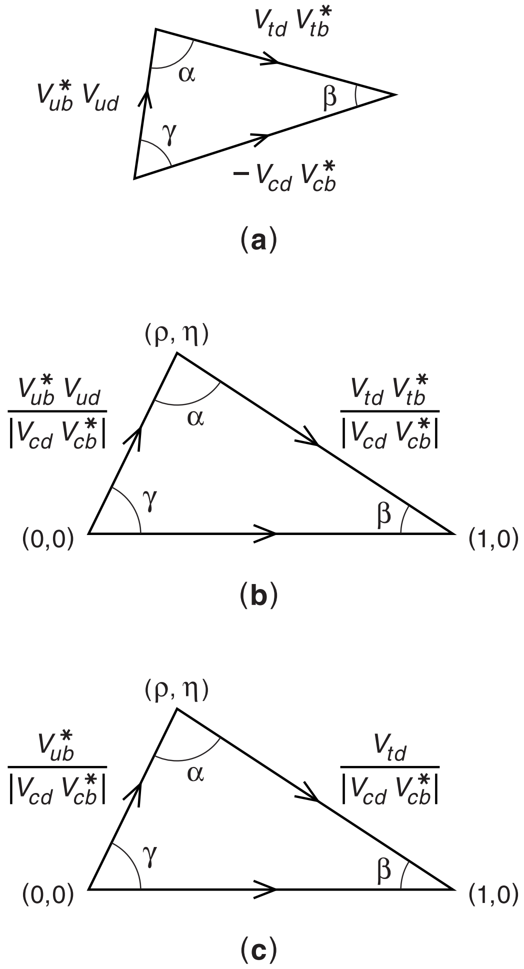

Figure 2.1: The CKM unitarity triangle based on the orthogonality between the first and third columns of the CKM matrix. From Ref. [49].

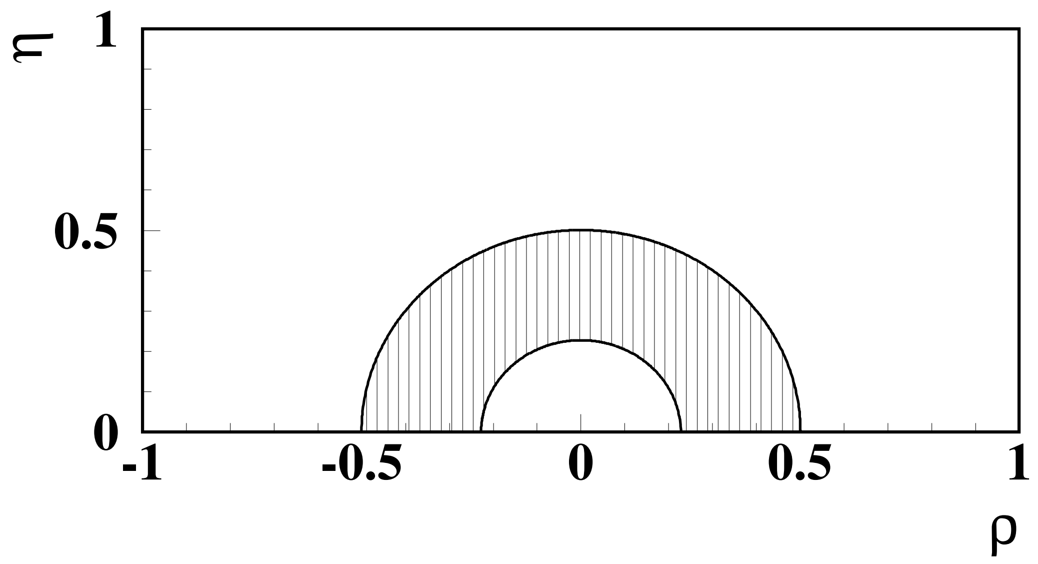

Figure 2.2: Current constraints on the unitarity triangle from measurements of $|V_{ub}|$ using inclusive B-meson decays at the $\Upsilon(4S)$. The largest uncertainty is due to the extrapolation from the lepton-energy endpoint region to the full range of allowed lepton energies. The hatched bands correspond to 1.5σ errors.

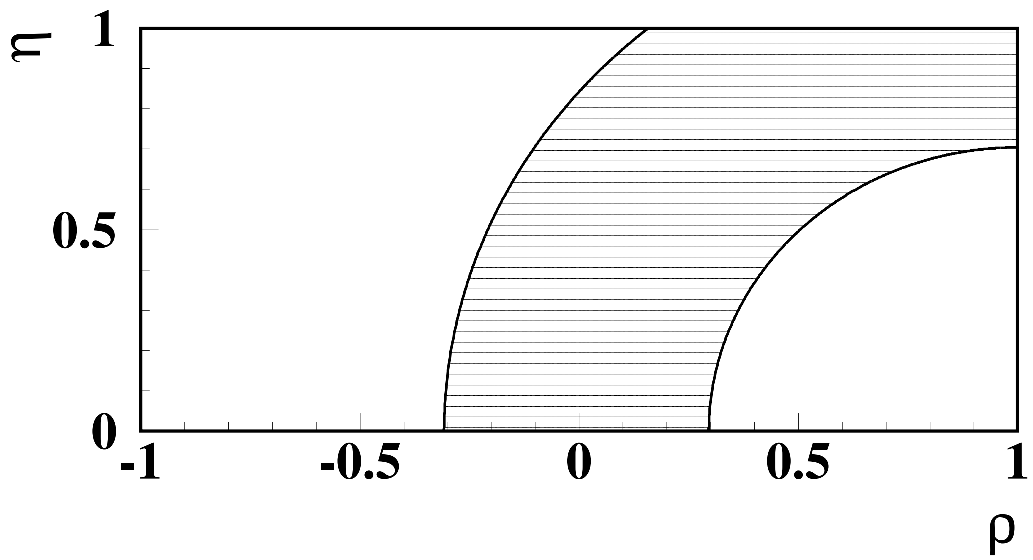

Figure 2.3: Current constraints on the unitarity triangle from measurements of $|V_{td}|$ using $B_d^0 - \bar{B}_d^0$ mixing. The dominant uncertainties are theoretical. The hatched band corresponds to a 1.5σ allowed region.

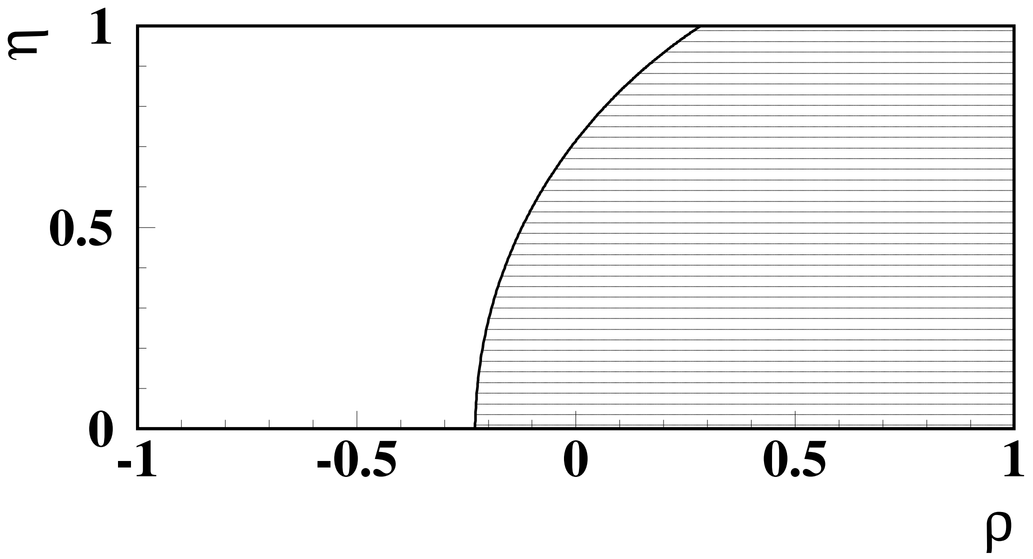

Figure 2.4: Current constraints on the unitarity triangle from measurements of $|V_{td}|$ using $B_d^0 - \bar{B}_d^0$ and $B_s^0 - \bar{B}_s^0$ mixing. The dominant uncertainty is due to the limit on B_s mixing. The hatched band corresponds to a 1.5σ allowed region.

which is the B_d decay constant. We have used $f_{B_d} = 175 \pm 25$ MeV [46]. The constraint on the values of $(\rho,\ \eta)$ from B_d mixing is shown in Fig. 2.3.

Additionally limits on $|V_{td}|/|V_{ts}|$ (see Eq. 2.2.13) provide circular constraints on the (ρ, η) plane centered at (1,0). Many theoretical errors cancel in the ratio of $\Delta M_d/\Delta M_s$. As there are currently only limits on ΔM_s, the limiting errors on this constraint are experimental. Figure 2.4 shows the region of the ρ-η plane allowed by current limits $|V_{td}|/|V_{ts}|$.

CP violation in the K^0 system is the sole constraint that $\eta \neq 0$. Measurements of $K_L \to 2\pi$ indicate that the mass eigenstates in the neutral kaon system are not the same as the CP eigenstates. The parameter [47, 48]

$$\epsilon_K \approx \frac{exp(i\pi/4)}{\sqrt{2}\Delta M_K} Im M_{12} \tag{2.4.5}$$

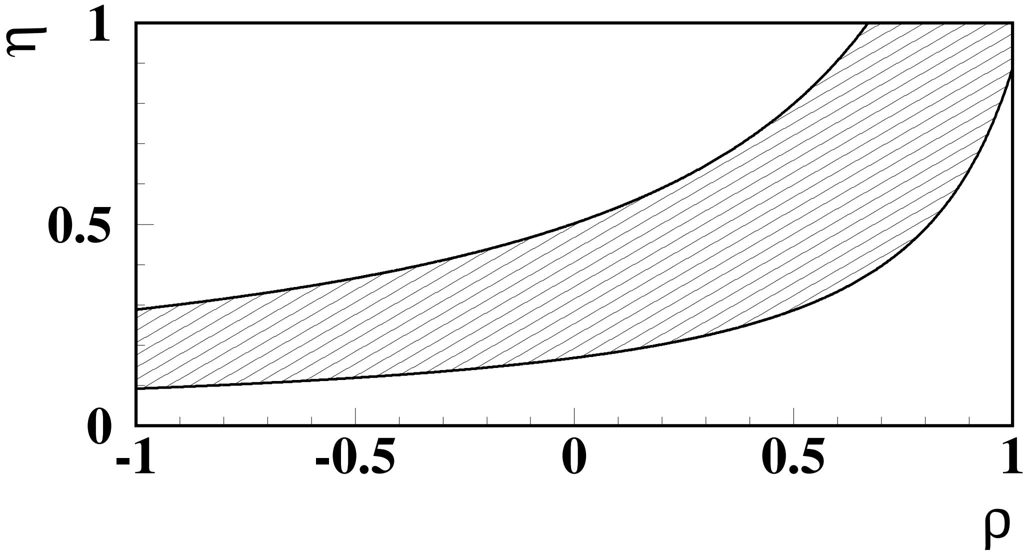

Figure 2.5: Current constraints on the unitarity triangle from measurements of ϵ_K, the parameter that describes indirect CP-violation in the neutral K system. The largest uncertainties are from $|V_{cb}|$ and on the bag constant, B_K. The hatched band corresponds to a 1.5σ allowed region.

is a measure of the amplitude for $K_L \to \pi\pi$ decay relative that for $K_S \to \pi\pi$ decay. M_{12} is the off-diagonal element of the mass matrix, and ΔM_K is the $K_L - K_S$ mass difference. Experimentally, ϵ_K has been measured to be [32]

$$\epsilon_K = (2.280 \pm 0.013) \times 10^{-3} e^{i\pi/4}. \tag{2.4.6}$$

We do not explicitly write out the form of M_{12}. The pieces of M_{12} that have the largest uncertainties are A and B_K. The dependence on A comes from V_{ts} and enters at the fourth power. Thus, ϵ_K effectively depends on $|V_{cb}|^4$. B_K parameterizes non-perturbative QCD effects, and is refered to as the bag constant. Other CKM matrix elements and theoretical factors in M_{12} have a realively small uncertainty. The constraint on the ρ-η plane is shown in Fig. 2.5.

Figure 2.6 shows the combined constraint on the ρ-η plane from the four sources described above. Experimentally, the allowed area in the ρ-η plane

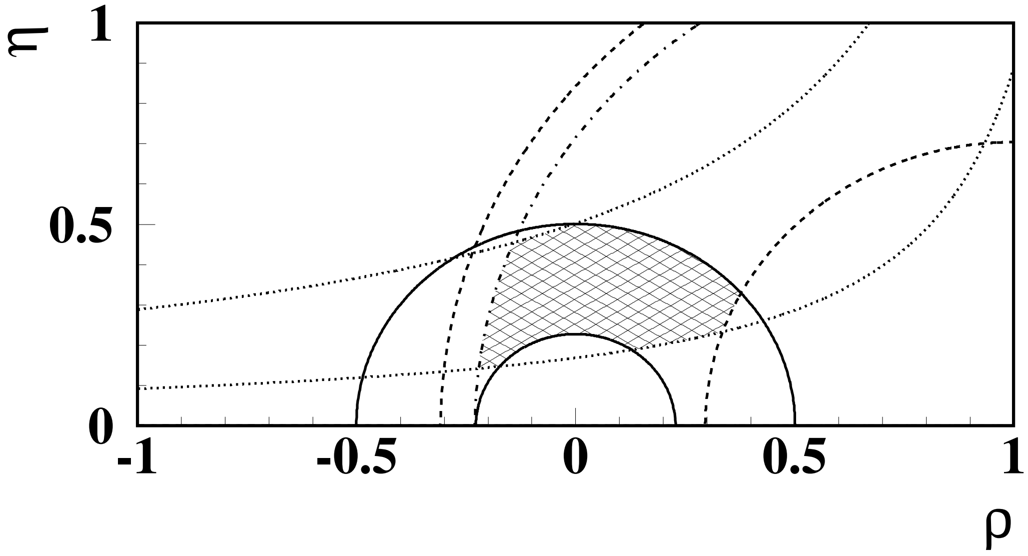

Figure 2.6: Current constraints on the unitarity triangle from measurements of $|V_{ub}|$ (solid lines), B_d mixing (dashed lines), B_s mixing (dot-dashed lines), and ϵ_K (dotted lines). The hatched band corresponds to a 1.5σ allowed region. Note that the individual constraints shown here do not lead to quite the correct overall constraint due to correlations. See Ref. [49].

can be reduced by improved measurements of $|V_{ub}|$ and $|V_{cb}|$, B_s mixing, and measurements of CP asymmetries in B-meson decays.

2.5 CP violation

It has been more than 30 years since CP violation was first observed in the $K^0\bar{K}^0$ system [2]. The source (or sources) of this violation (in the $K^0\bar{K}^0$ system, the violation is of order 10^{-3}) is still not known. Within the standard model, the explaination for CP violation lies within the CKM matrix. This mechanism will be verified (or refuted) by studies of CP asymmetries in the $B^0\bar{B}^0$ system in the relatively near future. In this section, we describe the formalism for CP violation due to interference between mixing and decay within the standard model and show that the CKM matrix plays an important role in the understanding of CP violation.

We consider an arbitrary coupled two-particle system, such as the B^0 and $\bar{B}^0$. Their time evolution is described by

$$i\frac{d}{dt}\begin{pmatrix} B^0 \\ \bar{B}^0 \end{pmatrix} = \begin{pmatrix} M - i\Gamma/2 & M_{12} - i\Gamma_{12}/2 \\ M_{12}^* - i\Gamma_{12}^*/2 & M - i\Gamma/2 \end{pmatrix} \begin{pmatrix} B^0 \\ \bar{B}^0 \end{pmatrix}. \tag{2.5.1}$$

Neither B^0 or $\bar{B}^0$ are in general eigenstates of the Hamiltonian. For CPT invariance to hold, the on-diagonal elements must be equal. For CP invariance, M_{12} and Γ_{12} must be real, such that the two off-diagonal elements are equal. We will now show how an imaginary M_{12} leads to asymmetries between the B^0 and $\bar{B}^0$ in shared decay modes. We begin by finding the eigenstates that diagonalize the matrix in Eq. 2.5.1

$$\begin{aligned} |B_1\rangle &= \frac{1}{\sqrt{p^*p + q^*q}}\left(p|B^0\rangle + q|\bar{B}^0\rangle\right) \\ |B_2\rangle &= \frac{1}{\sqrt{p^*p + q^*q}}\left(p|B^0\rangle - q|\bar{B}^0\rangle\right), \end{aligned} \tag{2.5.2}$$

which have eigenvalues $M \pm M_{12} - i(\Gamma \pm \Gamma_{12})/2$. In the $B^0 - \bar{B}^0$ system, Γ_{12} is small and can be neglected. In this case $p/q = \sqrt{M_{12}^*/M_{12}}$ and $|p/q| = 1$. These new eigenstates (and their eigenvalues) allow us to write the time evolution of an initial state consisting of a B^0 or a $\bar{B}^0$

$$\begin{aligned} |B^0(t)\rangle &= \frac{\sqrt{p^*p + q^*q}}{p} \\ &\times \left(e^{-i(M+M_{12}-i\Gamma/2)t}|B_1\rangle + e^{-i(M-M_{12}-i\Gamma/2)t}|B_2\rangle\right) \\ |B^0(t)\rangle &= \frac{\sqrt{p^*p + q^*q}}{q} \\ &\times \left(e^{-i(M+M_{12}-i\Gamma/2)t}|B_1\rangle + (p/q)e^{-i(M-M_{12}-i\Gamma/2)t}|B_2\rangle\right). \end{aligned} \tag{2.5.3}$$

We can rewrite these in terms of the original set of basis states, $|B^0\rangle$ and $|\bar{B}^0\rangle$,

$$\begin{aligned}
|B^0(t)\rangle &= e^{-iMt}e^{-\Gamma/2t}\cos(M_{12}t)|B^0\rangle \\
&+ (iq/p)e^{-iMt}e^{-\Gamma/2t}\sin(M_{12}t)|\bar{B}^0\rangle \\
|\bar{B}^0(t)\rangle &= (ip/q)e^{-iMt}e^{-\Gamma/2t}\sin(M_{12}t)|B^0\rangle \\
&+ e^{-iMt}e^{-\Gamma/2t}\cos(M_{12}t)|\bar{B}^0\rangle. \qquad (2.5.4)
\end{aligned}$$

To illustrate the conditions necessary for the presence of CP asymmetries, we consider decays of a B^0 and $\bar{B}^0$ to final states that are CP eigenstates, such as $\pi^+\pi^-$, $D^{*+}D^-$, and $J/\psi K_s$, which will be denoted as f_{CP}. The amplitude for these decays will be denoted as

$$\begin{aligned}
A &= \langle f_{CP}|\mathcal{H}|B^0\rangle \\
\bar{A} &= \langle f_{CP}|\mathcal{H}|\bar{B}^0\rangle \qquad (2.5.5)
\end{aligned}$$

Using Eq. 2.5.4 we now can write the time dependent decay amplitudes for a state at $t = 0$ that is either a B^0 or $\bar{B}^0$ to decay into f_{CP}:

$$\begin{aligned}
\langle f_{CP}|\mathcal{H}|B^0(t)\rangle &= Ae^{-iMt}e^{-\Gamma/2t}\cos(M_{12}t) \\
&+ (i\bar{A}q/p)e^{-iMt}e^{-\Gamma/2t}\sin(M_{12}t) \\
\langle f_{CP}|\mathcal{H}|\bar{B}^0(t)\rangle &= (iAp/q)e^{-iMt}e^{-\Gamma/2t}\sin(M_{12}t) \\
&+ \bar{A}e^{-iMt}e^{-\Gamma/2t}\cos(M_{12}t). \qquad (2.5.6)
\end{aligned}$$

It is now convenient to define λ as

$$\lambda \equiv \frac{q\bar{A}}{pA}. \qquad (2.5.7)$$

Squaring these amplitudes to determine decay widths, we find

$$\begin{aligned}
\Gamma(B^0 &\rightarrow f_{CP}) = \\
|A|^2 \quad & e^{-\Gamma t}\left(\frac{1+|\lambda|^2}{2} - \frac{1-|\lambda|^2}{2}\cos(M_{12}t) - Im\lambda\sin(M_{12}t)\right) \\
\Gamma(\bar{B}^0 &\rightarrow f_{CP}) = \\
|A|^2 \quad & e^{-\Gamma t}\left(\frac{1+|\lambda|^2}{2} - \frac{1-|\lambda|^2}{2}\cos(M_{12}t) + Im\lambda\sin(M_{12}t)\right)(2.5.8)
\end{aligned}$$

Thus, these rates are different if λ is not completely real. To be quantitative, we define a CP asymmetry as

$$a_{CP} = \frac{\Gamma(B^0 \to f_{CP}) - \Gamma(\bar{B}^0 \to f_{CP})}{\Gamma(B^0 \to f_{CP}) + \Gamma(\bar{B}^0 \to f_{CP})}, \tag{2.5.9}$$

which is a function of time. In principle $|A/\bar{A}|$ does not have to be equal to unity. However, if it is, the expression for a_{CP} is quite simple

$$a_{CP} = -Im\lambda \sin(M_{12}t). \tag{2.5.10}$$

The condition for $|A/\bar{A}| = 1$, which we will not prove, is that all amplitudes that make up A must depend on the same CKM phase.

We have now shown that $\lambda = (q\bar{A}/pA)$ must be complex to observe a CP asymmetry. Now we discuss the example $B \to \pi^+\pi^-$, which proceeds via a $b \to u$ transition by an external spectator diagram (See Fig. 1.2c).

First we will compute q/p. Recall that

$$\frac{q}{p} = \sqrt{\frac{M_{12}^*}{M_{12}}} \tag{2.5.11}$$

where M_{12} describes the mixing between the B^0 and $\bar{B}^0$ mesons. In particular, $M_{12} \propto (V_{td}V_{td}^*)^2$ as illustrated in Fig. 1.2h. Thus,

$$\frac{q}{p} = \frac{V_{tb}^*V_{td}}{V_{tb}V_{td}^*}. \tag{2.5.12}$$

Now we must consider the $B \to \pi\pi$ piece of the decay in order to compute $A/\bar{A}$. For the decay $\bar{B}^0 \to \pi^+\pi^-$, there is a $b \to uW^-$ transition followed by a $W^- \to \bar{u}d$ decay. Thus the amplitude is proportional to $V_{ub}V_{ud}^*$. Conversely, the amplitude for $B^0 \to \pi^+\pi^-$ is proportional to $V_{ub}^*V_{ud}$. Thus,

$$\frac{\bar{A}}{A} = \frac{V_{ub}V_{ud}^*}{V_{ub}^*V_{ud}}. \tag{2.5.13}$$

Combining these expressions,

$$\lambda = \left(\frac{V_{tb}^*V_{td}}{V_{tb}V_{td}^*}\right)\left(\frac{V_{ub}V_{ud}^*}{V_{ub}^*V_{ud}}\right). \tag{2.5.14}$$

$Im\lambda$ is then equal to $\sin(2\alpha)$, where α is defined in Fig. 2.1. The same procedure can be repeated for other final states that are CP eigenstates.

We can draw conclusions from the calculation presented in this section. First, complex phases in the CKM triangle are necessary to observe a CP asymmetry in the mechanism within the standard model. In addition, observing such asymmetries in the B system, which effectively measure the angles of the unitarity triangle, will provide additional information with which to constrain the apex (ρ, η) of this triangle. If these angles are found to be inconsistent with one another, or with the current constraints from $|V_{ub}|$, B mixing, and ϵ_K, then CP violation in the B system will be a sign of new physics.

2.6 B decays to measure $|V_{\rm CKM}|$

We discuss how B-meson decays can be used to measure elements of the CKM matrix, in particular $|V_{cb}|$ and $|V_{ub}|$. In broad terms, there are three classes of B decays: leptonic, hadronic, and semileptonic. We discuss each of these.

The decay rate for leptonic decays, which proceed via the process shown in Fig. 2.7, such as $B^- \to \mu^- \bar{\nu}$, can be exactly written as

$$\Gamma(M_{Q\bar{q}} \to \ell^- \bar{\nu}) = \frac{G_F^2}{8\pi}|V_{qQ}|^2 f_M^2 M m_\ell^2 \left(1 - \frac{m_\ell^2}{M^2}\right)^2, \tag{2.6.1}$$

where f_M is the decay constant of the parent meson. Theoretically, leptonic decays are clean because the strong interactions effects are present only in this decay constant. Experimentally, however, the branching fraction for $B \to \mu^- \bar{\nu}$ is very small and is expected to be $\approx 3 \times 10^{-7}$. In practice, leptonic decays, in particular $D_s \to \mu^- \bar{\nu}$, have been used to measure f_M.

Diagrams for hadronic decays are depicted in Fig. 2.8. Theoretically, it is very difficult relate an experimental branching fraction to the magnitude of a CKM matrix element. This is true for two reasons, both unique to hadronic decays. First, there are multiple diagrams, for example the external and internal spectator diagrams shown in Fig. 2.8. Also, strong interaction effects are

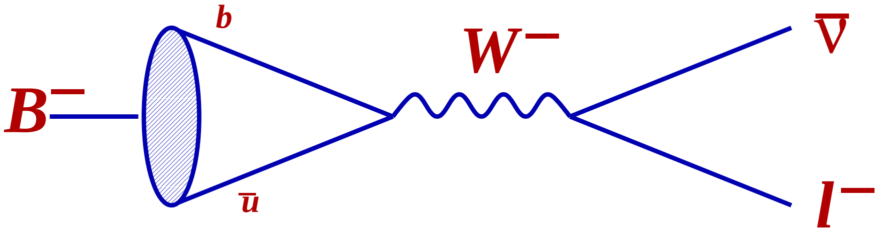

Figure 2.7: Diagram for leptonic decays, such as $B^- \to \mu^- \bar{\nu}$.

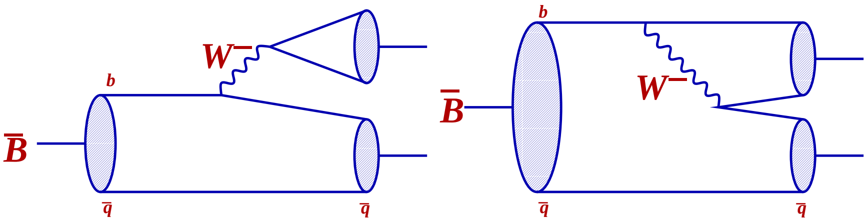

Figure 2.8: Diagrams for hadronic decays. Because of strong interaction effects and the presence of multiple diagrams, measurements of hadronic decays are difficult to interrept in terms of absolute values of CKM elements. The presence of multiple diagrams, however, allows for the measurement of interference effects and CP-violating phases.

present throughout the diagram. In contrast to semileptonic decays, these effects can not be isolated to a single hadronic current (say, that which describes the interaction of quark from the $b \to qW$ decay and spectator quark). For example, in the external spectator diagram, final-state interactions between the quark from the $b \to qW$ decay and those from the W decay can be significant, and difficult to parametrize.

While hadronic decays are difficult to use for measuring magnitudes of CKM matrix elements, they uniquely can measure interference effects between different diagrams for the same decay. In this way, hadronic B decays can be used to measure the angles α, β, and γ of the unitarity triangle, shown in Fig. 2.1.

The third class of B decays is semileptonic decays. The diagram for $B \to$

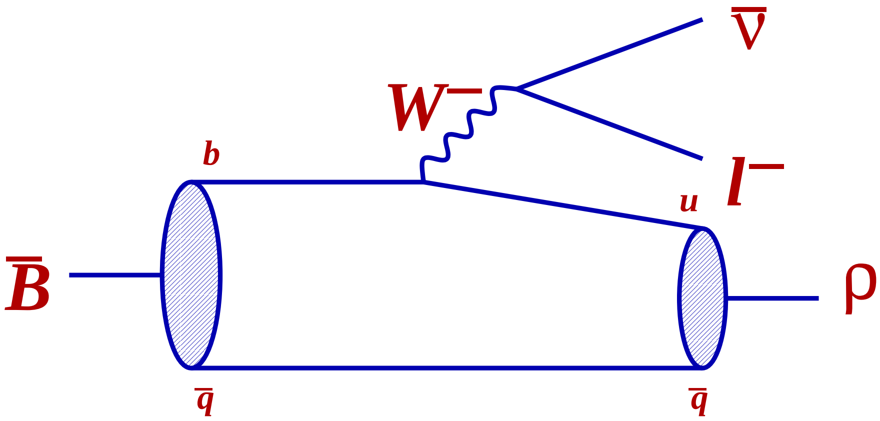

Figure 2.9: Diagram for $B \to \rho\ell\nu$ decay. Semileptonic decays are usefull for measuring magnitudes of CKM matrix elements because the strong interaction effects are isolated to the lower part of the diagram and can be described in terms of a single hadronic current in the amplitude.

$\rho\ell\nu$ is shown in Fig. 2.9. Branching fractions range from 5% for $B \to D^*\ell\nu$ down to 10^{-4} for $b \to u\ell\nu$ processes. Strong interaction effects are isolated to the lower piece of the diagram in Fig. 2.9. As we will describe in Chapter 3, the matrix element for semileptonic decay can be written in terms of a leptonic current and a single hadronic current. The hadronic current can be rigorously parameterized in terms of form factors, which can be predicted theoretically. Thus, semileptonic decays are good processes to measure magitudes of CKM matrix elements. In particular, semileptonic B-meson decays are used to measure $|V_{cb}|$ and $|V_{ub}|$.

Chapter 3

Theoretical predictions for $b \to u\ell\nu$

We introduce the kinematics of semileptonic decays of heavy mesons. The matrix element for semileptonic decay factors into a leptonic and a hadronic current. Theoretical predictions for form factors are needed to parameterize the hadronic current. In Sec. 3.1 we describe the matrix element and decay kinematics of semileptonic decays as well as the consequences of the $V - A$ coupling of the weak interaction. In Sec. 3.2 we then detail form-factor models of $B \to \rho\ell\nu$ decay. In particular we describe the theoretical approach and give the parametrization of each model that is utilizied in the extraction of results in this thesis.

3.1 Semileptonic decay kinematics

The matrix element for the semileptonic decay $P(Q\bar{q}) \to V(q'\bar{q})\ell^-\bar{\nu}$ of a pseudoscalar meson, $P(Q\bar{q})$, to a vector meson, $V(q'\bar{q})$, can be written [50]

$$\mathcal{M}(P \to V\ell\nu) = -i\frac{G_F}{\sqrt{2}}V_{q'Q}L^\mu J_\mu, \tag{3.1.1}$$

where $V_{q'Q}$ is the CKM matrix element for the $Q \to q'$ transition [51], L^μ is the leptonic current

$$L^\mu = \bar{u}_\ell \gamma^\mu (1-\gamma_5) v_\nu, \tag{3.1.2}$$

and the hadronic current

$$\begin{aligned} J_\mu = \langle V(p_V,\varepsilon)|(V-A)_\mu|P(p_P)\rangle = & - \varepsilon^*_\mu (m_P+m_V) A_1(q^2) \\ & + (p_V+p_P)_\mu (\varepsilon^* \cdot q) \frac{A_2(q^2)}{(m_P+m_V)} \\ & + q_\mu (\varepsilon^* \cdot q) \frac{2m_V}{q^2} \big(A_3(q^2) - A_0(q^2)\big) \\ & + 2i\epsilon_{\mu\nu\rho\sigma} \varepsilon^{*\nu} p_V^\rho p_P^\sigma \frac{V(q^2)}{m_P+m_V}, \end{aligned} \tag{3.1.3}$$

is written in terms of four form factors, $A_1(q^2)$, $A_2(q^2)$, $V(q^2)$, and $A_0(q^2)$, where $A_0(0) = A_3(0)$ and

$$A_3(q^2) = \frac{m_P+m_V}{2m_V} A_1(q^2) - \frac{m_P-m_V}{2m_V} A_2(q^2). \tag{3.1.4}$$

Here m_P, m_V, p_P, and p_V are the pseudoscalar and vector meson masses and four-momenta, $q \equiv p_P - p_V$, and ε is the vector-meson polarization four-vector. Terms in J_μ proportional to q_μ vanish in the limit of massless leptons, so that the decay $B \to \rho\ell\nu$ depends effectively on only three form factors ($A_1(q^2)$, $A_2(q^2)$, and $V(q^2)$) for electrons or muons.

Figure 3.1 shows the $q^2 = (p_P - p_V)^2 = (p_\ell + p_\nu)^2$ kinematic configurations at $q^2 = q^2_{\text{max}}$ and $q^2 = q^2_{\text{min}} \approx 0$. It is most straightforward to work in the B meson rest frame, which is essentially the rest frame of the b quark because $m_b \gg m_d$. At q^2_{max}, the daughter meson remains at rest, while the lepton and neutrino recoil in opposite directions. In contrast, at q^2_{min} the daughter u quark moves opposite of the lepton and neutrino, which are colinear.

The q^2_{max} configuration points out an important difference between $b \to u\ell\nu$ and $b \to c\ell\nu$ transitions. In the latter case, the meson momentum is still essentially determined by the heavy charm quark. Thus at q^2_{max}, $\mathbf{p}_{\text{charm quark}} \approx$

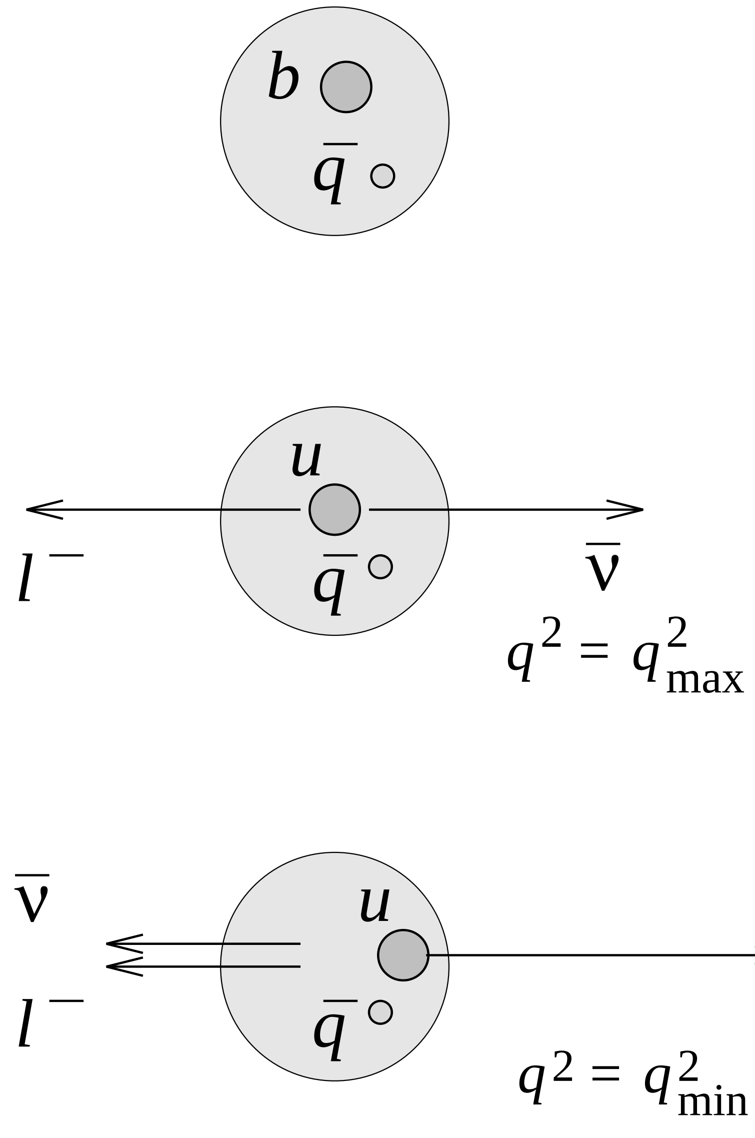

Figure 3.1: Extreme q^2 configurations in $b \to u\ell\nu$ decay. At $q^2_{\rm max}$ (b), the daughter meson remains at rest, while the lepton and neutrino recoil in opposite directions. In contrast, at $q^2_{\rm min}$ the daughter u quark moves opposite of the lepton and neutrino, which are colinear. From Ref. [49].

Decay	q^2 range (GeV$^2/c^4$)	w range
$B \to D^*\ell\nu$	$m_\ell^2 \approx 0 \to 10.7$	$1 \to 1.50$
$B \to D\ell\nu$	$m_\ell^2 \approx 0 \to 11.7$	$1 \to 1.59$
$B \to \rho\ell\nu$	$m_\ell^2 \approx 0 \to 20.3$	$1 \to 3.51$
$B \to \pi\ell\nu$	$m_\ell^2 \approx 0 \to 26.4$	$1 \to 18.9$
$D \to K^*\ell\nu$	$m_\ell^2 \approx 0 \to 0.94$	$1 \to 1.28$
$D \to K\ell\nu$	$m_\ell^2 \approx 0 \to 1.20$	$1 \to 2.01$
$D \to \rho\ell\nu$	$m_\ell^2 \approx 0 \to 1.87$	$1 \to 1.42$
$D \to \pi\ell\nu$	$m_\ell^2 \approx 0 \to 2.97$	$1 \to 6.70$

Table 3.1: Allowed range for q^2 and w for various semileptonic decays of B and D mesons. The range for $b \to u\ell\nu$ decay is significantly greater than for other decay processes.

$\mathbf{p}_{\text{daughter meson}} \approx 0$. In this way, q^2_{max} is a relatively straightforward point at which to normalize theoretical predictions. In $b \to u\ell\nu$ transitions, the daughter u quark does not determine the daughter meson momentum, and this normalization point less reliable.

q^2 is also related to the relativistic γ factor of the daugther hadron,

$$w = \frac{m_P^2 + m_V^2 - q^2}{2m_P m_V}. \tag{3.1.5}$$

Table 3.1 shows the allowed range for q^2 and w for semileptonic decays of B and D mesons. This points out another important distinction between the predictions $b \to u\ell\nu$ decays and other semileptonic decays. Because the allowed q^2 (and w) range is significantly larger than for other decay modes, predictions for $B \to \rho\ell\nu$ and $B \to \pi\ell\nu$ must be extrapolated over a larger range of q^2.

The amplitudes for the vector meson to have helicity $+1$, -1, or 0, denoted by $H_+(q^2)$, $H_-(q^2)$, and $H_0(q^2)$, can be expressed in terms of the form factors:

$$
\begin{aligned}
H_\pm(q^2) &= (m_P + m_V)A_1(q^2) \mp \frac{2m_P|\mathbf{p}_V|}{m_P + m_V}V(q^2), \\
H_0(q^2) &= \frac{1}{2m_V\sqrt{q^2}}\big[(m_P^2 - m_V^2 - q^2)(m_P + m_V)A_1(q^2) \\
&- 4\frac{m_P^2|\mathbf{p}_V|^2}{m_P + m_V}A_2(q^2)\big],
\end{aligned} \tag{3.1.6}
$$

where $\mathbf{p}_V$ is the vector meson three-momentum in the B-meson rest frame, which is a function of q^2

$$
|\mathbf{p}_V| = \sqrt{\left(\frac{m_P^2 + m_V^2 - q^2}{2m_P}\right)^2 - m_V^2}. \tag{3.1.7}
$$

As q^2 decreases from $q^2_{\max} = (m_P - m_V)^2$ to $q^2_{\min} = m_\ell^2 \approx 0$, $|\mathbf{p}_V|$ increases from $|\mathbf{p}_V|_{\min} = 0$ to $|\mathbf{p}_V|_{\max} = (m_P^2 - m_V^2)/2m_P^2$. At large q^2, the $A_1(q^2)$ form factor therefore dominates all three of the helicity amplitudes. The full differential decay rate for $P \to V\ell\nu$ ($V \to P_1P_2$) is given by [50]

$$
\begin{aligned}
\frac{d\Gamma}{dq^2 d\cos\theta_\ell d\cos\theta_V d\chi} &= \frac{3}{8(4\pi)^4}G_F^2|V_{q'Q}|^2\frac{|\mathbf{p_V}|q^2}{m_P^2}\mathcal{B}(V \to P_1P_2) \\
&\times \Big[(1 - \eta\cos\theta_\ell)^2\sin^2\theta_V|H_+(q^2)|^2 \\
&+ (1 + \eta\cos\theta_\ell)^2\sin^2\theta_V|H_-(q^2)|^2 \\
&+ 4\sin^2\theta_\ell\cos^2\theta_V|H_0(q^2)|^2 \\
&- 2\eta\sin\theta_\ell(1 - \eta\cos\theta_\ell)\sin 2\theta_V\cos\chi H_+(q^2)H_0(q^2) \\
&+ 2\eta\sin\theta_\ell(1 + \eta\cos\theta_\ell)\sin 2\theta_V\cos\chi H_-(q^2)H_0(q^2) \\
&- 2\sin^2\theta_\ell\sin^2\theta_V\cos 2\chi H_+(q^2)H_-(q^2)\Big],
\end{aligned} \tag{3.1.8}
$$

where $q^2 = (p_P - p_V)^2$, θ_ℓ is the polar angle of the lepton in the W rest frame with respect to the W flight direction in the B rest frame, and θ_V is the polar angle of one of the pseudoscalar daughters in the rest frame of the vector meson with respect to the vector-meson flight direction in the B rest frame. χ is the

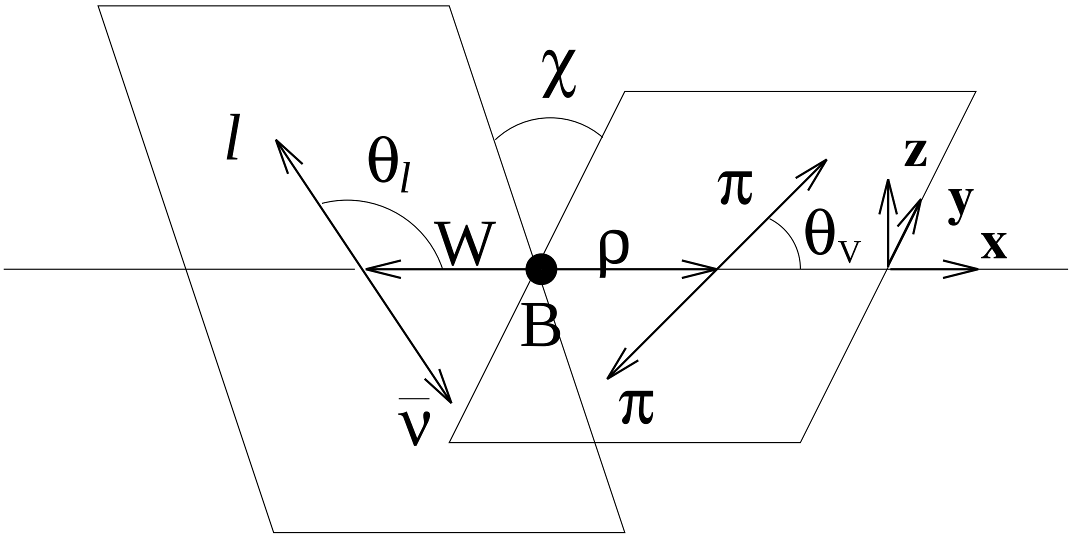

Figure 3.2: Definition of $\cos\theta_\ell$, $\cos\theta_V$, and χ in $B \to \rho\ell\nu$ decay. $theta_\ell$ is defined to be the angle between the lepton momentum in the W rest frame and the W momentum in the B-meson rest frame. Similarly, θ_V is the angle between the momentum of one of the pions from the ρ decay and the ρ momentum in the B-meson rest frame. χ is defined to be the angle between the ρ and W decay planes.

angle between the decay planes of the W and the vector meson. These angles are illustrated in Fig. 3.2. The factor η is equal to $+1$ (-1) when the quark Q has charge $-1/3$ $(+2/3)$.

3.2 Form-factor models of $B \to \rho\ell\nu$

For the extraction of $\mathcal{B}(B \to \rho\ell\nu)$ and $\Delta\Gamma$ in bins of q^2 from the data, we use Eq. 3.1.8 to extrapolate our measurements based primarily on the high lepton energy part of the decay phase space to the entire phase space. The form factors $A_1(q^2)$, $A_2(q^2)$, and $V(q^2)$ are evaluated using various models, whose predictions are shown in Figs. 3.3, 3.4, and 3.5. For the measurement of $|V_{ub}|$, models additionally provide the normalization $\tilde{\Gamma}_{\rm thy} \equiv \Gamma(B \to$

$\rho\ell\nu)/|V_{ub}|^2$. We use a set of form-factor models representative of current theoretical work, including results from two quark model approaches (ISGW2 [17] and Melikhov/Beyer [18]), lattice QCD (UKQCD [23]), light-cone sum rules (LCSR [25]), and a method incorporating form-factor measurements in $D \to K^*\ell\nu$ decay (Wise/Ligeti+E791 [27]). In all cases we have used form-factor parametrizations as described in the above references. A theoretical error is added to the branching fraction and $\Delta\Gamma$ measurements based on one-half of the full spread in results among these models. The $|V_{ub}|$ measurement has an additional theoretical uncertainty due to the determination of $\tilde{\Gamma}_{\rm thy}$.

The Dalitz plot for $B \to \rho\ell\nu$ decay predicted by the ISGW2 model is shown in Fig. 3.6. For a given value of q^2, $\cos\theta_\ell$ varies from -1 to $+1$ across the allowed range of lepton energies. The Dalitz plot shows that positive values of $\cos\theta_\ell$ are favored over negative values; this effect, which produces a hard lepton-energy spectrum, is a consequence of the $V-A$ coupling, and is discussed further below. We are most sensitive to $B \to \rho\ell\nu$ decay in the endpoint region to the right of the vertical line, $E_\ell > 2.3$ GeV. Although a significant fraction of the total predicted rate for $B \to \rho\ell\nu$ lies at high lepton energy, Table 3.2 shows that different theoretical approaches differ, giving results between 24% and 35%.

Table 3.3 shows the quantity $\tilde{\Gamma}_{\rm thy}$ predicted by each form-factor model. Even with a perfectly measured $B \to \rho\ell\nu$ branching fraction, $|V_{ub}|$ would be uncertain due to the spread in $\tilde{\Gamma}_{\rm thy}$ values among form-factor models. We can summarize the model predictions as $\tilde{\Gamma}_{\rm thy} = (16.8 \pm 2.6)$ ps^{-1}, a 15% spread. As explained in Chapter 11, we assign a 30% error on $\tilde{\Gamma}_{\rm thy}$.

Figures 3.7 and 3.8 show the q^2 distribution predicted by our implementation of these models. Integrated over all lepton energies, there is a substantial difference among the models at low q^2 (large daughter-hadron recoil). At high lepton energy, however, the shapes of the q^2 distributions predicted by each of the form-factor models are very similar. To distinguish among form-factor models on the basis of the q^2 distribution, the lepton-energy region below 2.0 GeV must be probed.

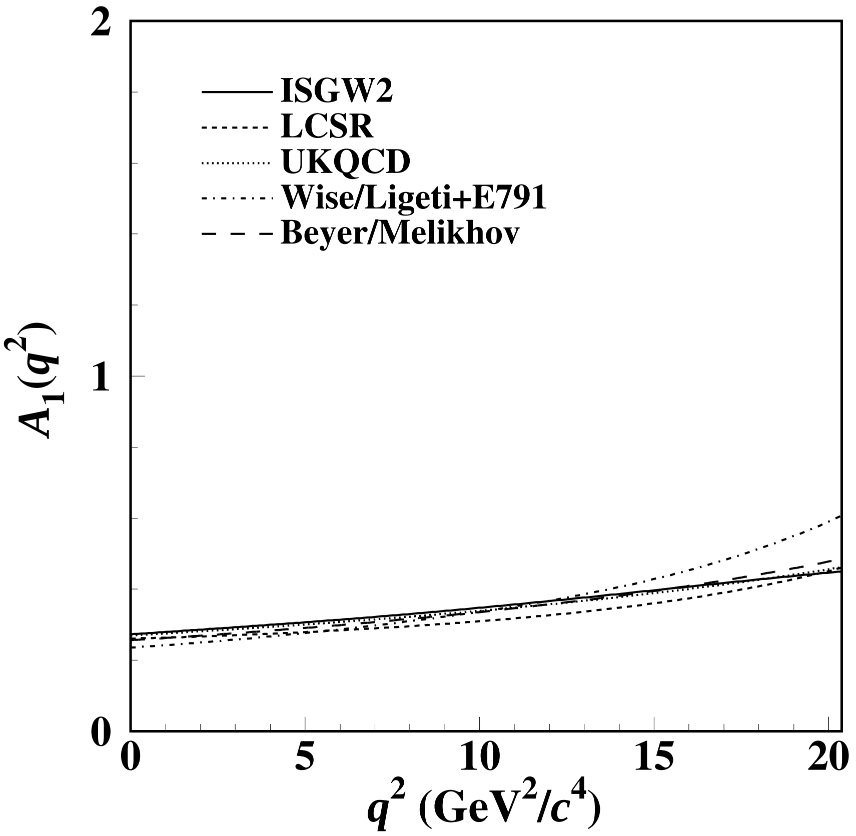

Figure 3.3: Predictions for the $A_1(q^2)$ form factor.

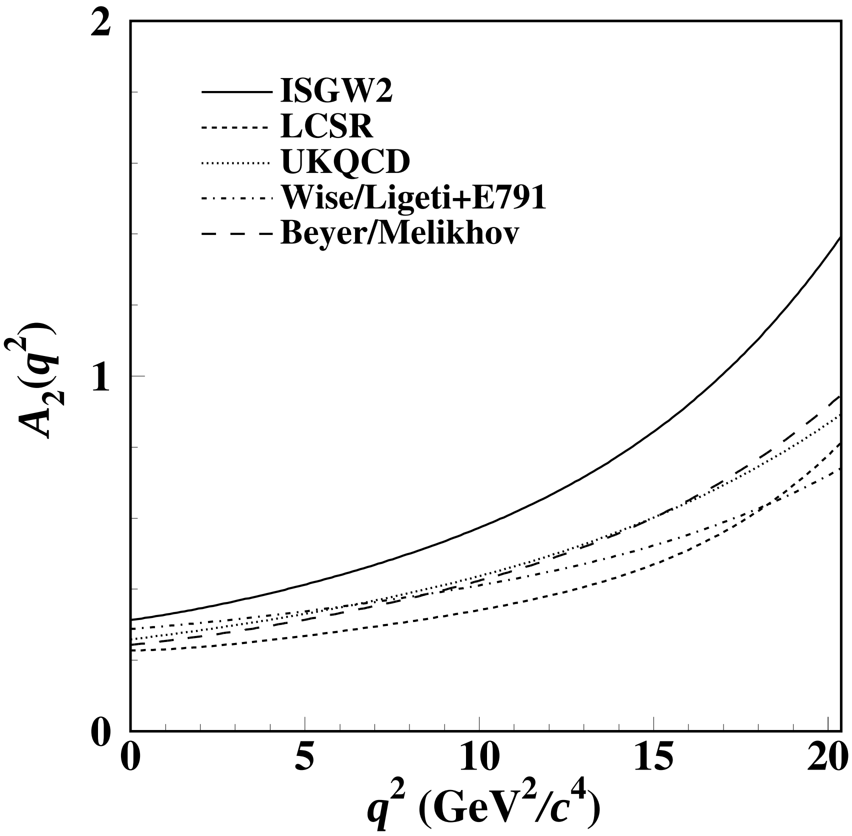

Figure 3.4: Predictions for the $A_2(q^2)$ form factor.

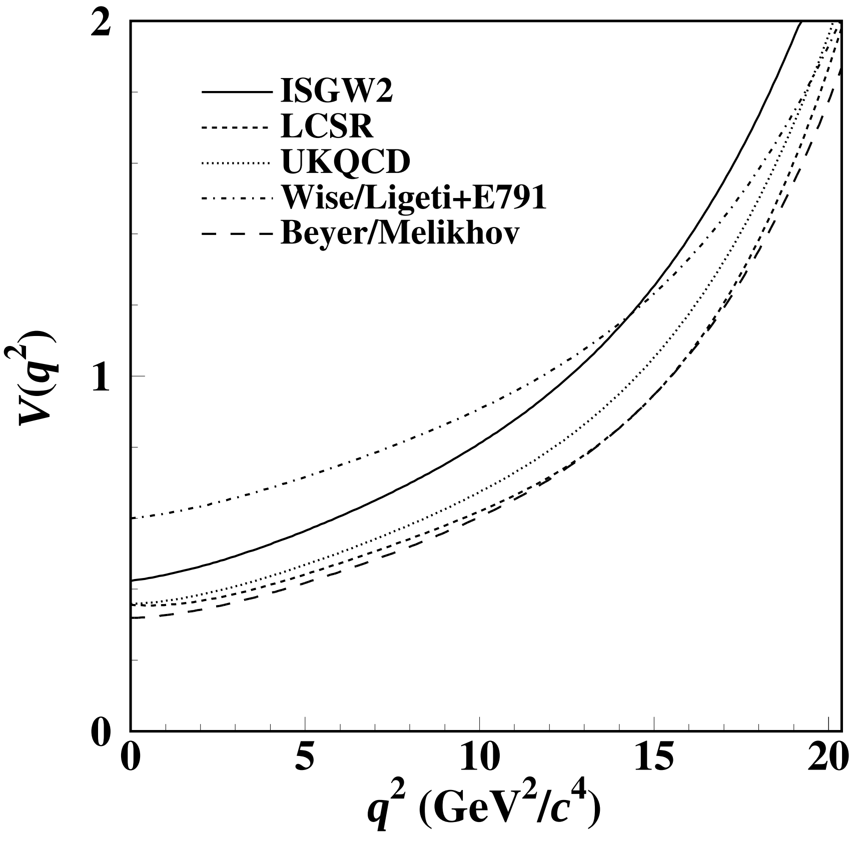

Figure 3.5: Predictions for the $V(q^2)$ form factor.

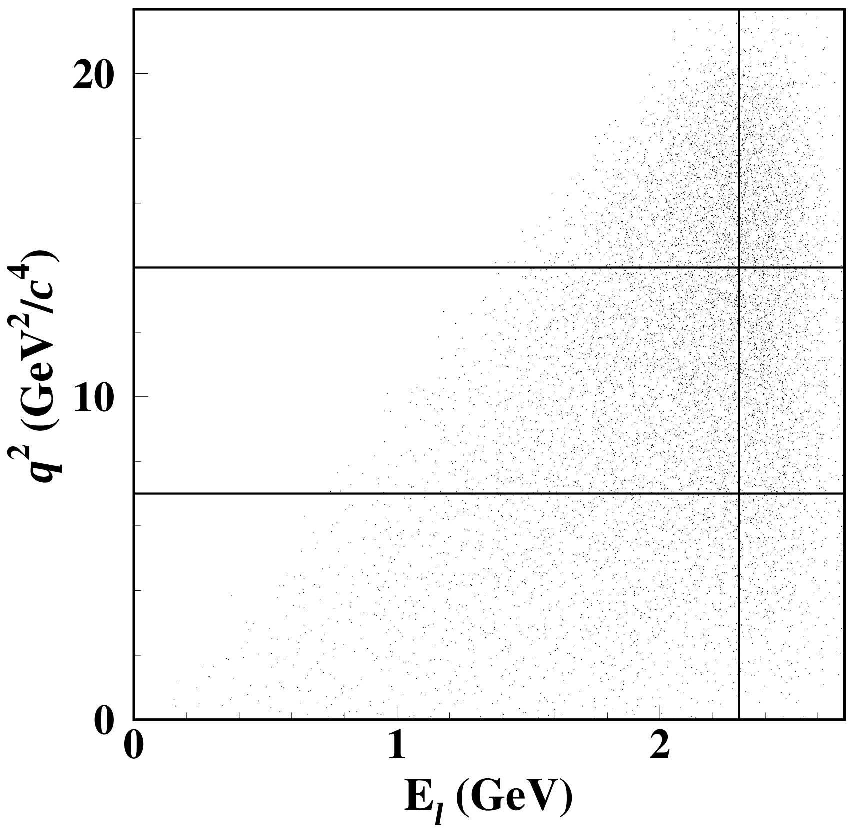

Figure 3.6: A simulated Dalitz plot, q^2 vs. E_ℓ, for $B \to \rho\ell\nu$ decay. The lepton energy, E_ℓ, is computed in the $\Upsilon(4S) \to B\bar{B}$ rest frame (lab frame), which differs slightly from the B rest frame. This analysis is most sensitive to $B \to \rho\ell\nu$ events in the lepton-energy region to the right of the vertical line, $E_\ell > 2.3$ GeV. The horizontal lines define the q^2 bins in the $\Delta\Gamma$ measurement: $0 < q^2 < 7$ GeV$^2/c^4$, $7 < q^2 < 14$ GeV$^2/c^4$, and $14 < q^2 < 21$ GeV$^2/c^4$. At high q^2, our lepton-energy requirement retains a much larger fraction of the phase space than it does at low q^2.

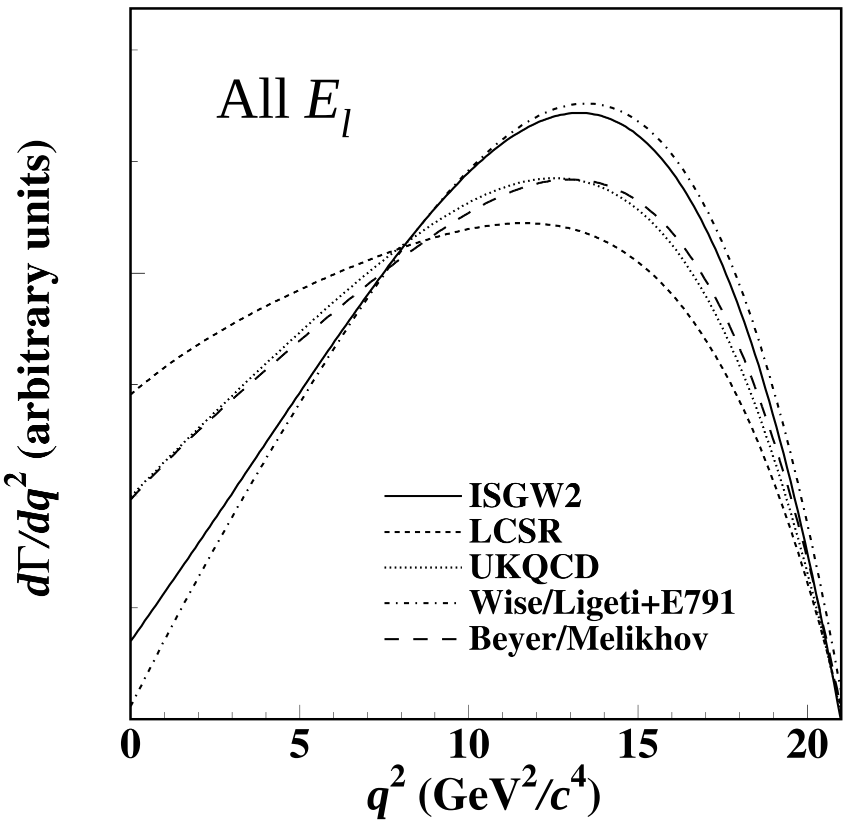

Figure 3.7: Theoretical q^2 distributions for the $B \to \rho\ell\nu$ form-factor models that we have considered over the full lepton-energy range. The lepton energy, E_ℓ, is computed in the $\Upsilon(4S) \to B\bar{B}$ rest frame (lab frame), which differs slightly from the B rest frame. All models have been normalized to equal areas.

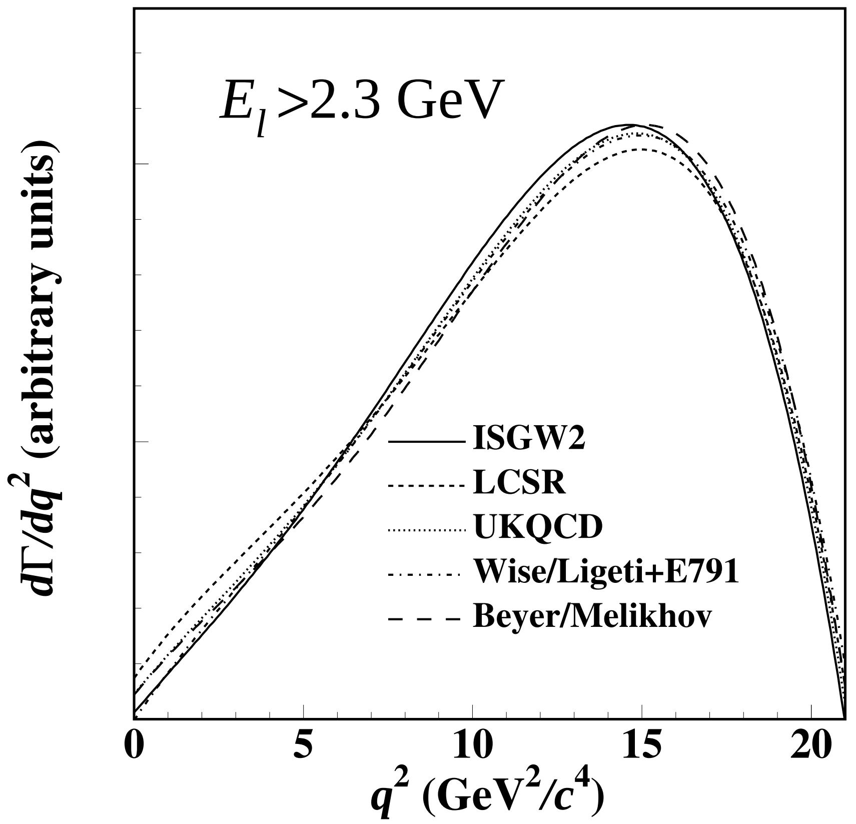

Figure 3.8: Theoretical q^2 distributions for the $B \to \rho\ell\nu$ form-factor models that we have considered for $E_\ell > 2.3$ GeV. The lepton energy, E_ℓ, is computed in the $\Upsilon(4S) \to B\bar{B}$ rest frame (lab frame), which differs slightly from the B rest frame. All models have been normalized to equal areas. For high lepton energies, $E_\ell > 2.3$ GeV, all of the models predict very similar q^2 distributions.

FF model	$\Gamma(E_\ell > 2.3\ \mathrm{GeV})/\Gamma$	$\Gamma(2.0 < E_\ell < 2.3\ \mathrm{GeV})/\Gamma$
ISGW2	0.35	0.33
LCSR	0.24	0.28
UKQCD	0.27	0.30
Wise/Ligeti+E791	0.31	0.34
Beyer/Melikhov	0.27	0.30

Table 3.2: Lepton-energy distribution predictions from each form-factor (FF) model. The lepton energy, E_ℓ, is computed in the $\Upsilon(4S) \to B\bar{B}$ rest frame (lab frame), which differs slightly from the B rest frame. For the branching fraction measurement, the primary source of model dependence is in the ratio $\Gamma(E_\ell > 2.3\ \mathrm{GeV})/\Gamma$.

FF model	$\tilde{\Gamma}_{\mathrm{thy}}$ (ps^{-1})
ISGW2	14.2
LCSR	16.9
UKQCD	16.5
Wise/Ligeti+E791	19.4
Beyer/Melikhov	16.0

Table 3.3: $\tilde{\Gamma}_{\mathrm{thy}}$ predictions from each form-factor (FF) model. For the $|V_{ub}|$ measurement, there is significant model dependence arising from the quantity $\tilde{\Gamma}_{\mathrm{thy}}$.

Table 3.4 shows how the efficiency of the lepton-energy requirement varies with q^2 for each form-factor model. Our lepton-energy requirement retains a much larger fraction of the phase space at high q^2 than it does at low q^2. Thus, at high q^2, the efficiency is quite high and a small variation is seen among models. At low q^2, on the other hand, the efficiency is relatively low with a large variation among the form-factor models.

Integrating Eq. 3.1.8 over the angular variables, we obtain

$$\begin{aligned} \frac{d\Gamma}{dq^2} &= \frac{G_F^2}{96\pi^3}|V_{q'Q}|^2\frac{|\mathbf{p}_V|q^2}{m_P^2}\mathcal{B}(V \to P_1P_2) \\ &\times \left[|H_+(q^2)|^2 + |H_-(q^2)|^2 + |H_0(q^2)|^2\right]. \end{aligned} \tag{3.2.1}$$

Figures 3.9 and 3.10 show the $d\Gamma/dq^2$ distribution for each term in Eq. 3.2.1. In each form-factor model, the term proportional to $|H_-|^2$ contributes the largest fraction of the total rate. As a consequence of the $V-A$ couplings of the W boson the vector meson is more likely to have helicity -1 than $+1$. For $B \to \rho\ell\nu$ decay, this asymmetry is quite large, except at very high q^2 (low daughter-hadron recoil momentum) where the A_1 form factor dominates each of the helicity amplitudes and the ρ is nearly unpolarized, and at small values of q^2, where only the zero-helicity component contributes significantly. Because the $|H_+|^2$ contribution is quite small, the theoretical error in the $\mathcal{B}(B \to \rho\ell\nu)$ and $\Delta\Gamma$ measurements is due primarily to the uncertainty in the relative size the $H_-(q^2)$ and $H_0(q^2)$.

Table 3.5 shows the predictions for $\Gamma/|V_{ub}|^2$ in bins of q^2 ($\Delta\tilde{\Gamma}_{\rm thy}$) for the form-factor models. These predictions can be used to extract $|V_{ub}|$ from a measurement of the q^2 distribution.

3.2.1 The form-factor models

We now describe the specific form-factor models that will be used to describe the kinematic distributions of $B \to \rho\ell\nu$ decay in the remainder of this thesis. As described above we have selected two quark models, a lattice QCD model,

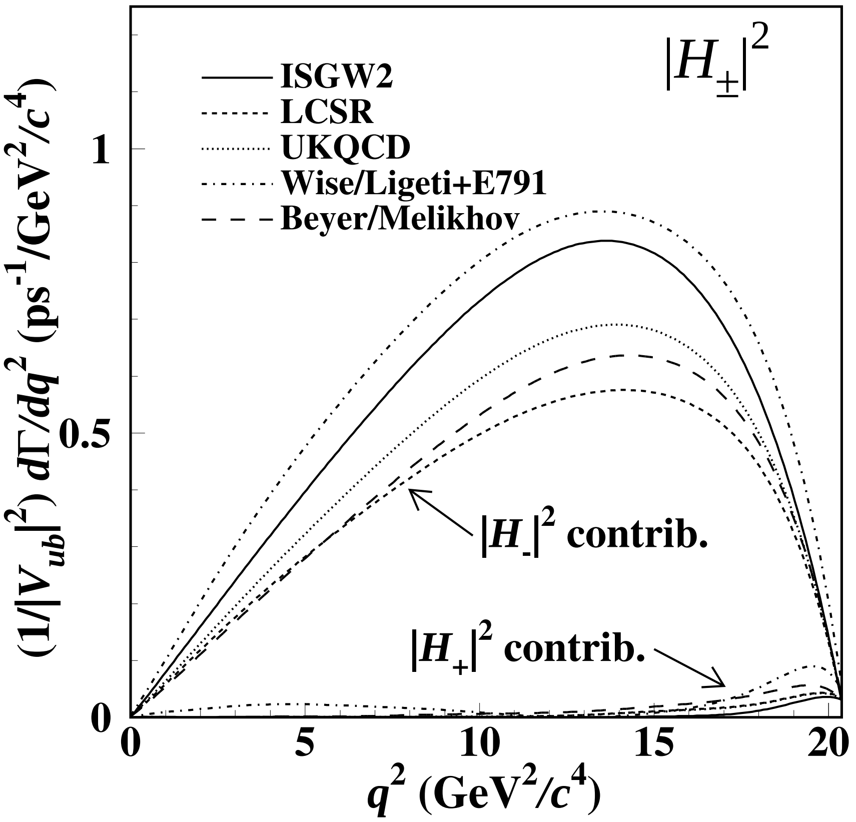

Figure 3.9: $d\Gamma/dq^2$ distributions for the terms proportional to $|H_-|^2$ and $|H_+|^2$ in Eq. 3.2.1.

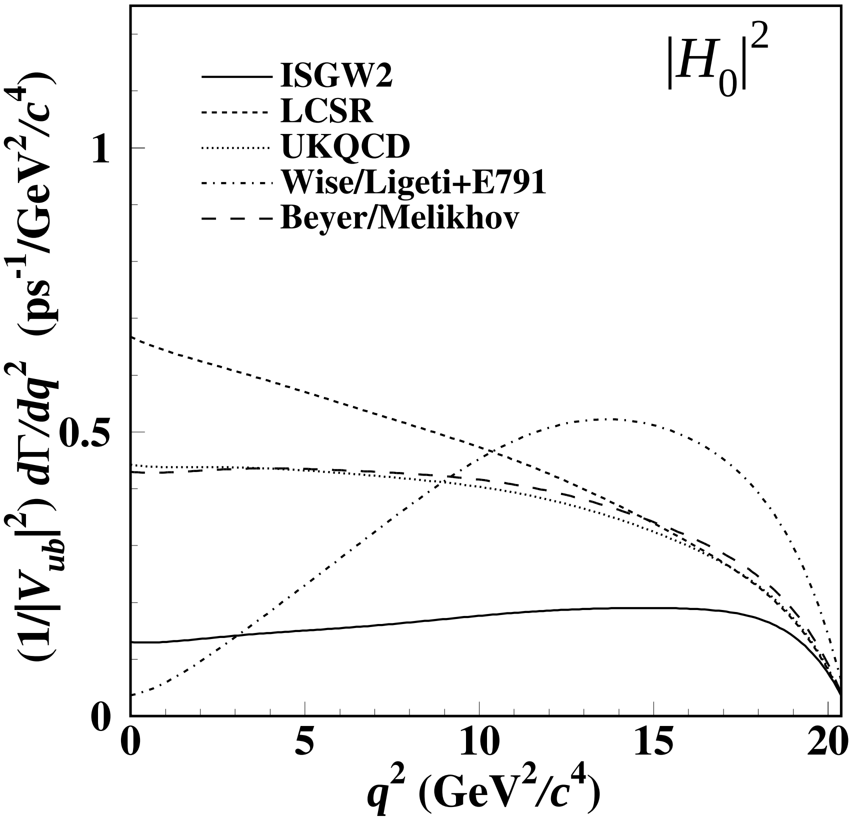

Figure 3.10: $d\Gamma/dq^2$ distributions for the term proportional to $|H_0|^2$ in Eq. 3.2.1.

FF model	$0 < q^2 < 7$ GeV^2/c^4	$7 < q^2 < 14$ GeV^2/c^4	$14 < q^2 > 21$ GeV^2/c^4
ISGW2	0.24	0.35	0.43
LCSR	0.12	0.25	0.38
UKQCD	0.15	0.28	0.39
Wise/Ligeti+E791	0.23	0.29	0.37
Beyer/Melikhov	0.14	0.27	0.38

Table 3.4: The fraction of events predicted to have $E_\ell > 2.3$ GeV in bins of q^2 for each form-factor (FF) model. The spread among the form-factor model results is the largest component of the theoretical in the $\Delta\Gamma$ measurement.

FF model	$\Delta\tilde{\Gamma}_{\mathrm{thy}}$ (ps^{-1}) $0 < q^2 < 7$ GeV^2/c^4	$\Delta\tilde{\Gamma}_{\mathrm{thy}}$ (ps^{-1}) $7 < q^2 < 14$ GeV^2/c^4	$\Delta\tilde{\Gamma}_{\mathrm{thy}}$ (ps^{-1}) $14 < q^2 < 21$ GeV^2/c^4
ISGW2	2.8	6.1	5.3
LCSR	5.4	6.6	4.9
UKQCD	4.5	6.7	5.3
Wise/Ligeti+E791	3.5	8.4	7.5
Beyer/Melikhov	4.3	6.4	5.3

Table 3.5: Predictions for the partial rate, $\Delta\tilde{\Gamma}_{\mathrm{thy}}$ in q^2 bins from each form-factor (FF) model.

a light cone sum rules model, and a model that uses measured $D \to K^*\ell\nu$ form factors to predict those for $B \to \rho\ell\nu$. These have been selected so as to have a fair sampling of the form-factor predictions currently published.

As may already be apparent from the figures and tables above, the overwelming features of these form-factor models are related to the characteristics of semileptonic decay and not to the details of the form-factors themselves. For example the structure of the Dalitz plot is directly connected to the $V - A$ coupling of the W boson. Nevertheless, the uncertainty of the form-factors will be a dominant error in the measurements presented in this thesis.

Most form-factor predictions are performed in two steps: an overall normalization (typically at one value of q^2, or a small range of values) is predicted and then is extrapolated to the entire q^2 range. The functional form of this extrapolation is typically quite simple, usually with only 2 or 3 free parameters. Each method used to predict form factors is therefore best at a particular q^2, typically q^2_{max}. One exception to this is the LCSR model, which makes predictions at low q^2 and then extrapolates to high values of q^2 in order to predict form factors for the full q^2 range.

3.2.2 The ISGW2 model

As discussed in Ref. [52] there are many distinct approaches to form-factor predictions using quark models. We consider two such approaches, the first of which is the ISGW2 model. One feature of quark-model approaches is that estimates of uncertainties are difficult to perform. This is will be evident in this section as well as in the discussion of the Beyer/Melikhov model below.

The ISGW model [16] is a nonrelativistic constituent quark model that predicts a mix of resonant decay modes for $b \to u\ell\nu$ decays (among other transitions). It was the first such model to do so. Final-state mesons are included as to saturate the lepton-energy endpoint region. Calculations are normalized at $q^2 = q^2_{\mathrm{max}}$, where the daughter meson is at rest in the parent meson rest frame. In this way, the wave function overlap between these mesons can be used to normalize the predictions.

The ISGW model was replaced by the ISGW2 [17] model, which incorporated several improvements. These include

- Constraints from heavy quark symmetry are explicitly imposed. In particular, constraints on form-factor ratios over the full q^2 range and on the slopes of form factors near $q^2_{\max}$ are considered.
- More realistic form-factor shapes.
- Relativistic corrections to coupling constants of the axial vector current.

The theoretical errors on the prediction of $\Gamma(B \to \rho\ell\nu)$ are quoted to be of order $\pm 50\%$, corresponding to a 25% uncertainty on the normalization of $|V_{ub}|$.

The form-factor definitions used in the ISGW2 paper differ slightly from those presented above:

$$\begin{aligned} f(q^2) &= \frac{A_1(q^2)}{m_B + m_\rho}, \\ a_+(q^2) &= A_2(q^2)(m_B + m_\rho), \\ g(q^2) &= V(q^2)(m_B + m_\rho). \end{aligned} \tag{3.2.2}$$

The q^2 dependence of the predicted form factors is

$$\left[1 + \frac{1}{12} r^2_{XB} (q^2_{\max} - q^2)\right]^{-2}. \tag{3.2.3}$$

Because of their complexity we do not write out the full form of the form-factor predictions explicitly. Refer to Appendix C of Ref. [17] for the full expressions. The predicted kinematic distributions for $B \to \rho\ell\nu$ in the ISGW2 model are shown in Figs. 3.11 and 3.12.

3.2.3 The LCSR model

Methods to compute form-factors within QCD must be accurate beyond the pertubative regime. QCD sum rules are one alternative for these calculations.

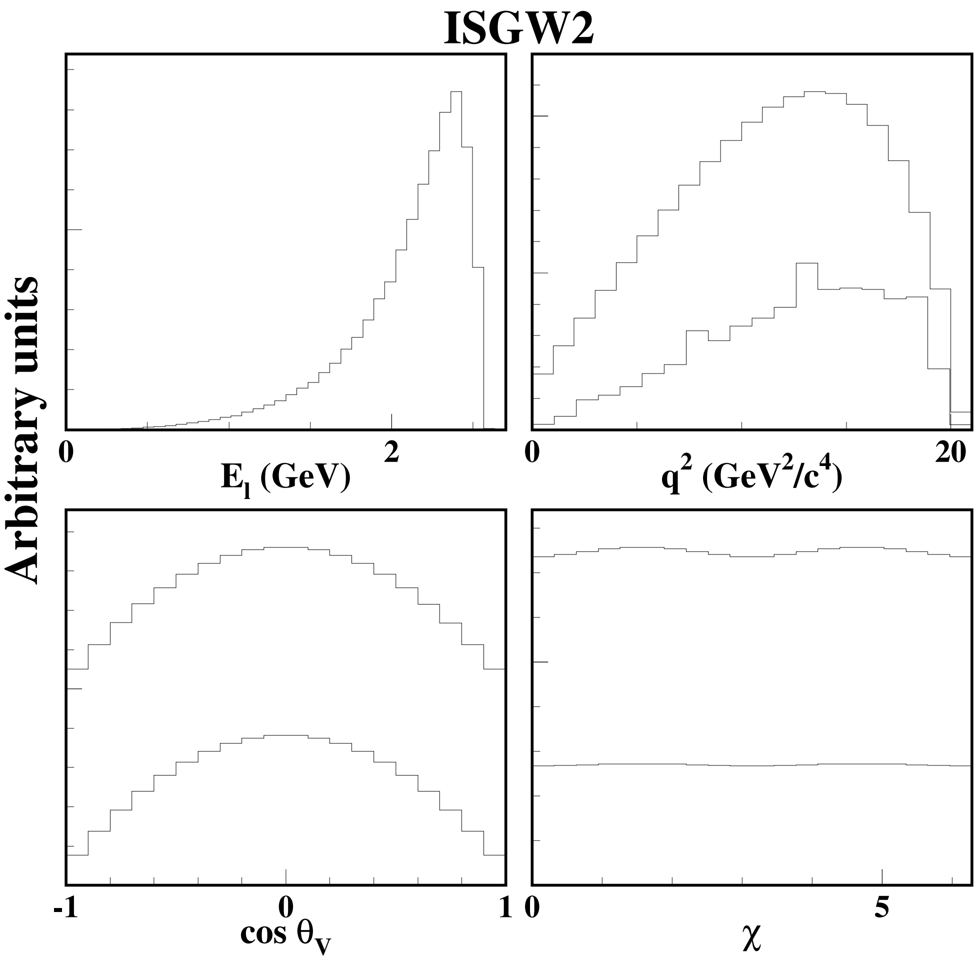

Figure 3.11: Kinematic distributions in the ISGW2 model: lepton-energy, q^2, $\cos\theta_V$, and χ. For the q^2, $\cos\theta_V$, and χ distributions, the upper (lower) line shows the distribution over the full lepton-energy range (only $E_\ell > 2.3$ GeV).

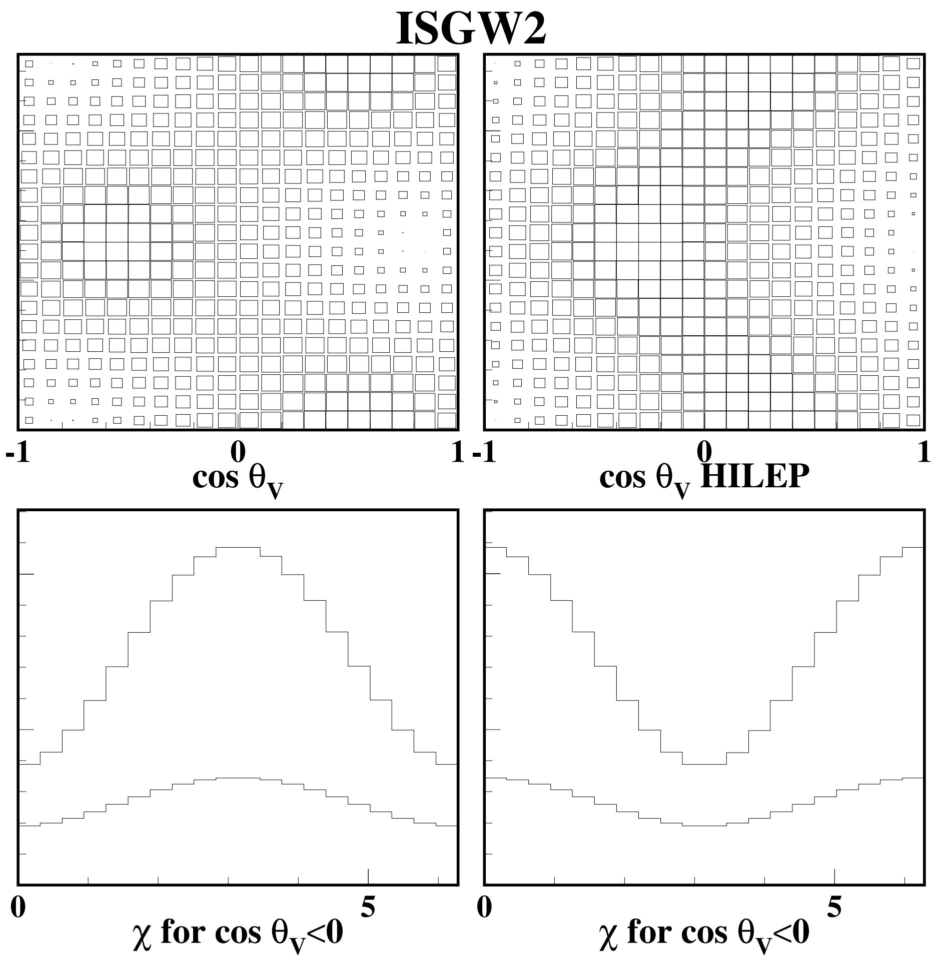

Figure 3.12: Kinematic distributions in the ISGW2 model: χ vs. $\cos\theta_V$, χ vs. $\cos\theta_V$ (HILEP), χ for events with $\cos\theta_V < 0$, and χ for events with $\cos\theta_V > 0$. For the χ distributions, the upper (lower) line shows the distribution over the full lepton-energy range (only $E_\ell > 2.3$ GeV).

Light cone sum rules techniques were developed as an alternative to traditional QCD sum rules for the study of heavy meson decays, and are especially useful in $b \to u\ell\nu$ transitions. In light cone sum rules, calculations are performed in expansions in the twist of operators. Practically, this expansion converges rather slowly. Thus, terms up to twist=4 are currently calculated.

Perhaps the most appealing thing about light cone sum rules is that their predictions are most accurate at low values of q^2. This provides a nice contrast with the lattice QCD calculations and quark models such as ISGW2. Given the large q^2 range in $B \to \rho\ell\nu$ decay, the extrapolation towards high q^2 is somewhat difficult, just as the extrapolation to low q^2 is for other methods.

Current uncertainties on form-factor calculations using LCSR are of order 15%, which corresponds to 30% on Γ and 15% on $|V_{ub}|$. These uncertainties come from a variety of sources.

The convergence of the light cone expansion (in increasing orders of twist) is such that the neglected terms are thought to contribute at most 3% to the form-factor predictions. Radiative corrections lead to only small (5%) effects at low q^2. For the $A_2(q^2)$ form factor at high q^2, however, the effects are nearly 20%. Dependence on input parameters to the sum rule, such as m_b, decay constants, and the Borel parameter, are taken into account, and also increase with q^2. The resulting kinematic distributions are shown in Figs. 3.13 and 3.14.

The form-factors in the LCSR model are parametrized by the form

$$F(q^2) = \frac{F(0)}{1.0 + a(q^2/m_B^2) + b(q^2/m_B^2)^2}, \tag{3.2.4}$$

where $F(q^2)$ is $A_1(q^2)$, $A_2(q^2)$, or $V(q^2)$. Table 3.6 gives the values for $F(0)$, a, and b for this model.

3.2.4 The UKQCD model

Lattice QCD is an approach to solving problems within QCD using a discrete lattice of space-time points. The calculations performed by UKQCD of $B \to \rho\ell\nu$ additionally use constraints of light cone sum rules and heavy quark

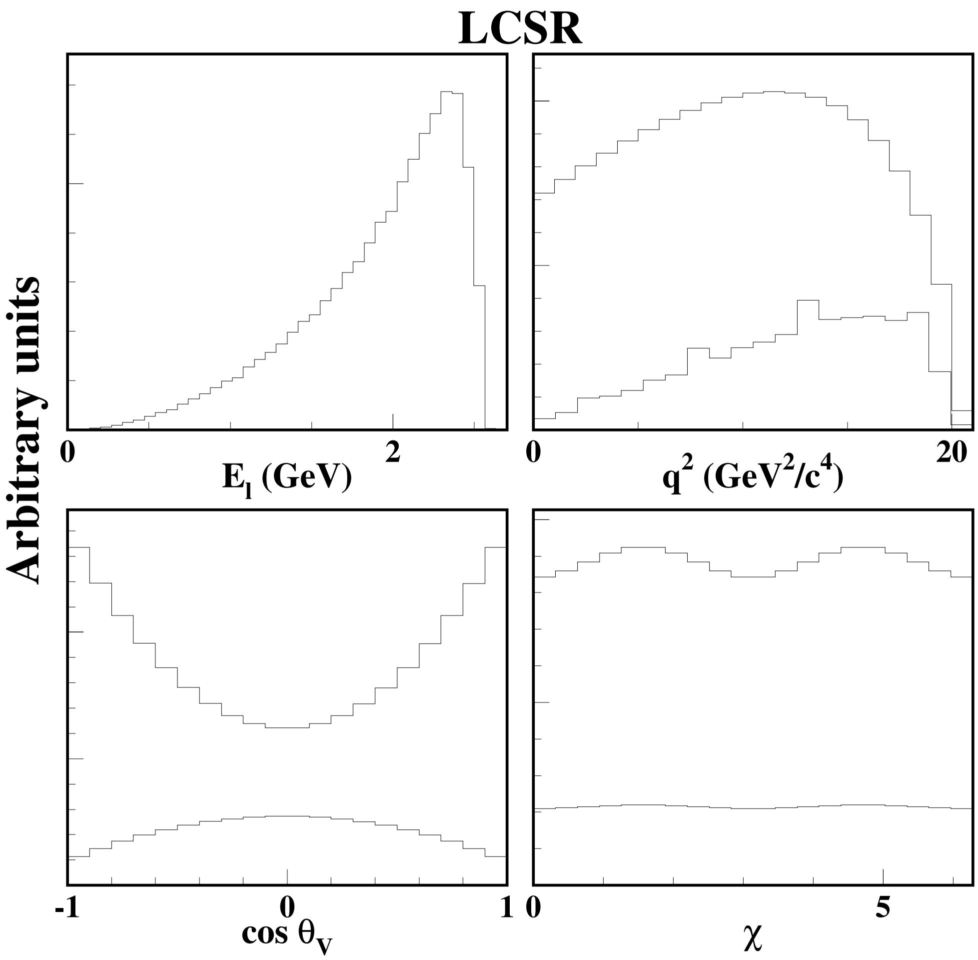

Figure 3.13: Kinematic distributions in the LCSR model: lepton-energy, q^2, $\cos\theta_V$, and χ. For the q^2, $\cos\theta_V$, and χ distributions, the upper (lower) line shows the distribution over the full lepton-energy range (only $E_\ell > 2.3$ GeV).

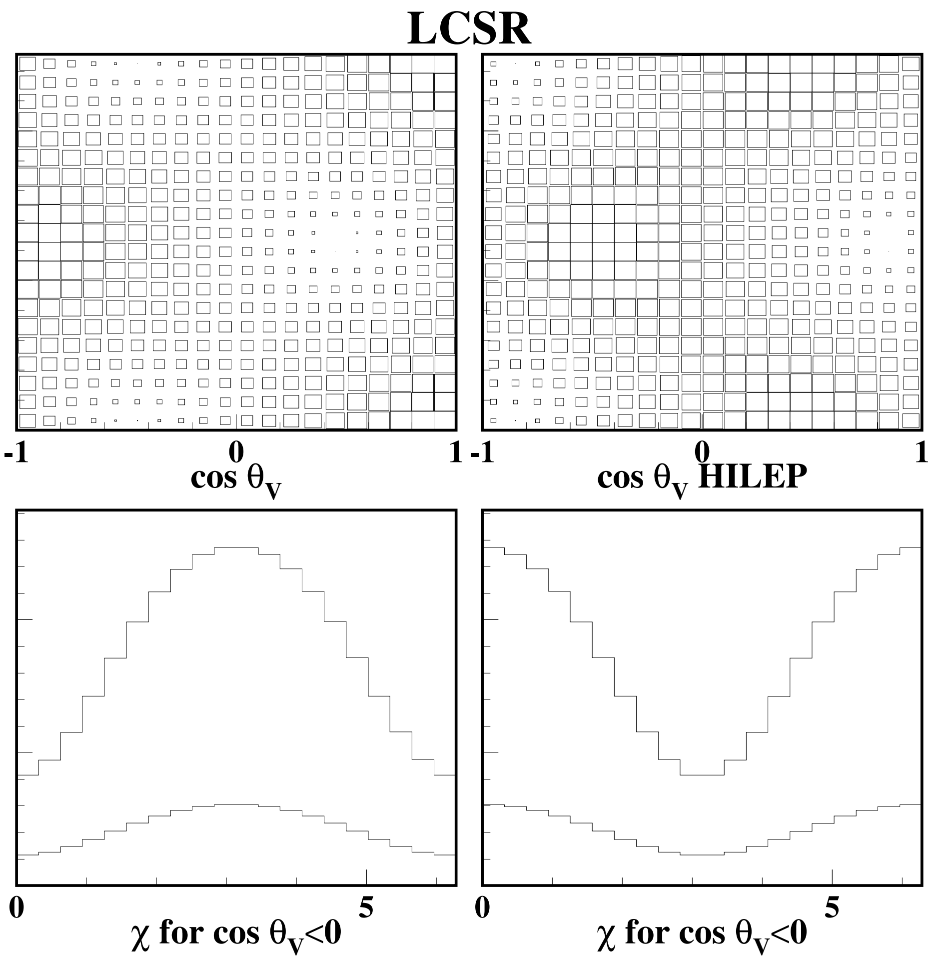

Figure 3.14: Kinematic distributions in the LCSR model: χ vs. $\cos\theta_V$, χ vs. $\cos\theta_V$ (HILEP), χ for events with $\cos\theta_V < 0$, and χ for events with $\cos\theta_V > 0$. For the χ distributions, the upper (lower) line shows the distribution over the full lepton-energy range (only $E_\ell > 2.3$ GeV).

Form factor	$F(0)$	a	b
$A_1(q^2)$	0.261	-0.29	-0.415
$A_2(q^2)$	0.223	-0.93	-0.092
$V(q^2)$	0.338	-1.37	0.315

Table 3.6: Form-factor parameters for the LCSR model. The parameters are defined in Eq. 3.2.4 and are taken from Ref. [25].

.

symmetry (HQS) to constrain the form-factor predictions. In this section we describe these constraints and show the form factors predicted by the UKQCD collaboration.

For $B \to \rho\ell\nu$ decay, current computing constraints allow for quenched calculations of form factors in lattice QCD between $q^2_{\max} \approx 21\ \mathrm{GeV}^2/c^4$ and $14\ \mathrm{GeV}^2/c^4$. Light cone sum rules are used to constrain form factors at $q^2 = 0$. In particular, each of the form factors are predicted to run like $m_B^{-3/2}$ at $q^2 = 0$ for large values of m_B. On the other hand, HQS can be used to relate the form factors at high q^2 [28]:

$$\begin{aligned}
V(q^2) &= \big(1 + \frac{m_\rho}{m_B}\big) A_0(q^2), \\
A_1(q^2) &= \frac{m_B^2 + m_\rho^2}{m_B(m_B + m_\rho)}\big(1 - \frac{q^2}{m_B^2 + m_\rho^2}\big) A_0(q^2), \\
A_2(q^2) &= \frac{m_B + m_\rho}{m_B}\big(1 - \frac{2m_\rho(m_B + m_\rho)}{(m_B + m_\rho)^2 - q^2}\big) A_0(q^2).
\end{aligned} \tag{3.2.5}$$

Thus, the lattice calculations on the four form factors in $B \to \rho\ell\nu$ decay can be used to effectively predict one form factor. The lattice calculations are extrapolated to low q^2 by fitting $A_1(q^2)$ to the form

$$A_1(q^2) = \frac{A_1(0)}{1 - q^2/M^2}, \tag{3.2.6}$$

which has two free parameters ($A_1(0)$ and M). The result of this fit is

$$\begin{aligned} A_1(0) &= 0.27^{+0.05}_{-0.04}, \\ M &= 7.0^{+1.2}_{-0.6}\ \mathrm{GeV}/c^2. \end{aligned} \tag{3.2.7}$$

The errors are due to the statistical lattice point errors only. These statistical errors are determined using Monte Carlo methods. The kinematic distributions from these form factors are shown in Figs. 3.15 and 3.16.

The systematic errors in lattice QCD predictions are not always easy to estimate. The largest sources of error are due to discretization, extrapolation to the physical quark masses, and quenching.

The discretization systematic error, the uncertainty due to the lattice spacing, can be estimated by performing the lattice calculation at several different spacings. These calculations can then be used to extrapolate to the continuum limit. For the UKQCD results, this systematic error is the largest systematic error, $\pm 20\%$ on Γ, or $\pm 10\%$ on $|V_{ub}|$.

For lattice calculations, the quark masses can be neither too big or too small. In particular, masses must be large enough to be insensitive to the lattice volume. The UKQCD calculation assumes that form factors are independent of the light spectator quark mass. In this way, predictions using the heaviest such quark, which have the smallest errors, can be used. A "worst-case" uncertainty of $\pm 13\%$ on Γ ($\pm 6.5\%$ on $|V_{ub}|$) is assigned. Discretization errors scale as the parent quark mass. In the UKQCD calculation the heavy quark mass is approximately the charm quark mass. For decays of the B meson, results are extrapolated up using heavy quark symmetry relations to the b-quark mass.

A lattice calculation is quenched if effects due to virtual quark loops are not considered. Quenching allows for a large increase in the number of lattice points for a given amount of computer speed. The uncertainty due to quenching is unknown. For the UKQCD predictions for $B \to \rho\ell\nu$, quenching effects are thought to be small because of the agreement observed in results for $|V_{cb}|$ between quenched approaches and other determinations.

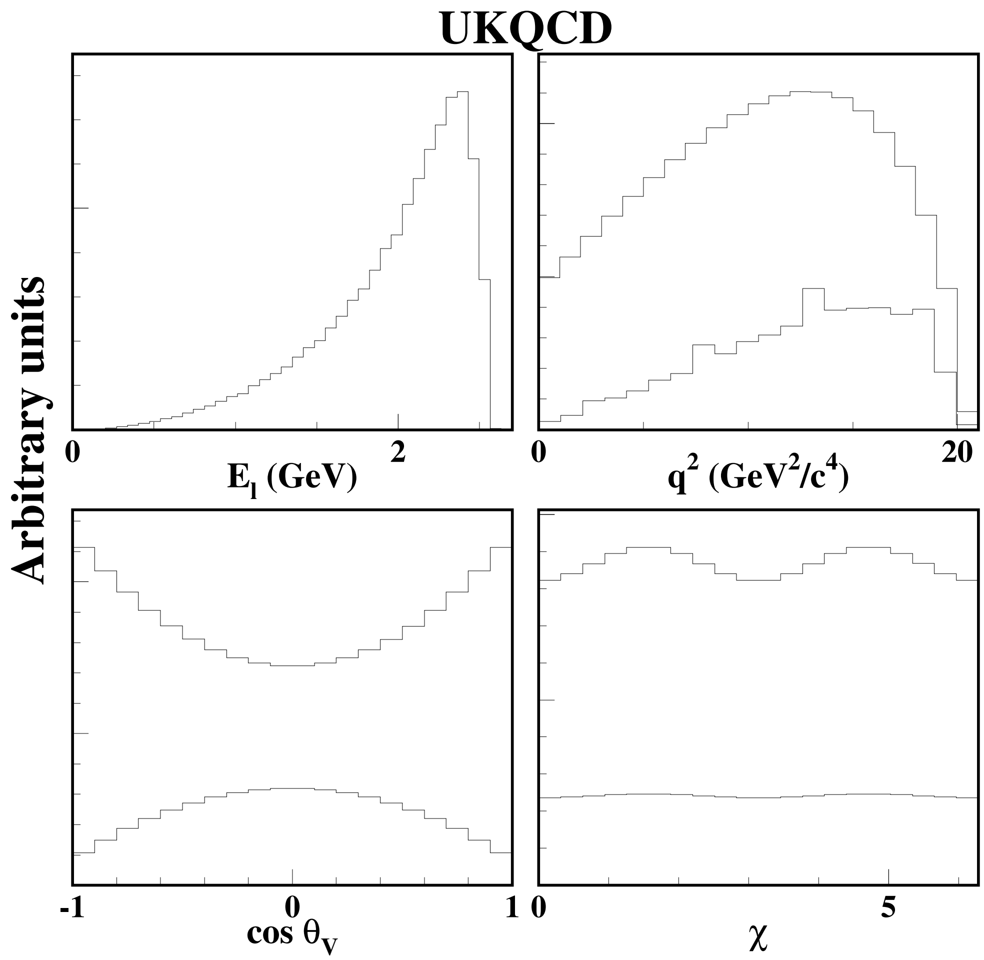

Figure 3.15: Kinematic distributions in the UKQCD model: lepton-energy, q^2, $\cos\theta_V$, and χ. For the q^2, $\cos\theta_V$, and χ distributions, the upper (lower) line shows the distribution over the full lepton-energy range (only $E_\ell > 2.3$ GeV).

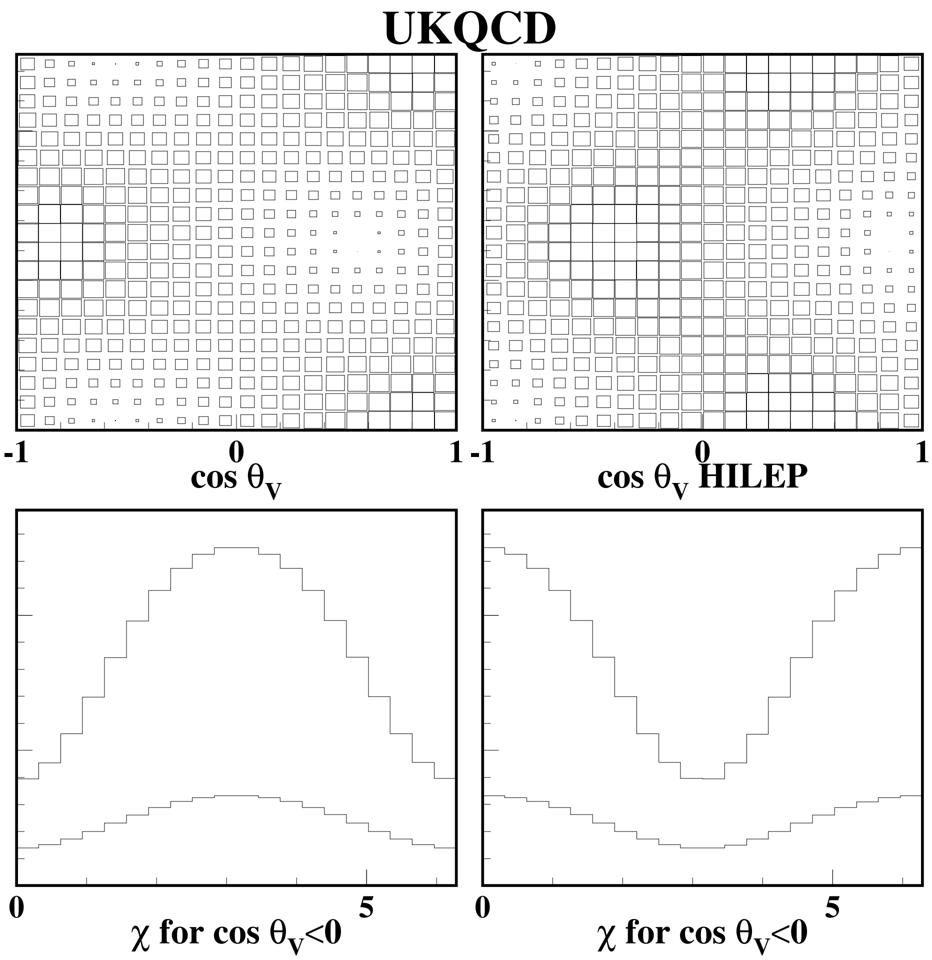

Figure 3.16: Kinematic distributions in the UKQCD model: χ vs. $\cos\theta_V$, χ vs. $\cos\theta_V$ (HILEP), χ for events with $\cos\theta_V < 0$, and χ for events with $\cos\theta_V > 0$. For the χ distributions, the upper (lower) line shows the distribution over the full lepton-energy range (only $E_\ell > 2.3$ GeV).

Form factor	$f(0)$	a	b
f	1.55	0.69	0.041
g	0.051	1.60	0.60
a_+	-0.04	1.40	0.50

Table 3.7: Paramters of the Beyer/Melikhov model as defined in Eq. 3.7.

The total systematic error is assigned to be $\pm 24\%$ on Γ, or $\pm 12\%$ on $|V_{ub}|$. The quoted statistical error on Γ is $^{+20}_{-15}\%$.

3.2.5 The Beyer/Melikhov model

The Beyer/Melikhov is the second quark model that we have examined. Unlike the ISGW2 model, the Beyer/Melikhov model is fully relativistic. However, the most important feature of this model is that the UKQCD lattice QCD results are used to normalize the form-factor predictions at large q^2. Quark model methods are then used to extrapolate towards $q^2 = 0$. The kinematic distributions predicted by this model are shown in Figs 3.17 and 3.18. In general the predictions are very similar to those of the UKQCD model, a less than surprising result.

The parametrizations of the predicted form factors are given by

$$f(q^2) = \frac{f(0)}{1 - at^2 + bt^4}, \tag{3.2.8}$$

where the form factors are defined as in Eq. 3.2.2 and $t^2 = q^2/M_{B^*}$, with $M_{B^*} = 5.324$ GeV$/c^2$. Table 3.7 shows the predictions for a and b.

3.2.6 The Wise/Ligeti+E791 model

The Wise/Ligeti+E791 [27] model is based on the idea of using measured form factors from $D \to K^*\ell\nu$ decay along with heavy quark symmetry and $SU(3)$ flavor symmetry. The longer range use of this formalizm is to make use

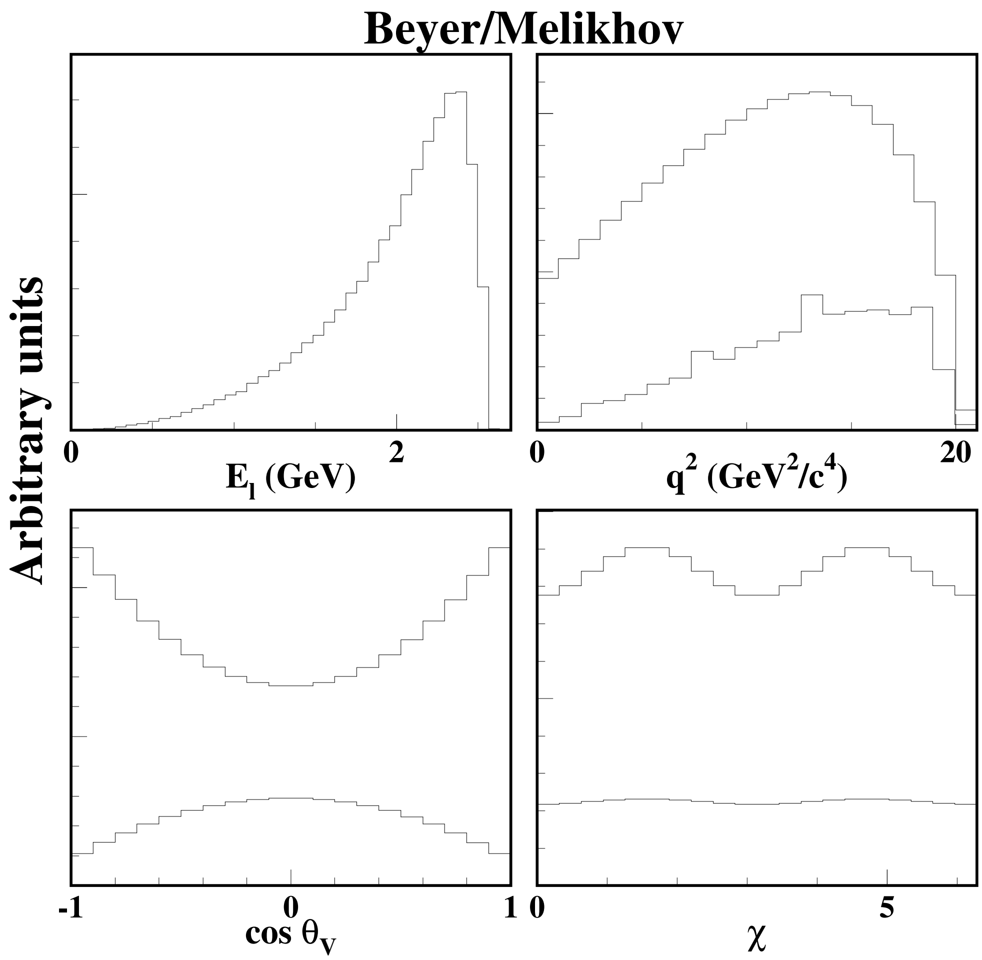

Figure 3.17: Kinematic distributions in the Beyer/Melikhov model: lepton-energy, q^2, $\cos\theta_V$, and χ. For the q^2, $\cos\theta_V$, and χ distributions, the upper (lower) line shows the distribution over the full lepton-energy range (only $E_\ell >$ 2.3 GeV).

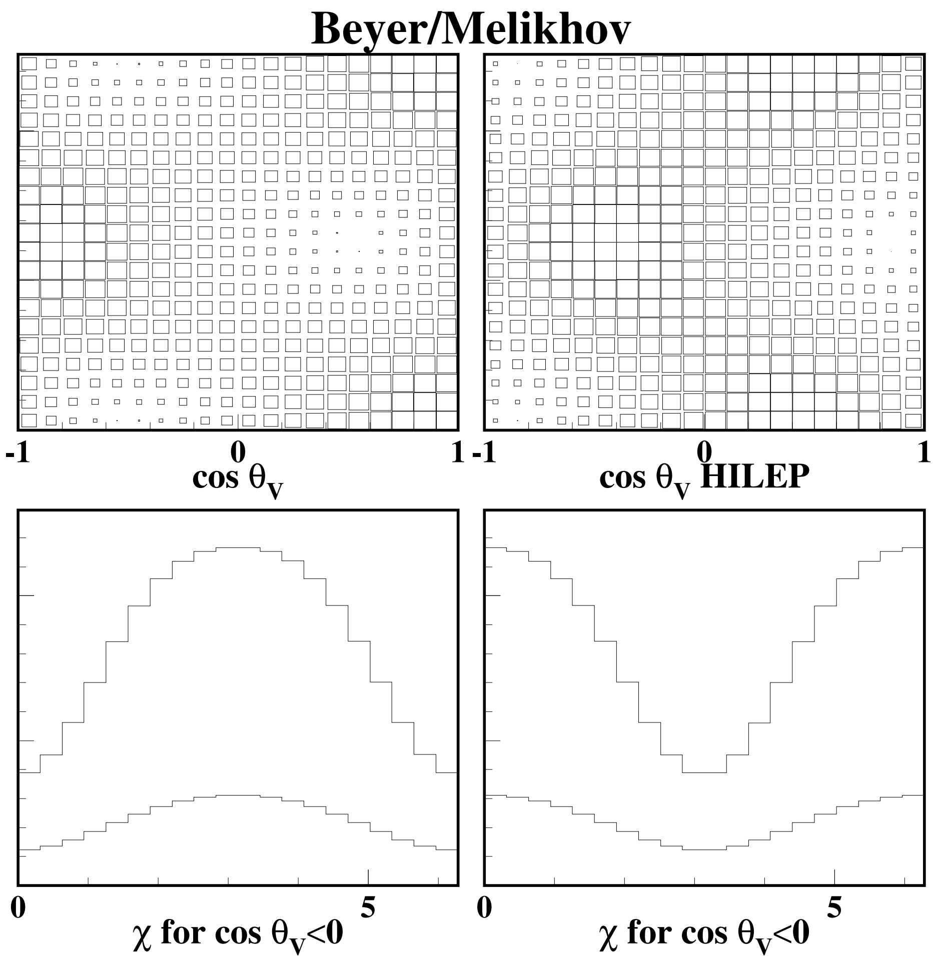

Figure 3.18: Kinematic distributions in the Beyer/Melikhov model: χ vs. $\cos\theta_V$, χ vs. $\cos\theta_V$ (HILEP), χ for events with $\cos\theta_V < 0$, and χ for events with $\cos\theta_V > 0$. For the χ distributions, the upper (lower) line shows the distribution over the full lepton-energy range (only $E_\ell > 2.3$ GeV).

of form factor measurements of $D \to \rho\ell\nu$ decay, as well as data on the decays $B \to \rho\ell\nu$ and $B \to K^*\ell\ell$ to extract a precise value of $|V_{ub}|$. Here we explain the piece of Ref. [27] that we have used to model the kinematics of $B \to \rho\ell\nu$ decay.

The E791 collaboration has measured the q^2 dependence of the form factors in $D \to K^*\ell\nu$ decay to be

$$\begin{aligned}
f(w)^{(D\to K^*)} &= \frac{A_1(q^2)}{m_D + m_{K^*}} = \frac{(1.9 \pm 0.1)\ \mathrm{GeV}}{(1 + 0.63(w-1))}, \\
a_+(w)^{(D\to K^*)} &= A_2(q^2)(m_D + m_{K^*}) = \frac{(0.18 \pm 0.03)\ \mathrm{GeV}^{-1}}{(1 + 0.63(w-1))}, \\
g(w)^{(D\to K^*)} &= V(q^2)(m_D + m_{K^*}) = \frac{(0.49 \pm 0.04)\ \mathrm{GeV}^{-1}}{(1 + 0.96(w-1))},
\end{aligned} \tag{3.2.9}$$

where w is the relativistic γ factor of the daughter K^* meson:

$$w = \frac{m_D^2 + m_{K^*}^2 - q^2}{2 m_D m_{K^*}}, \tag{3.2.10}$$

which ranges between 1 and approximately 1.3 for $D \to K^*\ell\nu$ decay.

Heavy quark symmetry relates the form factors of $D \to K^*\ell\nu$ decay to those of $B \to K^*$ decays, such as $B \to K^*\gamma$. $SU(3)$ flavor symmetry ($s \leftrightarrow u \leftrightarrow d$) is used to further relate these to $B \to \rho\ell\nu$ form factors. In Ref. [27] these are written as

$$\begin{aligned}
f(w)^{(B\to\rho)} &= \left(\frac{m_B}{m_D}\right)^{1/2} \left[\frac{\alpha_s(m_b)}{\alpha_s(m_c)}\right]^{-6/25} f^{(D\to K^*)}(w) \\
a_1(w)^{(B\to\rho)} &= \left(\frac{m_D}{m_B}\right)^{1/2} \left[\frac{\alpha_s(m_b)}{\alpha_s(m_c)}\right]^{-6/25} a_1^{(D\to K^*)}(w) \\
g(w)^{(B\to\rho)} &= \left(\frac{m_D}{m_B}\right)^{1/2} \left[\frac{\alpha_s(m_b)}{\alpha_s(m_c)}\right]^{-6/25} g^{(D\to K^*)}(w)
\end{aligned} \tag{3.2.11}$$

The stated uncertainties in these expressions due to the use of $SU(3)$ flavor symmetry are $10-20\%$. Also, heavy quark symmetry breaking is expected at a similar level. More importantly, because the w range in $D \to K^*\ell\nu$ is small ($\Delta w \approx 0.3$), these relations are most reliable at small w, in particular for $1 < w < 1.5$. The w range for $B \to \rho\ell\nu$ decay is $1 < w < 3.4$. Thus, there is a large range over which to extrapolate the predictions of Eq. 3.2.11. Nevertheless, we use these expressions to model $B \to \rho\ell\nu$ form factors over the full w (q^2) range.

In our implementation of this model, we use $\alpha_s(m_b) = 0.22$ and $\alpha_s(m_c) = 0.39$. The kinematic distributions predicted are shown in Figs. 3.19 and 3.20.

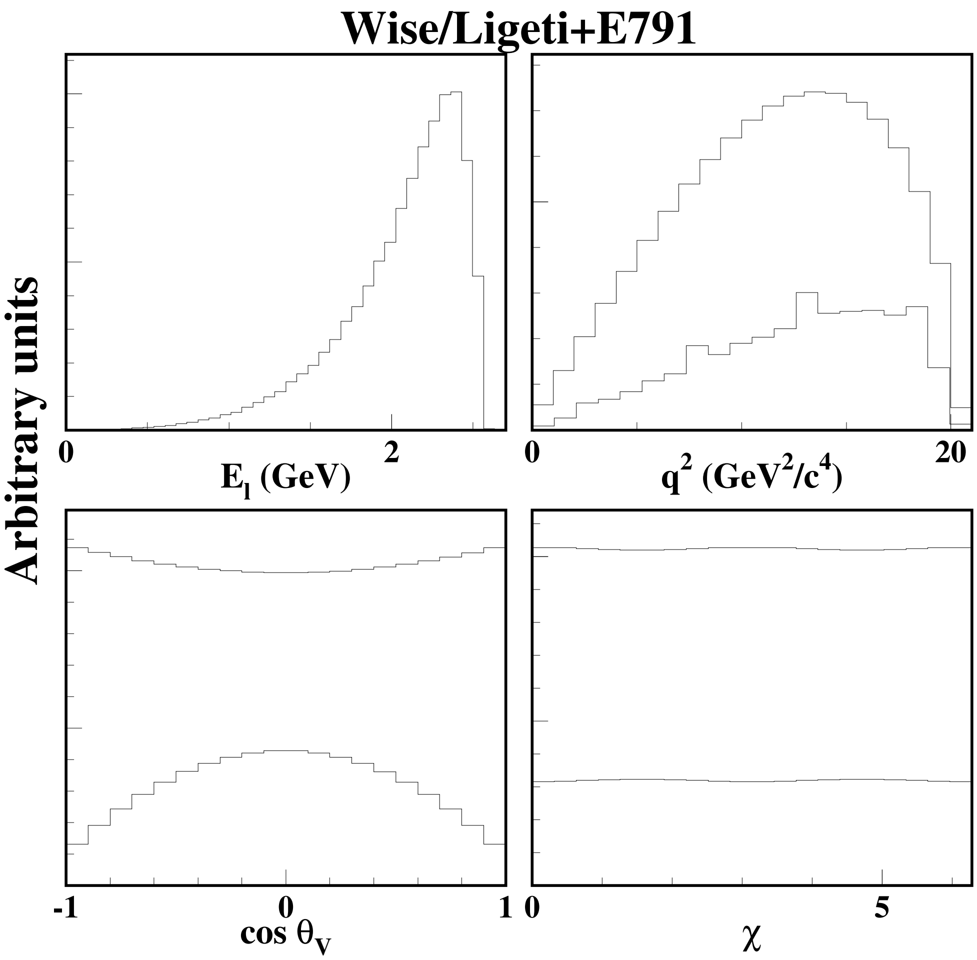

Figure 3.19: Kinematic distributions in the Wise/Ligeti+E791 model: lepton-energy, q^2, $\cos\theta_V$, and χ. For the q^2, $\cos\theta_V$, and χ distributions, the upper (lower) line shows the distribution over the full lepton-energy range (only $E_\ell >$ 2.3 GeV).

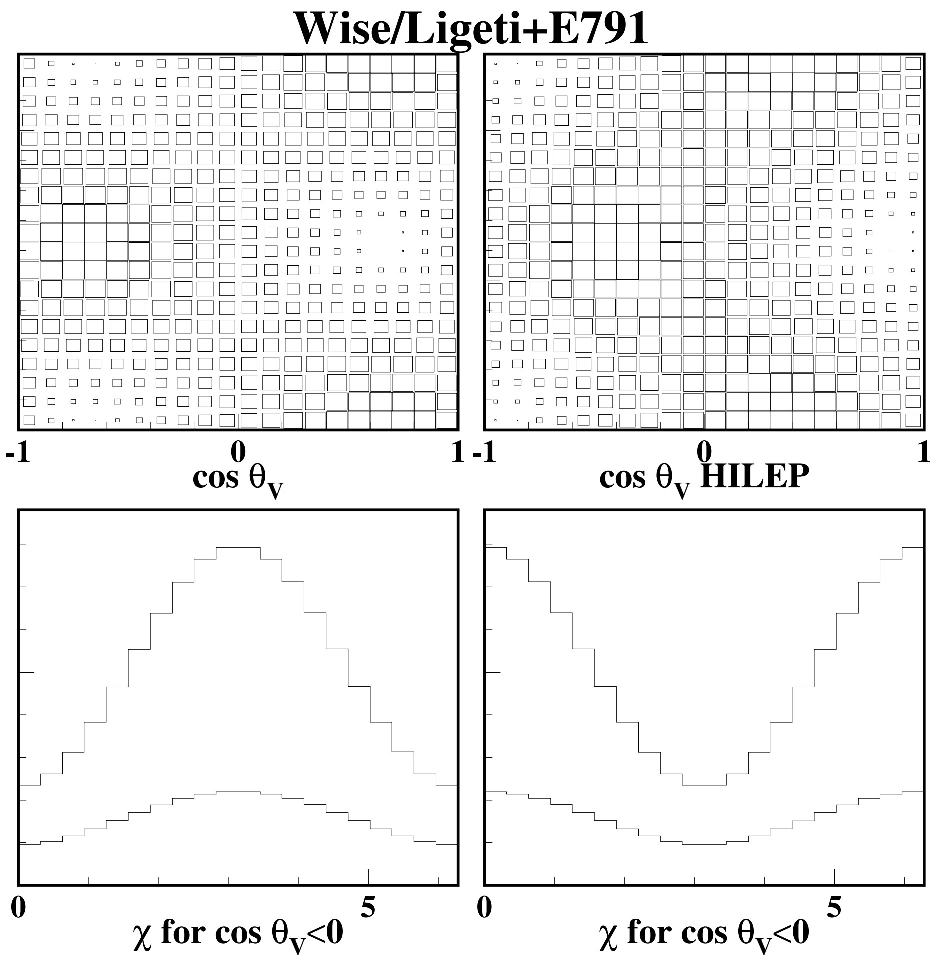

Figure 3.20: Kinematic distributions in the Wise/Ligeti+E791 model: χ vs. $\cos\theta_V$, χ vs. $\cos\theta_V$ (HILEP), χ for events with $\cos\theta_V < 0$, and χ for events with $\cos\theta_V > 0$. For the χ distributions, the upper (lower) line shows the distribution over the full lepton-energy range (only $E_\ell > 2.3$ GeV).

Chapter 4

Experimental status of semileptonic decay

In this chapter, we discuss the current experimental status of semileptonic decays of B mesons as well as other sources of leptons in hadronic events at CLEO. As we will show, semileptonic B decays are a large background source in the study of $B \to \rho\ell\nu$ decay, and currently limit the study of these decays at CLEO to only high-energy leptons ($E_\ell > 2.0$ GeV). In particular, much of the inclusive semileptonic decay rate is yet to be measured in exclusive decay modes. Additionally, only the kinematics of $B \to D\ell\nu$ and $B \to D^*\ell\nu$ decay have been studied with precision. We must account for the uncertainties in the understanding of $b \to c\ell\nu$ decay in our measurement of $B \to \rho\ell\nu$.

We begin in Sec. 4.1 with inclusive $b \to c\ell\nu$ decays. Sections 4.3 and 4.4 describe the current status of exclusive $b \to c\ell\nu$ and $b \to u\ell\nu$, respectively.

4.1 Inclusive $b \to c\ell\nu$ decay

The inclusive semileptonic decay branching fraction has been measured using both $\Upsilon(4S) \to B\bar{B}$ and $Z \to b\bar{b}$ decays. At the $\Upsilon(4S)$, two methods have been used by both the ARGUS [53] and CLEO [54] collaborations to measure the inclusive decay spectrum. The first of these is simply to reconstruct single

Experiment	Inclusive $b \to c\ell\nu$ branching fraction (%)
ARGUS	$9.7 \pm 0.5 \pm 0.4$
CLEO	$10.49 \pm 0.17 \pm 0.43$
ALEPH	$11.01 \pm 0.23 \pm 0.28 \pm 0.11$
DELPHI	$11.06 \pm 0.39 \pm 0.19 \pm 0.12$
OPAL	$10.5 \pm 0.6 \pm 0.4 \pm 0.3$
L3	$10.85 \pm 0.12 \pm 0.43$
PDG average	10.41 ± 0.29

Table 4.1: Inclusive B meson semileptonic decay branching fraction results.

leptons in hadronic events. Experimental results of D meson decays and theoretical models of B meson semileptonic decay are used to unfold the various contributions to the full semileptonic B decay spectrum. The CLEO decay spectrum is shown in Figure 4.1. At low lepton energy, $E_\ell < 1.0$ GeV, secondary leptons, those from hadronic B decays where the charm hadron decay semileptonically, are the dominant contribution. Leptons from $b \to c\ell\nu$ decay typically are more energetic, and dominate for $E_\ell > 1.0$ GeV. Also included in Figure 4.1 is the tiny contribution from $b \to u\ell\nu$ decay. Suppression of $b \to c\ell\nu$ backgrounds is crucial to measurements of $b \to u\ell\nu$ decay processes.

The second method utilized at the $\Upsilon(4S)$ is to examine the lepton spectrum in events that contain an additional high-energy lepton. Using the charge correlations between the two leptons allows for the large secondary lepton contribution to be separated from the primary $b \to c\ell\nu$ spectrum without depending on models. The results of this method from the ARGUS and CLEO collaborations are shown in Table 4.1.

Also included in Table 4.1 are results from the four LEP experiments using 0.5 to 1.4 million Z decays each to measure the inclusive $b \to c\ell\nu$ branching fraction [55, 56, 57, 58]. At LEP, $b\bar{b}$ events are tagged using separated vertices with an efficiency of $\approx 25\%$ and a purity of $\approx 95\%$. As at the $\Upsilon(4S)$ single

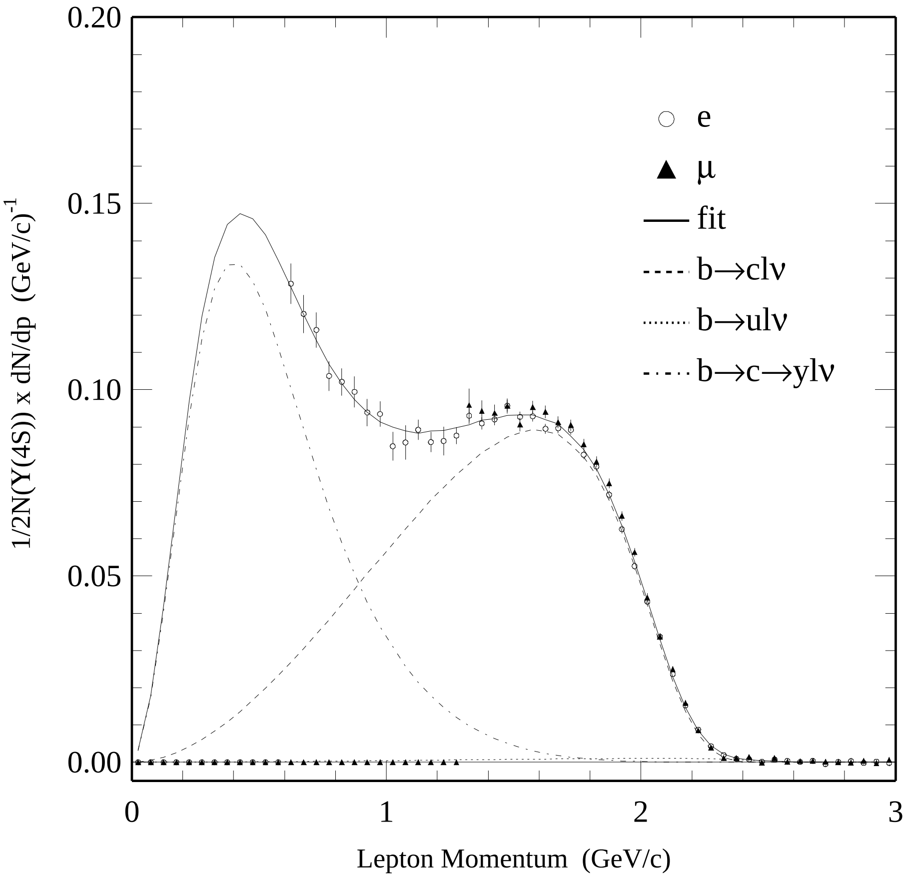

Figure 4.1: Inclusive leptonic spectrum from B-meson decays as measured by the CLEO collaboration. The points have been corrected for acceptance inefficiencies. There are three contributions to the full lepton spectrum: 1. The large component that peaks at large lepton energy is due to $b \to c\ell\nu$ decay; 2. The large component that peaks at low lepton energy is due to $b \to c \to d(s)\ell\nu$; and 3. The small component at large lepton energy is due to $b \to u\ell\nu$ decay. Other contributions, such as continuum and leptons from J/ψ mesons, have been subtracted. From Ref. [54].

lepton and dilepton samples are used to best extract the $b \to \ell$ branching fraction. At the Z, B_d, B_s, and b baryon decays are included in the measurement of $\mathcal{B}(b \to c\ell\nu)$.

4.2 Inclusive $b \to u\ell\nu$ decay

Figure 4.1 illustrates that the inclusive $b \to u\ell\nu$ branching fraction is significantly smaller than that for $b \to c\ell\nu$ decays. A prediction by Rosner [59] gives

$$\frac{\mathcal{B}(B \to X_u\ell\nu)}{\mathcal{B}(B \to X_c\ell\nu)} = (1.85 \text{ to } 2.44)\left|\frac{V_{ub}}{V_{cb}}\right|^2. \tag{4.2.1}$$

Current experimental results for $|V_{ub}/V_{cb}|$ give a ratio of widths of approximately 2%. As is the case for inclusive $b \to c\ell\nu$ decay, inclusive $b \to u\ell\nu$ branching fractions have been determined both at the $\Upsilon(4S)$ and Z resonances.

CLEO [38, 39] and ARGUS [40] observed inclusive $b \to u\ell\nu$ decay by examining the lepton-energy spectrum from B-meson decays for leptons with an energy beyond that allowed for $b \to c\ell\nu$ decay. Large $b \to c\ell\nu$ backgrounds for $E_\ell < 2.3$ GeV currently prevent measurement of $b \to u\ell\nu$ decay over the full lepton-energy range. A large background in the lepton-energy endpoint region is due to leptons from $e^+e^- \to c\bar{c}$ decay. As is described in Chapter 7, $B\bar{B}$ events can be statistically distinguished from such events by considering how jet-like the event is. Figure 4.2 shows the endpoint region of the lepton-energy spectrum observed by the CLEO collaboration for two sets of event requirements. In both cases, there is a clear excess above the $b \to c\ell\nu$ and $e^+e^- \to c\bar{c}$ background in the lepton-energy region above 2.3 GeV.

As these measurements are performed at only very high lepton energies, there is a large theoretical error associated with the extrapolation of the measured yields to a branching fraction over the full lepton energy range. We quote [32]

$$\left|\frac{V_{ub}}{V_{cb}}\right| = 0.08 \pm 0.02, \tag{4.2.2}$$

as the combined result for the CLEO and ARGUS measurements.

More recently the L3 [11], ALEPH [12] and DELPHI [41] collaborations have performed measurements of the inclusive $b \to u\ell\nu$ branching fraction. The extracted values for $|V_{ub}|$ are

$$\begin{aligned}
|V_{ub}| &= (6.0^{+0.8}_{+1.0}\,{}^{+1.4}_{-1.9} \pm 0.2) \times 10^{-3}\ (L3), \\
|V_{ub}| &= (4.32 \pm 0.69 \pm 0.69 \pm 0.17) \times 10^{-3}\ (ALEPH), \\
|V_{ub}| &= (4.10 \pm 0.47 \pm 0.59 \pm 0.36) \times 10^{-3}\ (DELPHI), \qquad (4.2.3)
\end{aligned}$$

where the errors are statistical, systematic, and theoretical. The theoretical error is due to the uncertainty in the normalization factor that is needed to extract $|V_{ub}|$ from a measured inclusive branching fraction. The systematic uncertainty on these measurements is quite large and is dominated by the experimental understanding of the $b \to c\ell\nu$ background normalization and composition. In this sense, the measurements performed at the $\Upsilon(4S)$ have an advantage in that the largest background source, the continuum, is measured directly using the data. No Monte Carlo prediction is needed to estimate the size and kinematic distributions of the continuum background at the $\Upsilon(4S)$.

Nevertheless there are advantages to measuring $|V_{ub}|$ at LEP. To illustrate this, we describe in some detail the DELPHI measurement. The basis of this measurement is the fact that for most $b \to u\ell\nu$ decays, the hadronic recoil mass will be less than M_D [42, 43]. Because B-meson decays are contained in a jet at LEP, the reconstruction of the recoil mass is somewhat more straightforward than at the $\Upsilon(4S)$. By reconstructing this mass, backgrounds from $b \to c\ell\nu$ decay can be suppressed. Additionally, the analysis takes advantage of the excellent particle identification to veto candidate events where a kaon is identified. Finally, the analysis examines the signed impact parameter of the lepton with respect to the secondary vertex of the reconstructed hadron candidate. In $b \to c\ell\nu$ decays, the hadronic vertex is not that of the B-meson decay, but rather that of the D-meson. Thus, the lepton should point back to a point between the primary event vertex and the secondary vertex. In contrast, for $b \to u\ell\nu$ events, the lepton and hadron originate from the same secondary

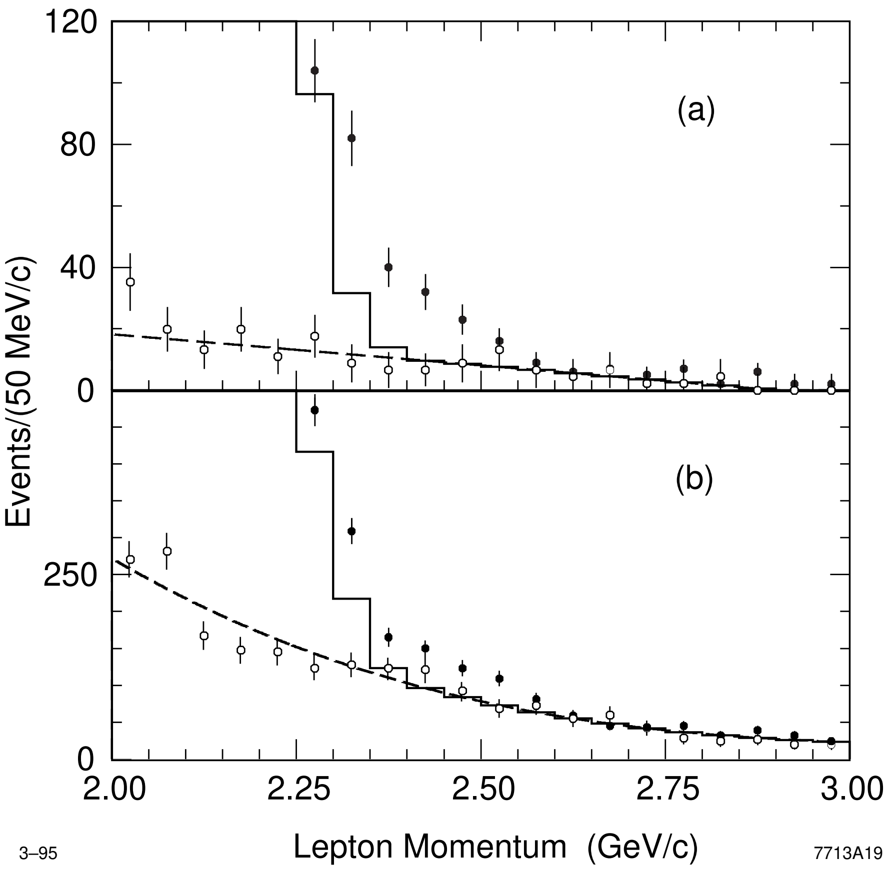

Figure 4.2: The lepton-momentum spectrum observed by the CLEO collaboration for $|\mathbf{p}_\ell| > 2.0$ GeV. The solid points are the data. The hollow points show the expected contribution from $e^+e^- \to q\bar{q}$ ($q \equiv u,\ d,\ s,$ and c) events. The histogram shows the background contribution due to $b \to c\ell\nu$ decays. A clear excess is observed for $|\mathbf{p}_\ell| > 2.3$ GeV. The upper and lower plots show results for different event selection criteria, which correspond to tight and loose requirements on the jet-like nature of candidate events. From Ref. [39].

vertex.

The last two requirements are used to create $b \to u\ell\nu$ enriched and depleted samples. The data sample is further divided according to the reconstructed hadronic mass (above and below 1.6 GeV/c^2). In the enriched sample with low hadronic mass, there is an excess of 205 ± 56 events over 2087 ± 30 background events. 68% of the $b \to u\ell\nu$ events that enter into the four regions are expected to be in this region.

The lepton-energy distribution (computed in the reconstructed B-meson rest frame) in these four regions is fit for the number of $b \to u\ell\nu$ events. The number of $b \to u\ell\nu$ decays relative to the number of $b \to c\ell\nu$ decays determines $|V_{ub}|^2/|V_{cb}|^2$ and is proportional to [44]:

$$\frac{|V_{ub}|^2}{|V_{cb}|^2} \times \frac{f(m_u/m_b)}{f(m_c/m_b)} \times \frac{1 + a_1^u \alpha_s(m_b)/\pi + a_2^u \alpha_s^2(m_b)/\pi^2}{1 + a_1^c \alpha_s(\sqrt{m_b m_c})/\pi + a_2^c \alpha_s^2(\sqrt{m_b m_c})/\pi^2} \qquad (4.2.4)$$

where f is a phase space factor and $a_i^{u(c)}$ are perturbative corrections. In the fit, there are two free parameters: $|V_{ub}|/|V_{cb}|$ and the overall normalization. By allowing the normalization to float in the fit, the sensitivity to the Monte Carlo modeling of absolute efficiencies as well as to the value of the inclusive $b \to c\ell\nu$ lepton-energy spectrum is removed. The result of this fit is

$$\frac{|V_{ub}|}{|V_{cb}|} = 0.104 \pm 0.012, \qquad (4.2.5)$$

where the error is statistical only. The background normalization agrees with the Monte Carlo prediction to 1.5%. Figures 4.3 and 4.4 show the results of this fit.

The largest systematic errors are due to:

- Understanding of the background compostion. There are several components to this systematic. The uncertainty in the fraction of background events from sectionary decays is the largest single component to this uncertainty. $\mathcal{B}(b \to \ell)/\mathcal{B}(c \to \ell)$ is varied according to $0.112 \pm 0.02/0.094 \pm 0.01$, resulting in an uncertainty of 0.0063 on $|V_{ub}|/|V_{cb}|$. Also, the fraction of $b \to c\ell\nu$ events from $B \to D^*\ell\nu$ and $B \to D^{**}\ell\nu$ decay is varied by 14% leading to an uncertainty of 0.0048.

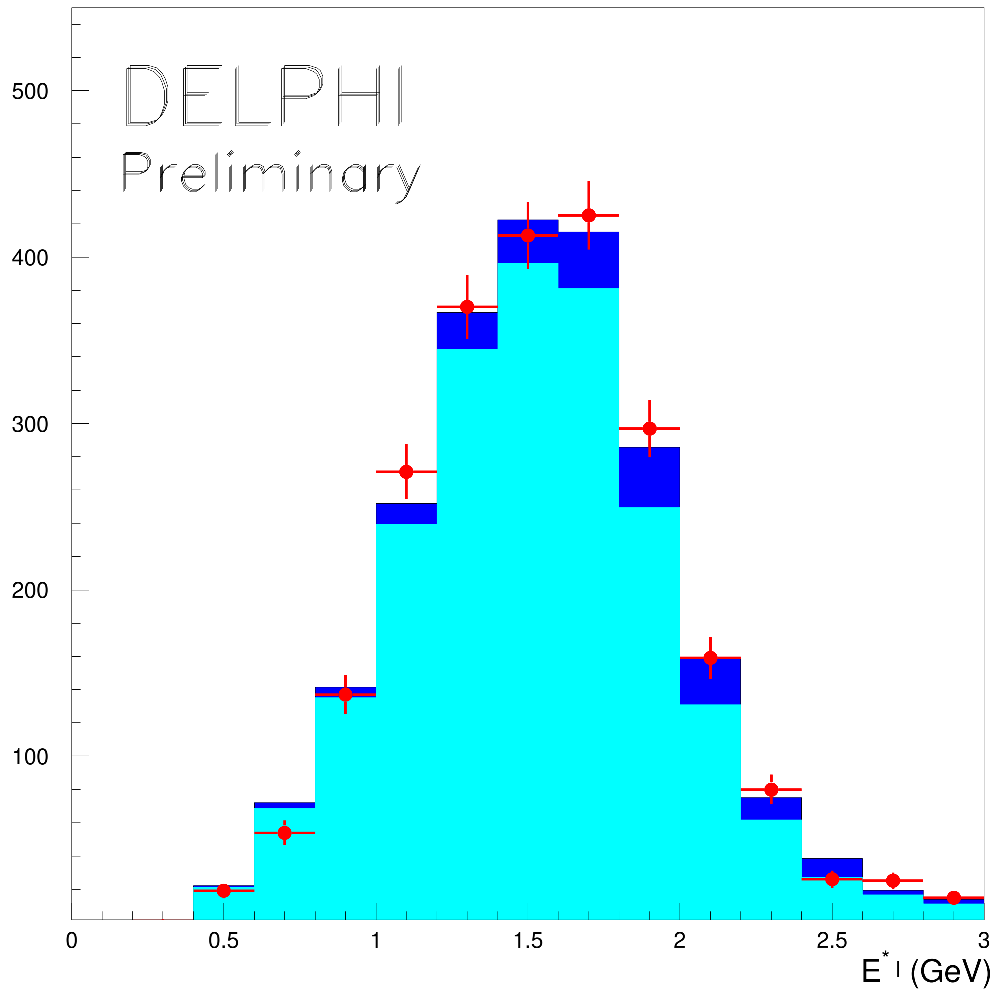

Figure 4.3: Lepton-energy distribution for the low hadronic mass, $b \to u$ enriched sample. The lightly (darkly) shaded region shows the background (signal) contribution. The lepton energy is evaluated in the measured rest frame of the B meson. From Ref. [41].

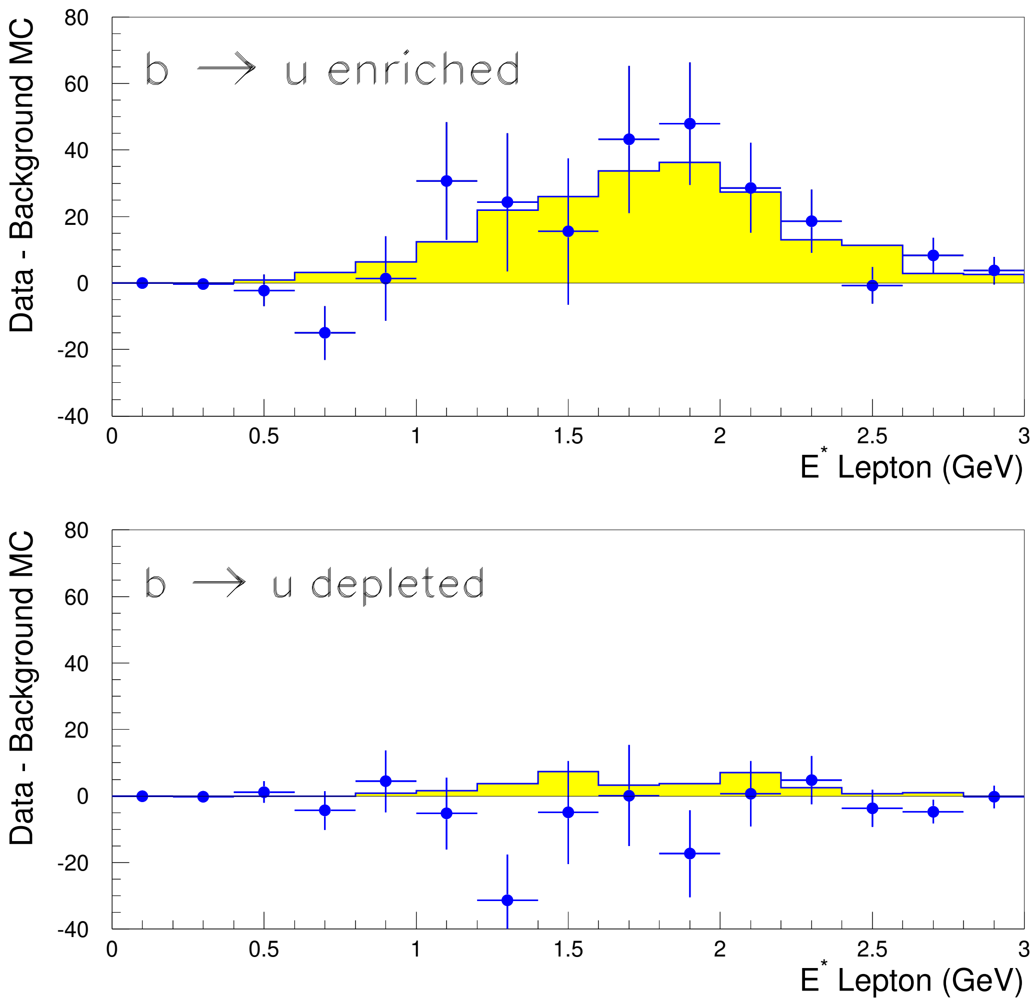

Figure 4.4: Background subtracted lepton-energy distribution for the $b \to u$ enriched and depleted low hadronic mass samples. The lepton energy is evaluated in the measured rest frame of the B meson. From Ref. [41].

- Lepton impact parameter resolution. Because of the cut on the production point of the lepton relative to the primary and secondary vertices, the uncertainty in the impact parameter resolution leads to a 0.0070 uncertainty on $|V_{ub}|/|V_{cb}|$.
- Hadron multiplicity. In the $b \to u\ell\nu$ depleted sample, the multiplicity is observed to agree to ± 0.02 particles per event between the data and Monte Carlo simulation. The systematic error is evaluated to be the change in the final results when the multiplicity in the Monte Carlo simulation is changed by this amount.
- Kinematics of $b \to u\ell\nu$ decay. In particular, the uncertainty in the input parameters (m_b and $< p_b^2 >$) of the inclusive $b \to u\ell\nu$ Monte Carlo prediction. The uncertainty on m_b also contributes an uncertainty in the extraction of $|V_{ub}|/|V_{cb}|$ from the measured number of $b \to u\ell\nu$ events. Additionally, the uncertainty due to the details of the hadronisation model are evaluated.

The total systematic error in 0.0177 on $|V_{ub}|/|V_{cb}|$. Of this, 0.009 is due to the model of $b \to u\ell\nu$ kinematics.

4.3 Exclusive $b \to c\ell\nu$ decay

Purely exclusive measurements of $b \to c\ell\nu$ decays are limited to $B \to D\ell\nu$, $B \to D^*\ell\nu$, and $B \to D_1\ell\nu$ final states. In addition, ALEPH has measured the inclusive branching fraction for $B \to D^{(*)}\pi\ell\nu$. We discuss the current status of each of these below.

The CLEO, ARGUS, and ALEPH collaborations have reported measurements of $B \to D\ell\nu$. For $B^0 \to D^-\ell^+\nu$, the D^- meson is reconstructed using $D^- \to K^-\pi^+\pi^+$ and for $B^+ \to D^0\ell^+\nu$, the $D^0 \to K^-\pi^+$ mode is used. Lepton and D combinations with kinematics that are consistent with coming from a B meson are used to measure $\mathcal{B}(B \to D\ell\nu)$ as well as the q^2 distribution of $B \to D\ell\nu$ decay. $D\ell$ candidates from background sources, such as $B \to D^*\ell\nu$

events, will often have a kinematic configuration that is inconsistent with a B-meson decay where only the undetected neutrino is missing.

ALEPH has measured $\mathcal{B}(B^0 \to D^-\ell^+\nu)$ to be $(2.35 \pm 0.20 \pm 0.44)\%$. Assuming that $\Gamma(B^0 \to D^-\ell^+\nu) = \Gamma(B^+ \to D^0\ell^+\nu)$, CLEO has measured

$$\begin{aligned} \mathcal{B}(B^+ \to D^0\ell^+\nu) &= (2.21 \pm 0.13 \pm 0.19)\% \\ \mathcal{B}(B^0 \to D^-\ell^+\nu) &= (2.09 \pm 0.13 \pm 0.18)\% \end{aligned} \tag{4.3.1}$$

where the errors are statistical and systematic. Both errors are completely correlated. CLEO has also measured the q^2 distribution in $B \to D\ell\nu$ decay.

As is the case for $B \to D\ell\nu$, both the branching fraction and decay kinematics for the decay $B \to D^*\ell\nu$ have been experimentally probed. Full reconstruction of a D^* and lepton candidate using the D-meson decay mode $D^0 \to K^-\pi^+$ (as well as $D^0 \to K^-\pi^+\pi^0$, $D^0 \to K^-\pi^+\pi^-\pi^+$ and $D^0 \to K_s^0\pi^-\pi^+$ in some cases) is used by experiments at LEP and at the $\Upsilon(4S)$. To reduce backgrounds, a missing mass variable is used to eliminate D^* plus lepton candidates that are from B-meson decays of the form $B \to D^*X\ell\nu$ as well as those from combinatoric background.

For the decay mode $B^0 \to D^{*-}\ell^+\nu$, measurements have been performed by the OPAL [60], ALEPH [61], DELPHI [62], CLEO [63], and ARGUS [64] collaborations. An average of

$$\mathcal{B}(B^0 \to D^{*-}\ell^+\nu) = (4.60 \pm 0.27)\% \tag{4.3.2}$$

has been determined by the Particle Data Group (PDG) [32].

The mode $B^+ \to \bar{D}^{*0}\ell^+\nu$, requires the detection of a low momentum π^0 in order to reconstruct the $\bar{D}^{*0}$. A result of this is that measurements have not been performed by the LEP experiements. Averaging CLEO [63] and ARGUS [65] results, the PDG [32] finds

$$\mathcal{B}(B^+ \to \bar{D}^{*0}\ell^+\nu) = (5.3 \pm 0.8).\% \tag{4.3.3}$$

The phenomenology of $B \to D^*\ell\nu$ decay is described in detail in Chapter 3. Two approaches have been employed to experimentally measure the kinematics of $B \to D^*\ell\nu$. Measurements of the q^2 distribution, or more exactly the slope of the form factor, have been described in Refs. [60, 61, 62, 63, 64].

We instead give results of a measurement [66] of the full four-dimensional kinematic decay distribution performed by the CLEO collaboration. This analysis found that at $q^2_{\max}$

$$\begin{aligned} R_1 &= \frac{V_1(q^2)}{A_1(q^2)\left[1 - \frac{q^2}{(M_B+M_{D^*})^2}\right]} = 1.18 \pm 0.30 \pm 0.12, \\ R_2 &= \frac{A_2(q^2)}{A_1(q^2)\left[1 - \frac{q^2}{(M_B+M_{D^*})^2}\right]} = 0.71 \pm 0.22 \pm 0.07. \end{aligned} \tag{4.3.4}$$

These ratios are motivated by heavy quark effective theory (HQET), in which the decay amplitude for $B \to D^*\ell\nu$ is expanded in powers of $1/m_b$ and $1/m_c$. In the limit of heavy-quark symmetry, $R_1 = R_2 = 1$. Figures 4.5 and 4.6 show some of the fit projections from this measurement. We have incorporated these measurements into a HQET based Monte Carlo prediction of $B \to D^*\ell\nu$ decay.

Finally, we summarize current measurements of $b \to c\ell\nu$ decays involving resonances with mass greater than M_{D^*} as well as nonresonant $B \to D^{(*)}X\ell\nu$ decays. The OPAL [67], CLEO [68], and ALEPH [69] collaborations have measured the branching fraction for $B^- \to D_1^0\ell^-\bar{\nu}$. Averaging these results we find $\mathcal{B}(B^- \to D_1^0\ell^-\bar{\nu})(= 0.65 \pm 0.11)\%$ [32]. Semileptonic decays to other D^{**} states have not yet been observed.

ALEPH has also measured the branching fraction for inclusive $B \to D^{(*)}\pi\ell\nu$ decay [69], either involving a D^{**} resonant state or a nonresonant decay mode. They find

$$\mathcal{B}(B \to D\pi\ell^+\nu) + \mathcal{B}(B \to D^*\pi\ell^+\nu) = (2.26 \pm 0.29 \pm 0.33)\%, \tag{4.3.5}$$

where the errors are statistical and systematic.

4.4 Exclusive $b \to u\ell\nu$ decay

CLEO has previously observed $B \to \rho\ell\nu$ and $B \to \pi\ell\nu$ decays [9], using approximately 2.8×10^6 $B\bar{B}$ decays and a method known as neutrino recon-

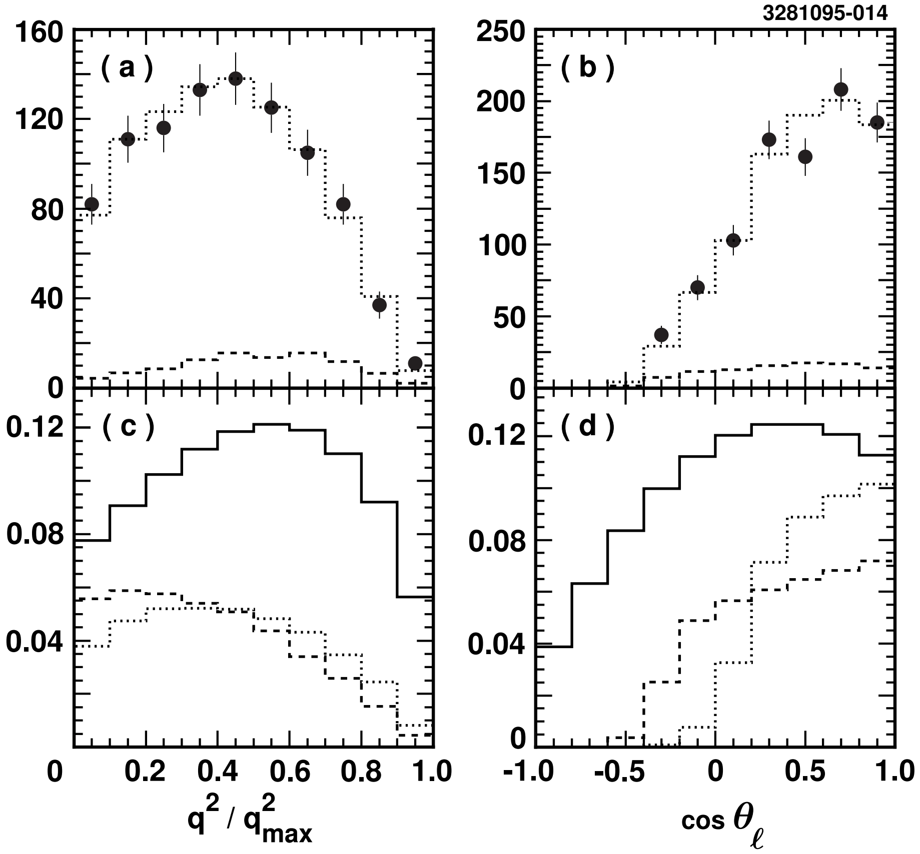

Figure 4.5: Measured kinematic distributions in $B \to D^*\ell\nu$ decay as observed by the CLEO collaboration. No efficiency correction has been performed. In (a) and (b), the points are the data and the histogram is the projection of the fit. In (c) and (d), the solid histogram shows the fit results as would be observed by a perfect detector. The dashed (dotted) line shows the distributions expected for electrons (muons) after acceptance effects are accounted for. From Ref. [66].

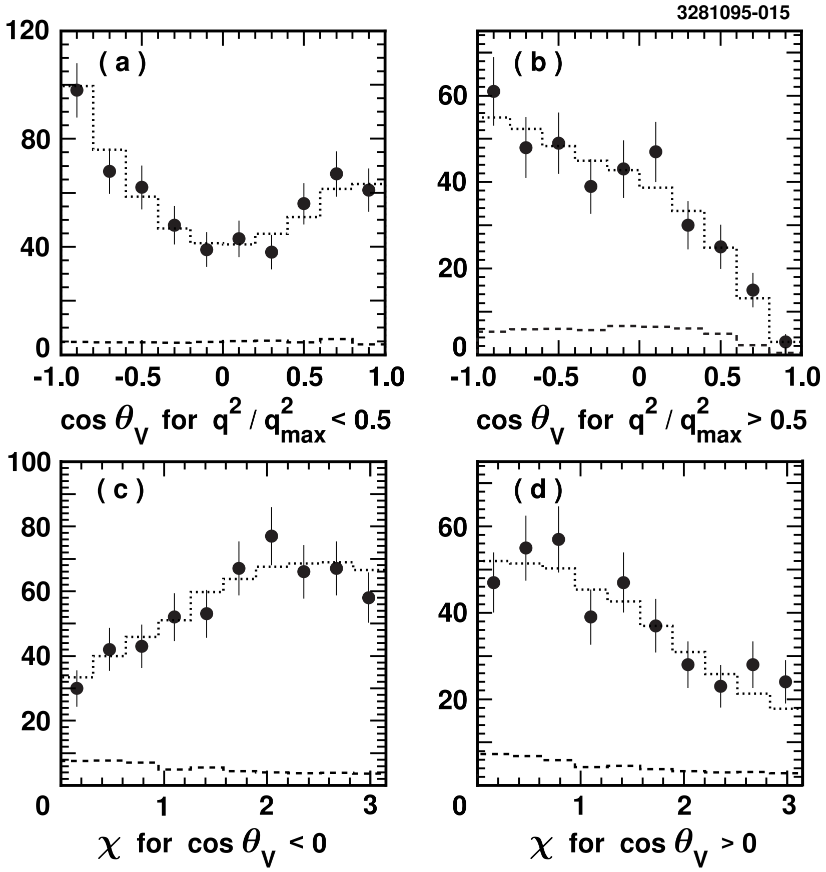

Figure 4.6: Measured kinematic distributions in $B \to D^*\ell\nu$ decay as observed by the CLEO collaboration. No efficiency correction has been performed. The points show the data, the dotted lines show the result of the fit, and the dashed lines show the expected background contribution. From Ref. [66].

struction. These are the only exclusive $b \to u\ell\nu$ decay modes that have been experimentally observed.

ν reconstruction takes advantage of the near 4π solid angle coverage of the tracking and calorimetry systems of the CLEO detector to reconstruct the missing momentum and missing energy of the event as a measure of the undetected neutrino momentum. To improve the resolution of these quantities, events are selected that are consistent with missing only the neutrino from the $B \to \rho\ell\nu$ decay. For example, events are required to have exactly one detected lepton and a reconstructed $\Sigma Q = 0$. Also, the missing energy and momentum must be consistent with being due to a zero mass particle ($M = \sqrt{E^2_{\rm miss} - p^2_{\rm miss}}$). These requirements result in a resolution of 100 MeV/c (260 MeV) on the missing momentum (energy).

To reduce the dominant $b \to c\ell\nu$ background, the search for $B \to \rho(\pi)\ell\nu$ decay is rescricted to the region about 2.0 (1.5) GeV. To extract branching fractions (and then $|V_{ub}|$) from measured yields thus depends on form-factor models to describe (most importantly) the lepton-energy spectrum of $B \to \rho\ell\nu$ and $B \to \pi\ell\nu$ decay.

Yields are extracted with a fit to three kinematic variables: $M(\pi\pi)$, $M_{\rm cand}$, and ΔE. The invariant mass of the ρ candidate is used for $B \to \rho\ell\nu$ candidates. $M_{\rm cand}$ and ΔE are common to the ρ and π semileptonic measurements, and are defined as:

$$\begin{aligned} M_{\rm cand} &= \sqrt{E^2_{\rm beam} - |\mathbf{p}_\rho + \mathbf{p}_\ell + \mathbf{p}_{\rm miss}|^2}, \\ \Delta E &= E_\rho + E_\ell + |\mathbf{p}_{\rm miss}| - E_{\rm beam}. \end{aligned} \tag{4.4.1}$$

For signal events, $M_{\rm cand}$ will peak at the B-meson mass, and ΔE at zero. The resolution on ΔE is dominated by that on $\mathbf{p}_{\rm miss}$. Figure 4.7 shows the $M_{\rm cand}$ and ΔE distributions for the data and fit results. In each plot, there is a clear peak at $M_{\rm cand} \approx 5.28$ MeV/c^2 and $\Delta E = 0$, indicating both $B \to \pi\ell\nu$ and $B \to \rho\ell\nu$ signals.

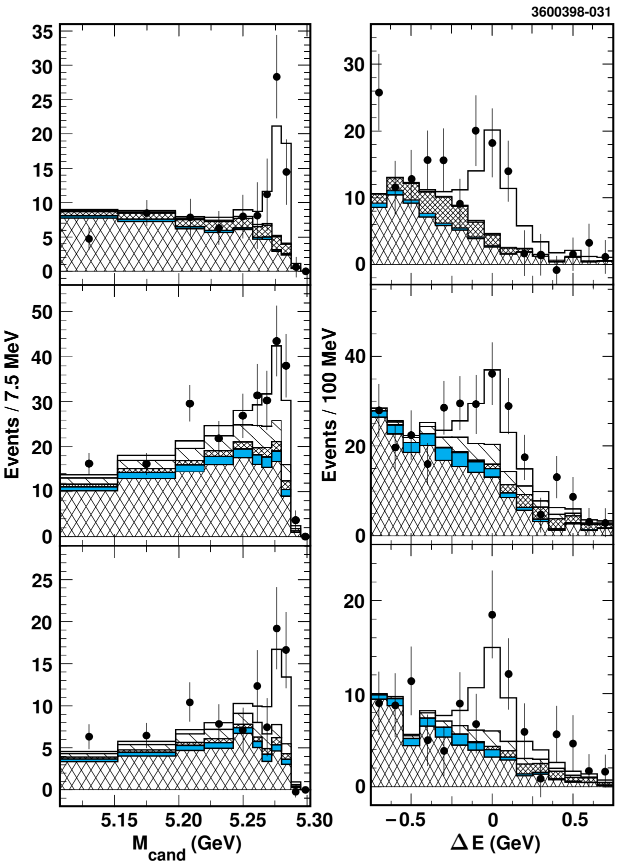

Figure 4.7: $B \to \rho\ell\nu$ and $B \to \pi\ell\nu$ results from CLEO. The left (right)-hand plots show the fit variable $M_{\rm cand}$ (ΔE). The top set of plots shows the $B \to \pi^{\pm}\ell\nu$ and $B \to \pi^{0}\ell\nu$ modes. The middle plots show the $B \to \rho^{\pm}\ell\nu$, $B \to \rho^{0}\ell\nu$, and $B \to \omega\ell\nu$ modes, including all invariant $\pi\pi$ and $\pi^{+}\pi^{-}\pi^{0}$ masses. Finally, the bottom plots show the $\rho^{\pm}$ and ρ^{0} modes for events with $|M(\pi\pi) - M(\rho)| < 150$ MeV$/c^2$. From Ref. [13].

This analysis found

$$\begin{aligned}
\mathcal{B}(B^0 \to \rho^- \ell^+ \nu) &= (2.5 \pm 0.4^{+0.5}_{-0.7} \pm 0.5) \times 10^{-4}, \\
\mathcal{B}(B^0 \to \pi^- \ell^+ \nu) &= (1.8 \pm 0.4 \pm 0.3 \pm 0.2) \times 10^{-4}, \\
|V_{ub}| &= (3.3 \pm 0.2^{+0.3}_{-0.4} \pm 0.7) \times 10^{-3},
\end{aligned} \tag{4.4.2}$$

where the errors are statistical, systematic, and theoretical. This analysis has been updated to use the set of form-factor models described in Chapter 3, most of which have been developed or updated since these results were published. The updated results are shown in Figs. 4.8 and 4.9.

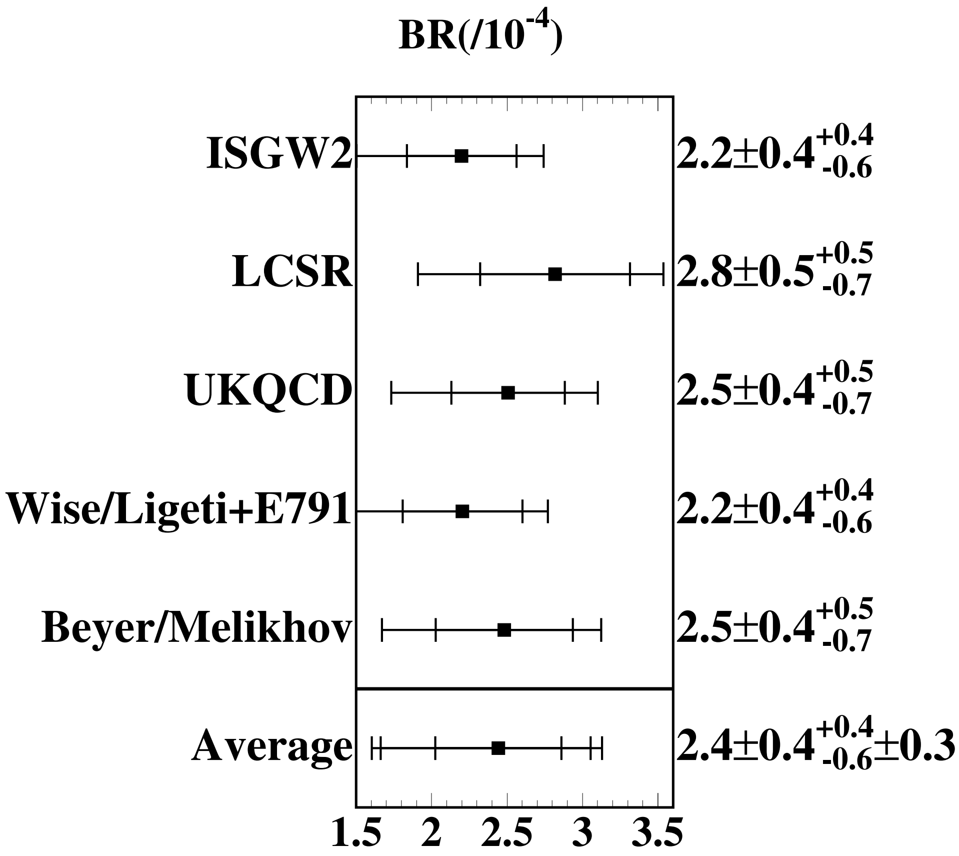

Figure 4.8: Updated results of Ref. [9] for $\mathcal{B}(B^0 \to \rho^- \ell^+ \nu)$ using the form-factor predictions described in Chapter 3. The errors are statistical, systematic, and theoretical (on the averages), successively combined in quadrature. The theoretical error is taken to be 1/2 of the full spread of results.

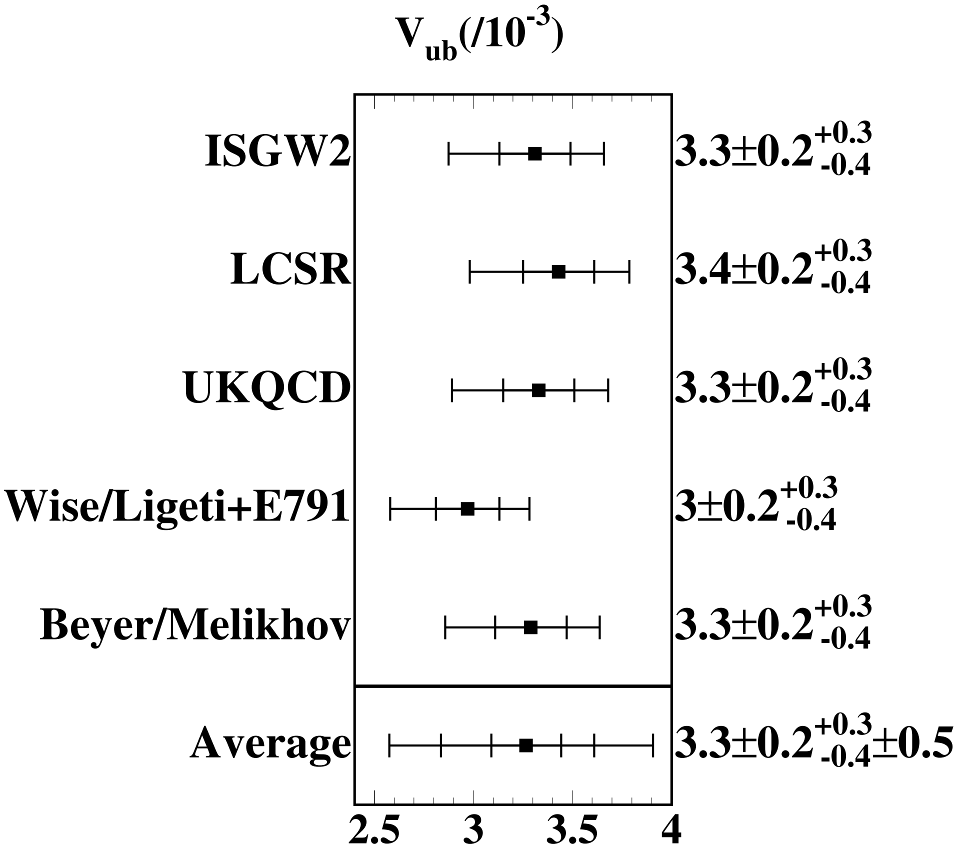

Figure 4.9: Updated results of Ref. [9] for $|V_{ub}|$ using the form-factor predictions described in Chapter 3. The errors are statistical, systematic, and theoretical (on the averages), successively combined in quadrature. The theoretical error is taken to be 1/2 of the full spread of results in quadrature with the additional uncertainty due to the determination of $\tilde{\Gamma}_{\rm thy}$.

Chapter 5

CLEO II and CESR overview

The data used in this analysis were collected by the CLEO II [70] detector located at the Cornell Electron Storage Ring (CESR), operating near the $\Upsilon(4S)$ resonance. In this chapter, we discuss CESR and detail the properties of the CLEO II detector.

5.1 CESR

CESR is capable of delivering e^+ and e^- beams with a center of mass energy between 9 and 12 GeV, with total currents around 500 mA. Recently, an instantaneous luminosity of greater than 0.8×10^{33} cm^{-2} sec^{-1} has been achieved. The majority of data taken with the CLEO II detector have been taken on, or just below, the $\Upsilon(4S)$, which is the first Υ resonance above the $B\overline{B}$ threshold. The $\Upsilon(4S)$ decays almost exclusively to $B^0\overline{B}^0$ and B^+B^- mesons. Figure 5.1 shows the cross section for $e^+e^- \to$ hadrons in the center of mass energy range near the Υ. The peak cross section (σ) of the $\Upsilon(4S)$ resonance is approximately 1.07 nb. The continuum ($e^+e^- \to q\overline{q}$ where $q = u, d, s, c$) below the $\Upsilon(4S)$, $\sigma \approx 3$ nb, is a significant source of background events for the analysis of $B \to \rho\ell\nu$. Data taken just below the $\Upsilon(4S)$ (and below the $B\overline{B}$ threshold) are useful in the study of this background.

Table 5.1 summarizes the current experimental understanding of $\Upsilon(4S)$

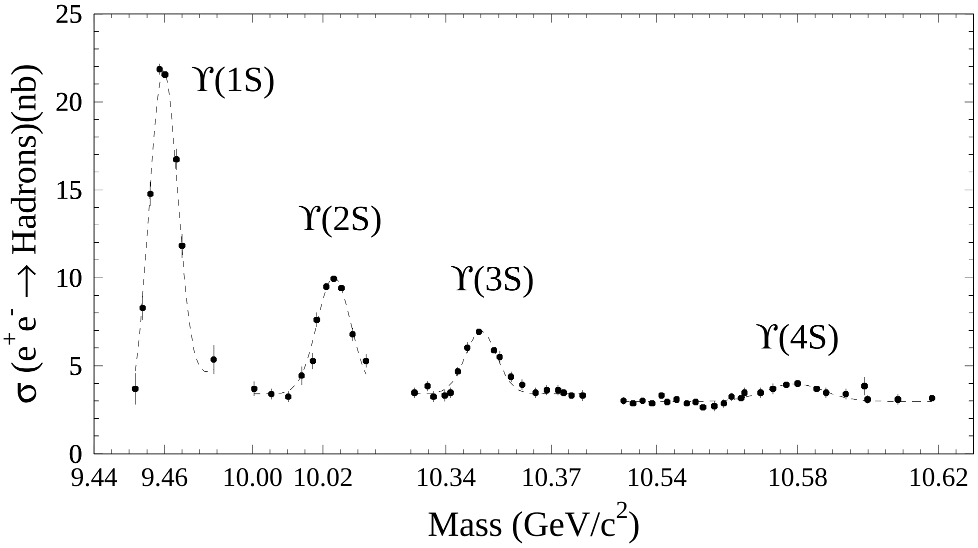

Figure 5.1: e^+e^- hadronic cross section for center of mass energies near the $\Upsilon(4S)$ resonance.

Decay mode	Branching fraction
$\Upsilon(4S) \to e^+e^-$	$(2.77 \pm 0.5 \pm 0.49) \times 10^{-5}$
$\Upsilon(4S) \to J/\psi X$	$(2.2 \pm 0.6 \pm 0.4) \times 10^{-3}$
$\Upsilon(4S) \to$ non-$B\bar{B}$	< 0.04
$(\Upsilon(4S) \to B^+B^-)/(\Upsilon(4S) \to B^0\bar{B}^0)$	$1.13 \pm 0.14 \pm 0.13 \pm 0.06$

Table 5.1: Decay modes of the $\Upsilon(4S)$.

decay. CLEO has placed a limit of 4% on the fraction of decays to final states other than $B\bar{B}$. Measurements of the ratio (f_{+-}/f_{00}) of $\Upsilon(4S)$ decays to B^+B^- and $B^0\bar{B}^0$ are consistent with 1. In this thesis, we will use the value $f_{+-}/f_{00} = 1.0 \pm 0.1$.

5.2 The CLEO II detector

The CLEO II detector is a multipurpose detector designed to provide excellent charged and neutral particle reconstruction efficiency and resolution. The design is similar to detectors found at other collider experiments. Three cylindrical tracking chambers are surrounded by a time of flight (TOF) system, a CsI calorimeter, as well as a muon system. We describe each of these systems below. Figure 5.2 shows a y-z slice (y is the vertical dimension, z is along the beam direction) of the full detector.

Specifications for the inner three tracking chambers are summarized in Table 5.2. The inner most device for the data analyzed here is a 6 layer strawtube chamber, known as the PTL. The intermediate drift chamber, the VD, consists of 2 cathode layers as well as 10 anode layers. The VD and PTL are schematically shown in Figure 5.3. The outer drift chamber, the DR, is a 51 layer device with 2 cathode layers, as shown in Figure 5.4. Particle identification using specific ionization (dE/dx) loss is performed using only the DR pulse height information.

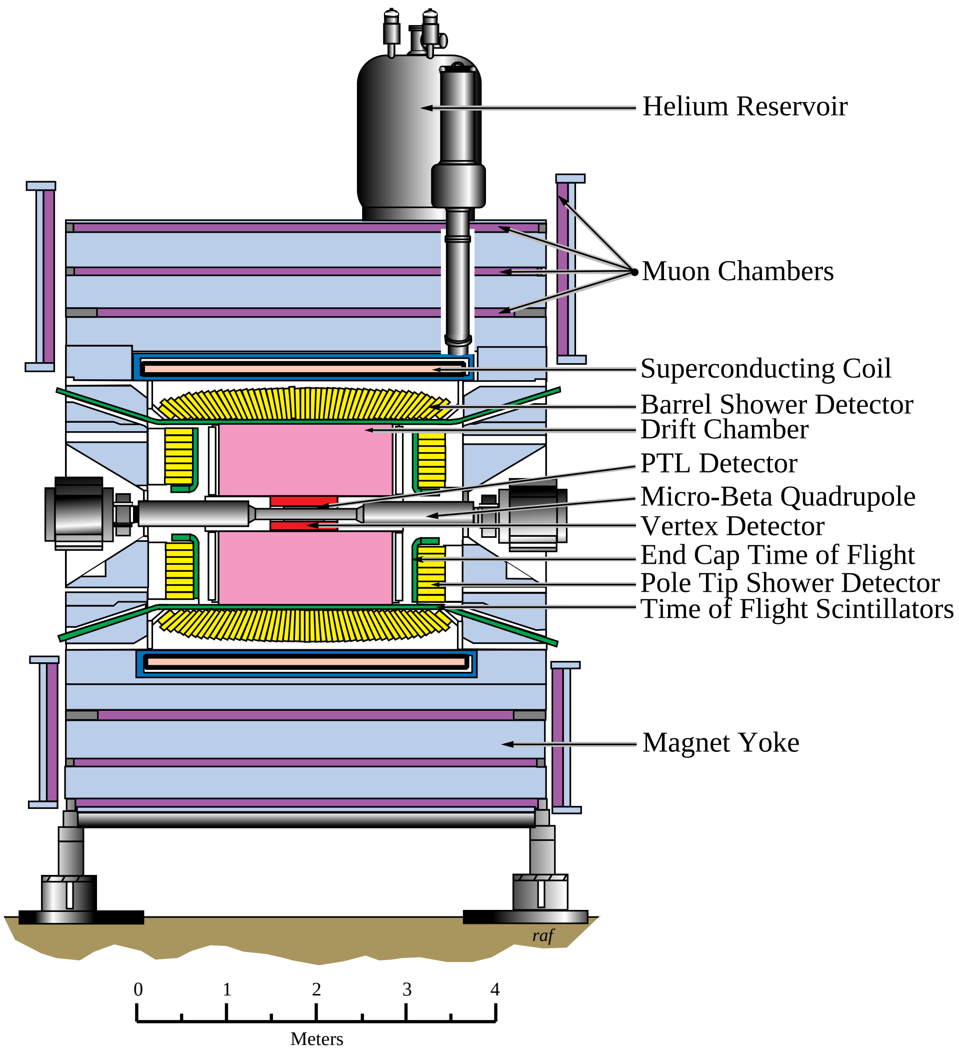

Figure 5.2: The CLEO II detector prior to the installation of the silicon vertex detector (SVX).

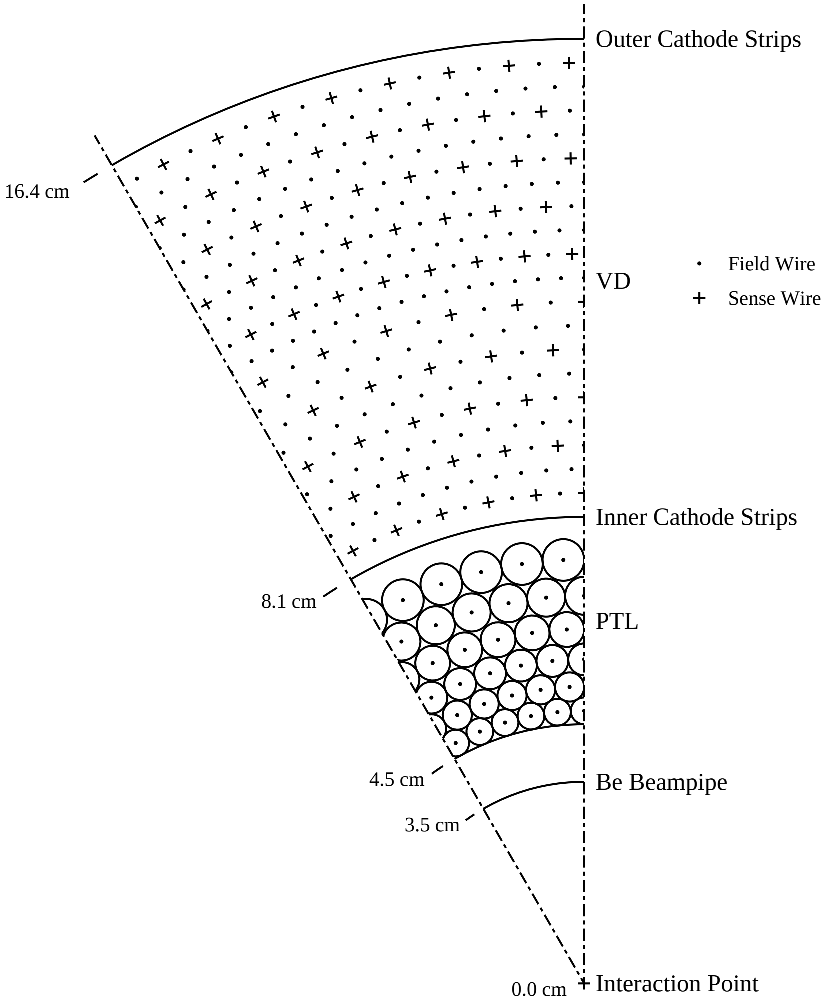

Figure 5.3: End view of the VD and PTL, including wire layout and radii. From Ref. [70].

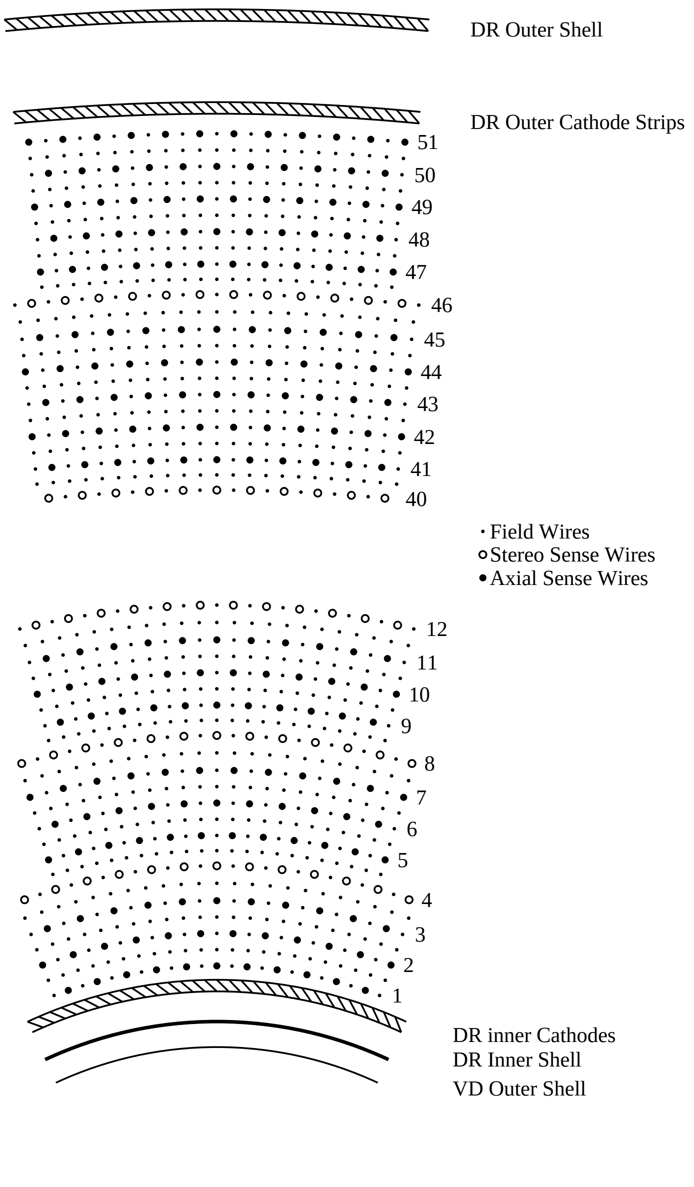

Figure 5.4: The wire layout of the DR. From Ref. [70].

Device	# Anode	# Stereo	# Cathode	Radii	Length
PTL	6	0	0	4.7-7.2 cm	50 cm
VD	10	0	2	8.5-16 cm	70 cm
DR	40	11	2	20-90 cm	192 cm

Table 5.2: Summary of the inner tracking system. For each device, the number of anode, stereo and cathode layers are given as well as the total length and radius of the first and last anode layer.

The tracking chambers are within a 1.5 T magnetic field along the beam direction, which allows for good charge separation and $|\mathbf{p}_{\mathrm{t}}|$ resolution. For tracks with $|\mathbf{p}_{\mathrm{t}}| = 0.5(5.3)$ GeV/c, $\delta|\mathbf{p}_{\mathrm{t}}|$ is 3.4 (47) MeV/c. At 5 GeV/c, $\delta\phi \approx 1$ mrad, and $\delta\theta \approx 4$ mrad. The resolution on θ is somewhat worse as the only track z (along the beam axis) information is provided by the 4 cathode layers, the 11 stereo layers, and charge division in the 10 VD anode layers. Track segments are identified in approximately 96% of the 4π solid angle. For tracks lying along the beam direction, the reduced number of z measurements leads to an increase in tracking inefficiency.

Outside of the DR is the time-of-flight (TOF) system, which is used primarily in the trigger and for low momentum particle identification. Consisting of 64 barrel and 28 endcap counters, the TOF measures the time for a charged particle to propagate from the interaction region through the tracking chambers. The barrel counter time resolution is approximately 125 ps in early data, and has degraded somewhat over time. The TOF system is not used in this analysis.

A CsI calorimeter covering 95% of the solid angle sits outside of the TOF system. For 100 MeV showers, the barrel ($|\cos\theta| < 0.71$, where θ is the dip angle with respect to the beam axis) angular resolution is approximately 11 mrad. In the endcap region, the resolution is degraded (approximately 19 mrad) due to the increase in material between the interaction region and the calorimeter. The barrel energy resolution is 4.2% at 100 MeV. The π^0 mass resolution is approximately 6 MeV$/c^2$.

The muon detector uses the iron flux return of the magnet to distinguish muons from other particles. Strongly interacting particles ($\pi^{\pm}$, $K^{\pm}$, etc.) will inelastically collide with nuclei with a mean free path set by the nuclear interaction length of the material. For iron, this length is 16.7 cm. The flux return includes the iron magnet housing and three 30 cm layers of iron positioned in octants around the inner detector. A "super-layer" of muon counters is located after each layer of iron, as well as on either end of the iron layers. Each super-layer is made up of 3 layers of muon counters with between 20 to 29 counters each, which ensure some redundancy. The muon counter inefficiency has increased over time at a rate of approximately 12 counters per year (6% total). The efficiency of the muon system over time can be seen in Figure 5.5.

In November of 1995, the PTL was replaced with a silicon vertex detector (SVX). This detector is shown in Fig. 5.6.

5.3 Data Sample

Table 5.3 and Figure 5.7 describe the data sample collected by the CLEO II detector near the $\Upsilon(4S)$ resonance between November, 1990 and Febuary, 1999. This analysis makes use of the 4s2 to 4sG datasets, corresponding to a total luminosity of 4.8 ± 0.1 pb^{-1}. Of this, 3.1 ± 0.06 pb^{-1} was taken on the $\Upsilon(4S)$ resonance, yielding approximately $(3.3 \pm 0.07) \times 10^6$ $B\overline{B}$ pairs. After the 4sG data sample several major changes took place. These include the SVX installation and a change of DR and VD gas to a Helium Propane mix. During the 4s2-4sG, other than degradation due to aging no major hardware changes occured. Aging effects are most prevalent in the PTL and VD systems. Software improvements were made, however. For this analysis, improvements made in the tracking software made after the 4s4 are the most noticable.

Table 5.3 also gives the number of $B\bar{B}$ events in each dataset up to the 4sG, a total of $(3.3 \pm 0.07) \times 10^6$. The uncertainty in this determination comes primarily from three sources. The largest contribution (approximately 1.5%) is

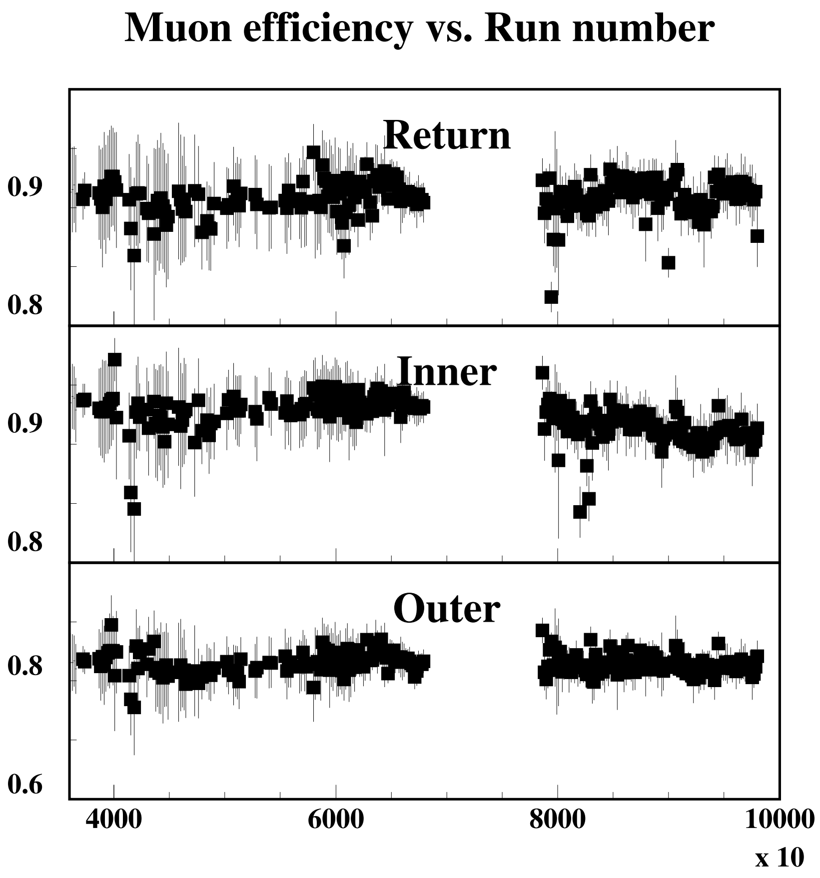

Figure 5.5: Muon efficiency for the barrel return, inner, outer muon superlayers vs. time. An average is performed over octants. Run number 36000 (98000) was taken in November of 1990 (January of 1999).

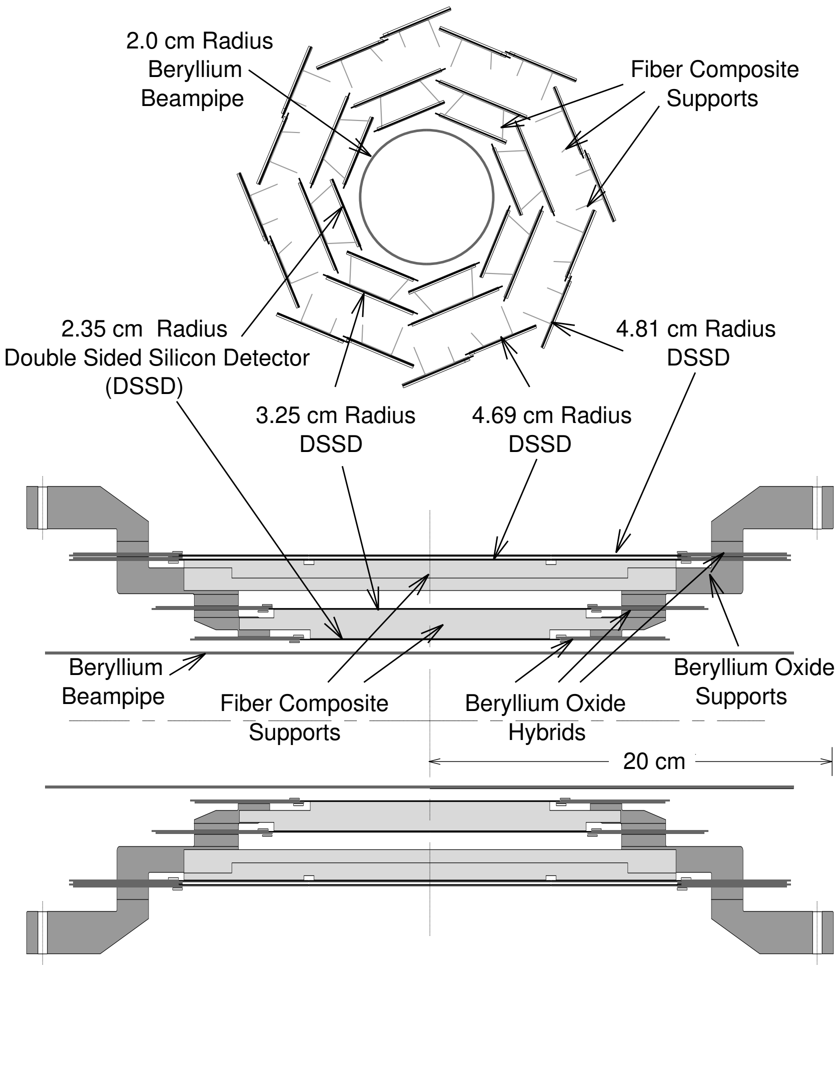

Figure 5.6: The CLEO II silicon vertex detector.

due to the variation in the determined cross section within each data sample. The other sources of uncertainty are the statistical error (0.3%) and the Monte Carlo modeling of the trigger efficiency (0.4%).

Sample	Run range	Dates	Lumin. (pb^{-1})
4s2	36233 - 40095	11 Nov. 1990 - 4 Jun. 1991	672.0
4s3	41386 - 45969	18 Sep. 1991 - 17 Feb. 1992	680.2
4s4	46035 - 48057	10 Apr. 1992 - 26 May 1992	317.5
4s5	48789 - 51406	9 Jul. 1992 - 5 Oct. 1992	342.7
4s6	51431 - 53702	3 Nov. 1992 - 19 Jan. 1993	316.5
4s7	53741 - 56976	16 Mar. 1993 - 6 Jul. 1993	461.3
4s8	57038 - 58813	1 Aug. 1993 - 27 Sep. 1993	274.4
4s9	58836 - 60576	22 Nov. 1993 - 10 Jan. 1994	340.1
4sA	60770 - 61778	20 Jan. 1994 - 28 Feb. 1994	190.8
4sB	61826 - 62855	19 Mar. 1994 - 16 May 1994	140.9
4sC	63086 - 64026	16 Jun. 1994 - 15 Aug. 1994	141.5
4sD	64085 - 64674	15 Sep. 1994 - 9 Oct. 1994	98.0
4sE	64675 - 65238	9 Oct. 1994 - 1 Nov. 1994	128.8
4sF	65252 - 65818	3 Nov. 1994 - 28 Nov. 1994	145.9
4sG	66539 - 68027	19 Jan. 1995 - 9 Apr. 1995	456.6
4sH	78621 - 80924	16 Nov. 1995 - 11 Mar. 1996	521.0
4sJ	80925 - 82975	3 Apr. 1996 - 8 Jul. 1996	677.0
4sK	82976 - 84602	19 Aug. 1996 - 28 Oct. 1996	595.0
4sL	84681 - 86980	17 Nov. 1996 - 10 Mar. 1997	1080.6
4sM	87049 - 88467	5 Apr. 1997 - 17 Jun. 1997	531.8
4sN	88482 - 90043	19 Jun. 1997 - 17 Aug. 1997	714.3
4sP	90494 - 92806	15 Oct. 1997 - 9 Feb. 1998	1103.6
4sQ	92908 - 94096	27 Feb. 1998 - 21 Apr. 1998	559.9
4sR	94098 - 94936	21 Apr. 1998 - 8 Jun. 1998	499.1
4sS	94976 - 96510	27 Jun. 1998 - 5 Oct. 1998	1214.0
4sT	96544 - 98337	10 Nov. 1998 - 15 Feb. 1999	1583.3

Table 5.3: Summary of the CLEO II data sample. The SVX detector was installed before the 4sH data sample.

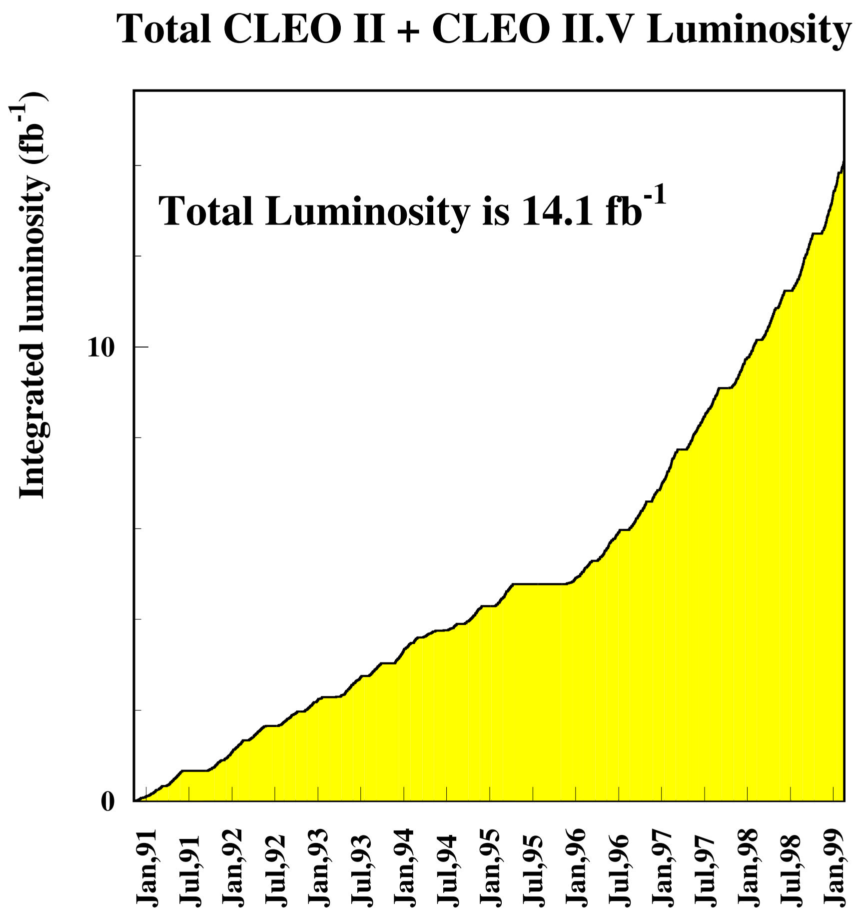

Figure 5.7: Luminosity collected by the CLEO II detector near the $\Upsilon(4S)$ resonance after November of 1990.

Chapter 6

Monte Carlo simulation

In this chapter we summarize the Monte Carlo samples that were used to model both signal and background distributions. For the signal, we describe the reweighting performed in order to mock up the predictions of different form-factor models. For the backgrounds, we describe the mix of $b \to u\ell\nu$ and $b \to c\ell\nu$ modes used. Figures 6.1 and 6.2 show the resulting q^2 and lepton-energy distributions from each Monte Carlo sample.

6.1 Monte Carlo generation

We describe the method used for the generation of Monte Carlo simulation. Generation is performed in three steps. First, simulated four-vectors are generated. Next, a full-detector simulation is used to mock up detector response to the generated particles. Finally, the reconstruction algorithm is used to process the Monte Carlo just as is done with the data. We discuss each of these steps.

In CLEO, simulation of the decay four-vectors is usually performed by a program known as QQ. This program allows the user to specify allowed decay modes, branching fractions, and particles properties. Events, beginning with an $\Upsilon(4S)$ decay, are then generated according to the user's input via random throws. The event is complete when only long lived particles, such as $\pi^{\pm}$, $K^{\pm}$, $e^{\pm}$, $\mu^{\pm}$, and γ, remain. These particles are then passed along to the

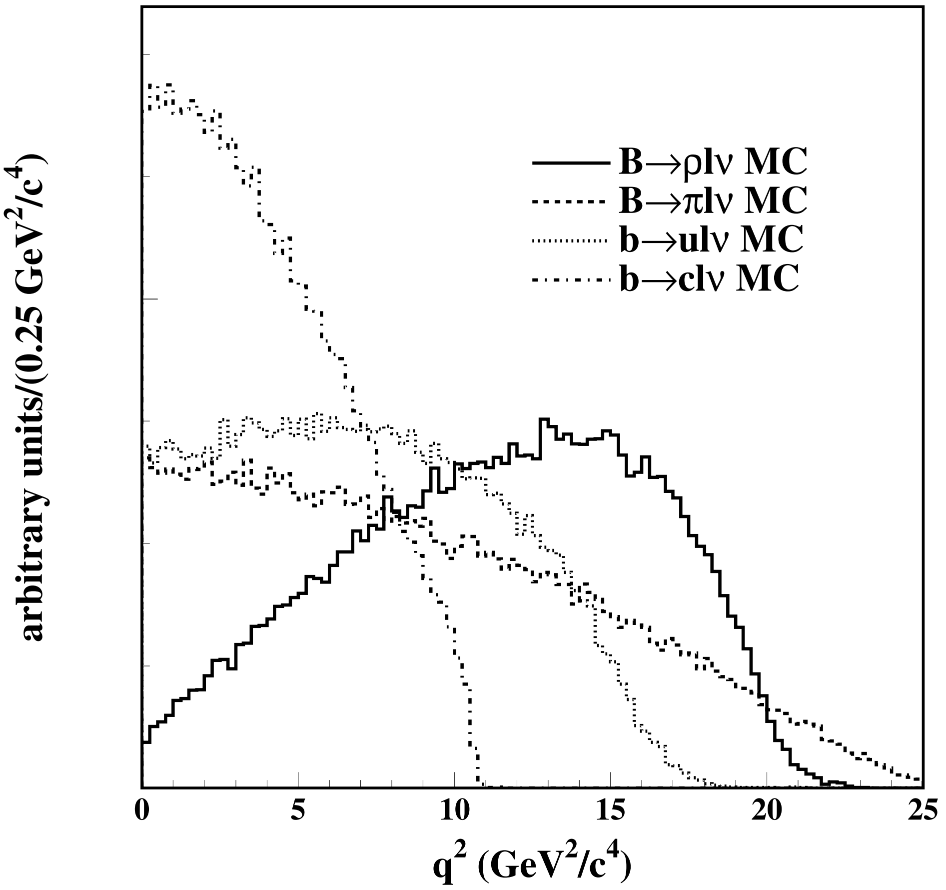

Figure 6.1: q^2 distributions for each Monte Carlo sample generated: $B \to \rho\ell\nu$ (ISGW2,solid), $B \to \pi\ell\nu$ (dashed, ISGW2), $b \to u\ell\nu$ (dotted, modes other than ρ, ω, or π), and $b \to c\ell\nu$ (dot-dashed). Plotted is the generated (not reconstructed) value of $q^2 = (p_\ell + p_\nu)^2$.

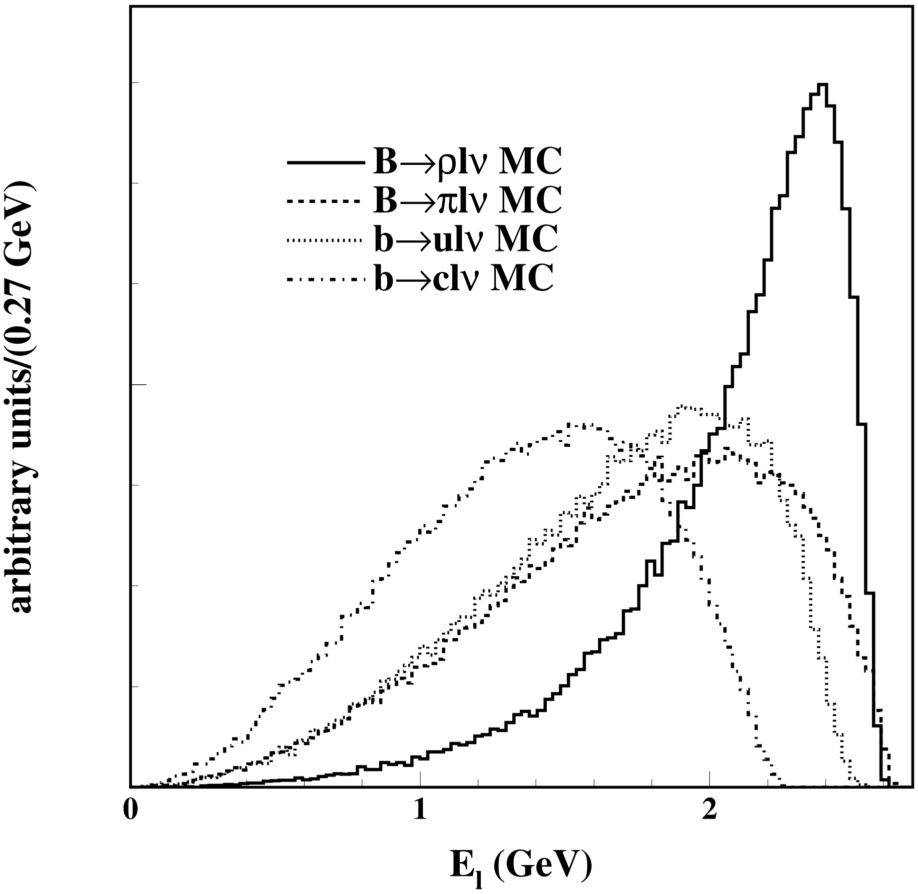

Figure 6.2: Lepton energy distributions for each Monte Carlo sample generated: $B \to \rho\ell\nu$ (ISGW2,solid), $B \to \pi\ell\nu$ (dashed, ISGW2), $b \to u\ell\nu$ (dotted, modes other than ρ, ω, or π), and $b \to c\ell\nu$ (dot-dashed).

detector simulation. For semileptonic decays an important addition to QQ is the EvtGen [71] package. As described in Sec. 6.2, EvtGen allows for the modeling of all correlations within a decay. These correlations are especially important for semileptonic decays such as $B \to D^*\ell\nu$, where sufficient data exist to measure the full decay distributions. EvtGen allows for the modeling of correlations between the $\ell\nu$ system and the decay products of the D^*, which is not otherwise easily done within the QQ.

CLEOG, a package based on GEANT [72] is used to simulate detector response to the particles generated in QQ. GEANT is a package developed at CERN to simulate the passage of particles through matter. In particular, CLEOG is responsible for modeling detector inefficiencies and smearing.

Finally, the detector hits from CLEOG are passed along to the standard event reconstruction in CLEO. The primary difference in the treatment of data and Monte Carlo simulation at this step is that detector noise and beam related backgrounds must be added to the physics hits generated by CLEOG. This is performed in a variety of ways. One possiblity is to use data taken with a trigger that fires at random beam crossings. Also, physics hits can be stripped out of events, such as $e^+e^- \to \mu^+\mu^-$. In either of these methods, the detector noise and beam background hits are merged with the physics hits generated by CLEOG.

At the analysis level, it is important that the Monte Carlo is treated in every way like the data so as not to introduce a bias. For example, the QQ output can not be used to determine which events are signal, which reconstructed signal mode is correct, or which reconstructed track is the correct lepton. We have been very careful to process the data and Monte Carlo simulation events using the same analysis code.

6.2 EvtGen

The EvtGen package, written in C++ by Anders Ryd and David Lange, provides a framework for implementation of physics processes relevant to decays of B mesons and other resonances. The framework includes tools needed to easily handle sequential decays, correctly simulating angular distributions, including their correlations. Individual physics processes are implemented in modules that allow users to build complicated decay chains from simple pieces. Each module calculates decay amplitudes, to be used by the framework to generate the correct kinematic distributions. In particular, EvtGen provides implementations of many detailed decays, including a variety of semileptonic decay models and time dependent CP asymmetries in neutral B meson decays, as well as a decay table for simulation of generic B decays. In this section we describe the treatment of decay amplitudes within EvtGen. The framework is discussed elsewhere [71].

To fully model the decay distributions in sequential decays, EvtGen works with decay amplitudes. To illustrate this, we will consider the example

$$\begin{aligned} B &\rightarrow D^*\tau\nu \\ D^* &\rightarrow D\pi \\ \tau &\rightarrow \pi\nu \end{aligned} \tag{6.2.1}$$

The full decay amplitude is written as a product of the decay amplitudes of each node in the decay tree and summed over all degrees of freedom not observable in the final state

$$A = \sum_{\lambda_{D^*}\lambda_\tau} A^{B\rightarrow D^*\tau\nu}_{\lambda_{D^*}\lambda_\tau} A^{D^*\rightarrow D\pi}_{\lambda_{D^*}} A^{\tau\rightarrow\pi\nu}_{\lambda_\tau} \tag{6.2.2}$$

where

$$A^{B\rightarrow D^*\tau\nu}_{\lambda_{D^*}\lambda_\tau} \equiv \langle \lambda_{D^*}\lambda_\tau | H | B \rangle \tag{6.2.3}$$

is the amplitude for the $B \rightarrow D^*\tau\nu$ decay. λ_{D^*} and λ_τ label the polarization states of the D^* and τ respectively. These states form a complete basis

$$\sum_{\lambda_{D^*}} |\lambda_{D^*}\rangle\langle\lambda_{D^*}| = I \quad \text{and} \quad \sum_{\lambda_\tau} |\lambda_\tau\rangle\langle\lambda_\tau| = I. \tag{6.2.4}$$

The decay amplitudes are a function of the parent and daughter momenta, as well as the polarization state of each particle. The decay probability, P, is proportional to $|A|^2$. Calculating the decay probability in this way allows the amplitude for each node to be written independently of the other nodes in tree.

The most straightforward implementation simply generates kinematics for the whole decay sequence and calculates the total decay amplitude according to Eq. 6.2.2. This approach has two major draw backs. First, it becomes very hard to manage the maximal probabilities used in a hit-and-miss algorithm. It also becomes inefficient when the decay chains are long.

The procedure used by EvtGen allows each node in the decay chain to be treated separately. This eliminates the two problems mentioned above. To illustrate how this works we continue with the $B \to D^*\tau\nu$ example. The first step is to generate the $B \to D^*\tau\nu$ decay. This is done by summing over D^* and τ polarization states

$$P = \sum_{\lambda_{D^*}\lambda_\tau} |A^{B\to D^*\tau\nu}_{\lambda_{D^*}\lambda_\tau}|^2. \tag{6.2.5}$$

The $D^* \to D\pi$ decay is then generated according to

$$P = \sum_{\lambda_{D^*}\lambda'_{D^*}} \rho^{D^*}_{\lambda_{D^*}\lambda'_{D^*}} (A^{D^*\to D\pi}_{\lambda_{D^*}})(A^{D^*\to D\pi}_{\lambda'_{D^*}})^* \tag{6.2.6}$$

where the D^* spin density matrix is calculated by summing over τ spins

$$\rho^{D^*}_{\lambda_{D^*}\lambda'_{D^*}} = \sum_{\lambda_\tau} (A^{B\to D^*\tau\nu}_{\lambda_{D^*}\lambda_\tau})(A^{B\to D^*\tau\nu}_{\lambda'_{D^*}\lambda_\tau})^*. \tag{6.2.7}$$

The algorithm continues with the τ decay, having the additional complication of incorporating the information about the D^* decay to generate the proper angular correlations between the D^* and τ decays. Given the decay amplitude, $A^{\tau\to\pi\nu}_{\lambda_\tau}$, for the $\tau \to \pi\nu$ decay, the τ is decayed according to

$$P = \sum_{\lambda_\tau\lambda'_\tau} \rho^{\tau}_{\lambda_\tau\lambda'_\tau} (A^{\tau\to\pi\nu}_{\lambda_\tau})(A^{\tau\to\pi\nu}_{\lambda'_\tau})^*, \tag{6.2.8}$$

where

$$\rho^{\tau}_{\lambda_\tau \lambda'_\tau} = \sum_{\lambda_{D^*} \lambda'_{D^*}} \hat{\rho}^{D^*}_{\lambda_{D^*} \lambda'_{D^*}} (A^{B\to D^*\tau\nu}_{\lambda_{D^*} \lambda_\tau})(A^{B\to D^*\tau\nu}_{\lambda'_{D^*} \lambda'_\tau})^*, \tag{6.2.9}$$

and

$$\hat{\rho}^{D^*}_{\lambda_{D^*} \lambda'_{D^*}} \equiv (A^{D^*\to D\pi}_{\lambda_{D^*}})(A^{D^*\to D\pi}_{\lambda'_{D^*}})^*. \tag{6.2.10}$$

In each step, the framework handles the bookkeeping of amplitudes and spin density matrices. The user only provides the amplitude for each node in the decay tree. As each node is simulated individually, the efficiency for this algorithm is independent of the length of the decay chain.

This formalism makes EvtGen an ideal tool for the generation of semileptonic decay processes, which are often composed of long sequential decay chains.

6.3 $B \to \rho\ell\nu$ Monte Carlo

In Chapter 3 we described the kinematics of $B \to \rho\ell\nu$ decay as well as the form-factor models that we have used to model these kinematics. Instead of generating large Monte Carlo samples for each of these models, we use a simple reweighting scheme.

We generated a large sample that is uniform in the q^2 vs. E_ℓ Dalitz plot as well as in $\cos\theta_V$ and χ, as defined in Chapter 3. For each event we compute $d\Gamma$ for the generated q^2, E_ℓ, $\cos\theta_V$, and χ, according to Eq. 3.1.8 and the predicted form factors and assign a weight to each event. This weight is then used in the analysis and likelihood fit in order to mock up the kinematic distributions predicted by each form-factor model.

This method was checked using Monte Carlo generated using the ISGW2 model. The analysis results using the reweighting scheme on flat in phase space Monte Carlo simulation were compared with those where the ISGW2 Monte Carlo simulation was used. The results using these two methods agree to better than 1%.

In total, more than 600,000 $B \to \rho\ell\nu$ and $B \to \omega\ell\nu$ events of flat in phase space Monte Carlo simulation were generated at UCSB for this analysis.

6.4 $B \to \pi\ell\nu$ Monte Carlo

The $B \to \pi\ell\nu$ Monte Carlo was generated according to ISGW2 predictions. To examine the systematic error associated with using this model were explored using a reweighting technique similar to that used for the signal Monte Carlo. Approximately 100,000 events were generated at UCSB to simulate the $B \to \pi\ell\nu$ contribution.

6.5 $B \to X_u\ell\nu$ Monte Carlo

The $B \to X_u\ell\nu$ Monte Carlo sample used is made up of a mix of resonant hadronic modes as predicted by the ISGW2 model [17]. Relative branching fractions and full kinematic distributions are predicted by the model for $b \to u\ell\nu$ resonances up the $\rho(1450)$. In this section we list the branching fractions used in our Monte Carlo sample and show some of the kinematic distributions predicted.

We assume, as we have in our fit, that the $\Upsilon(4S)$ decays exclusively to $B\bar{B}$ final states, evenly split between $B^0\bar{B}^0$ and B^+B^-. Our $B \to X_u\ell\nu$ sample is then made up of the following $\Upsilon(4S)$ decays:

$$\begin{aligned}
25\%\ \Upsilon(4S) &\to (B^0 \to X_u\ell\nu)(\bar{B}^0 \to X), \\
25\%\ \Upsilon(4S) &\to (B^0 \to X)(\bar{B}^0 \to X_u\ell\nu), \\
25\%\ \Upsilon(4S) &\to (B^- \to X_u\ell\nu)(B^+ \to X), \\
25\%\ \Upsilon(4S) &\to (B^- \to X)(B^+ \to X_u\ell\nu),
\end{aligned} \tag{6.5.1}$$

where $B \to X$ represents decay to a generic set of final states that we will not describe in detail.

The $B^0 \to X_u \ell\nu$ decay branching fractions used are

$$
\begin{aligned}
24.8\%\ B^0 &\to \pi^- \ell^+ \nu, \\
1.3\%\ B^0 &\to a_0^- \ell^+ \nu, \\
22.4\%\ B^0 &\to a_1^- \ell^+ \nu, \\
8.5\%\ B^0 &\to a_2^- \ell^+ \nu, \\
28.1\%\ B^0 &\to b_1^- \ell^+ \nu, \\
4.4\%\ B^0 &\to \pi^-(1300) \ell^+ \nu, \\
10.5\%\ B^0 &\to \rho^-(1450) \ell^+ \nu,
\end{aligned}
\tag{6.5.2}
$$

where the lepton in the final state is either an electron or muon, each present in 1/2 of the generated events. The B^+ branching fractions are:

$$
\begin{aligned}
11.6\%\ B^+ &\to \pi^0 \ell^+ \nu, \\
0.6\%\ B^+ &\to a_0^0 \ell^+ \nu, \\
10.5\%\ B^+ &\to a_1^0 \ell^+ \nu, \\
3.9\%\ B^+ &\to a_2^0 \ell^+ \nu, \\
13.2\%\ B^+ &\to b_1^0 \ell^+ \nu, \\
1.9\%\ B^+ &\to \pi^0(1300) \ell^+ \nu, \\
4.9\%\ B^+ &\to \rho^0(1450) \ell^+ \nu, \\
10.9\%\ B^+ &\to \eta \ell^+ \nu, \\
6.8\%\ B^+ &\to \eta' \ell^+ \nu, \\
0.7\%\ B^+ &\to f_0^{0\prime} \ell^+ \nu, \\
10.0\%\ B^+ &\to f_1^0 \ell^+ \nu, \\
4.4\%\ B^+ &\to f_2^0 \ell^+ \nu, \\
13.8\%\ B^+ &\to h_1^0 \ell^+ \nu, \\
1.9\%\ B^+ &\to \eta(1295) \ell^+ \nu, \\
4.9\%\ B^+ &\to \omega(1420) \ell^+ \nu
\end{aligned}
\tag{6.5.3}
$$

Often the $B \to \pi\ell\nu$ mode is treated separately from the other $b \to u\ell\nu$ modes.

In this case, these events are stripped out of this Monte Carlo sample. As described above, we have a separate sample of $B \to \pi\ell\nu$ sample of events. Because $\pi^{\pm}$ and π^0 are not the only modes in the ${}^1S_0$ spin state (η and η' also are), generating a generic $B \to X_u\ell\nu$ sample that includes these modes makes the bookkeeping of the B branching fractions more straightforward.

In Tables 6.1, 6.2, and 6.3 we list the masses, widths, and decay modes of the mesons that make up X_u final states. These are primarily taken from the Particle Data Book [32].

1/2 million $B \to X_u\ell\nu$ events were generated for this analysis at UCSB. Although the final Monte Carlo was generated using the EvtGen package, credit should be given to Lawrence Gibbons for the debugging of the initial CLEO ISGW2 model. His work allowed for easy debugging of the EvtGen output.

6.6 $B \to X_c\ell\nu$ Monte Carlo

Because we are examining the endpoint region of the $b \to c\ell\nu$ lepton-energy spectrum, a large sample of Monte Carlo events is needed to model the details of this background contribution. We made use of two Monte Carlo samples: a relatively low statistics sample for low lepton energies where the number of $b \to c\ell\nu$ events is large, and a high statistics sample for the endpoint region.

The lower statistics sample, corresponding to approximately 7 times the number of $B\bar{B}$ events in the data, was a generic sample used in many semileptonic analyses at CLEO. This sample was generated using the predictions of the ISGW2 model as well as a model of nonresonant $B \to D^{(*)}\pi\ell\nu$ decay, with branching fractions tuned as to simulate the measured inclusive lepton-energy spectrum at CLEO. In addition a heavy quark effective theory based model is used to mock up $B \to D^*\ell\nu$ events using measurements of form-factors [66]. This event sample was generated at The University of Florida.

For the higher statistics sample only events with a lepton generated in QQ with an energy greater than 2.2 GeV are simulated using CLEOG. This allows a large sample (large compared to the number of $B\bar{B}$ events in the lepton-energy

Meson	Mass	Width	Decay mode	$\mathcal{B}(\%)$
π^-	0.140	0	NA	NA
a_0^-	0.982	0.057	$\eta\pi^-$	90
			$\bar{K}^0 K^+$	10
a_1^-	1.23	0.4	$\rho^0\pi^-$	49.2
			$\rho^-\pi^0$	50.8
a_2^-	1.32	0.11	$\rho^0\pi^-$	35
			$\rho^-\pi^0$	35
			$\eta\pi^-$	14.4
			$\omega\pi^-\pi^0$	10.5
b_1^-	1.23	0.142	$\omega\pi^-$	99.8
$\pi^-(1300)$	1.3	0.3	$\pi^+\pi^-\pi^-$	44
			$\pi^0\pi^0\pi^-$	22
			$\rho^0\pi^-$	17
			$\rho^-\pi^0$	17
$\rho^-(1450)$	1.465	0.31	$\pi^+\pi^-\pi^0\pi^-$	81.8
			$\pi^0\pi^0\pi^0\pi^-$	16.4

Table 6.1: Particle properties for charged mesons produced in $B \to X_u \ell \nu$ decays. When the width is given as zero, the actual particle width is much less than the CLEO mass resolution. Modes with branching fractions smaller than 10% are not included.

Meson	Mass	Width	Decay mode	$\mathcal{B}(\%)$
π^0	0.1350	0	$\gamma\gamma$	98.8
a_0^0	0.982	0.057	$\eta\pi^0$	90
a_1^0	1.23	0.4	$\rho^+\pi^-$	50
			$\rho^-\pi^+$	50
a_2^0	1.32	0.11	$\rho^+\pi^-$	35
			$\rho^-\pi^+$	35
			$\eta\pi^0$	14.4
			$\omega\pi^+\pi^-$	10.5
b_1^0	1.23	0.142	$\omega\pi^-$	99.8
$\pi^0(1300)$	1.3	0.3	$\pi^+\pi^-\pi^0$	44
			$\pi^0\pi^0\pi^0$	22
			$\rho^-\pi^+$	17
			$\rho^+\pi^-$	17
$\rho^0(1450)$	1.465	0.31	$\pi^+\pi^-\pi^0\pi^0$	65.3
			$\pi^+\pi^-\pi^+\pi^-$	32.7

Table 6.2: Particle properties for neutral, isospin one, mesons produced in $B \to X_u \ell\nu$ decays. When the width is given as zero, the actual particle width is much less than the CLEO mass resolution. Modes with branching fractions smaller than 10% are not included.

Meson	Mass (GeV/c^2)	Width (GeV)	Decay mode	$\mathcal{B}$(%)
η	0.548	0	$\gamma\gamma$	38.8
			$\pi^0\pi^0\pi^0$	31.9
			$\pi^-\pi^+\pi^0$	23.6
η'	0.958	0	$\pi^+\pi^-\eta$	43.7
			$\pi^0\pi^0\eta$	20.8
			$\gamma\rho^0$	30.2
$f_0^{0\prime}$	1.40	0.25	$\pi^+\pi^-$	62
			$\pi^0\pi^0$	31
f_1^0	1.282	0.024	$\rho^0\pi^+\pi^-$	15
			$a_0^0\pi^0$	14
			$a_0^+\pi^-$	14
			$a_0^-\pi^+$	14
f_2^0	1.275	0.185	$\pi^+\pi^-$	56.7
			$\pi^0\pi^0$	28.4
h_1^0	1.17	0.36	$\rho^+\pi^-$	33.3
			$\rho^0\pi^0$	33.3
			$\rho^-\pi^+$	33.3
$\eta(1295)$	1.295	0.053	$a_0^0\pi^0$	25
			$a_0^-\pi^+$	25
			$a_0^+\pi^-$	25
			$\eta\pi^+\pi^-$	17
$\omega(1420)$	1.42	0.174	$\rho^+\pi^-$	33
			$\rho^-\pi^+$	33
			$\rho^0\pi^0$	33

Table 6.3: Particle properties for neutral, isospin zero, mesons produced in $B \to X_u \ell \nu$ decays. When the width is given as zero, the actual particle width is much less than the CLEO mass resolution. Modes with branching fractions smaller than 10% are not included.

endpoint region in the data) to be generated relatively quickly. Effectively 45 million events were generated using the computing at UCSB with this lepton-energy requirement.

We now list the semileptonic branching fractions used in these Monte Carlo samples. As in the $B \to X_u \ell\nu$ sample, the $\Upsilon(4S)$ meson decays exclusively into $B\bar{B}$ mesons, half $B^0\bar{B}^0$ and half B^+B^- (see Eq. 6.5.1). The branching fractions for semileptonic decays are:

$$\begin{array}{cc}
5.4\%\ B^- \to \bar{D}^{*0}\ell^+\nu & 5.4\%\ B^0 \to D^{*-}\ell^+\nu \\
2.0\%\ B^- \to \bar{D}^{0}\ell^+\nu & 2.0\%\ B^0 \to D^{-}\ell^+\nu \\
1.1\%\ B^- \to \bar{D}^{**0}(^3P_0)\ell^+\nu & 1.1\%\ B^0 \to D^{**-}(^3P_0)\ell^+\nu \\
1.1\%\ B^- \to \bar{D}^{**0}(^3P_1)\ell^+\nu & 1.1\%\ B^0 \to D^{**-}(^3P_1)\ell^+\nu \\
0.66\%\ B^- \to \bar{D}^{**0}(^1P_1)\ell^+\nu & 0.66\%\ B^0 \to D^{**-}(^1P_1)\ell^+\nu \\
0.33\%\ B^- \to \bar{D}^{**0}(^3P_2)\ell^+\nu & 0.33\%\ B^0 \to D^{**-}(^3P_2)\ell^+\nu \\
0.02\%\ B^- \to \bar{D}^{*0\prime}\ell^+\nu & 0.02\%\ B^0 \to D^{*-\prime}\ell^+\nu \\
0.22\%\ B^- \to \bar{D}^{0\prime}\ell^+\nu & 0.22\%\ B^0 \to D^{-\prime}\ell^+\nu \\
0.17\%\ B^- \to \bar{D}^{0}\pi^0\ell^+\nu & 0.17\%\ B^0 \to D^{-}\pi^0\ell^+\nu \\
0.33\%\ B^- \to D^{-}\pi^+\ell^+\nu & 0.33\%\ B^0 \to \bar{D}^{0}\pi^+\ell^+\nu \\
0.23\%\ B^- \to \bar{D}^{*0}\pi^0\ell^+\nu & 0.23\%\ B^0 \to D^{*-}\pi^0\ell^+\nu \\
0.47\%\ B^- \to D^{*-}\pi^+\ell^+\nu & 0.47\%\ B^0 \to \bar{D}^{*0}\pi^+\ell^+\nu
\end{array}$$

Additionally, $B \to J/\psi X$ decays are a background at large lepton-energies. The input branching fractions for these decays have an inclusive branching fraction of 0.8%.

Chapter 7

Event selection

7.1 Overview

Hadronic events collected by the CLEO II detector were examined for signatures of $B \to \rho\ell\nu$ decay. We first reconstruct leptons plus $\rho \to \pi\pi$ (also $\omega \to \pi^+\pi^-\pi^0$ and π) candidates. In addition, all charged tracks and CsI clusters are considered in order to reconstruct the missing momentum of the event, defined as

$$\mathbf{p}_{\text{miss}} \equiv -\Sigma\mathbf{p}_i, \tag{7.1.1}$$

where the sum is over reconstructed charged tracks and CsI clusters in the event, as described below. If the event contains no undetected particles other than the ν from the $B \to \rho\ell\nu$ decay, $\mathbf{p}_{\text{miss}} \approx \mathbf{p}_\nu$. The resolution on $\mathbf{p}_{\text{miss}}$ is determined by undetected particles, such as K_L^0 mesons, and our experimental resolution. As discussed in the following chapter, $\mathbf{p}_{\text{miss}}$ is used to calculate one of our three fit variables.

Background events come from continuum, $b \to c\ell\nu$, $b \to u\ell\nu$ (non ρ/ω), and fake-lepton events. The $b \to c\ell\nu$ background dominates at lower lepton energy. To most effectively distinguish signal events from background we consider three lepton-energy ranges:

- $E_\ell > 2.3$ GeV (denoted as HILEP in the remainder of this paper),

- $2.0 < E_\ell < 2.3$ GeV (LOLEP),
- $1.7 < E_\ell < 2.0$ GeV (LOLOLEP),

where the lepton energy is evalated in the lab frame. Results for $B \to \rho\ell\nu$ are primarily determined by the HILEP lepton-energy bin, where the $b \to c\ell\nu$ background is quite small. Here, the backgrounds are primarily continuum and $b \to u\ell\nu$ events. In LOLEP, the $b \to c\ell\nu$ background dominates. However, one must include the $b \to u\ell\nu$ contributions in this region to correctly describe the normalization and shape of the data. Events with $1.7 < E_\ell < 2.0$ GeV are included primarily to verify our understanding of the $b \to c\ell\nu$ backgrounds.

Various event selection criteria are used to enhance $B \to \rho\ell\nu$ events over events from background contributions. In particular, we require

- hadronic ($e^+e^- \to q\overline{q}$ ($q = u, d, s, c$) and $B\overline{B}$) events,
- well reconstructed charged tracks and CsI clusters,
- events consistent with $B\overline{B}$ decay (not $e^+e^- \to q\overline{q}$ events),
- and events that are consistent with containing a $B \to \rho\ell\nu$ decay.

We describe each set of requirements below.

7.2 Selecting hadronic events

Requirements to select hadronic events are choosen to maximize the efficiency for selecting $B\overline{B}$ events with minimal non-hadronic backgrounds. We have used requirements that are standard in the CLEO collaboration. At least 3 detected charged tracks are required. The sum of the detected track and CsI cluster energies must be greater than 20% of the beam energy. If only 3 charged tracks are present, the sum of the CsI cluster energies must be greater than 15% of the beam energy. The event must also not be classified as an $e^+e^- \to e^+e^-\gamma$ event, which contain a CsI cluster with a significant fraction of the beam energy. These requirements select at least 99% of hadronic ($B\overline{B}$) events at CLEO.

7.3 Charged track and CsI cluster selection

We use two sets of requirements to determine "good" charged tracks and CsI clusters. The philosophy for the first set of requirements is to find exactly one track or cluster for each charged particle or γ leaving hits the detector. These tracks and clusters are used to best determine the momentum of the undetected particle(s) in the event. The second set of criteria are more restrictive, corresponding to tracks and clusters that we will use to form $\rho + \ell$ candidates.

To optimize the computation of $\mathbf{p}_{\text{miss}}$, the charged track reconstruction should identify exactly one track for each charged particle passing through the inner tracking system. There are two examples of a single charged particle being doublely counted by the track reconstruction algorithm. Low momentum particles, those with insufficient momentum to reach the outer edge of the drift chamber and with low dip angle will potentially spiral multiple times before leaving the drift chamber. Such particles are known as "curlers". Multiple tracks are often reconstructed using the hits left by curlers.

Higher momentum particles may also be double counted. Noise hits, or a scattering of the particle, may lead the track reconstruction to identify two plausible track candidates, each using some of the drift chamber hits left by the particle. These track candidates are known as "ghosts". For both curlers and ghosts, to best measure the missing momentum of the event, only one track segment should be selected.

CsI calorimeter clusters must

- have an energy greater than 25 MeV. Clusters below this threshold are almost always noise hits;
- be consistent with not coming from splitoffs due to charged tracks. Considering such clusters will result both in an increased background while finding π^0 candidates, as well as a double counting of momenta in the missing momentum computation.

The splitoff rejection criteria are loosened somewhat on CsI clusters that combine to form a π^0 candidate with $M(\gamma\gamma)$ close to the nominal π^0 mass. One measure of the number of true γ candidates rejected by these requirements is the $M(\gamma\gamma)$ distribution of the π^0 candidates kept and rejected, as shown in Figure 7.2.

We define the missing momentum in the event as in Equation 7.1.1. The sum is over all tracks and CsI clusters in the event that meet the above criteria. In well reconstructed signal events, $\mathbf{p}_{\text{miss}} = \mathbf{p}_\nu$ within our experimental resolution.

To be considered as part of a hadron or lepton candidate, charged tracks and CsI clusters must satisfy several additional requirements. For charged tracks, the impact parameter of the track along (transverse to) the beam direction must be less than 5 cm (2 mm). Transverse to the beam direction, the resolution on the impact parameter is approximately 0.3 mm. The spread in the impact parameter along the beam direction is dominated by the beam width in that direction, and is approximately 1.5 cm. The r.m.s. residual for the hits on the track must be less than 1 mm. Finally, we require that at least 15 out of the 67 tracking layers are used in the track fit. These requirements are illustrated in Figure 7.1.

CsI clusters meeting the requirements described above are used to make up π^0 candidates. Two clusters must additionally have a combined invarient mass, $M(\gamma\gamma)$, less than two σ away from the nominal π^0 mass. Their combined energy, $E_{\gamma\gamma}$, is required to be greater than 325 MeV. Figure 7.2 shows the $M(\gamma\gamma)$ distribution for low and high energy π^0 candidates. Despite the large number of π^0 candidates rejected by the $E_{\gamma\gamma}$ requirement we do not see a drop in signal efficiency due to this requirement after all analysis cuts are applied. In addition, at least one cluster must have a polar dip angle of less than 0.71. If a cluster is used in multiple candidates using the above criteria, one is selected by choosing the candidate with $M(\gamma\gamma)$ closest to the nominal π^0 mass. The mass resolution for π^0 reconstruction is approximately 6 MeV$/c^2$.

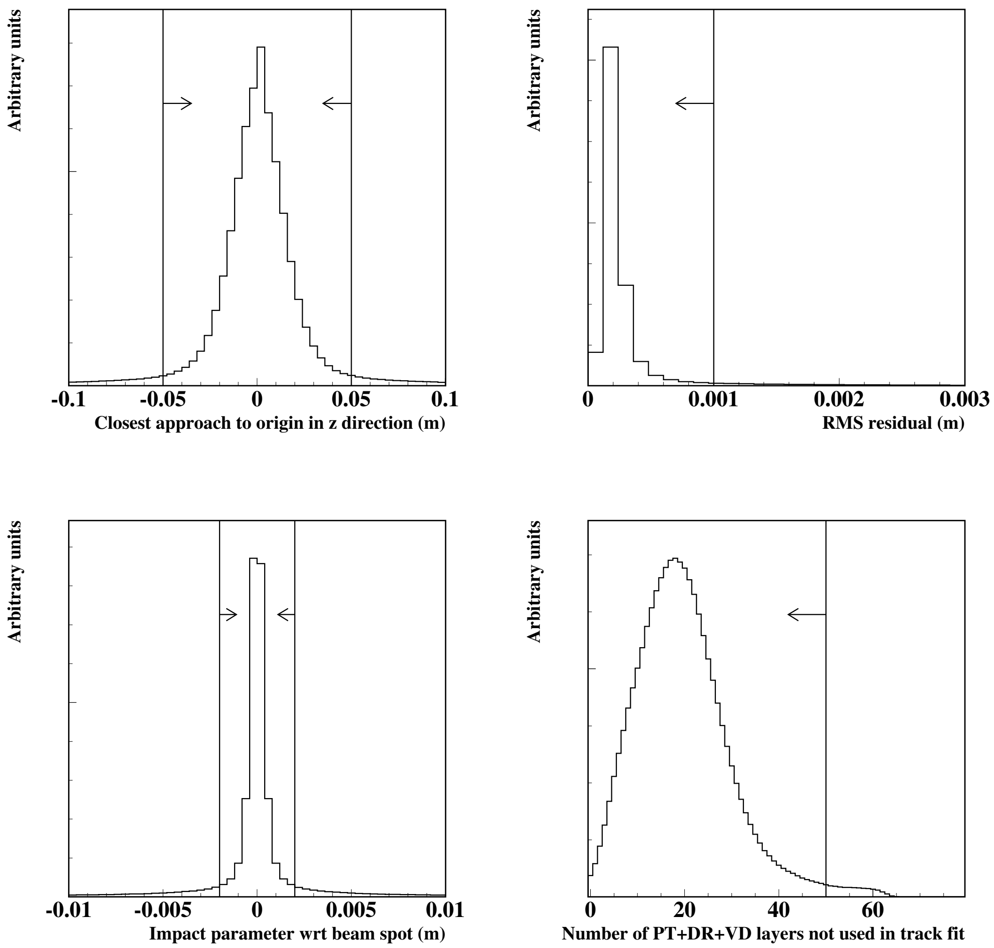

Figure 7.1: Quantities used to qualify charged tracks for use in lepton and hadron candidates. All plots are for the data using all tracks that enter the $\mathbf{p}_{\text{miss}}$ calculation. The upper left plot shows distribution of the point of closest point along the beam direction. The upper right shows the RMS residual and the lower left plot shows the impact parameter with respect the beam spot. The lower right plot shows the number of tracking layers not used in the track fit. The vertical lines with arrows indicate the location of the cut that is applied.

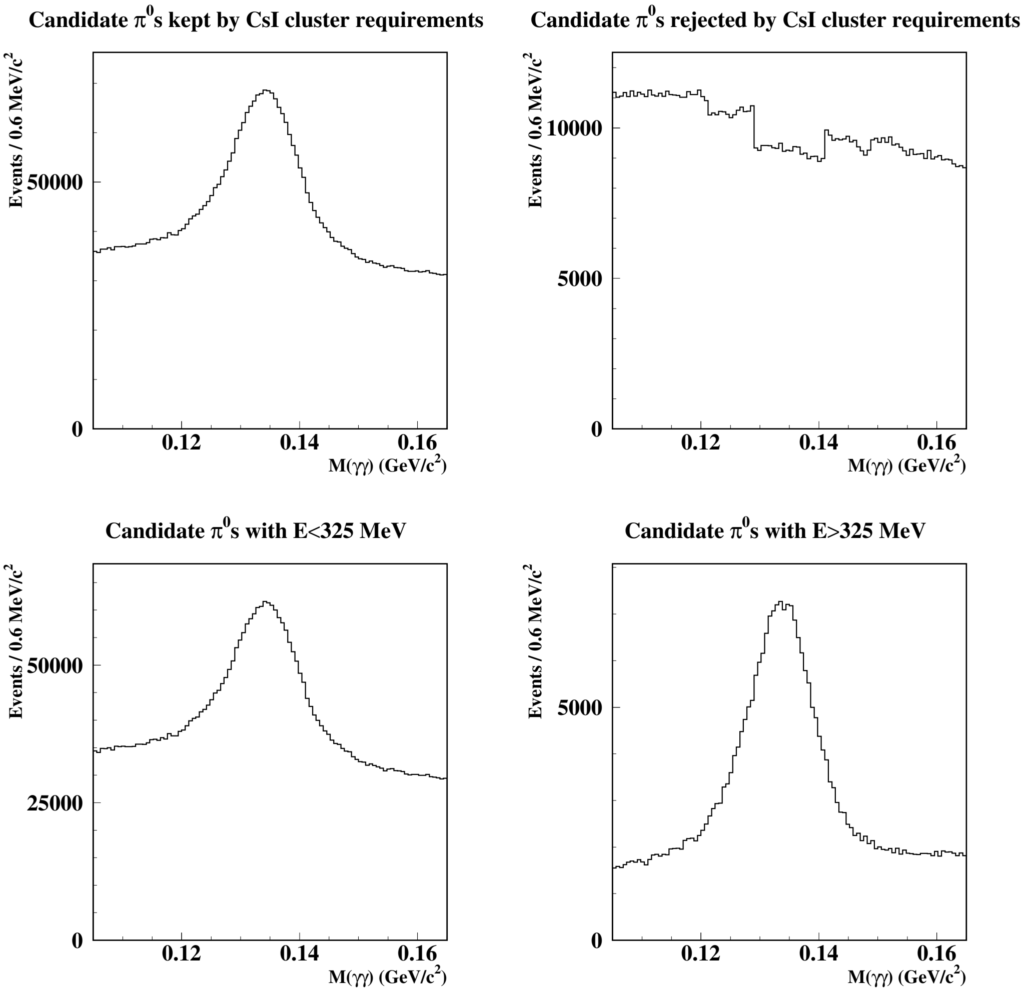

Figure 7.2: $M(\gamma\gamma)$ distributions for π^0 candidates are shown. The upper left (right) plot shows the π^0 candidates retained (rejected) by the requirements used to determine the CsI clusters that enter the $\mathbf{p}_{\rm miss}$ calculation. The lower left (right) plot shows $M(\gamma\gamma)$ for π^0 candidates with $E_{\gamma\gamma} < (>)325$ MeV.

7.4 Electron and muon identification requirements

Electron and muon identification requirements are chosen to achieve high efficiency and maintain a small hadronic fake rate. To extract results from the measured event yields, it is important to understand the lepton identification efficiency well. Below we discuss the criteria for electron and muon identification.

We have used an electron identification package that is standard within the CLEO collaboration. We consider tracks that satisfy $|\cos\theta| < 0.85$, where θ is the dip angle with respect to the beam direction. Electrons are identified using the calorimeter energy to track momentum ratio (E/p), specific ionization (dE/dx) information, and several shower shape variables. These variables are combined to form a single variable that is used to best distinguish electrons from backgrounds due to hadrons, protons, and muons. This variable (referred to below as R_e), is defined as

$$R_e = \sum_{\text{variables}} ln(P_e/P_{\not{e}}), \tag{7.4.1}$$

where P_e ($P_{\not{e}}$) is the probability that the track is (not) an electron. When available, E/p and dE/dx information is used to identify electrons in all regions of the detector. The shower shape variables, discussed below, are used only in the "good barrel" region of the detector, defined to be $|\cos\theta| < 0.71$, where θ is the angle with respect to the beam direction.

E/p is the best variable for the identification of high momentum electrons. Figure 7.3 shows the E/p distribution for electrons and background tracks. The electron sample is radiative bhabhas, which have a large high side tail in E/p due to radiation in the beam pipe. Often electrons will radiate, producing a photon that is most likely to lie exactly along the direction of the electron. The CsI calorimeter clustering algorithm is often unable to distinguish this photon from the interaction of the electron and finds a single cluster with an energy greater than the electron momentum.

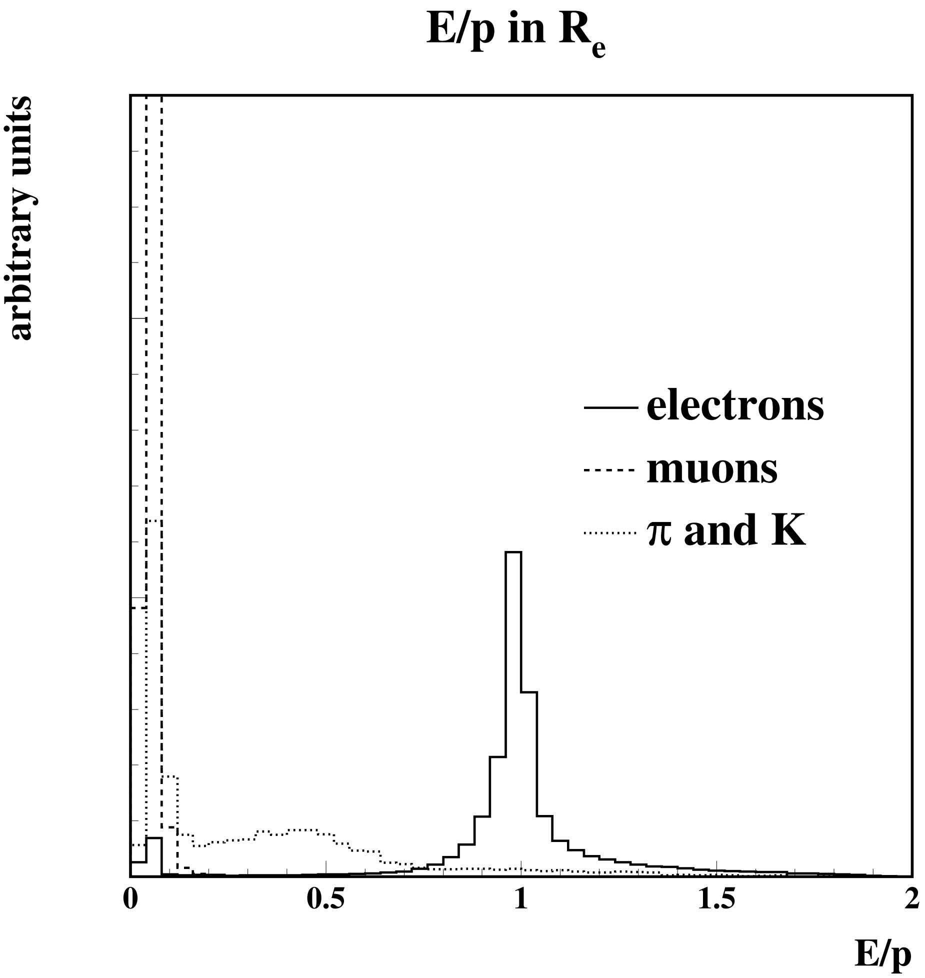

Figure 7.3: E/p for tracks identified as electrons (solid histogram) and backgrounds (dashed histogram). All tracks have a momentum between 2.0 and 2.7 GeV/c. No cut on R_e has been applied.

The DR pulse height is used to determine the dE/dx energy loss. Information from each DR hit is combined to determine the number of standard deviations that the track differs from the average dE/dx loss by an electron. Figure 7.4 shows this distribution for electrons and background tracks.

Three CsI cluster shape variables are used to identify electrons. The first of these, known as $E(9)/E(25)$, is a measure of how the cluster energy is distributed around the crystal with the largest energy. $E(9)$ ($E(25)$) is the sum of the energy of the nine (25) crystals centered on this crystal. The $E(9)/E(25)$ distribution is shown in Figure 7.5. In addition to $E(9)/E(25)$, we consider the RMS width of the CsI shower, Figure 7.6 as well as the ratio of the θ (along the beam direction) to ϕ (perpendicular to it) widths, shown in Figure 7.7. Finally, the distance between the projection of the charged track into the calorimeter and the centroid of the CsI cluster tends to be less for electrons than for other tracks. Figure 7.8 shows this distance.

We require that R_e is greater than 2.0. The efficiency for electrons whose energy is between 2.3 and 2.7 GeV that satsify the $\cos\theta$ requirement and match to a well identified track candidate is approximately 94%. The rate of hadrons passing muon identification criteria is determined from data, and is approximately 0.1%.

The muon detector is described in Chapter 5. Muons candidates are found by extrapolating tracks from the central detector into the muon counters. Tracks are required to match to hits through at least seven absorption lenths of iron and satsify $|\cos\theta| < 0.85$, where θ is the dip angle with respect to the beam direction to be considered as a candidate muon. The efficiency for muons whose energy is between 2.3 and 2.7 GeV that satsify the $\cos\theta$ requirement and match to a well identified track candidate is approximately 82%. The rate of hadrons passing muon identification criteria is determined from data, and is approximately 0.6%.

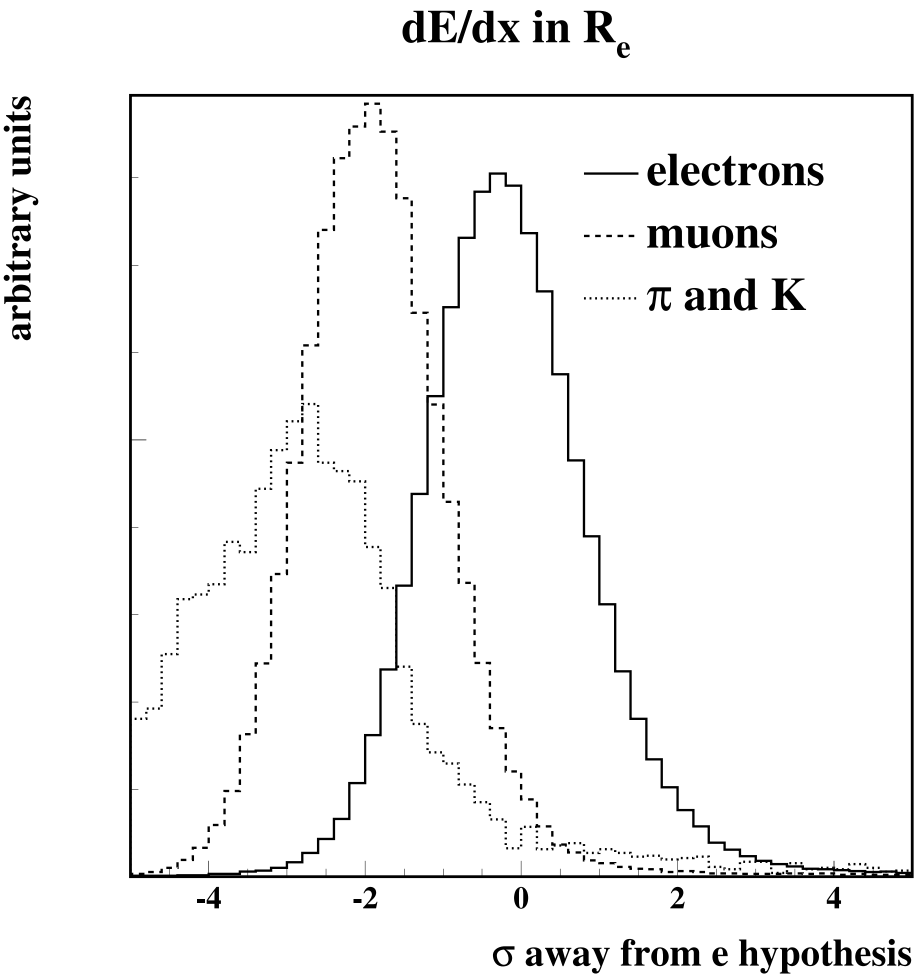

Figure 7.4: dE/dx information for tracks identified as electrons (solid histogram) and backgrounds (dashed histogram). All tracks have a momentum between 2.0 and 2.7 GeV/c. No cut on R_e has been applied.

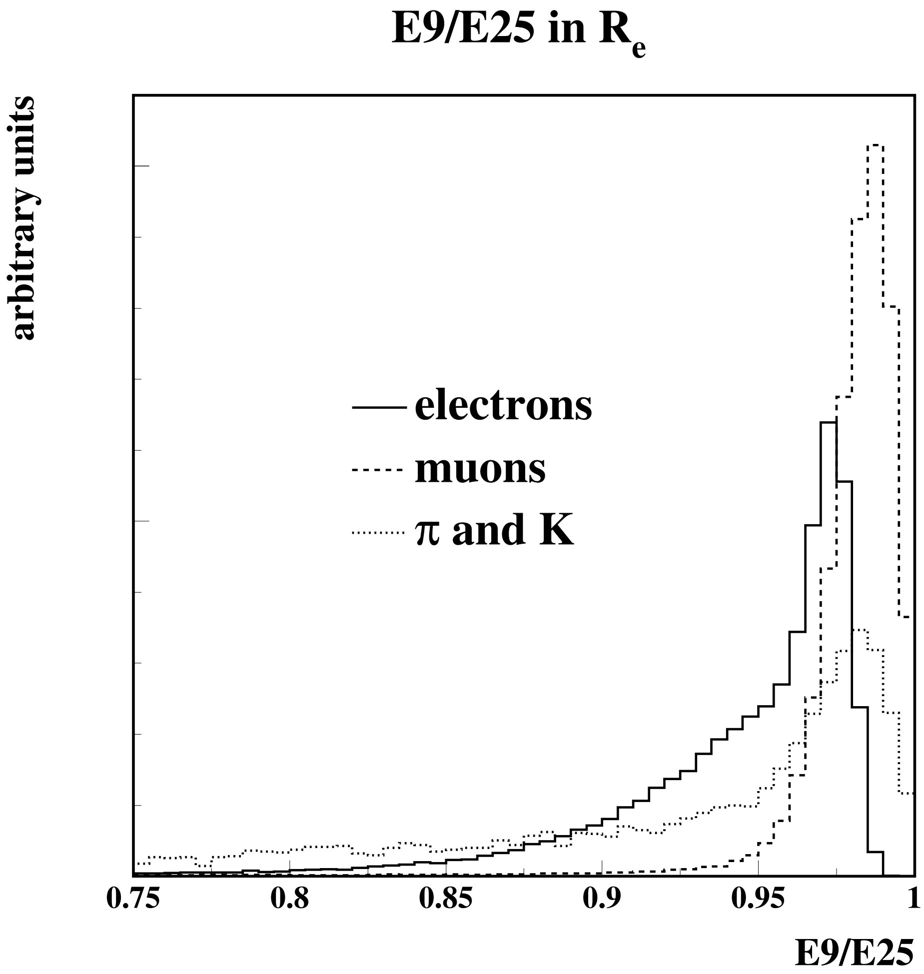

Figure 7.5: $E(9)/E(25)$ for tracks identified as electrons (solid histogram) and backgrounds (dashed histogram). All tracks have a momentum between 2.0 and 2.7 GeV/c. No cut on R_e has been applied.

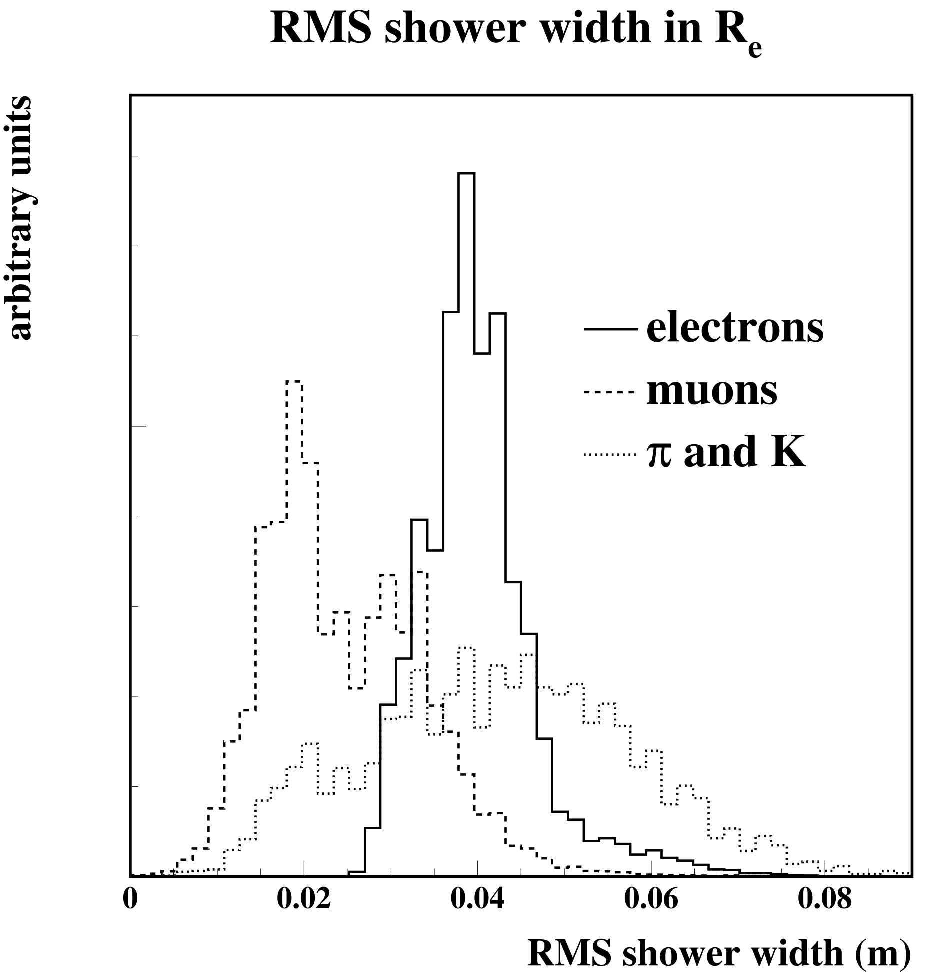

Figure 7.6: The RMS shower width for tracks identified as electrons (solid histogram) and backgrounds (dashed histogram). All tracks have a momentum between 2.0 and 2.7 GeV/c. No cut on R_e has been applied.

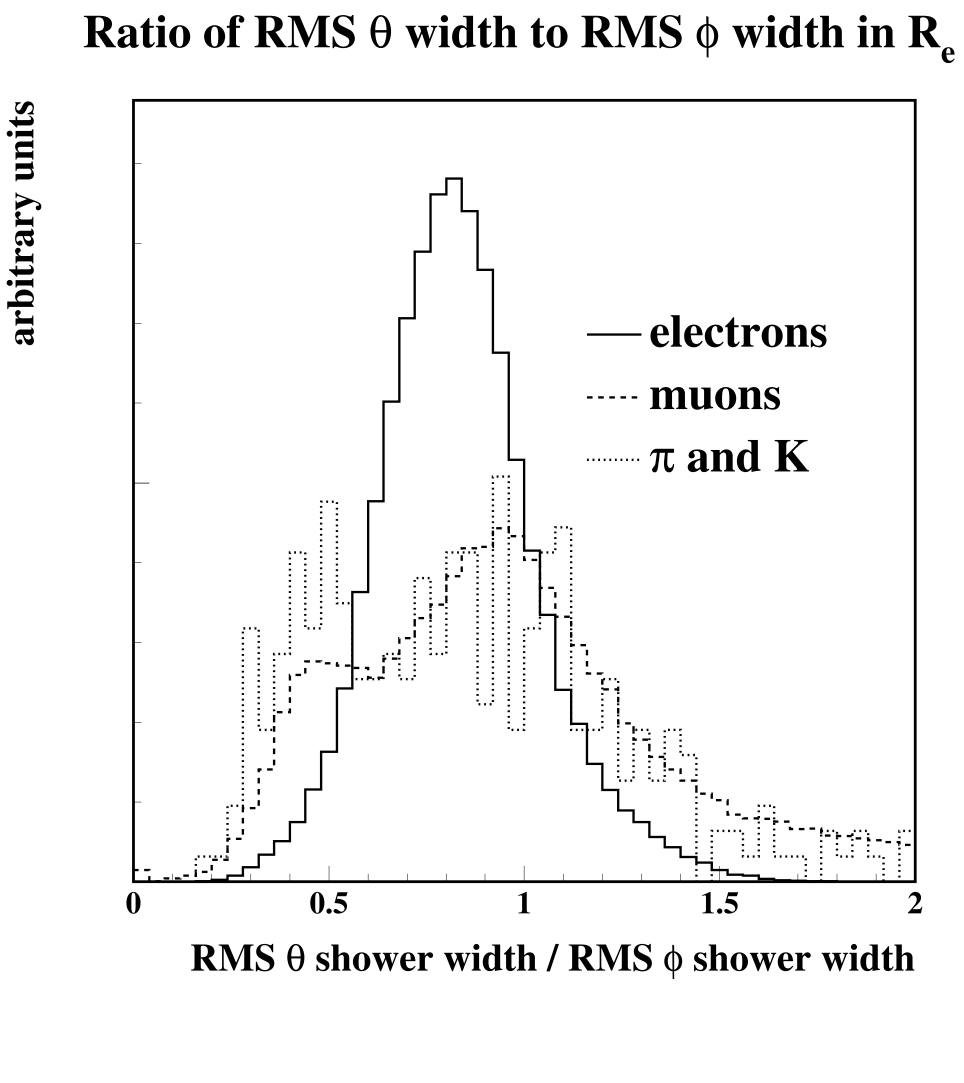

Figure 7.7: The ratio of the θ to ϕ RMS shower widths for tracks identified as electrons (solid histogram) and backgrounds (dashed histogram). All tracks have a momentum between 2.0 and 2.7 GeV/c. No cut on R_e has been applied.

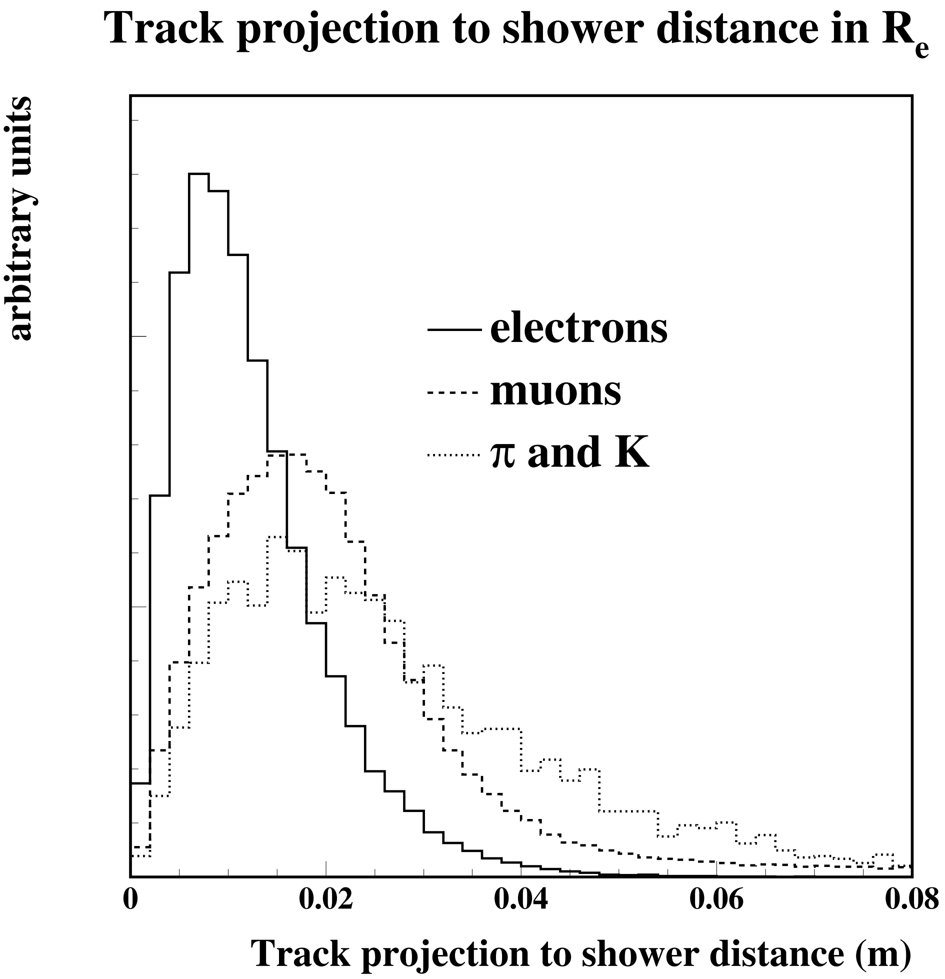

Figure 7.8: The distance from the track projection in the calorimeter to the centroid of the CsI cluster. for tracks identified as electrons (solid histogram) and backgrounds (dashed histogram). All tracks have a momentum between 2.0 and 2.7 GeV/c. No cut on R_e has been applied.

7.5 Selection of ρ, ω, and π candidates

To search for $B \to \rho(\omega/\pi)\ell\nu$ events, electron or muon candidates are combined with $\pi^{\pm}\pi^{0}$, $\pi^{+}\pi^{-}$, $\pi^{+}\pi^{-}\pi^{0}$, $\pi^{\pm}$, or π^{0} candidates. Combinatoric backgrounds are suppressed by requiring hadronic candidates to have a momentum greater than 300 MeV/c.

The combinatoric background is further suppressed in the $\pi^{+}\pi^{-}\pi^{0}$ mode by making a cut on the $\omega \to \pi^{+}\pi^{-}\pi^{0}$ Dalitz amplitude. We require that the π^{+}, π^{-}, and π^{0} are configured such that the decay amplitude ($\mathcal{M} \propto |\mathbf{p}_{\pi^+} \times \mathbf{p}_{\pi^-}|$ where $\mathbf{p}_{\pi^+}$ and $\mathbf{p}_{\pi^-}$ are evaluated in the ω rest frame) is at least 25% of the maximum decay amplitude. Figure 7.9 shows the $\omega \to \pi^{+}\pi^{-}\pi^{0}$ Dalitz plot. Figure 7.10 shows the decay amplitude distribution as a fraction of the maximum decay amplitude for signal and background events.

7.6 Suppression of $e^{+}e^{-} \to q\bar{q}$ events

Because our best sensitivity to $B \to \rho\ell\nu$ is in the HILEP region, suppression of continuum background is a key issue in the analysis. At the $\Upsilon(4S)$ center-of-mass energy, $\Upsilon(4S) \to B\bar{B}$ decays can be distinguished from continuum events, which have a three times larger cross section, on the basis of various quantities that describe the overall distribution of tracks and photons in the event. Such event shape, or event topology, variables exploit the fact that the B mesons are produced nearly at rest ($\beta \approx 0.065$), so their decay products are distributed roughly uniformly in solid angle. In contrast, continuum events yield a much more collimated, or jet-like event topology. Figures 7.11, 7.12, and 7.13 show an example $B\bar{B}$, $q\bar{q}$ Monte Carlo, and possible $B \to \rho\ell\nu$ data event, respectively. We use several event-shape requirements in selecting our event sample:

- The ratio, $R2$, of the second to zeroth Fox-Wolfram moments [73] is required to be less than 0.3. This ratio of moments tends to be close to

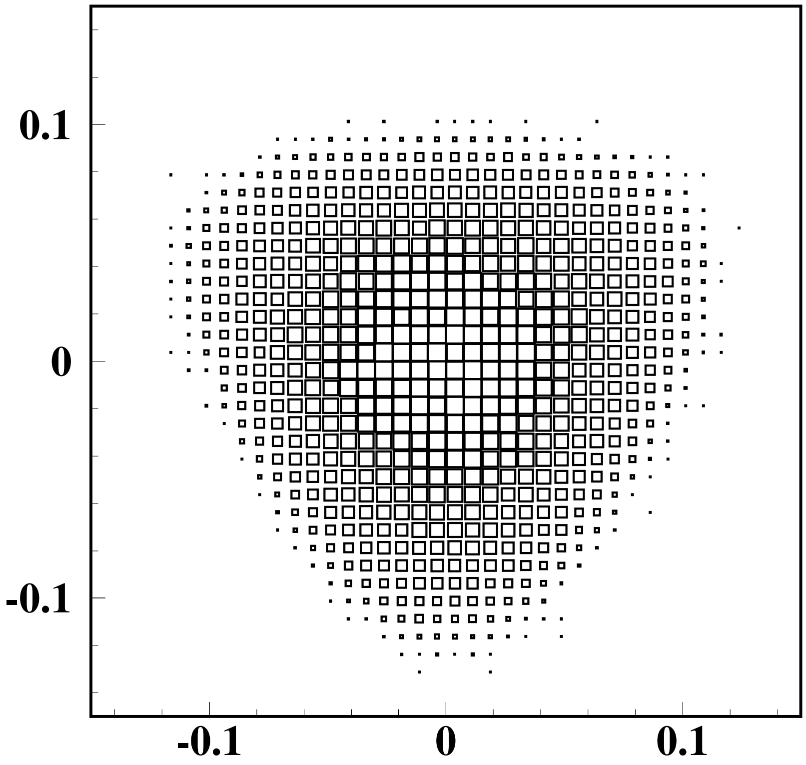

Figure 7.9: Monte Carlo Dalitz distribution for $w \to \pi^+\pi^-\pi^0$ decays. The x-axis is $(T_2 - T_1)/\sqrt{3}$ and the y-axis is $T_3 - Q/3$, where T_i is the kinetic energy of the ith pion and Q is the total kinetic energy. All quantities are defined in the rest frame of the w.

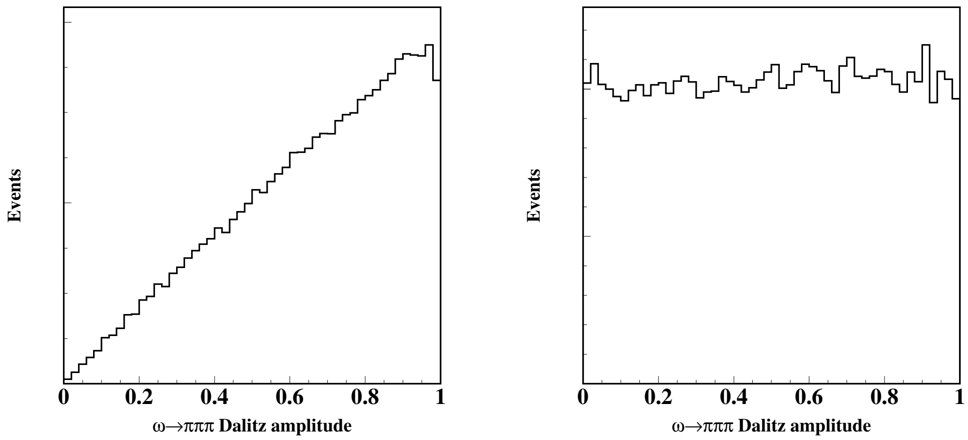

Figure 7.10: Distributions of the decay amplitude for $\omega \to \pi^+\pi^-\pi^0$ for signal ($B \to \omega\ell\nu$) and background events as a fraction of the maximum decay amplitude. $\pi^+\pi^-\pi^0$ combinations that lie above 0.25 are considered for ω candidates.

zero for spherical events, and near unity for jet-like events. Figure 7.14 shows the R2 distribution for the data after all other cuts are applied.

- $\rho\ell$, $\omega\ell$ and $\pi\ell$ candidates are required to have $|\cos\theta_{\text{thrust}}| \leq 0.8$, where θ_{thrust} is defined to be the angle between the thrust axis of the $\rho + \ell$ candidate and the thrust axis of the rest of the event. Figure 7.15 shows the $\cos\theta_{\text{thrust}}$ distribution for the data after all other cuts are applied.

- We select events with $|\cos\theta_{\text{miss}}| \leq 0.9$, where θ_{miss} is the polar angle of the missing momentum ($\mathbf{p}_{\text{miss}}$) with respect to the beam axis (see Eq. 7.1.1). Figure 7.16 shows the $\cos\theta_\nu$ distribution for the data after all other cuts are applied.

- We select events whose energy is evenly distributed around the momentum axis of the candidate lepton using a Fisher discriminant [74]. The input variables to the Fisher discriminant are the track and CsI cluster energies in nine cones of equal solid angle around the lepton-momentum

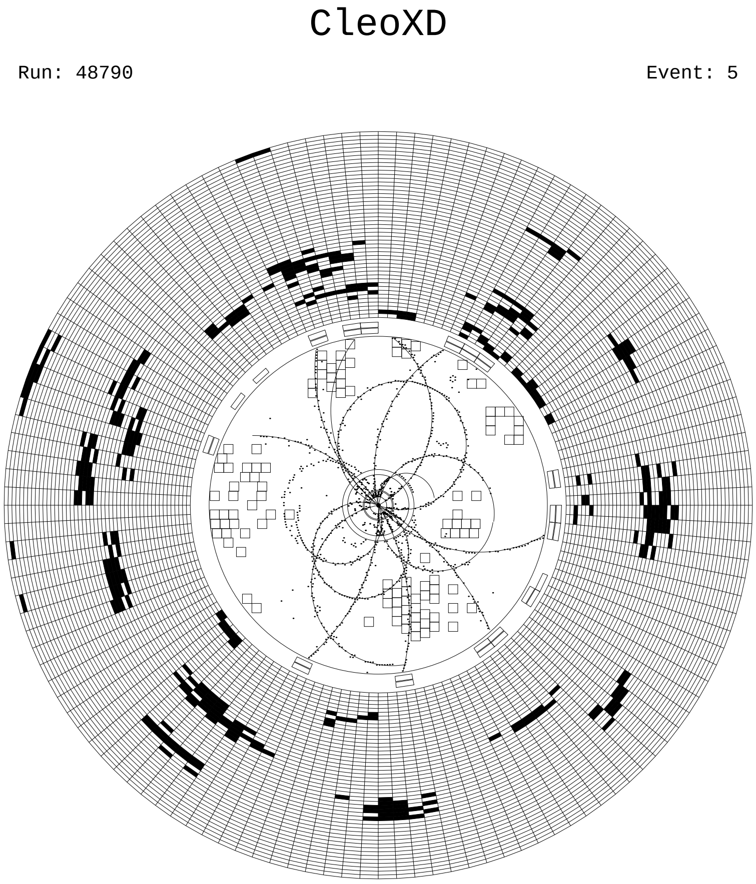

Figure 7.11: A typical $B\overline{B}$ event at CLEO. The beam direction is coming out of the page. Shown are the central tracking system (with reconstructed track segments), the barrel TOF system, and the barrel CsI calorimeter.

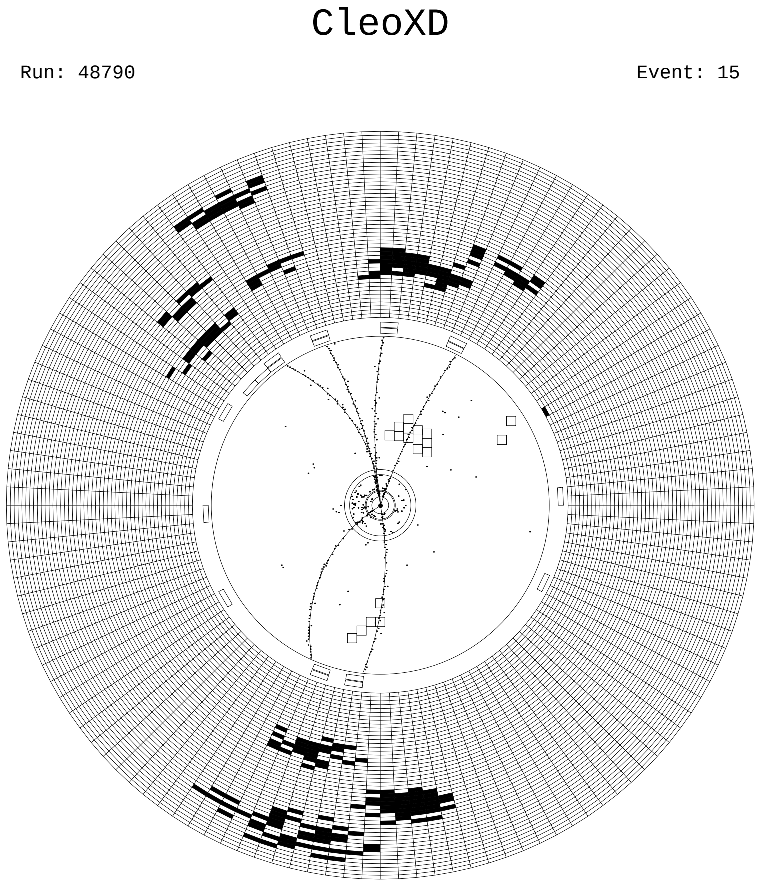

Figure 7.12: A typical $q\overline{q}$ event at CLEO. The beam direction is coming out of the page. Shown are the central tracking system (with reconstructed track segments), the barrel TOF system, and the barrel CsI calorimeter.

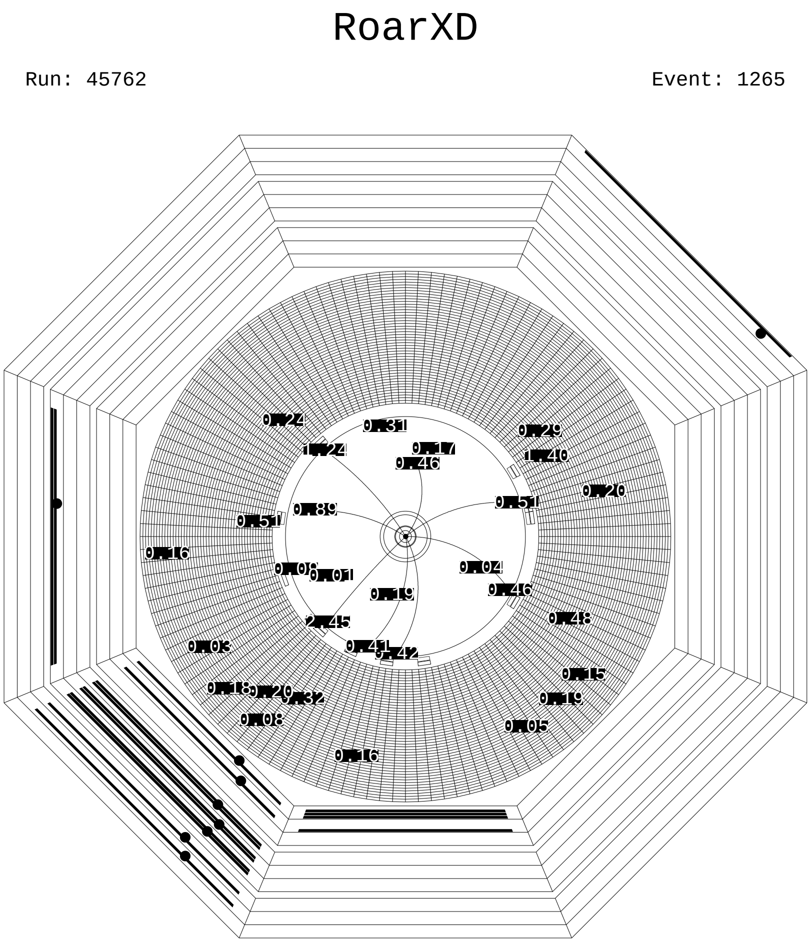

Figure 7.13: A possible $B \to \rho^{\pm}\ell\nu$ event from the on-resonant data sample. The lepton is the 2.45 GeV muon in the lower-left. The beam direction is coming out of the page. Shown are the central tracking system (with reconstructed track segments), the barrel TOF system, the barrel CsI calorimeter, and the barrel muon detector.

axis. Energy in $B\bar{B}$ events tend to be more evenly distributed in these cones than in jetty continuum events. Table 7.1 summarizes how these variables are combined to form the Fisher discriminant. Figure 7.17 shows the distribution of the Fisher discriminant for the data after all other cuts are applied.

7.7 $B \to \rho\ell\nu$ consistency requirements

To suppress combinatoric backgrounds from $b \to c\ell\nu$ and from $b \to u\ell\nu$ sources other than $B \to \rho\ell\nu$ and $B \to \omega\ell\nu$, we require that the event kinematics be consistent with that of $B \to \rho\ell\nu$ decay. Using the constraints $E_B = E_{\text{Beam}}$ and $p_\nu^2 = 0 = (p_B - p_\rho - p_\ell)^2$, we compute the angle between the B momentum direction and that of the reconstructed $Y \equiv (\rho,\ \omega,\ \pi) + \ell$ system:

$$\cos\theta_{BY} \equiv \frac{2E_B E_Y - m_B^2 - m_Y^2}{2|\mathbf{p}_B||\mathbf{p}_Y|}. \tag{7.7.1}$$

The $|\mathbf{p}_B| \cdot \cos\theta_{BY}$ distribution is shown in Fig. 7.18 for signal and continuum events that satisfy all other analysis requirements. We require that $|\mathbf{p}_B| \cdot |\cos\theta_{BY}| \leq 385$ MeV/c. For well-reconstructed signal events with a B momentum of less than 385 MeV/c, this cut is 100% efficient, but $b \to u\ell\nu$ (other than $B \to (\rho,\ \omega,\ \pi)\ell\nu$), $b \to c\ell\nu$, and continuum events often produce unphysical values of $\cos\theta_{BY}$ and can be rejected. At CESR, the average B meson momentum is approximately 320 MeV/c, with a σ of 50 MeV/c due to the beam energy spread from synchrotron emission, so this cut is nearly 100% efficient for well-reconstructed signal events. Figure 7.19 shows the distribution for $|\mathbf{p}_B| \cdot \cos\theta_{BY}$ for the data after all other cuts are applied.

Finally, we compare the direction of the missing momentum ($\mathbf{p}_{\text{miss}}$) with that of the $\mathbf{p}_\nu$ inferred from the $\rho + \ell$ momentum. The later is known to within an azimuthal ambiguity around the B momentum direction. We require that the angle between these two directions be less than 0.6 radians. Figure 7.20 shows the distribution for $\Delta\theta$ for the data after all other cuts are applied.

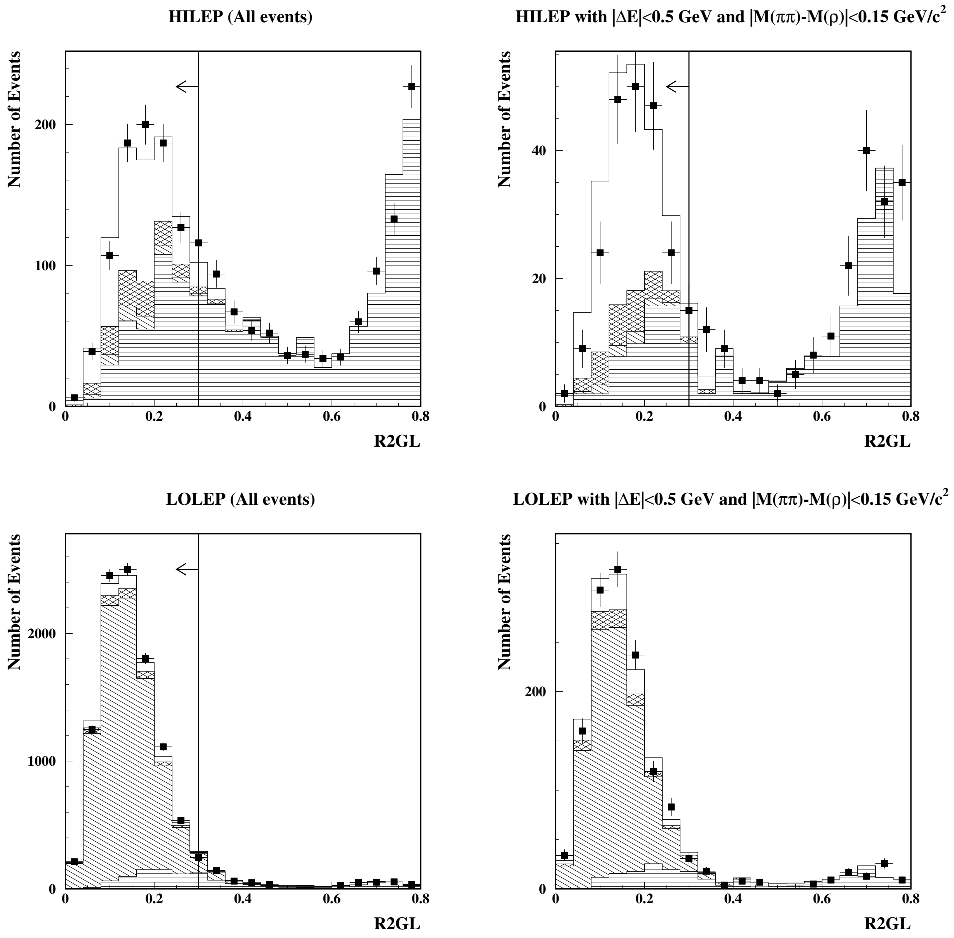

Figure 7.14: Plots of R2 after all other cuts have been applied. All plots are for the $\pi\pi$ modes. The upper (lower) plots are for HILEP (LOLEP). The left hand side plots show all events considered in the fit, while the right hand plots show only events that satisfy $|M(\pi\pi) - M(\rho)| < 0.15$ GeV and $|\Delta E| < 0.5$ GeV requirements. The plots with error bars are the on-resonance data. The horizontally hatched area is the contribution from $e^+e^- \to q\overline{q}$ events. The slant hatched region is from $b \to c\ell\nu$ and fake lepton events. The double hatched region is the $b \to u\ell\nu$ (non ρ/ω) contribution. The unhatched region shows the signal events. The errors on the $e^+e^- \to q\overline{q}$ contribution, which has approximately 1/2 the statistics of the on-resonance data, are not shown.

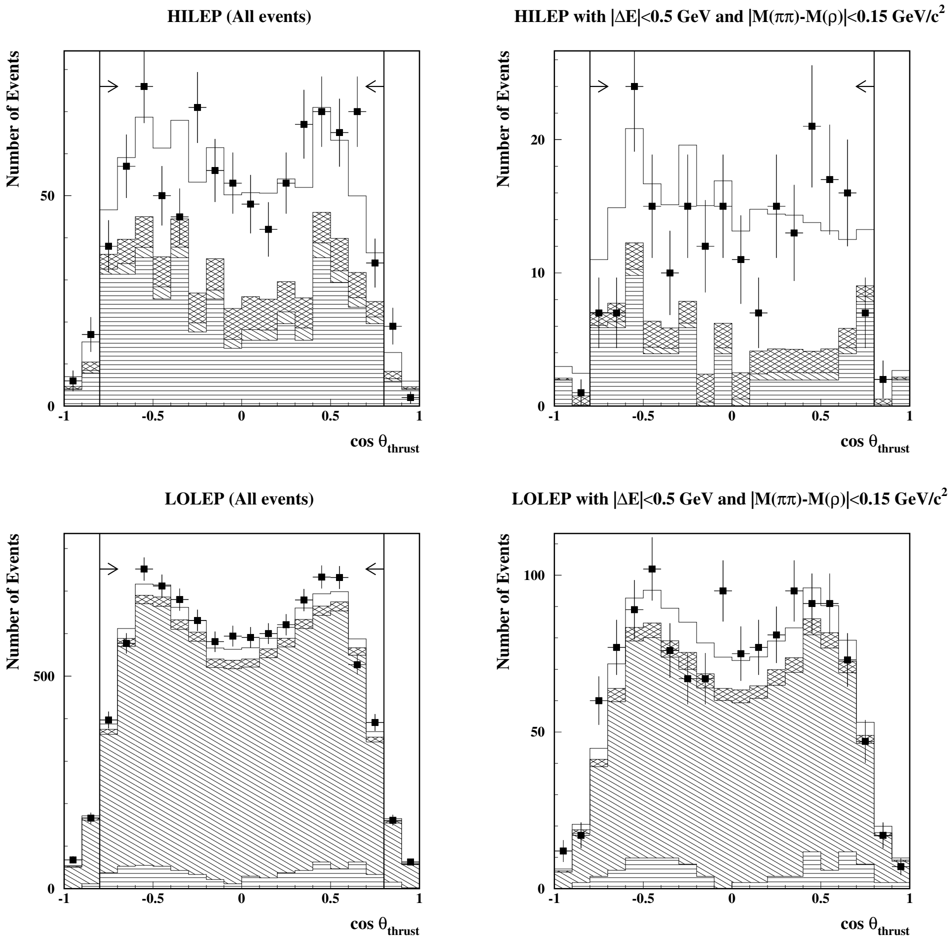

Figure 7.15: Plots of $\cos\theta_{\rm thrust}$ after all other cuts have been applied. All plots are for the $\pi\pi$ modes. The upper (lower) plots are for HILEP (LOLEP). The left hand side plots show all events considered in the fit, while the right hand plots show only events that satisfy $|M(\pi\pi) - M(\rho)| < 0.15$ GeV and $|\Delta E| < 0.5$ GeV requirements. The plots with error bars are the on-resonance data. The horizontally hatched area is the contribution from $e^+e^- \to q\overline{q}$ events. The slant hatched region is from $b \to c\ell\nu$ and fake lepton events. The double hatched region is the $b \to u\ell\nu$ (non ρ/ω) contribution. The unhatched region shows the signal events. The errors on the $e^+e^- \to q\overline{q}$ contribution, which has approximately 1/2 the statistics of the on-resonance data, are not shown.

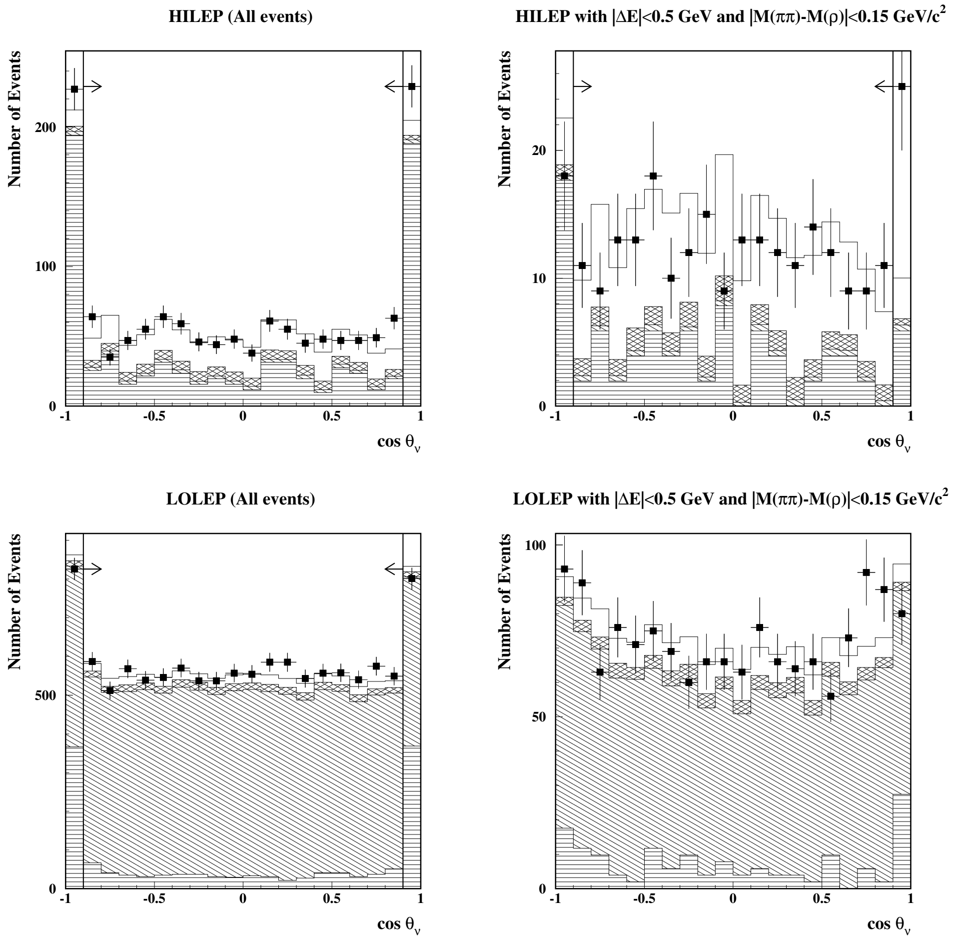

Figure 7.16: Plots of $\cos\theta_\nu$ after all other cuts have been applied. All plots are for the $\pi\pi$ modes. The upper (lower) plots are for HILEP (LOLEP). The left hand side plots show all events considered in the fit, while the right hand plots show only events that satisfy $|M(\pi\pi) - M(\rho)| < 0.15$ GeV and $|\Delta E| < 0.5$ GeV requirements. The plots with error bars are the on-resonance data. The horizontally hatched area is the contribution from $e^+e^- \to q\overline{q}$ events. The slant hatched region is from $b \to c\ell\nu$ and fake lepton events. The double hatched region is the $b \to u\ell\nu$ (non ρ/ω) contribution. The unhatched region shows the signal events. The errors on the $e^+e^- \to q\overline{q}$ contribution, which has approximately 1/2 the statistics of the on-resonance data, are not shown.

Variable (x_i)	Coefficient (α_i)
$E_{0-0.1}$	-0.2616
$E_{0.1-0.2}$	-0.3077
$E_{0.2-0.3}$	-0.2503
$E_{0.3-0.4}$	-0.1949
$E_{0.4-0.5}$	-0.1026
$E_{0.5-0.6}$	0.0935
$E_{0.6-0.7}$	0.0288
$E_{0.7-0.8}$	0.1594
$E_{0.8-0.9}$	0.3204
$E_{0.9-1.0}$	0.6470
$\lvert\cos\theta_{\mathrm{thrust}}\rvert$	0.6367
$\lvert\cos\theta_B\rvert$	-0.1254

Table 7.1: Summary of inputs to the Fisher discriminant, which is defined as $\mathcal{F} = \Sigma\alpha_i x_i$. x_i are the variables used in the discriminant and α_i are the coefficients with which these variables are combined. We have used 12 variables in the Fisher discriminant. Ten of these correspond to energy flow in segments of solid angle centered around the thrust axis of the $\rho + \ell$ candidate. We define $E_{s_1-s_2} \equiv \Sigma|\mathbf{p}_i| + \Sigma E_i$, where $\mathbf{p}_i$ and E_i are the momenta of tracks and energies of clusters, respectively, that lie in the solid angle determined by $s_1 < |\cos\theta_i| < s_2$. θ_i is the angle between the track or cluster and the thrust axis of the $\rho+\ell$. Particles that make up the $\rho+\ell$ candidate are not included in these sums. $\cos\theta_{\mathrm{thrust}}$ is the angle between the $\rho+\ell$ thrust axis and the beam direction. Finally, $\cos\theta_B$ is the angle between the B candidate and the beam direction. The B candidate momentum is defined to be $\mathbf{p}_\ell + \mathbf{p}_\rho + \mathbf{p}_{\mathrm{miss}}$. The α_i are determined using the covariance matrices of the input variables for samples of signal and background events. We used signal and continuum Monte Carlo samples to determine the covariance matrices.

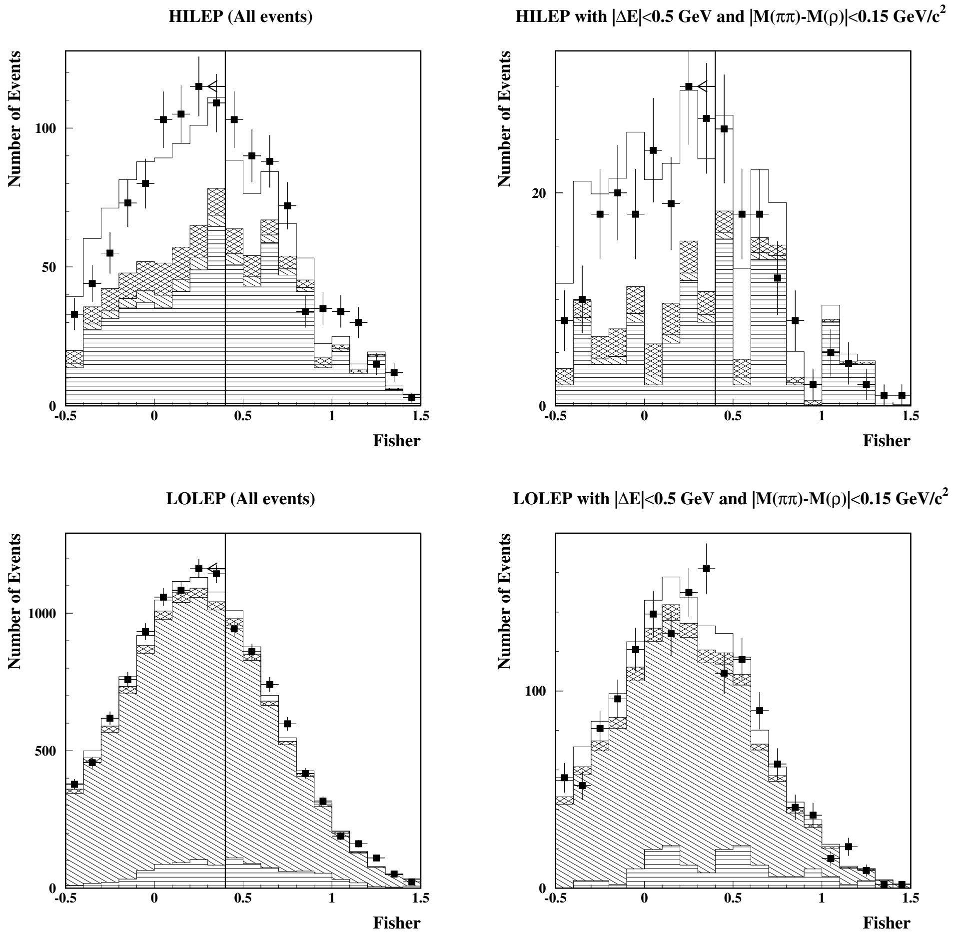

Figure 7.17: Plots of fisher variable after all other cuts have been applied. All plots are for the $\pi\pi$ modes. The upper (lower) plots are for HILEP (LOLEP). The left hand side plots show all events considered in the fit, while the right hand plots show only events that satisfy $|M(\pi\pi) - M(\rho)| < 0.15$ GeV and $|\Delta E| < 0.5$ GeV requirements. The plots with error bars are the on-resonance data. The horizontally hatched area is the contribution from $e^+e^- \to q\overline{q}$ events. The slant hatched region is from $b \to c\ell\nu$ and fake lepton events. The double hatched region is the $b \to u\ell\nu$ (non ρ/ω) contribution. The unhatched region shows the signal events. The errors on the $e^+e^- \to q\overline{q}$ contribution, which has approximately 1/2 the statistics of the on-resonance data, are not shown.

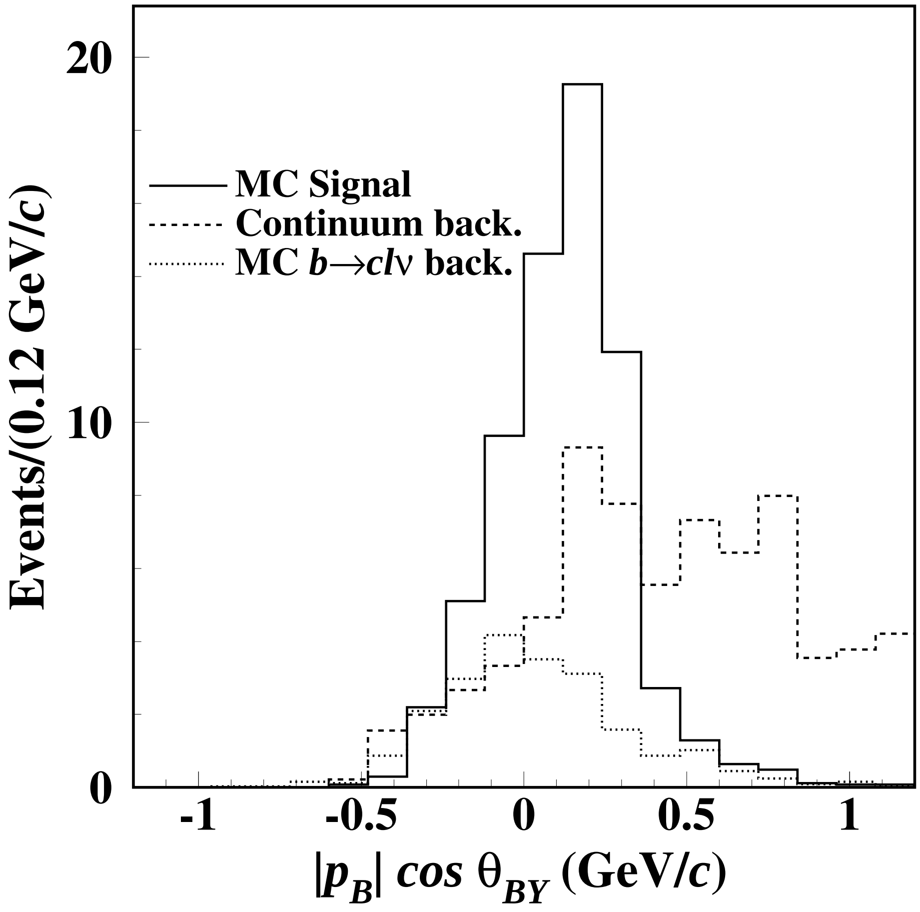

Figure 7.18: Signal and background $|\mathbf{p}_B|\cos\theta_{\rm BY}$ distributions for the HILEP $\pi\pi$ modes for events that pass all other requirements including $|M(\pi\pi) - M(\rho)| < 0.15$ GeV/c^2 and $|\Delta E| < 0.5$ GeV. Shown are the Monte Carlo signal, continuum data, and Monte Carlo $b \to c\ell\nu$ contributions. Each has been normalized using the results of the likelihood fit described in Sec. 8. The signal contribution includes events from one signal mode that have been reconstructed in another signal mode. The $|\mathbf{p}_B| \cdot |\cos\theta_{BY}| \leq 385$ MeV/c requirement keeps almost all signal events, while rejecting much of the background.

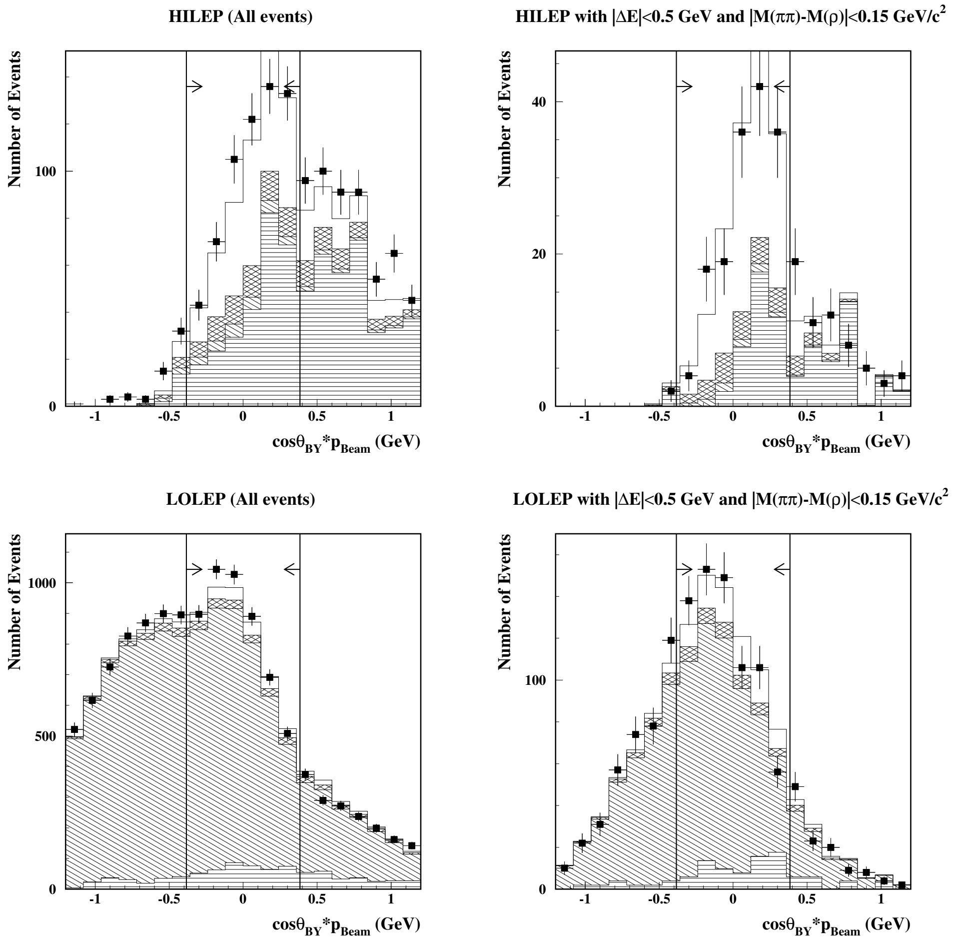

Figure 7.19: Plots of $\cos\theta_{\rm BY}$ after all other cuts have been applied. All plots are for the $\pi\pi$ modes. The upper (lower) plots are for HILEP (LOLEP). The left hand side plots show all events considered in the fit, while the right hand plots show only events that satisfy $|M(\pi\pi) - M(\rho)| < 0.15$ GeV and $|\Delta E| < 0.5$ GeV requirements. The plots with error bars are the on-resonance data. The horizontally hatched area is the contribution from $e^+e^- \to q\overline{q}$ events. The slant hatched region is from $b \to c\ell\nu$ and fake lepton events. The double hatched region is the $b \to u\ell\nu$ (non ρ/ω) contribution. The unhatched region shows the signal events. The errors on the $e^+e^- \to q\overline{q}$ contribution, which has approximately 1/2 the statistics of the on-resonance data, are not shown.

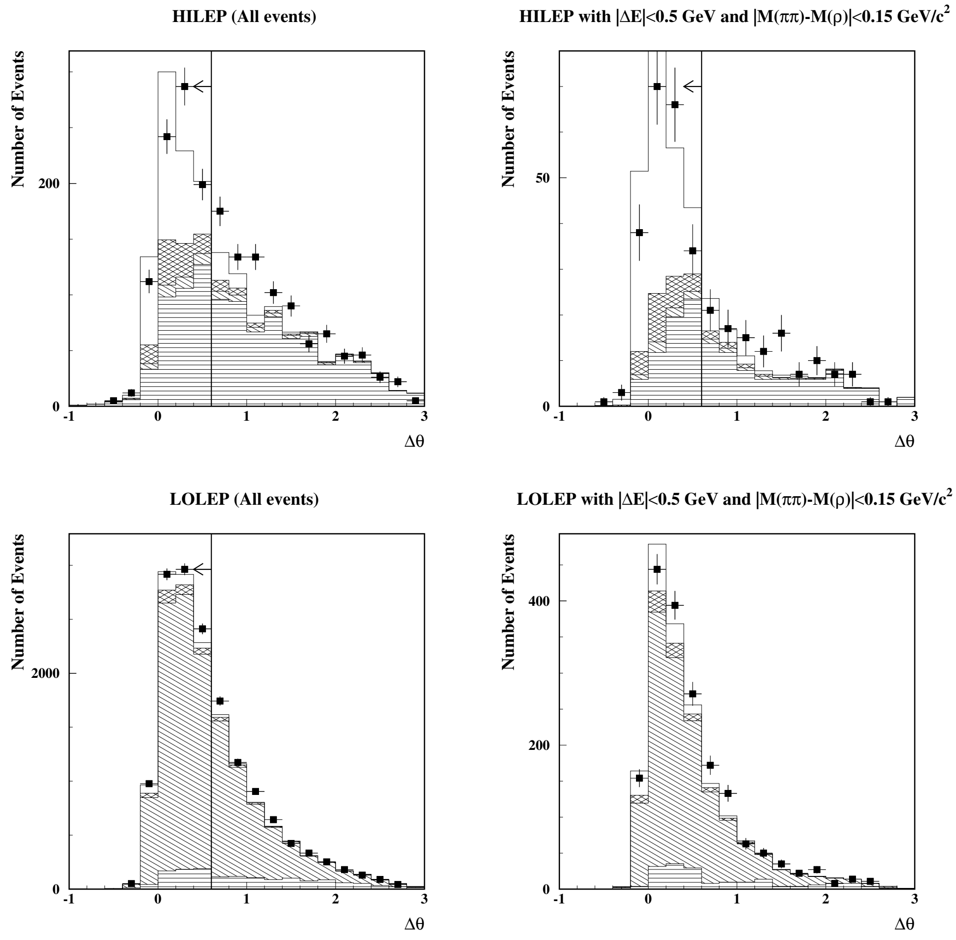

Figure 7.20: Plots of $\Delta\theta$ after all other cuts have been applied. All plots are for the $\pi\pi$ modes. The upper (lower) plots are for HILEP (LOLEP). The left hand side plots show all events considered in the fit, while the right hand plots show only events that satisfy $|M(\pi\pi) - M(\rho)| < 0.15$ GeV and $|\Delta E| < 0.5$ GeV requirements. The plots with error bars are the on-resonance data. The horizontally hatched area is the contribution from $e^+e^- \to q\overline{q}$ events. The slant hatched region is from $b \to c\ell\nu$ and fake lepton events. The double hatched region is the $b \to u\ell\nu$ (non ρ/ω) contribution. The unhatched region shows the signal events. The errors on the $e^+e^- \to q\overline{q}$ contribution, which has approximately 1/2 the statistics of the on-resonance data, are not shown.

Because the ρ has a large width and we are reconstructing several different hadronic modes, events with multiple entries passing all of the above requirements are common. To avoid the statistical difficulties associated with this, we choose one combination per event after all other criteria are imposed, picking the combination with a momentum $(\mathbf{p}_\rho + \mathbf{p}_\ell + \mathbf{p}_{\text{miss}})$ closest to that expected from the measured beam energy and known M_B. In Figure 7.21 we show the number of combinations in signal Monte Carlo that pass all of the above requirements and are considered in this one combination per event selection. We find that this distribution does not depend significantly on the lepton-energy region. Also, the distribution for background events is similar to the signal distribution shown. In $B^0 \to \rho^- \ell^+ \nu$ events, in events where there is at least one candidate that passes each of the above requirements, the the correct combination of candidate tracks and clusters is selected approximately 35% of the time.

The large ρ width also leads to an important effect in signal events. The reconstructed $\pi\pi$ system may not consist of the true daughter particles. For example, it is possible for a $B \to \rho^0 \ell \nu$ event to be reconstructed in the $\pi^+\pi^0$ mode. Although the kinematic distributions of these crossfeed events are somewhat different from correctly reconstructed signal events, these events are due to true signal decays, and are counted as such.

Figure 7.22 shows the $M(\pi\pi)$ distribution expected from signal, continuum, and $b \to c\ell\nu$ events in the HILEP $\pi\pi$ modes. Each contribution has been normalized using the results of the likelihood fit described in Chapter 8.

Finally, we show that the above selection requirements, with the exception of the E_ℓ requirement, do not restrict the event sample to a small portion of the kinematically allowed region of phase space. Figures 7.23 to 7.28 show the generated and reconstructed distributions for ISGW2 signal Monte Carlo for E_ℓ, $|\mathbf{p}_\rho|$, E_{π^+}, E_{π^0}, and E_γ.

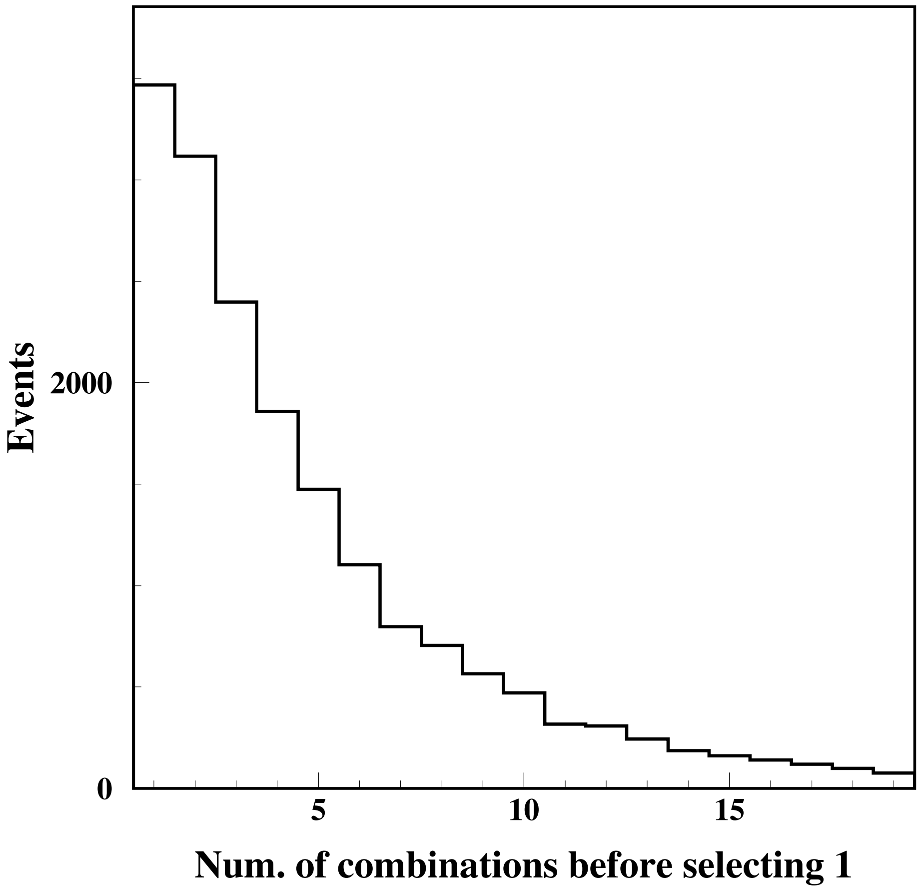

Figure 7.21: Number of combinations per event before the 1 combination per event selection is performed. This distribution is for events with any lepton energy above 1.7 GeV. The observed distribution does not depend strongly on lepton energy or whether or not the event is due to signal or background.

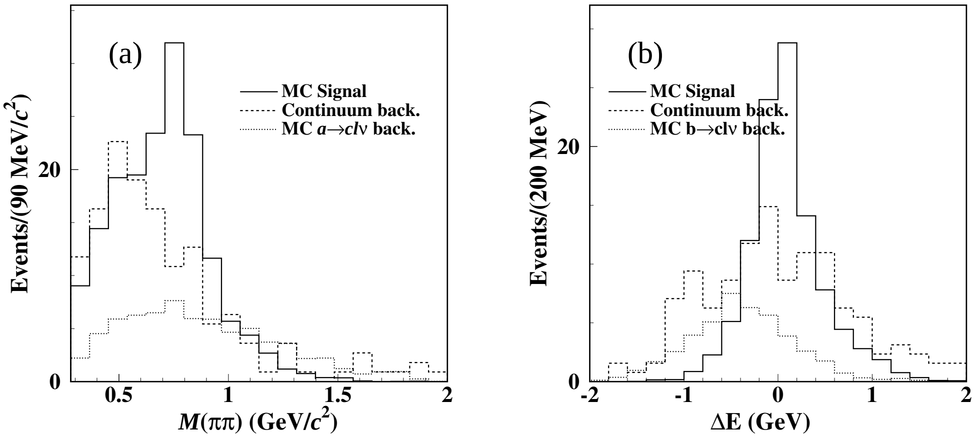

Figure 7.22: Signal and background distributions for the HILEP $\pi\pi$ modes: (a) $M(\pi\pi)$ for events that pass all requirements including $|\Delta E| < 0.5$ GeV and (b) ΔE for events that pass all requirements including $|M(\pi\pi) - M(\rho)| < 0.15$ GeV$/c^2$. Shown are the Monte Carlo signal, continuum data, and Monte Carlo $b \to c\ell\nu$ contributions. Each has been normalized using the results of the likelihood fit described in Sec. 8. The signal contribution includes events from one signal mode that have been reconstructed in another signal mode.

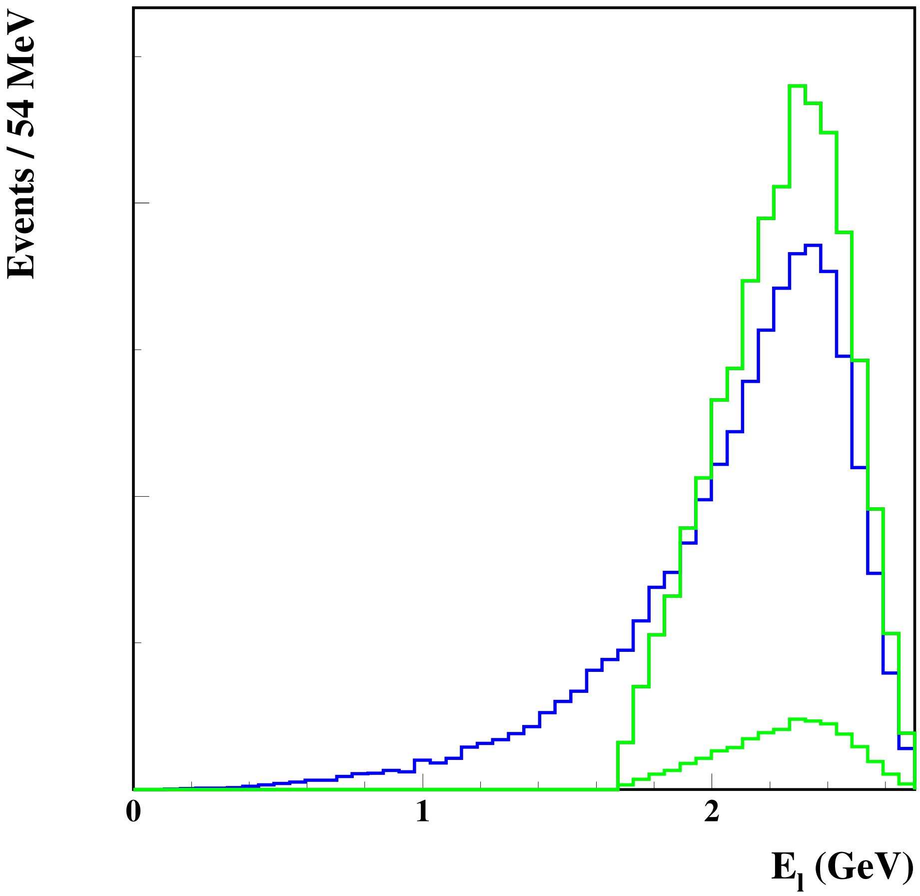

Figure 7.23: E_ℓ distribution for ISGW2 $B \to \rho^{\pm}\ell\nu$ Monte Carlo before and after all event selection criteria have been applied. The dark histogram shows the generated distribution, and the light histograms show the distribution for reconstructed events. For the reconstructed events, we show the resulting distribution normalized to have the same area as the generated distribution as well as with incorporating the absolute efficiency of the selection requirements.

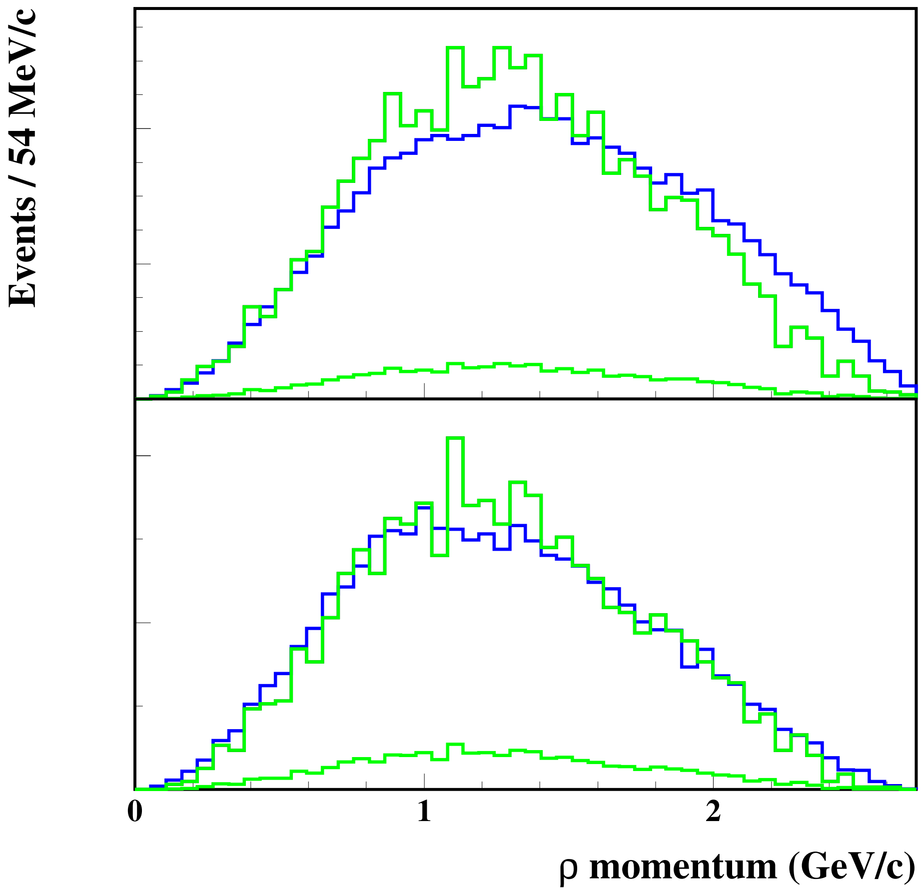

Figure 7.24: $|\mathbf{p}_\rho|$ distribution for ISGW2 $B \to \rho^\pm \ell \nu$ Monte Carlo before and after all event selection criteria have been applied. The upper plot shows the results for the full lepton-energy range, while the lower plot is only for $E_\ell >$ 2.3 GeV events. The dark histogram shows the generated distribution, and the light histograms show the distribution for reconstructed events. For the reconstructed events, we show the resulting distribution normalized to have the same area as the generated distribution as well as with incorporating the absolute efficiency of the selection requirements.

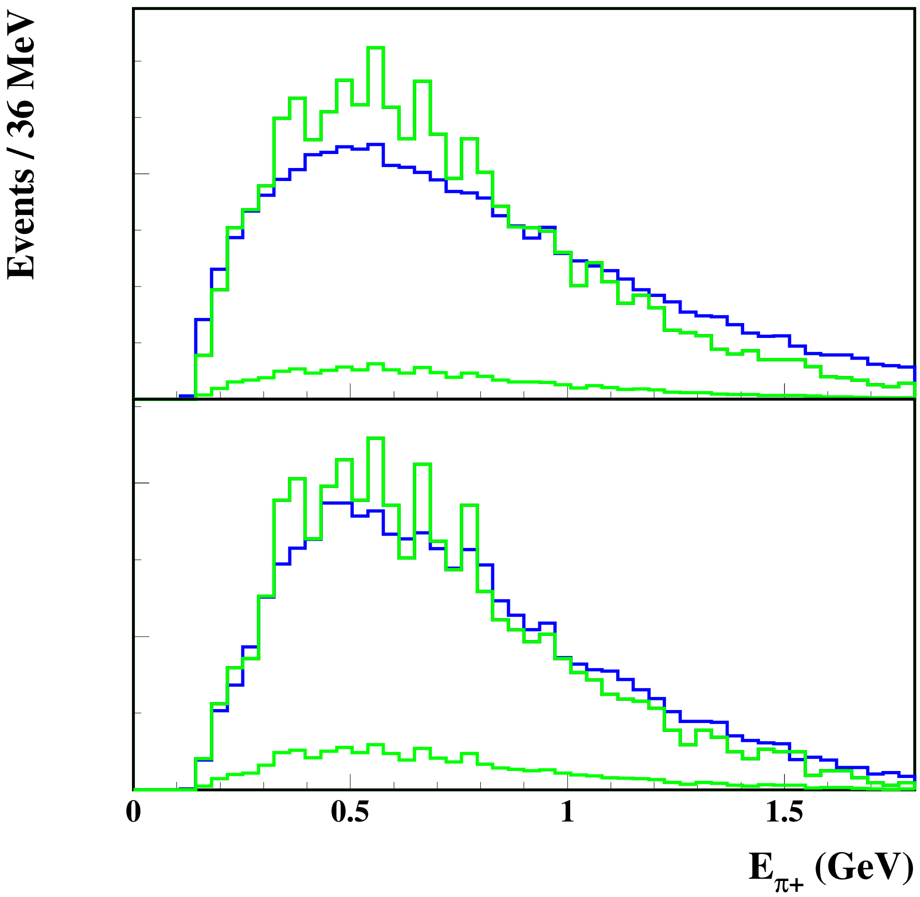

Figure 7.25: E_{π^+} distribution for ISGW2 $B \to \rho^{\pm}\ell\nu$ Monte Carlo before and after all event selection criteria have been applied. The upper plot shows the results for the full lepton-energy range, while the lower plot is only for $E_\ell >$ 2.3 GeV events. The dark histogram shows the generated distribution, and the light histograms show the distribution for reconstructed events. For the reconstructed events, we show the resulting distribution normalized to have the same area as the generated distribution as well as with incorporating the absolute efficiency of the selection requirements.

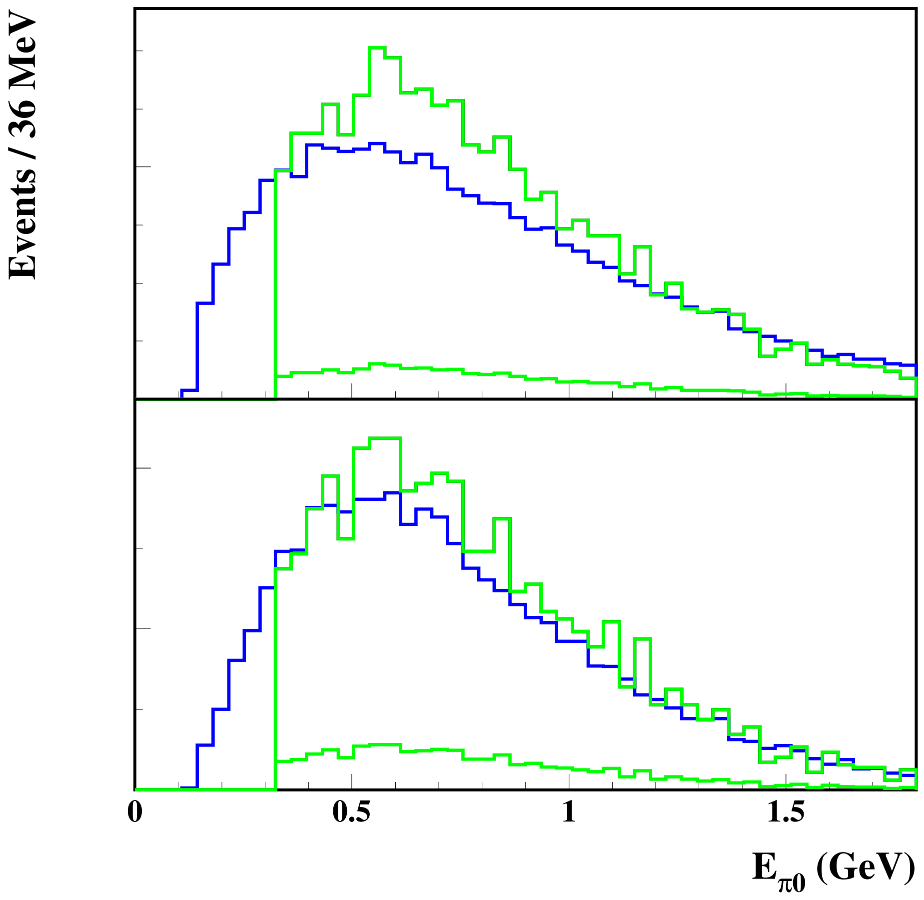

Figure 7.26: E_{π^0} distribution for ISGW2 $B \to \rho^{\pm}\ell\nu$ Monte Carlo before and after all event selection criteria have been applied. The upper plot shows the results for the full lepton-energy range, while the lower plot is only for $E_\ell >$ 2.3 GeV events. The dark histogram shows the generated distribution, and the light histograms show the distribution for reconstructed events. For the reconstructed events, we show the resulting distribution normalized to have the same area as the generated distribution as well as with incorporating the absolute efficiency of the selection requirements.

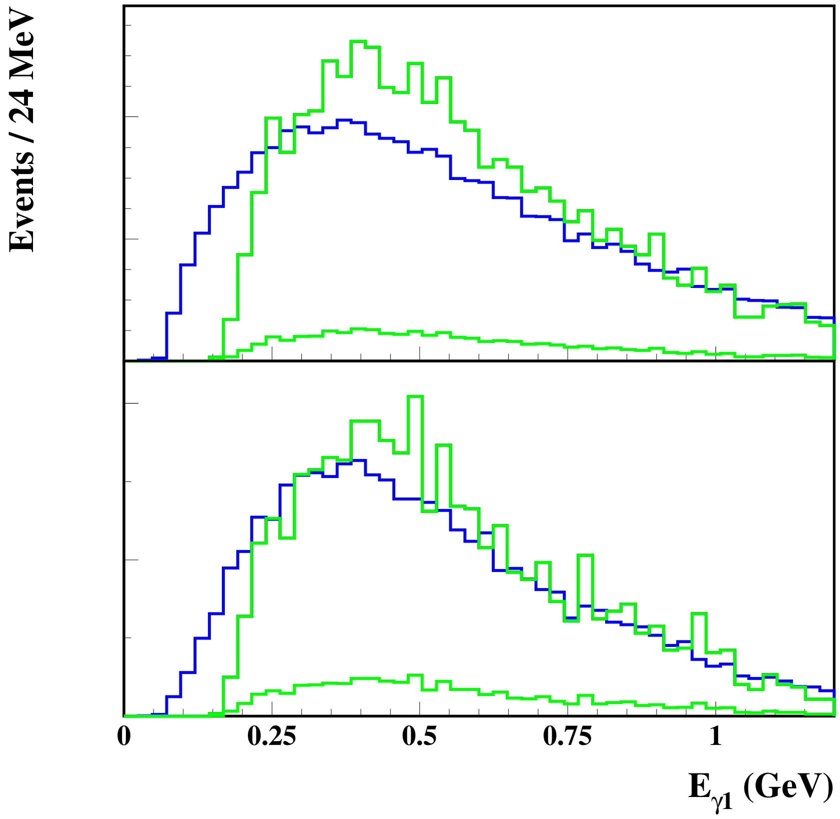

Figure 7.27: E_γ distribution for ISGW2 $B \to \rho^\pm \ell\nu$ Monte Carlo before and after all event selection criteria have been applied for the most energetic photon in the π^0 candidate. The upper plot shows the results for the full lepton-energy range, while the lower plot is only for $E_\ell > 2.3$ GeV events. The dark histogram shows the generated distribution, and the light histograms show the distribution for reconstructed events. For the reconstructed events, we show the resulting distribution normalized to have the same area as the generated distribution as well as with incorporating the absolute efficiency of the selection requirements.

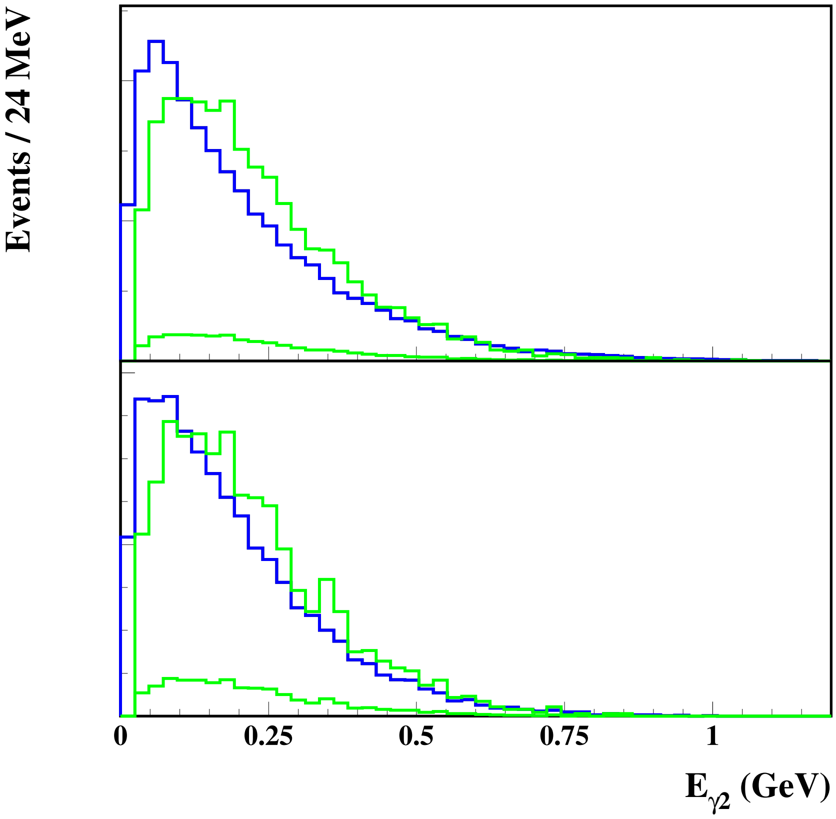

Figure 7.28: E_γ distribution for ISGW2 $B \to \rho^\pm \ell\nu$ Monte Carlo before and after all event selection criteria have been applied for the least energetic photon in the π^0 candidate. The upper plot shows the results for the full lepton-energy range, while the lower plot is only for $E_\ell > 2.3$ GeV events. The dark histogram shows the generated distribution, and the light histograms show the distribution for reconstructed events. For the reconstructed events, we show the resulting distribution normalized to have the same area as the generated distribution as well as with incorporating the absolute efficiency of the selection requirements.

Chapter 8

Fit method

We perform a binned maximum-likelihood fit using MINUIT [75] in three lepton-energy ranges and five decay modes. In addition to lepton energy, we fit two kinematic variables, so we are in effect performing a three dimensional correlated fit. Our fit includes contributions from $B \to \rho\ell\nu$, $B \to \omega\ell\nu$, $B \to \pi\ell\nu$, other $b \to u\ell\nu$ modes, $b \to c\ell\nu$, continuum events, as well as a contribution from events where hadrons fake leptons. In this chapter, we describe the fit variables and constraints, the modeling of signal and background components, and our method for extracting the rate as a function of q^2.

8.1 Fit variables

The three fit variables, E_ℓ, $M_{\rm had}$, and ΔE, are constructed from the three decay products in semileptonic decay: the lepton, the final-state hadron, and the neutrino. The three lepton-energy bins were discussed in Chapter 7. The invariant mass of the daughter hadron, $M_{\rm had}$, is reconstructed in the $\pi^+\pi^-$ and $\pi^\pm\pi^0$ channels for $B \to \rho\ell\nu$ and in the $\pi^+\pi^-\pi^0$ channel for $B \to \omega\ell\nu$. The bin size for the fit is 90 MeV/c^2 for both $M(\pi\pi)$ and $M(\pi\pi\pi)$. The momentum of the hadron is not used as a fit variable but is the basis for measuring the q^2 distribution after the fit is performed.

The presence of a neutrino consistent with $B \to \rho\ell\nu$ decay is signaled by a peak in the distribution of

$$\Delta E \equiv E_\rho + E_\ell + |\mathbf{p}_{\text{miss}}| - E_{\text{Beam}} \tag{8.1.1}$$

at $\Delta E = 0$. Backgrounds from $b \to c\ell\nu$ and $b \to u\ell\nu$ (except for $B \to \pi\ell\nu$) events tend to have $\Delta E < 0$. On the other hand, $B \to \pi\ell\nu$ events have $\Delta E > 0$ when reconstructed in the $\pi\pi$ or $\pi^+\pi^-\pi^0$ modes, since extra particles beyond the actual B decay products are included in the decay hypothesis. The ΔE bin size for the fit is 200 MeV.

ΔE vs. $M(\pi\pi)$ distributions for signal and background contributions in the HILEP region are shown in Fig. 8.1. Shapes of distributions for signal, $b \to c\ell\nu$, and $b \to u\ell\nu$ are taken from Monte Carlo simulations using theoretical models of B-meson decays and full detector simulations based on GEANT [72], while the continuum background is measured with the off-resonance data. An additional background, not shown, arises from hadrons passing the lepton identification requirements in $B\bar{B}$ events. This contribution is determined using measured fake rates and data, as described below. The data or Monte Carlo samples that are used to estimate the non-continuum contributions are sufficiently large that their statistical fluctuations are negligible compared with those of the data. We now discuss each of these fit components in more detail.

8.2 Signal contribution

For signal, the Monte Carlo simulation provides the *shapes* of the three-dimensional distribution of E_ℓ, M_{had}, and ΔE. There is very little model dependence in the ΔE vs. M_{had} distributions, but the distribution of signal events across the three lepton-energy bins varies significantly among form-factor models. The variation among the $B \to \rho\ell\nu$ form-factor models is a significant systematic error for our measurement of $\mathcal{B}(B \to \rho\ell\nu)$ and $|V_{ub}|$.

There are a large number of crossfeed signal events, as described in the previous section. The size of the crossfeed contribution relative to the direct

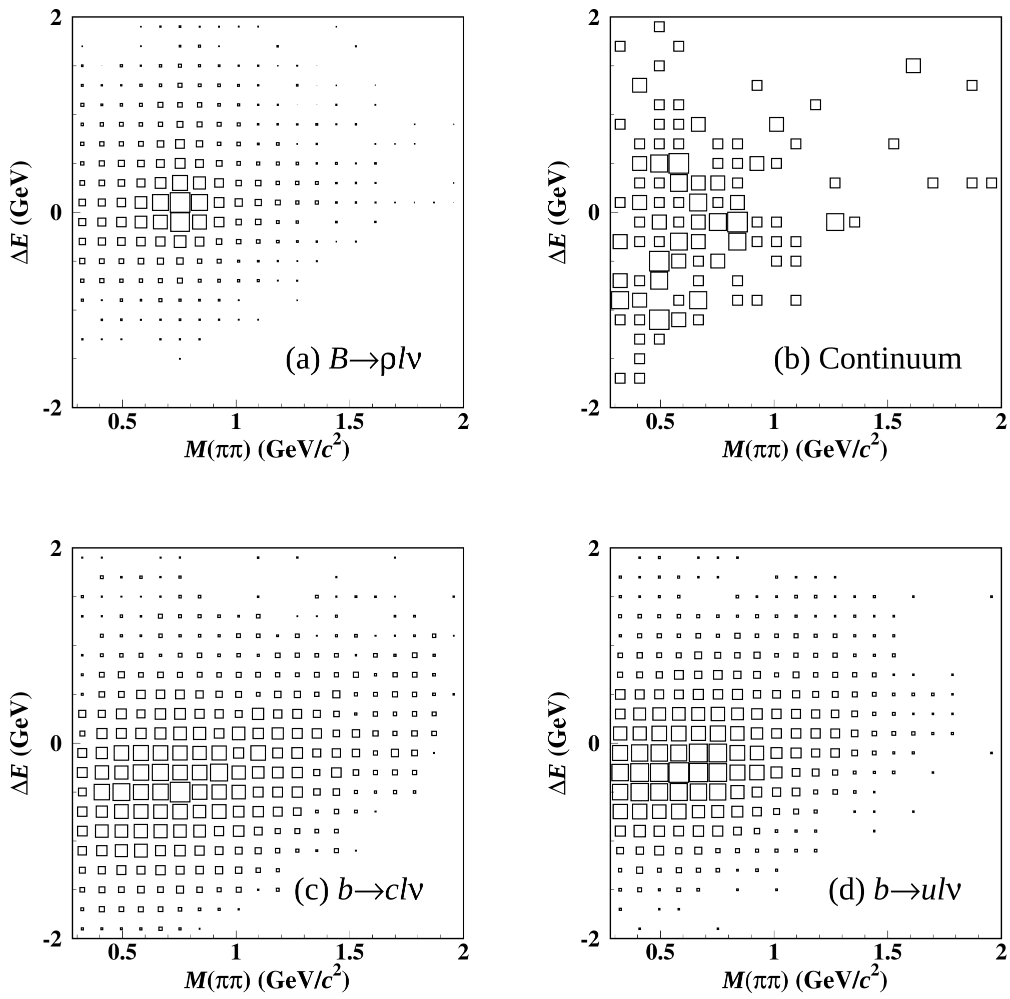

Figure 8.1: Signal and background ΔE vs. $M(\pi\pi)$ distributions for the combined $\pi^{\pm}\pi^{0}$ and $\pi^{+}\pi^{-}$ modes in HILEP: (a) the direct signal contribution; background events from (b) the continuum; (c) $b \to c\ell\nu$ events; (d) $b \to u\ell\nu$ events. The continuum contribution is modeled using the off-resonance data, while the other contributions are taken from Monte Carlo samples. Signal events are centered on $\Delta E = 0$ and are clustered around the ρ mass in $M(\pi\pi)$.

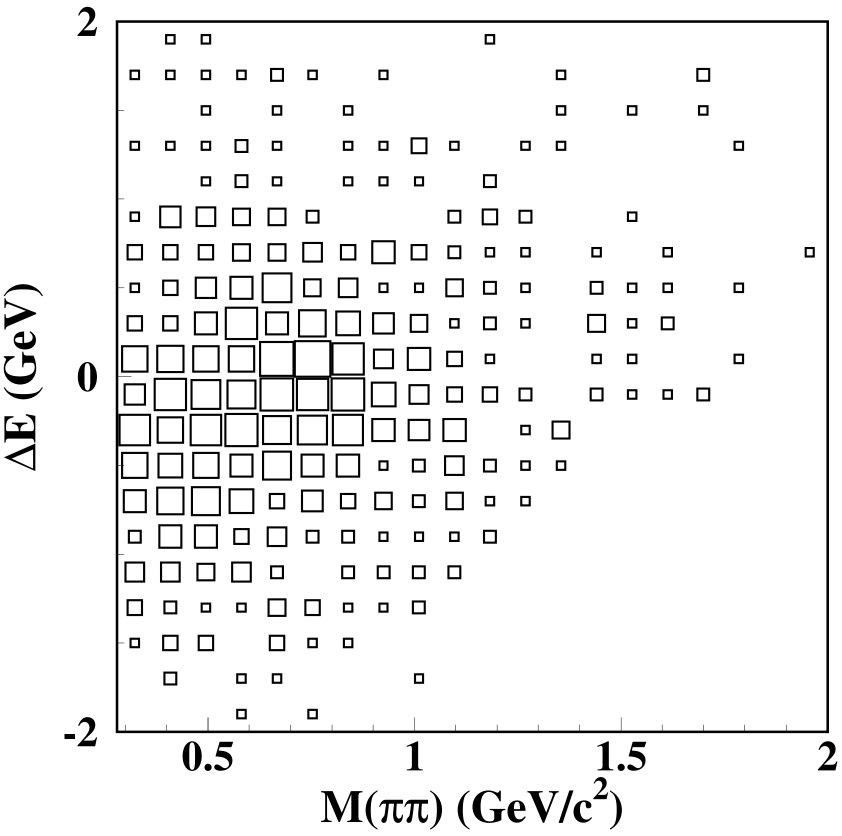

Figure 8.2: ΔE vs. $M(\pi\pi)$ distributions of the on-resonance data for the combined $\pi^{\pm}\pi^{0}$ and $\pi^{+}\pi^{-}$ modes in HILEP.

signal is determined using Monte Carlo simulation. These events are misreconstructed signal decays and their kinematic distributions can be somewhat different from direct signal events.

Isospin and quark-model relations are used to constrain the relative normalizations of $B^0 \to \rho^- \ell^+ \nu$, $B^+ \to \rho^0 \ell^+ \nu$, and $B^+ \to \omega \ell^+ \nu$ and, separately, those of $B^0 \to \pi^- \ell^+ \nu$ and $B^+ \to \pi^0 \ell^+ \nu$. Isospin symmetry implies that

$$\begin{aligned} \Gamma(B^0 \to \rho^- \ell^+ \nu) &= 2\Gamma(B^+ \to \rho^0 \ell^+ \nu), \\ \Gamma(B^0 \to \pi^- \ell^+ \nu) &= 2\Gamma(B^+ \to \pi^0 \ell^+ \nu), \end{aligned} \tag{8.2.1}$$

while the ω and ρ^0 wave functions are expected to be very similar in the quark model, giving

$$\Gamma(B^+ \to \rho^0 \ell^+ \nu) = \Gamma(B^+ \to \omega \ell^+ \nu). \tag{8.2.2}$$

Possible isospin breaking effects are discussed in Chapter 11.4 and Ref. [76]. We assume that the $\Upsilon(4S)$ decays only to $B\bar{B}$ in equal proportions of $B^0\bar{B}^0$ and B^+B^- mesons ($f_{+-}/f_{00} = 1.0 \pm 0.1$). We also use the value $\tau_{B^+}/\tau_{B^0} = 1.04 \pm 0.04$ [32] for the ratio of charged to neutral B-meson lifetimes.

8.3 Continuum background

The shape and normalization of the continuum background are measured using the off-resonance data sample. The statistical fluctuations in the off-resonance sample are accounted for by fitting the on- and off-resonance samples simultaneously, accounting for the difference in luminosity and cross section. For each bin in the fit, the mean number of continuum background events is determined so as to maximize the combined likelihood. This simultaneous fit will be described below.

8.4 $b \to c\ell\nu$ background

The normalization of the $b \to c\ell\nu$ background is determined to a large extent from the data. A mix of resonant and non-resonant final states, as described in Chapter 6.6, is used to describe this contribution. This background arises primarily from two extensively studied decays, $B \to D\ell\nu$ and $B \to D^*\ell\nu$, and the associated kinematic distributions are well known. As for the signal modes, the shapes of the ΔE vs. $M_{\rm had}$ distributions due to $b \to c\ell\nu$ are obtained using the Monte Carlo calculations. With these constraints, there remain 15 $b \to c\ell\nu$ normalization parameters, one for each of the five signal modes in each of three lepton-energy bins.

In our fit, there are in fact only seven free parameters associated with the $b \to c\ell\nu$ background, defined in the following way. Five of the parameters, one for each signal mode, are scale factors that give the overall normalization of the $b \to c\ell\nu$ background relative to that expected from the Monte Carlo simulation. Two additional parameters describe the ratios of scale factors among the three lepton-energy bins. A common set of ratios is used for all five modes, so we have two rather than 2×5 parameters for the $b \to c\ell\nu$ lepton energy spectrum. The reason for this choice is that the same set of background modes, dominated by $B \to D^*\ell\nu$ and $B \to D\ell\nu$, contributes to each of the five signal modes. The relative contributions of the different $b \to c\ell\nu$ modes are essentially independent of the $b \to u\ell\nu$ mode we reconstruct. In Chapter. 9, we show that our fit results for all seven of these $b \to c\ell\nu$ background parameters agree well with Monte Carlo predictions.

8.5 $B \to \pi\ell\nu$ events

The normalization for the contribution from $B \to \pi\ell\nu$ decay is also determined by the data. As for the signal contribution, form-factor models are used to describe the kinematic distributions. A systematic error is assigned based on the variation observed in the $B \to \rho\ell\nu$ fit results for different $B \to \pi\ell\nu$

form-factor models.

8.6 $b \to u\ell\nu$ background

The ISGW2 [17] predictions are used to model the distributions of $b \to u\ell\nu$ sources other than $B \to \rho\ell\nu$, $B \to \omega\ell\nu$, and $B \to \pi\ell\nu$ for resonances up to the $\rho(1450)$. The dominant resonances are η, b_1, and a_1. The relative normalization of each resonant contribution is listed in Chapter 6.5. The uncertainty on the composition of this background is considered as a systematic error. To reduce this systematic uncertainty, we allow for a separate normalization for the $b \to u\ell\nu$ component in each lepton-energy bin.

8.7 Fake lepton background

The small contribution from fake leptons is found using the data. The shapes of the ΔE vs. $M(\pi\pi)$ distribution, along with that of E_ℓ, are found by combining ρ candidates with charged tracks not identified as leptons. These combinations are required to pass all analysis criteria except for the lepton-identification requirements. The normalization of the fake-lepton component is determined by measurements of the probability for hadrons to satisfy the lepton identification requirements using π, K, and p samples from the data (see Chapter 7).

8.8 Likelihood function and $\mathcal{B}(B \to \rho\ell\nu)$

There are thus twelve free parameters in the fit:

- $\mathcal{B}(B \to \rho\ell\nu)$ (1 parameter).
- $\mathcal{B}(B \to \pi\ell\nu)$ (1 parameter).
- The yield of $b \to u\ell\nu$ events in each lepton-energy bin (3 parameters).

- The seven parameters that describe the normalization of the $b \to c\ell\nu$ contribution.

We do not include a contribution from $B \to \pi\pi\ell\nu$ nonresonant events in our fit. Instead, we use the data to constrain the size of this contribution and assign a systematic error (see Chapter 10).

We now describe the likelihood function that is maximized in order to determine the values of the above fit parameters. We consider both the on-resonance data and the off-resonance data jointly and write

$$\begin{aligned} \mathcal{L} &\equiv \prod_i^{N_{\rm bin}} \mathcal{L}_i(\mathrm{on-res.}) \times \mathcal{L}_i(\mathrm{off-res.}) \\ &= \prod_i^{N_{\rm bin}} \frac{(\mu_{B\bar{B},i} + s\mu_{c,i})^{N_{4S,i}}}{N_{4S,i}!} e^{-(\mu_{B\bar{B},i}+s\mu_{c,i})} \times \frac{\mu_{c,i}^{N_{c,i}}}{N_{c,i}!} e^{-\mu_{c,i}}. \end{aligned} \tag{8.8.1}$$

where

- $N_{4S,i}$ is the number of on-resonance data events in the ith bin.
- $N_{c,i}$ is the number of off-resonance data events in the ith bin.
- s is the ratio of on-resonance to off-resonance luminosities.
- $\mu_{B\bar{B},i}$ is the mean of the parent distribution of $B\bar{B}$ events in the ith bin. (the sum of the signal, crossfeed, $B \to \pi\ell\nu$, $b \to u\ell\nu$ (modes other than ρ, ω, or π), $b \to c$, and fake lepton contribtuions)
- $\mu_{c,i}$ is the (unknown) mean of the parent distribution of the off-resonance events in the ith bin.

The parent distribution for $B\bar{B}$ events is specified, at each iteration of the fit, as a sum of the contributions from $B \to \rho(\omega)\ell\nu$, $B \to \pi\ell\nu$, $b \to u\ell\nu$ feeddown, $b \to c\ell\nu$, and fake lepton events. The shapes of their distributions are taken from Monte Carlo and are assumed (apart from studies of systematic errors) to be exactly known. In contrast, the continuum event distributions are poorly known, due to the small number of off-resonance events passing the analysis cuts. This is why the fit is structured differently for the continuum background. In each bin, for a given $B\bar{B}$ parent distribution (a fixed $\mu_{B\bar{B},i}$), we can find the $\mu_{c,i}$ which minimizes the negative log likelihood by calculating the derivative of the negative log likelihood with respect to $\mu_{c,i}$.

$$\frac{\partial(-\ln\mathcal{L})}{\partial\mu_{c,i}} = -\frac{sN_{4S,i}}{\mu_{B\bar{B},i} + s\mu_{c,i}} + s - \frac{N_{c,i}}{\mu_{c,i}} + 1 = 0 \tag{8.8.2}$$

$$0 = (s)(s+1){\mu_{c,i}}^2 + ((1+s)\mu_{B\bar{B},i} - s(N_{4S,i} + N_{c,i}))\mu_{c,i} - N_{c,i}\mu_{B\bar{B},i} \tag{8.8.3}$$

$$\begin{aligned}\mu_{c,i} &= \frac{-((1+s)\mu_{B\bar{B},i} - s(N_{4S,i} + N_{c,i}))}{2(s)(s+1)} \\ &\pm \frac{\sqrt{((1+s)\mu_{B\bar{B},i} - s(N_{4S,i} + N_{c,i}))^2 + 4(s)(s+1)N_{c,i}\mu_{B\bar{B},i}}}{2(s)(s+1)}\end{aligned} \tag{8.8.4}$$

The positive solution for $\mu_{c,i}$ is always taken. In each bin, given a $\mu_{B\bar{B},i}$, we can solve for the value of $\mu_{c,i}$ which in turn minimizes the negative log likelihood. We iterate this process until we find the $\mu_{B\bar{B}}$ (what we are really interested in) which minimizes the negative log likelihood. Writing the likelihood in this way allows us to properly account for the errors on the off-resonance data. As described in Chapter 10.7 we have performed Monte Carlo studies to confirm that this likelihood fit method is unbiased.

8.9 $|V_{ub}|$ measurement

The $\mathcal{B}(B \to \rho\ell\nu)$ result from the likelihood fit is used to compute

$$|V_{ub}| = \sqrt{\frac{\mathcal{B}}{\tilde{\Gamma}_{\text{thy}}\tau_{B^0}}}. \tag{8.9.1}$$

$\mathcal{B}$ is the result for the $B^0 \to \rho^- \ell^+ \nu$ branching fraction from the likelihood fit, which depends on the form-factor model used to describe the signal distributions. Results for $\tilde{\Gamma}_{\rm thy}$ are given for each of the five form-factor models in Table 3.3. We use $\tau_{B^0} = 1.56 \pm 0.04$ ps [32].

8.10 $\Delta\Gamma$ measurement

The likelihood fit results are also used to measure the q^2 distribution in $B \to \rho\ell\nu$ decay. The large $b \to c\ell\nu$ backgrounds in LOLEP limit this measurement to the HILEP lepton-energy region. To determine the q^2 distribution, we consider events in the $\pi^\pm\pi^0$ and $\pi^+\pi^-$ modes with $|M(\pi\pi) - M(\rho)| < 0.15$ GeV/c^2 and $|\Delta E| < 0.5$ GeV. The background contributions in each q^2 interval are estimated using the results of the likelihood fit. We count the number of events in the background samples and subtract them from the data. Below we discuss the determination of q^2 for each event and describe the extraction of the q^2 distribution.

If the B meson momentum vector were known, q^2 could be determined unambiguously from the energy of the daughter hadron. For $B \to \rho\ell\nu$,

$$q^2 = M_B^2 + M_\rho^2 - 2E_B E_\rho + 2\mathbf{p}_B \cdot \mathbf{p}_\rho. \tag{8.10.1}$$

We know the magnitude of the B momentum, but not its direction, which introduces an uncertainty in q^2. Using the beam-energy constraint, we compute the minimum and maximum allowed q^2 values for each ρ+ℓ combination. These correspond to the kinematic configurations where the B momentum direction is closest to, or furthest from, the ρ momentum direction. The midpoint of the allowed q^2 range is our estimate of q^2. The q^2 resolution function is shown in Fig. 8.3.

To find the true q^2 distribution from the data, we must determine the efficiency of our analysis requirements as a function of q^2, including the smearing effects shown in Fig. 8.3. We perform this measurement in three equal bins of q^2. Monte Carlo simulation is used to compute the efficiency of events generated with a particular q^2 to be reconstructed at a different value of q^2. This efficiency matrix is computed for each of the five form-factor models that we consider; model dependence arises primarily from the efficiency of the $E_\ell > 2.3$ GeV requirement. The reconstructed q^2 distribution of the HILEP data and this efficiency matrix are used to determine the true q^2 distribution.

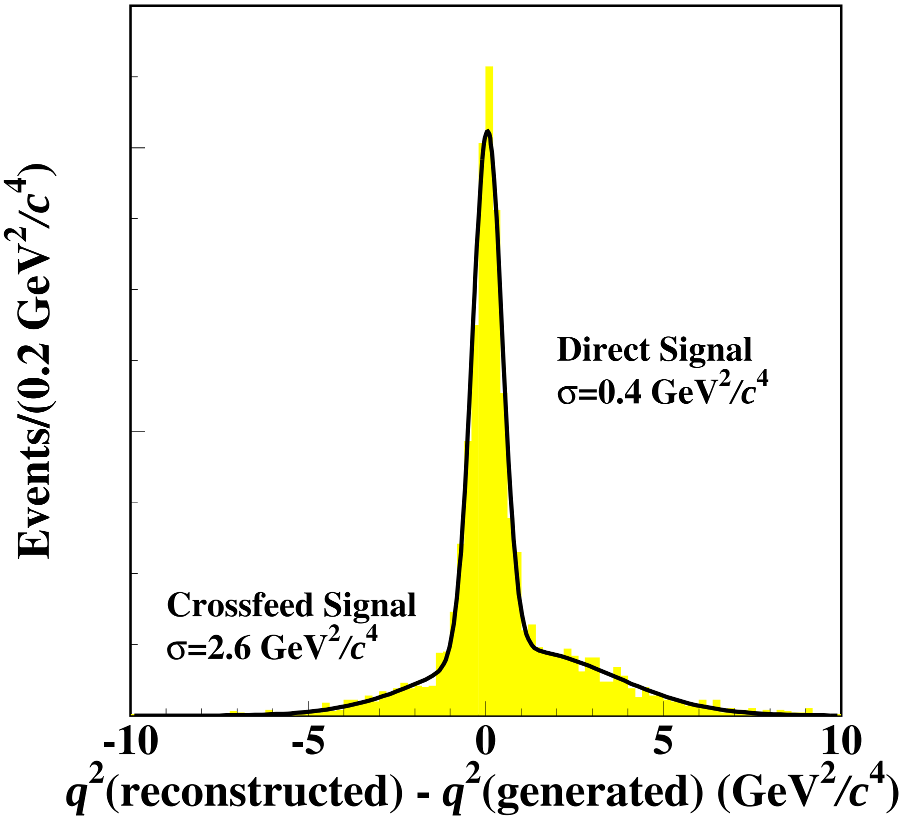

Figure 8.3: The q^2 resolution for signal Monte Carlo events. The curve shows a fit to the Monte Carlo events (shaded histogram) using two Gaussians. The narrow ($\sigma = 0.4$ GeV$^2/c^4$) component is due to events where the correct hadronic mode is reconstructed. The broader ($\sigma = 2.6$ GeV$^2/c^4$) component is from crossfeed events. We account for this smearing in our measurement of $\Delta\Gamma$ in bins of q^2. The full q^2 range for $B \to \rho\ell\nu$ is $\Delta q^2 \approx 21$ GeV$^2/c^4$.

Chapter 9

Fit results

9.1 Yields and residuals

The signal and background yields extracted from the fit in HILEP, LOLEP and LOLOLEP are shown in Tables 9.1 to 9.6 for the $\pi\pi$ and $\pi^+\pi^-\pi^0$ modes. The signal yields for the combined $\pi^+\pi^0$ and $\pi^+\pi^-$ modes in HILEP, where our sensitivity to the signal is best, are 123 ± 18 (direct) and 93 ± 14 (crossfeed), for a total of 216 ± 32 signal events. The five $b \to c\ell\nu$ normalization scale factors are consistent with Monte Carlo predictions to better than 5%. The two scale factor ratios that determine the lepton-energy distribution for the $b \to c\ell\nu$ contribution are within one standard deviation of unity. The $b \to u\ell\nu$ (modes other than $B \to \rho\ell\nu$, $B \to \omega\ell\nu$, and $B \to \pi\ell\nu$) normalizations in the three lepton-energy bins agree with each other to better than 20%, within one standard deviation, indicating that the ISGW2 cocktail of $b \to u\ell\nu$ modes is adequate, at least to within our sensitivity.

In addition, the above tables show the overall direct-signal efficiency of our selection criteria for each of the form-factor models used in this analysis. For the HILEP $\rho^\pm$ mode, this efficiency is between 2.6% and 4.0%. Recall that direct signal corresponds to signal events that are reconstructed in the correct mode. Thus, for the ISGW2 model, 4.0% is the fraction of the total number of $B \to \rho^\pm\ell\nu$ Monte Carlo events that are reconstructed in the $\pi^\pm\pi^0$ mode with a lepton whose energy is greater than 2.3 GeV.

Because there is a significant rate of misconstructed signal events, the efficiency for a generated signal event to be considered in the final fit is somewhat higher. In particular, there are three possibilities for misreconstructing a $B \to \rho^{\pm}\ell\nu$ event. First, such an event can be reconstructed in either the $\pi^+\pi^-$ or $\pi^+\pi^-\pi^0$ modes. This contribution is called crossfeed. Also, $B \to \rho^{\pm}\ell\nu$ events can be reconstructed in either of the π modes. These events are called background when fitting for the size of the $B \to \pi\ell\nu$ contribution. Nevertheless, these events are treated as $B \to \rho\ell\nu$ signal events in the fit. Finally, it is possible to reconstruct $B \to \rho^{\pm}\ell\nu$ events in the $\pi^{\pm}\pi^0$ mode, but with charged track or γ candidates that are not due to the true signal tracks. This contribution makes up a small part of the direct signal. For $B \to \rho^{\pm}\ell\nu$ Monte Carlo events approximately 1/3 of the events that pass all selection requirements are counted as direct signal.

Figures 9.1 to 9.4 show the fit residuals for the combined $\pi\pi$ modes in HILEP, LOLEP, and LOLOLEP, as well as the fit residuals for the $\pi^{=}\pi^-\pi^0$ mode in HILEP. We observe good agreement between the data and fit in each of these plots.

9.2 Fit projections

We show projections of the fit in both signal- and background-dominated regions of the ΔE vs. $M(\pi\pi)$ distributions. Figures 9.5, 9.6, and 9.7 show HILEP and LOLEP projections onto $M(\pi\pi)$ for $|\Delta E| < 0.5$ GeV and onto ΔE for $|M(\pi\pi) - M(\rho)| < 0.15$ GeV/c^2. We observe a significant $B \to \rho\ell\nu$ signal in the $M(\pi\pi)$ and ΔE distributions in HILEP. Figures 9.9 and 9.10 show the same distributions for sidebands with $|\Delta E| > 0.5$ GeV and $|M(\pi\pi) - M(\rho)| > 0.15$ GeV/c^2, where we expect much less signal. In both signal- and background-dominated distributions, we observe good agreement between the data and the fit projections. In the projections shown, the signal component is modeled using the ISGW2 form-factor model, and the continuum contribution

	$\rho^\pm$	ρ^0	ω
Υ(4S) yield	198	621	460
$e^+e^- \to q\bar{q}$ bkg.	63 ± 11	248 ± 22	250 ± 22
$b \to c\ell\nu$ bkg.	39 ± 5	90 ± 7	52 ± 5
fake lepton bkg.	4 ± 2	13 ± 7	10 ± 5
$b \to u\ell\nu$ feeddown bkg.	25 ± 10	57 ± 23	43 ± 17
$B \to \pi\ell\nu$ bkg.	9 ± 3	20 ± 6	4 ± 1
Signal yield	56 ± 8	67 ± 10	21 ± 3
Xfeed yield	13 ± 2	80 ± 12	32 ± 5

Table 9.1: Summary of data yields for the $\rho^\pm$, ρ^0, and ω modes with lepton energies between 2.3 and 2.7 GeV (HILEP). Yields of the background contributions are insensitive to the form-factor model used to model $B \to \rho\ell\nu$ events; the yields presented in this table were obtained using the UKQCD model. The $b \to u\ell\nu$ background includes all $B \to X_u\ell\nu$ modes except for ρ, ω, and π. The crossfeed (Xfeed) signal contribution corresponds to events from one vector mode passing the selection cuts of another vector mode ($\rho^0\ell\nu \leftrightarrow \rho^\pm\ell\nu$ or $\rho\ell\nu \leftrightarrow \omega\ell\nu$) and is constrained to the signal in the fit. All errors are statistical only. The errors on the direct and crossfeed signal yields are completely correlated, as are those on the yields of $B \to \pi\ell\nu$ events. Errors on the $b \to u\ell\nu$ background are completely correlated among modes, but not between HILEP and LOLEP.

	$\rho^\pm$	ρ^0	ω
Υ(4S) yield	2249	7298	8552
$e^+e^- \to q\bar{q}$ bkg.	127 ± 16	398 ± 28	437 ± 29
$b \to c\ell\nu$ bkg.	1941 ± 47	6419 ± 114	7804 ± 129
fake lepton bkg.	11 ± 7	35 ± 21	44 ± 22
$b \to u\ell\nu$ feeddown bkg.	97 ± 24	222 ± 57	236 ± 60
$B \to \pi\ell\nu$ bkg.	15 ± 5	32 ± 10	6 ± 2
Signal yield (UKQCD)	61 ± 9	79 ± 12	31 ± 5
Xfeed yield (UKQCD)	23 ± 3	100 ± 15	52 ± 8

Table 9.2: Summary of data yields for the $\rho^\pm$, ρ^0, and ω modes with lepton energies between 2.0 and 2.3 GeV (LOLEP). Yields of the background contributions are insensitive to the form-factor model used to model $B \to \rho\ell\nu$ events; the yields presented in this table were obtained using the UKQCD model. The $b \to u\ell\nu$ background includes all $B \to X_u\ell\nu$ modes except for ρ, ω, and π. The crossfeed (Xfeed) signal contribution corresponds to events from one vector mode passing the selection cuts of another vector mode ($\rho^0\ell\nu \leftrightarrow \rho^\pm\ell\nu$ or $\rho\ell\nu \leftrightarrow \omega\ell\nu$) and is constrained to the signal in the fit. All errors are statistical only. The correlations between errors are described in Table 9.1.

	$\rho^\pm$	ρ^0	ω
Υ(4S) yield	4755	14904	23506
$e^+e^- \to q\bar{q}$ bkg.	121 ± 15	393 ± 28	574 ± 47
$b \to c\ell\nu$ bkg.	4416 ± 108	14183 ± 254	22544 ± 372
fake lepton bkg.	28 ± 14	79 ± 39	160 ± 80
$b \to u\ell\nu$ feeddown bkg.	108 ± 28	251 ± 65	356 ± 92
$B \to \pi\ell\nu$ bkg.	10 ± 3	20 ± 6	7 ± 2
Signal yield (UKQCD)	29 ± 4	36 ± 5	21 ± 3
Xfeed yield (UKQCD)	9 ± 1	42 ± 6	30 ± 5

Table 9.3: Summary of data yields for the $\rho^\pm$, ρ^0, and ω modes with lepton energies between 1.7 and 2.0 GeV (LOLOLEP). Yields of the background contributions are insensitive to the form-factor model used to model $B \to \rho\ell\nu$ events; the yields presented in this table were obtained using the UKQCD model. The $b \to u\ell\nu$ background includes all $B \to X_u\ell\nu$ modes except for ρ, ω, and π. The crossfeed (Xfeed) signal contribution corresponds to events from one vector mode passing the selection cuts of another vector mode ($\rho^0\ell\nu \leftrightarrow \rho^\pm\ell\nu$ or $\rho\ell\nu \leftrightarrow \omega\ell\nu$) and is constrained to the signal in the fit. All errors are statistical only. The correlations between errors are described in Table 9.1.

	$\rho^{\pm}$	ρ^{0}	ω
Signal eff. (ISGW2)	0.040	0.091	0.032
Signal yield (ISGW2)	58 ± 9	68 ± 10	21 ± 3
Xfeed yield (ISGW2)	14 ± 2	80 ± 12	34 ± 5
Signal eff. (LCSR)	0.026	0.061	0.022
Signal yield (LCSR)	56 ± 8	66 ± 10	21 ± 3
Xfeed yield (LCSR)	14 ± 2	80 ± 11	32 ± 5
Signal eff. (UKQCD)	0.031	0.070	0.025
Signal yield (UKQCD)	56 ± 8	67 ± 10	21 ± 3
Xfeed yield (UKQCD)	14 ± 2	80 ± 12	33 ± 5
Signal eff. (Wise/Ligeti+E791)	0.035	0.080	0.028
Signal yield (Wise/Ligeti+E791)	56 ± 8	66 ± 10	21 ± 3
Xfeed yield (Wise/Ligeti+E791)	14 ± 2	80 ± 12	32 ± 5
Signal eff. (Beyer/Melikhov)	0.029	0.067	0.024
Signal yield (Beyer/Melikhov)	55 ± 8	66 ± 10	21 ± 3
Xfeed yield (Beyer/Melikhov)	14 ± 2	80 ± 12	32 ± 5

Table 9.4: Summary of direct and crossfeed (Xfeed) signal yields for the $\rho^{\pm}$, ρ^{0}, and ω modes with lepton energies between 2.3 and 2.7 GeV (HILEP). Signal efficiencies are normalized to the number of events in the full lepton-energy range. The crossfeed contribution corresponds to events from one vector mode passing the selection cuts of another vector mode ($\rho^0\ell\nu \leftrightarrow \rho^{\pm}\ell\nu$ or $\rho\ell\nu \leftrightarrow \omega\ell\nu$) and is constrained to the signal in the fit. All errors are statistical only. Errors on the direct and crossfeed signal yields are completely correlated.

	$\rho^\pm$	ρ^0	ω
Signal eff. (ISGW2)	0.039	0.094	0.040
Signal yield (ISGW2)	55 ± 9	70 ± 11	26 ± 4
Xfeed yield (ISGW2)	20 ± 3	89 ± 13	48 ± 7
Signal eff. (LCSR)	0.030	0.076	0.034
Signal yield (LCSR)	64 ± 10	84 ± 13	33 ± 5
Xfeed yield (LCSR)	24 ± 3	105 ± 15	54 ± 8
Signal eff. (UKQCD)	0.033	0.083	0.036
Signal yield (UKQCD)	61 ± 9	79 ± 12	31 ± 5
Xfeed yield (UKQCD)	23 ± 3	100 ± 15	52 ± 8
Signal eff. (Wise/Ligeti+E791)	0.037	0.094	0.040
Signal yield (Wise/Ligeti+E791)	60 ± 9	79 ± 12	30 ± 4
Xfeed yield (Wise/Ligeti+E791)	24 ± 3	102 ± 15	52 ± 8
Signal eff. (Beyer/Melikhov)	0.033	0.083	0.036
Signal yield (Beyer/Melikhov)	61 ± 10	81 ± 12	31 ± 5
Xfeed yield (Beyer/Melikhov)	24 ± 3	104 ± 15	53 ± 8

Table 9.5: Summary of direct and crossfeed (Xfeed) signal yields for the $\rho^\pm$, ρ^0, and ω modes with lepton energies between 2.0 and 2.3 GeV (LOLEP). Signal efficiencies are normalized to the number of events in the full lepton-energy range. The crossfeed contribution corresponds to events from one vector mode passing the selection cuts of another vector mode ($\rho^0\ell\nu \leftrightarrow \rho^\pm\ell\nu$ or $\rho\ell\nu \leftrightarrow \omega\ell\nu$) and is constrained to the signal in the fit. All errors are statistical only. Errors on the direct and crossfeed signal yields are completely correlated.

	$\rho^{\pm}$	ρ^0	ω
Signal eff. (ISGW2)	0.015	0.035	0.024
Signal yield (ISGW2)	22 ± 3	26 ± 4	15 ± 2
Xfeed yield (ISGW2)	7 ± 1	30 ± 5	24 ± 4
Signal eff. (LCSR)	0.016	0.037	0.026
Signal yield (LCSR)	33 ± 5	41 ± 6	25 ± 4
Xfeed yield (LCSR)	10 ± 2	47 ± 7	33 ± 5
Signal eff. (UKQCD)	0.016	0.037	0.025
Signal yield (UKQCD)	29 ± 4	36 ± 5	21 ± 3
Xfeed yield (UKQCD)	9 ± 1	42 ± 6	30 ± 5
Signal eff. (Wise/Ligeti+E791)	0.017	0.039	0.026
Signal yield (Wise/Ligeti+E791)	27 ± 4	33 ± 5	19 ± 3
Xfeed yield (Wise/Ligeti+E791)	9 ± 1	41 ± 6	29 ± 4
Signal eff. (Beyer/Melikhov)	0.016	0.038	0.026
Signal yield (Beyer/Melikhov)	30 ± 5	37 ± 6	22 ± 3
Xfeed yield (Beyer/Melikhov)	10 ± 2	44 ± 7	31 ± 5

Table 9.6: Summary of direct and crossfeed (Xfeed) signal yields for the $\rho^{\pm}$, ρ^0, and ω modes with lepton energies between 1.7 and 2.0 GeV (LOLOLEP). Signal efficiencies are normalized to the number of events in the full lepton-energy range. The crossfeed contribution corresponds to events from one vector mode passing the selection cuts of another vector mode ($\rho^0\ell\nu \leftrightarrow \rho^{\pm}\ell\nu$ or $\rho\ell\nu \leftrightarrow \omega\ell\nu$) and is constrained to the signal in the fit. All errors are statistical only. Errors on the direct and crossfeed signal yields are completely correlated.

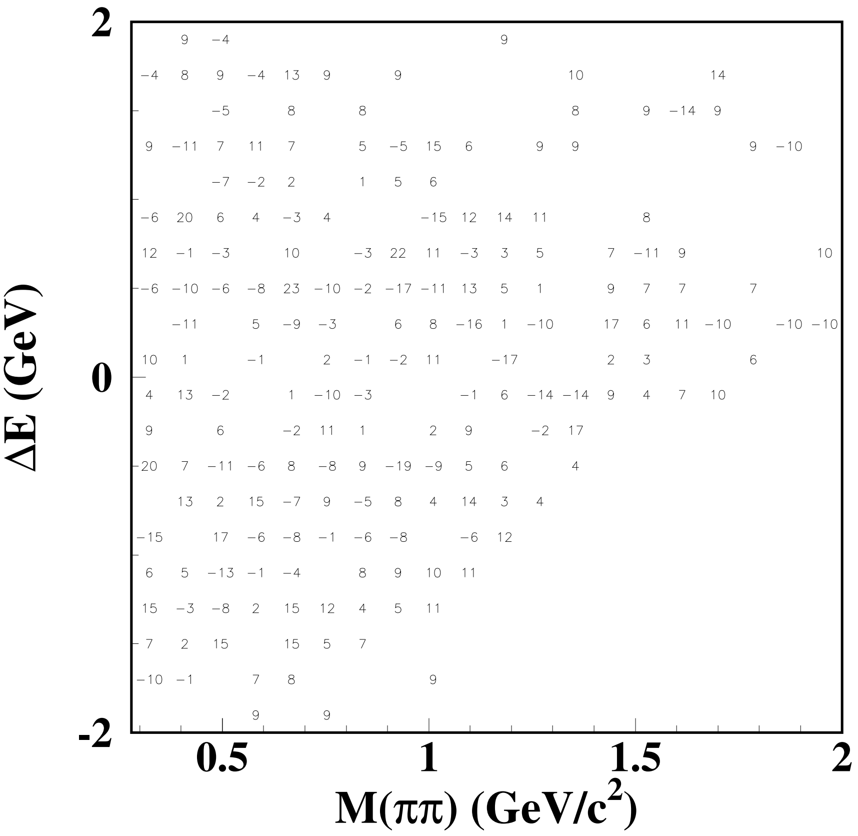

Figure 9.1: Residuals for the HILEP $\pi\pi$ modes. For each bin, $10(\text{data} - \text{fit})/\sigma$, where σ is the $\sqrt{n}$ error due to the statistics of the on-resonance and off-resonance data, is shown.

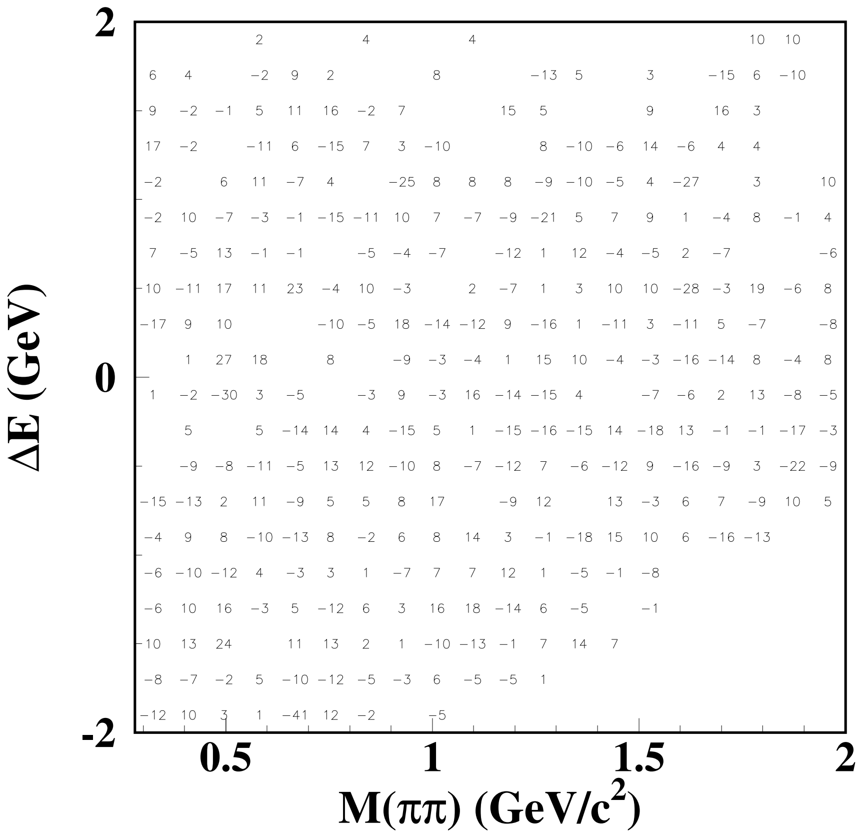

Figure 9.2: Residuals for the LOLEP $\pi\pi$ modes. For each bin, $10(\text{data}-\text{fit})/\sigma$, where σ is the $\sqrt{n}$ error due to the statistics of the on-resonance and off-resonance data, is shown.

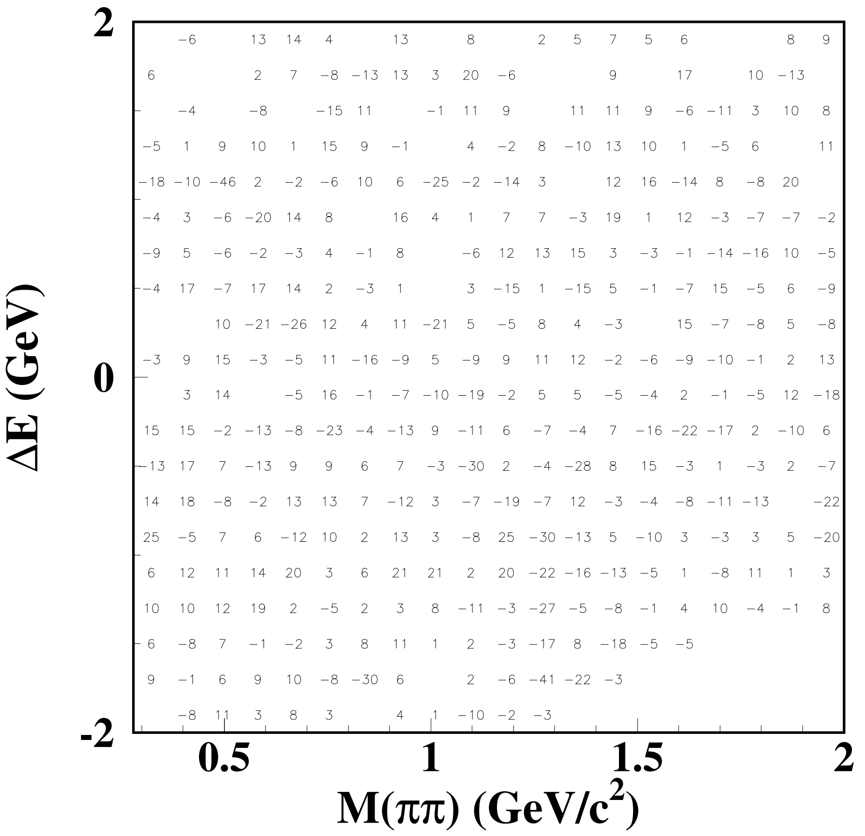

Figure 9.3: Residuals for the LOLOLEP $\pi\pi$ modes. For each bin, 10(data $-$ fit)$/\sigma$, where σ is the $\sqrt{n}$ error due to the statistics of the on-resonance and off-resonance data, is shown.

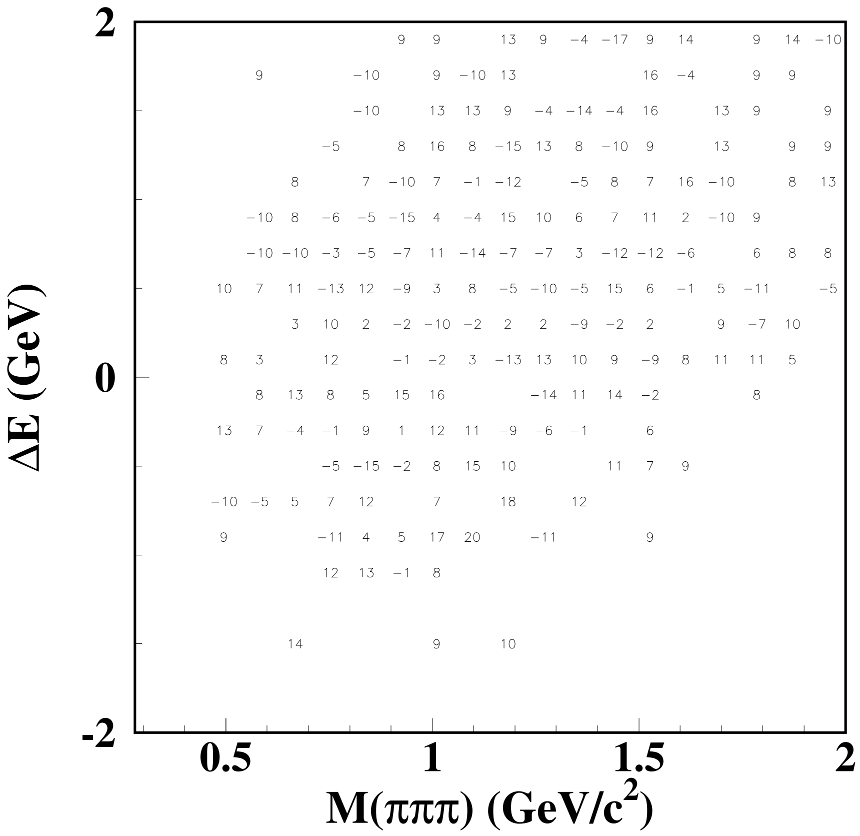

Figure 9.4: Residuals for the HILEP $\pi^+\pi^-\pi^0$ modes. For each bin, 10(data $-$ fit)$/\sigma$, where σ is the $\sqrt{n}$ error due to the statistics of the on-resonance and off-resonance data, is shown.

has been subtracted.

The $b \to c\ell\nu$ background is quite small in the HILEP plots but is dominant in all of the LOLEP projections. The peak in the LOLEP $\pi\pi$ modes at large $M(\pi\pi)$ is due to $B \to D\ell\nu$, with $D \to K\pi$, where the K has been misinterpreted as a pion. LOLEP sideband projections in Fig. 9.10 show that the shape of the $b \to c\ell\nu$ Monte Carlo distribution describes the data well in regions of the fit where the $b \to u\ell\nu$ contributions are small. In Fig. 9.7, the shape of the $M(\pi\pi)$ distribution in the LOLEP lepton-energy bin indicates that the $b \to u\ell\nu$ contributions are necessary to describe properly the data below the $b \to c\ell\nu$ lepton-energy endpoint region. We do not show fit projections for the data with $E_\ell < 2.0$ GeV, but the fit agrees well with the data in this region. The $b \to c\ell\nu$ Monte Carlo simulates $M(\pi\pi)$ and ΔE projections of the data well in both shape and normalization.

Figures 9.11, 9.12, and 9.13 show the reconstructed q^2 and lepton-energy distributions for the $\pi\pi$ modes with $|\Delta E| < 0.5$ GeV and $|M(\pi\pi) - M(\rho)| < 0.15$ GeV$/c^2$ requirements. We observe good agreement between the data and the q^2 distribution predicted in HILEP by the form-factor models. Also, the $b \to c\ell\nu$ Monte Carlo prediction agrees well with the q^2 distribution in the LOLEP and LOLOLEP data. The lepton-energy spectrum predicted from the fit results shows good agreement with the data over the full range of lepton-energy used ($E_\ell > 1.7$ GeV). A large excess in the lepton-energy spectrum, consistent with the fit projection, is observed above the continuum contribution in the region beyond the $b \to c\ell\nu$ lepton energy endpoint.

In the above projections, the $\pi^\pm\pi^0$ and $\pi^+\pi^-$ modes have been combined. Figure 9.14 shows the $M(\pi\pi)$ distribution with a $|\Delta E| < 0.5$ GeV requirement for these modes individually where the ratio of $\Gamma(B^0 \to \rho^-\ell^+\nu)$ to $\Gamma(B^+ \to \rho^0\ell^+\nu)$ has been allowed to float in the fit. We find $\Gamma(B^0 \to \rho^-\ell^+\nu)/\Gamma(B^+ \to \rho^0\ell^+\nu) = 1.7^{+1.0}_{-0.6}$, where the error is statistical only. This value is in good agreement with the isospin relation in Eq. 8.2.1, which is used to determine our final results.

In Fig. 9.15 we show the $M(\pi^+\pi^-\pi^0)$ plot for the HILEP lepton-energy bin.

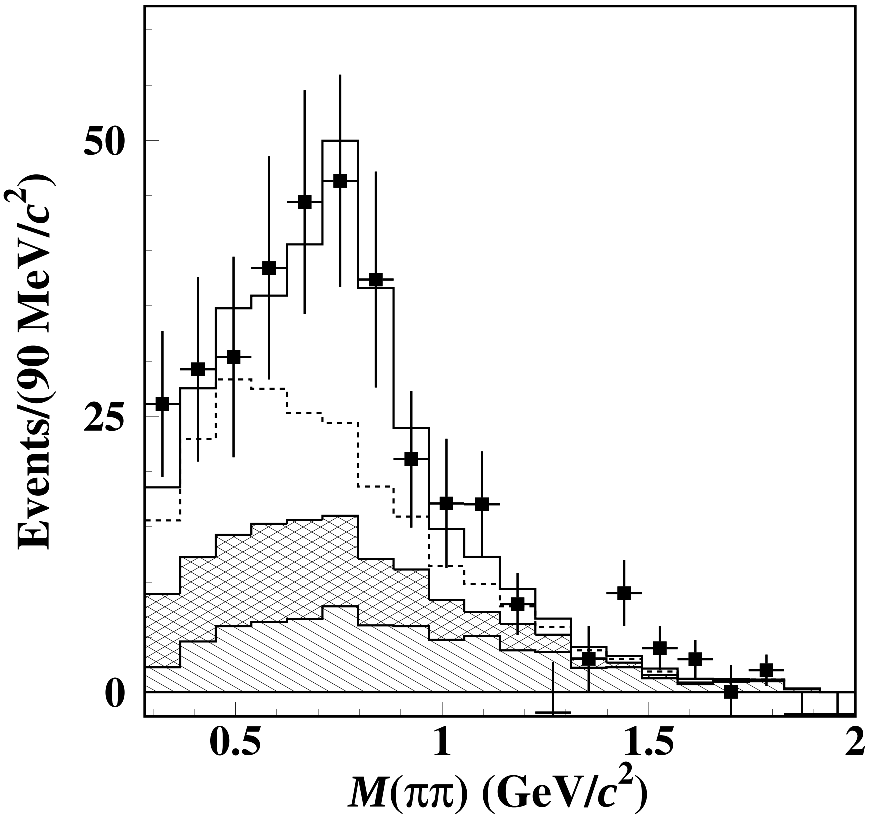

Figure 9.5: Projection of the fit onto $M(\pi\pi)$ after a $|\Delta E| < 0.5$ GeV cut for the combined HILEP ($E_\ell > 2.3$ GeV) $\pi^{\pm}\pi^0$ and $\pi^+\pi^-$ modes. The points with error bars show the on-resonance data after continuum background subtraction, while the histogram shows the projection of the fit. The contributions to the fit are the direct and cross-feed components of the signal (unhatched regions, above and below the dashed line, respectively); the background from $b \to u\ell\nu$ non-signal modes (double-hatched region); and the background from $b \to c\ell\nu$ (single-hatched region). The $b \to u\ell\nu$ background includes $B \to \pi\ell\nu$ contributions.

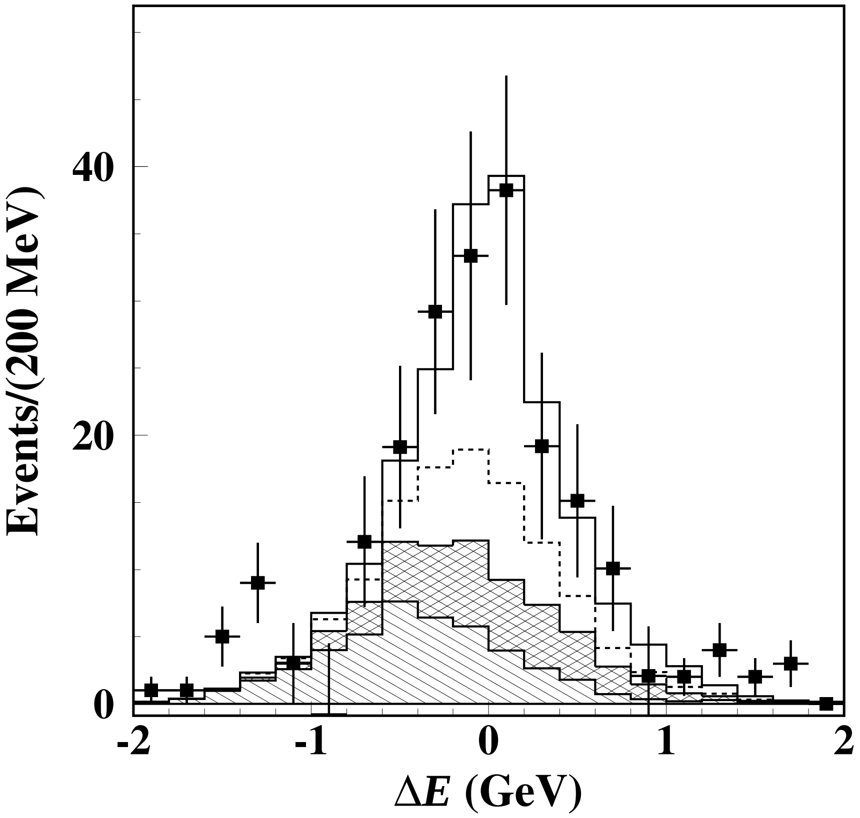

Figure 9.6: Projections of the fit onto ΔE after a $|M(\pi\pi) - M(\rho)| < 0.15\ \mathrm{GeV}/c^2$ cut for the combined HILEP ($E_\ell > 2.3$ GeV) $\pi^\pm\pi^0$ and $\pi^+\pi^-$ modes. The points with error bars show the on-resonance data after continuum background subtraction, while the histogram shows the projection of the fit. The contributions to the fit are the direct and cross-feed components of the signal (unhatched regions, above and below the dashed line, respectively); the background from $b \to u\ell\nu$ non-signal modes (double-hatched region); and the background from $b \to c\ell\nu$ (single-hatched region). The $b \to u\ell\nu$ background includes $B \to \pi\ell\nu$ contributions.

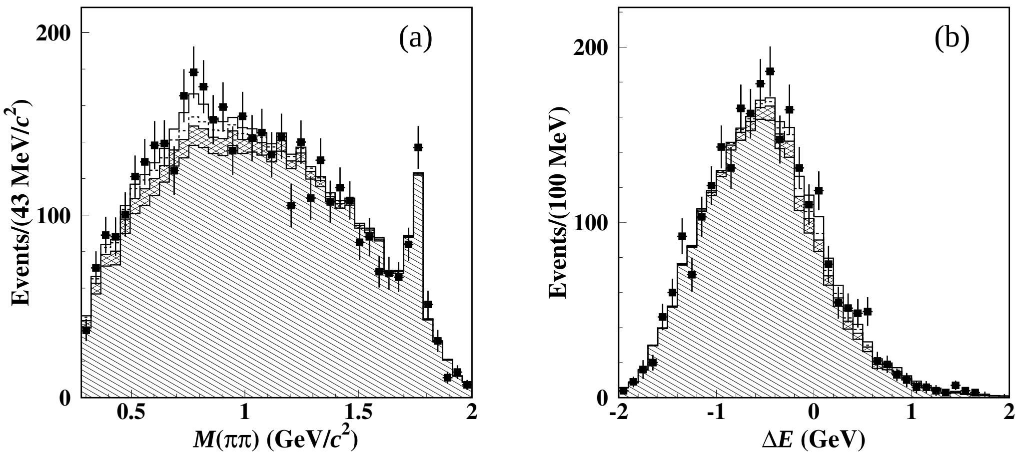

Figure 9.7: Projections of the fit for the $\rho^{\pm}$ and ρ^0 modes for LOLEP ($2.0 < E_\ell < 2.3$ GeV, lower plots): (a) $M(\pi\pi)$ after a $|\Delta E| < 0.5$ GeV cut and (b) ΔE after a $|M(\pi\pi) - M(\rho)| < 0.15$ GeV/c^2 cut. In each plot, the points with error bars show the on-resonance data after continuum background subtraction, while the histogram shows the projection of the fit. The contributions to the fit are the direct and cross-feed components of the signal (unhatched regions, above and below the dashed line, respectively); the background from $b \to u\ell\nu$ non-signal modes (double-hatched region); and the background from $b \to c\ell\nu$ (single-hatched region). The $b \to u\ell\nu$ background includes $B \to \pi\ell\nu$ contributions.

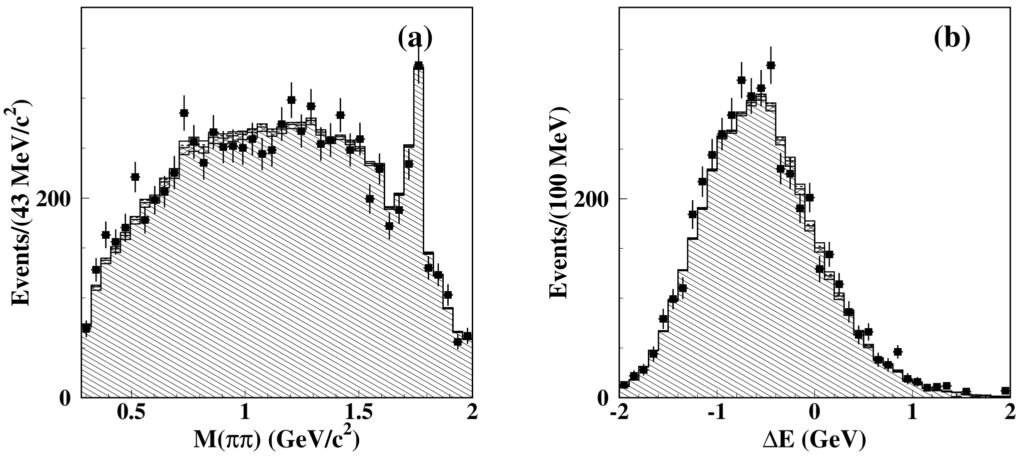

Figure 9.8: Projections of the fit for the combined $\rho^{\pm}$ and ρ^{0} modes in LOLOLEP ($1.7 < E_{\ell} < 2.0$ GeV, lower plots): (a) $M(\pi\pi)$ after a $|\Delta E| < 0.5$ GeV cut and (b) ΔE after a $|M(\pi\pi) - M(\rho)| < 0.15$ GeV$/c^2$ cut. In each plot, the points with error bars show the on-resonance data after continuum background subtraction, while the histogram shows the projection of the fit. The contributions to the fit are the direct and cross-feed components of the signal (unhatched regions, above and below the dashed line, respectively); the background from $b \to u\ell\nu$ non-signal modes (double-hatched region); and the background from $b \to c\ell\nu$ (single-hatched region). The $b \to u\ell\nu$ background includes $B \to \pi\ell\nu$ contributions.

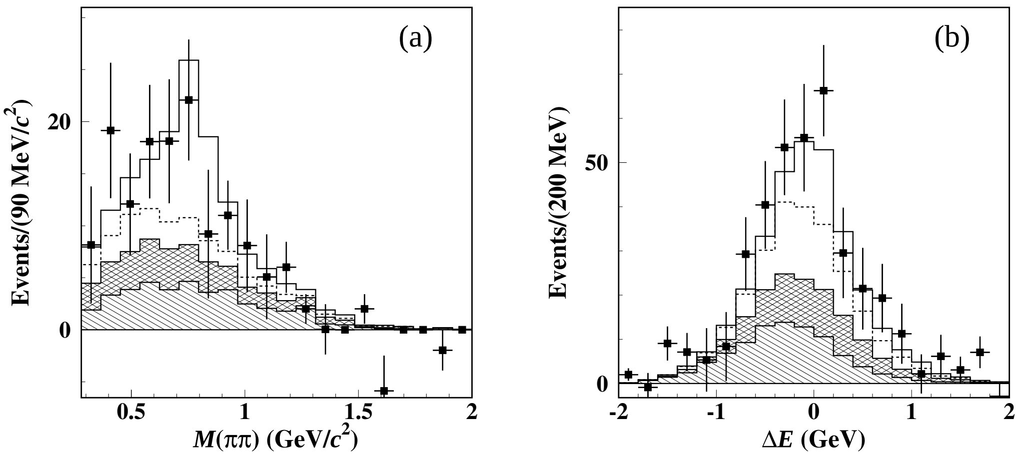

Figure 9.9: Projections of the fit for the combined $\rho^{\pm}$ and ρ^0 modes in HILEP ($E_\ell > 2.3$ GeV): (a) $M(\pi\pi)$ for HILEP after a $|\Delta E| > 0.5$ GeV cut and (b) ΔE for HILEP after a $|M(\pi\pi) - M(\rho)| > 0.15$ GeV/c^2 cut has been applied. In each plot, the points with error bars show the on-resonance data after continuum background subtraction, while the histogram shows the projection of the fit. The contributions to the fit are the direct and cross-feed components of the signal (unhatched regions, above and below the dashed line, respectively); the background from $b \to u\ell\nu$ non-signal modes (double-hatched region); and the background from $b \to c\ell\nu$ (single-hatched region). The $b \to u\ell\nu$ background includes $B \to \pi\ell\nu$ contributions.

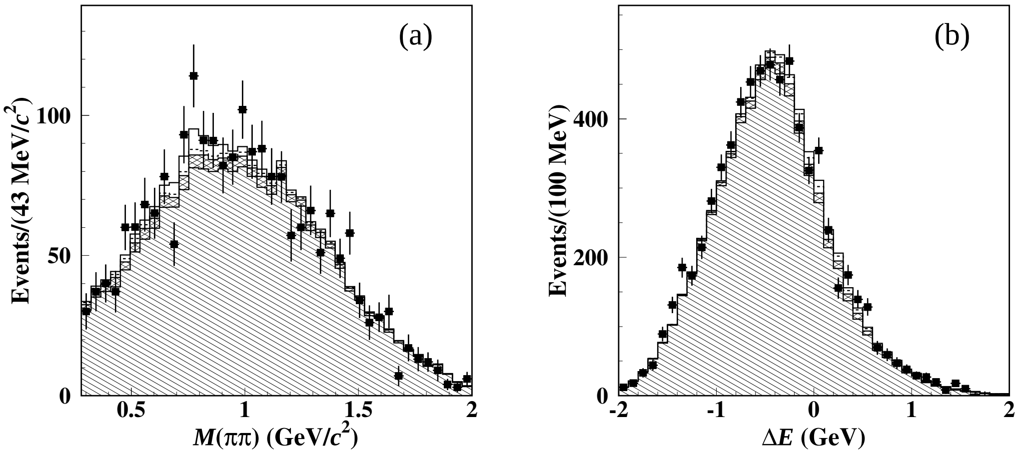

Figure 9.10: Projections of the fit for the combined $\rho^{\pm}$ and ρ^0 modes in LOLEP ($2.0 < E_\ell < 2.3$ GeV): (a) $M(\pi\pi)$ for LOLEP after a $|\Delta E| > 0.5$ GeV cut and (b) ΔE for LOLEP after a $|M(\pi\pi) - M(\rho)| > 0.15$ GeV/c^2 cut. In each plot, the points with error bars show the on-resonance data after continuum background subtraction, while the histogram shows the projection of the fit. The contributions to the fit are the direct and cross-feed components of the signal (unhatched regions, above and below the dashed line, respectively); the background from $b \to u\ell\nu$ non-signal modes (double-hatched region); and the background from $b \to c\ell\nu$ (single-hatched region). The $b \to u\ell\nu$ background includes $B \to \pi\ell\nu$ contributions.

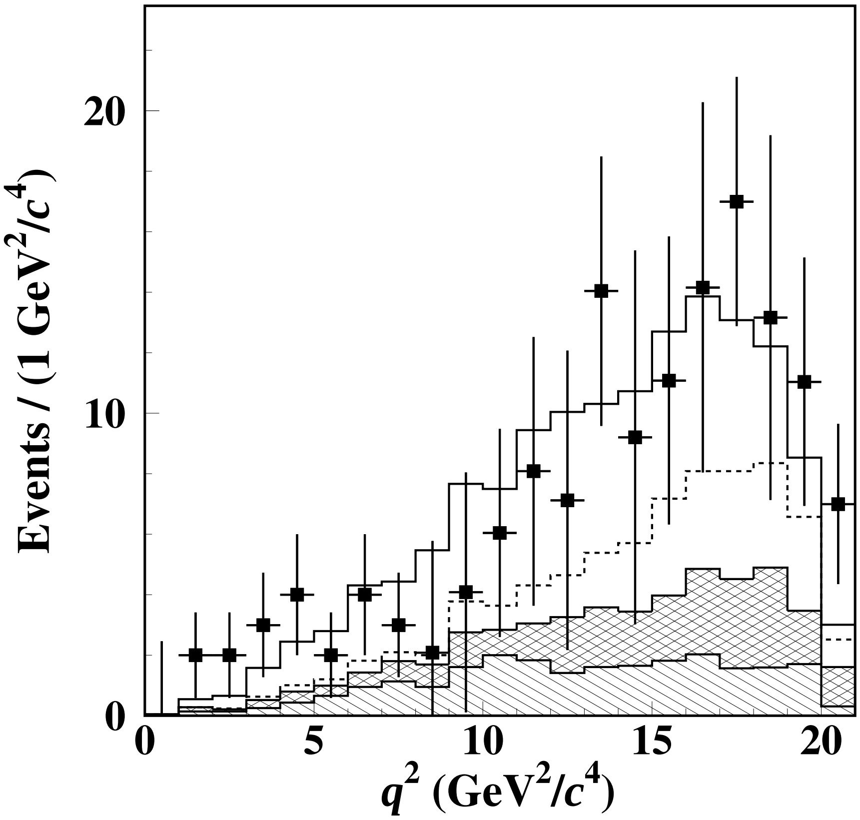

Figure 9.11: Projection of the kinematic variable q^2 for the combined $\rho^{\pm}$ and ρ^0 modes in HILEP ($E_\ell > 2.3$ GeV) for events with $|\Delta E| < 0.5$ GeV $|M(\pi\pi) - M(\rho)| < 0.15$ GeV/c^2. The points with error bars show the on-resonance data after continuum background subtraction, while the histogram shows the projection of the fit. The contributions to the fit are the direct and cross-feed components of the signal (unhatched regions, above and below the dashed line, respectively); the background from $b \to u\ell\nu$ non-signal modes (double-hatched region); and the background from $b \to c\ell\nu$ (single-hatched region). The $b \to u\ell\nu$ background includes $B \to \pi\ell\nu$ contributions.

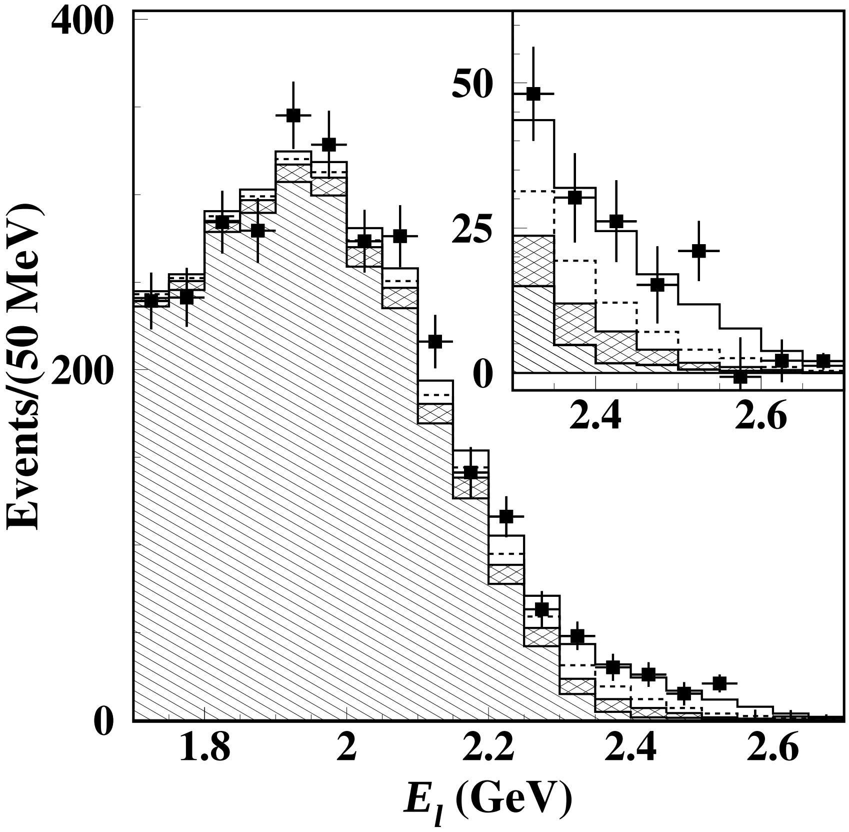

Figure 9.12: Projections of the kinematic variable E_ℓ for the combined $\rho^\pm$ and ρ^0 modes for events with $|\Delta E| < 0.5$ GeV $|M(\pi\pi) - M(\rho)| < 0.15$ GeV$/c^2$. The points with error bars show the on-resonance data after continuum background subtraction, while the histogram shows the projection of the fit. The contributions to the fit are the direct and cross-feed components of the signal (unhatched regions, above and below the dashed line, respectively); the background from $b \to u\ell\nu$ non-signal modes (double-hatched region); and the background from $b \to c\ell\nu$ (single-hatched region). The $b \to u\ell\nu$ background includes $B \to \pi\ell\nu$ contributions.

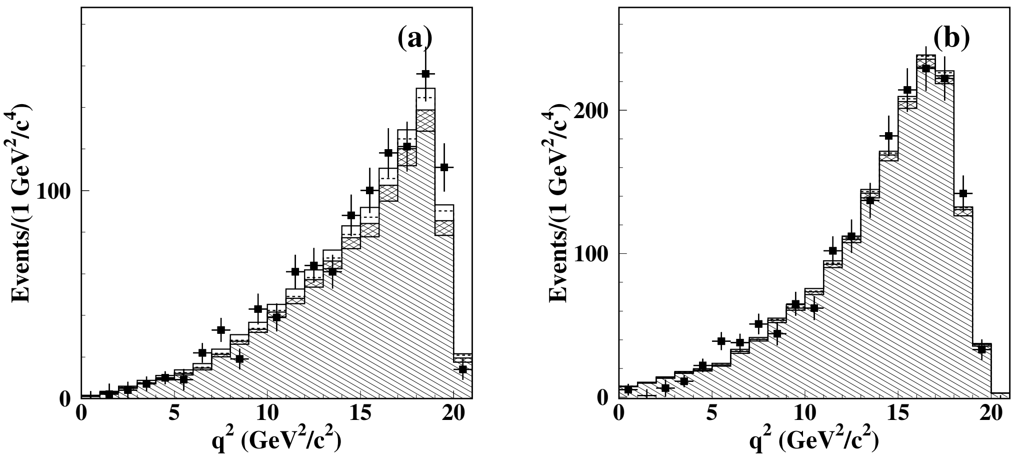

Figure 9.13: Projections of the kinematic variable q^2 for the combined $\rho^{\pm}$ and ρ^0 modes in the (a) LOLEP ($2.0 < E_\ell < 2.3$ GeV) and (b) LOLOLEP ($1.7 < E_\ell < 2.0$ GeV) lepton-energy bins for events with $|\Delta E| < 0.5$ GeV $|M(\pi\pi) - M(\rho)| < 0.15$ GeV$/c^2$. The points with error bars show the on-resonance data after continuum background subtraction, while the histogram shows the projection of the fit. The contributions to the fit are the direct and cross-feed components of the signal (unhatched regions, above and below the dashed line, respectively); the background from $b \to u\ell\nu$ non-signal modes (double-hatched region); and the background from $b \to c\ell\nu$ (single-hatched region). The $b \to u\ell\nu$ background includes $B \to \pi\ell\nu$ contributions.

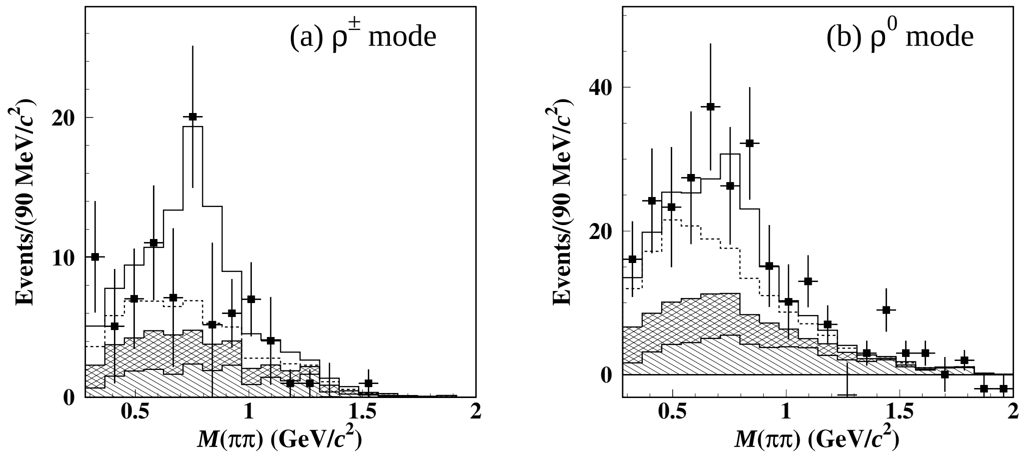

Figure 9.14: Projections of the fit onto $M(\pi\pi)$ for HILEP ($E_\ell > 2.3$ GeV) with a $|\Delta E| < 0.5$ GeV requirement: (a) for the $\pi^\pm\pi^0$ mode and (b) for the $\pi^+\pi^-$ mode. In each plot, the points with error bars show the on-resonance data after continuum background subtraction, while the histogram shows the projection of the fit. The contributions to the fit are the direct and cross-feed components of the signal (unhatched regions, above and below the dashed line, respectively); the background from $b \to u\ell\nu$ non-signal modes (double-hatched region); and the background from $b \to c\ell\nu$ (single-hatched region). The $b \to u\ell\nu$ background includes $B \to \pi\ell\nu$ contributions.

FF model	$\Delta\Gamma$	$\Delta\Gamma$	$\Delta\Gamma$
	$(/10^{-2}\ \mathrm{ns}^{-1})$	$(/10^{-2}\ \mathrm{ns}^{-1})$	$(/10^{-2}\ \mathrm{ns}^{-1})$
q^2 range (GeV^2/c^4)	$0 < q^2 < 7$	$7 < q^2 < 14$	$14 < q^2 < 21$
	$E_\ell > 2.3$ GeV	$E_\ell > 2.3$ GeV	$E_\ell > 2.3$ GeV
ISGW2	1.2 ± 0.5	1.4 ± 0.8	2.7 ± 0.8
LCSR	1.3 ± 0.5	1.4 ± 0.8	2.7 ± 0.8
UKQCD	1.2 ± 0.5	1.4 ± 0.8	2.7 ± 0.8
Wise/Ligeti+E791	1.1 ± 0.5	1.4 ± 0.8	2.8 ± 0.8
Beyer/Melikhov	1.1 ± 0.5	1.4 ± 0.8	2.8 ± 0.8

Table 9.7: Results for $\Delta\Gamma(B^0 \to \rho^- \ell^+ \nu)$ in bins of q^2 for events with $E_\ell >$ 2.3 GeV. The errors are statistical only.

We do not observe a significant $B \to \omega\ell\nu$ signal, but the fit describes the data well.

Figure 9.16 shows the ΔE distributions for the HILEP (9.16a) and LOLEP (9.16b) combined $\pi^\pm$ and π^0 modes. The HILEP $B \to \pi\ell\nu$ modes are dominated by $B \to \rho\ell\nu$ backgrounds. We find $\mathcal{B}(B^0 \to \pi^- \ell^+ \nu) = (1.3 \pm 0.4) \times 10^{-4}$, where the quoted error is statistical only, consistent with the previous CLEO result [9]. We do not quote a full $B \to \pi\ell\nu$ result as it is very sensitive to systematics related to the large $B \to \rho\ell\nu$ backgrounds.

9.3 $\Delta\Gamma$ fit results

Table 9.7 shows the results of the $\Delta\Gamma$ measurement before the correction for the lepton-energy cut is performed. The small spread seen among form-factor models is due to differences in the background subtraction and the smearing correction. Results for the full lepton-energy range are computed using the predictions in Table 3.4 and are given below.

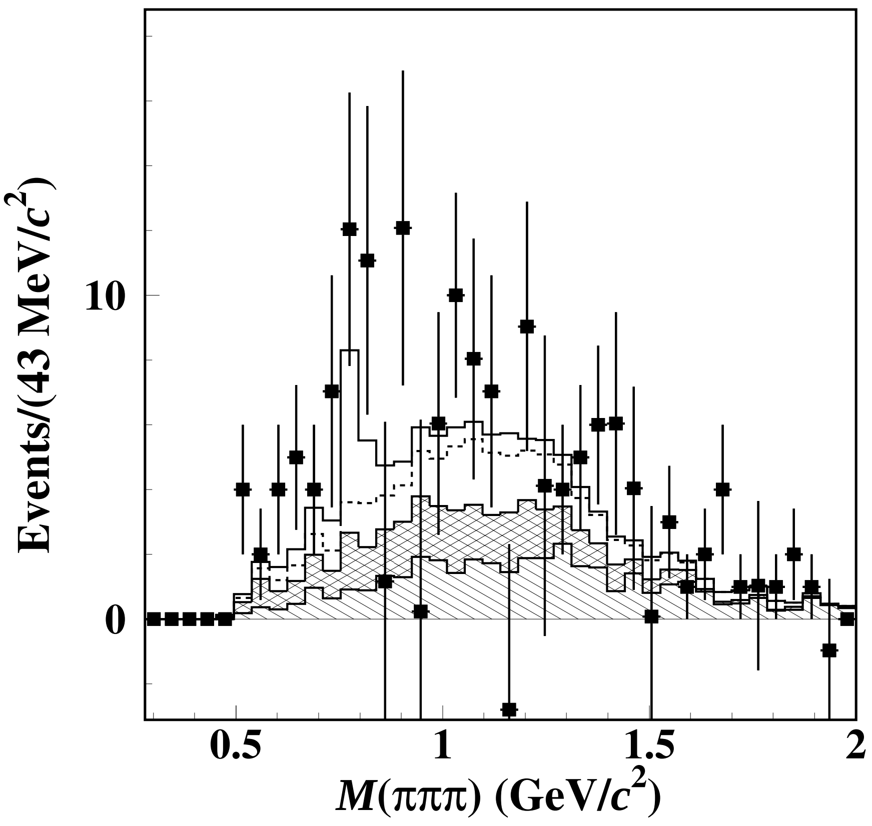

Figure 9.15: Projection of the fit in the $\pi^+\pi^-\pi^0$ mode onto the HILEP $M(\pi^+\pi^-\pi^0)$ distribution with $|\Delta E| < 0.5$ GeV. The points with error bars show the on-resonance data after continuum background subtraction, while the histogram shows the projection of the fit. The contributions to the fit are the direct and cross-feed components of the signal (unhatched regions, above and below the dashed line, respectively); the background from $b \to u\ell\nu$ non-signal modes (double-hatched region); and the background from $b \to c\ell\nu$ (single-hatched region). The $b \to u\ell\nu$ background includes $B \to \pi\ell\nu$ contributions.

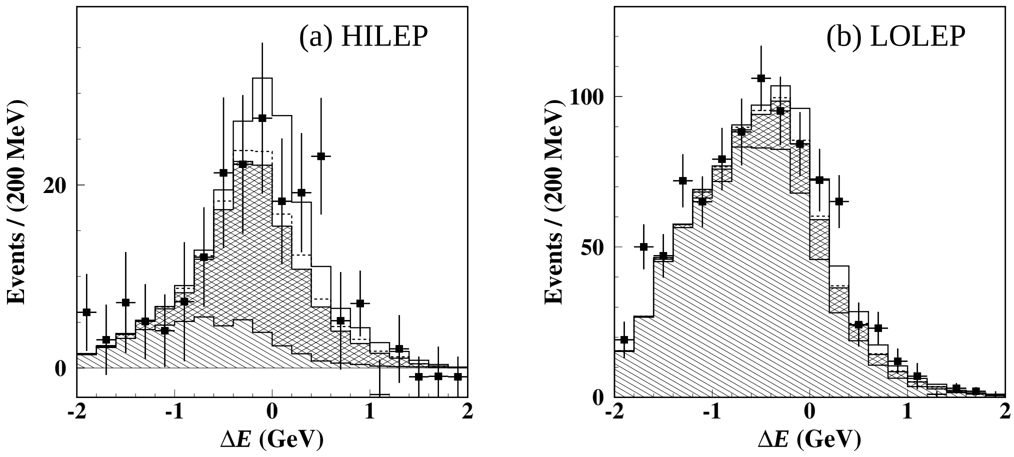

Figure 9.16: Projections of the fit onto the π modes in HILEP and LOLEP: (a) the HILEP ΔE distribution for the $\pi^{\pm}$ and π^{0} modes and (b) the HILEP ΔE distribution for the $\pi^{\pm}$ and π^{0} modes. In each plot, the points with error bars show the on-resonance data after continuum background subtraction, while the histogram shows the projection of the fit. The contributions to the fit are the direct and cross-feed components of the signal (unhatched regions, above and below the dashed line, respectively); the background from $b \to u\ell\nu$ non-signal modes (double-hatched region); and the background from $b \to c\ell\nu$ (single-hatched region). The $b \to u\ell\nu$ background includes $B \to \rho(\omega)\ell\nu$ contributions.

Chapter 10

Systematic errors

In this chapter we describe the systematic errors on the branching fraction, $|V_{ub}|$, and $\Delta\Gamma$ measurements. Table 10.1 summarizes these errors. The uncertainty associated with each source of systematic error is evaluated by repeating the analysis, changing the source of uncertainty within its errors. The uncertainty on the results due to each systematic source is assigned to be the change in results seen when the analysis is redone. These pulls are shown for each systematic error in Tables 10.2 and 10.3. The largest systematic errors are due to uncertainties on the $b \to u\ell\nu$ and $b \to c\ell\nu$ backgrounds, the dependence of the efficiencies of our selection criteria on the Monte Carlo modeling of the detector, and the possible contamination due to $B \to \pi\pi\ell\nu$ nonresonant events. Below, we describe how each systematic uncertainty is evaluated.

10.1 $b \to c\ell\nu$ background uncertainty

The leptons in $b \to c\ell\nu$ background events are primarily from $B \to D\ell\nu$, $B \to D^*\ell\nu$, and $B \to J/\psi X$ decays. The $B \to D^{**}\ell\nu$ contribution is small but is nevertheless included in the fit. For events with $|\Delta E| < 0.5$ GeV and $|M(\pi\pi) - M(\rho)| < 0.15$ GeV$/c^2$ for the $\pi\pi$ modes and $|M(\pi^+\pi^-\pi^0) - 0.782| < 0.05$ GeV$/c^2$ for the $\pi^+\pi^-\pi^0$ mode, the Monte Carlo simulation predicts the following mix of $b \to c\ell\nu$ modes in HILEP (LOLEP): 23% (17%) for $B \to D\ell\nu$,

Systematic contribution	$\delta\mathcal{B}_\rho/\mathcal{B}_\rho$	$\delta\lvert V_{ub}\rvert/\lvert V_{ub}\rvert$	$\delta\Gamma/\Gamma$	$\delta\Gamma/\Gamma$	$\delta\Gamma/\Gamma$
q^2 range (GeV$^2/c^4$)			$(0 < q^2 < 7)$	$(7 < q^2 < 14)$	$(14 < q^2 < 21)$
Simulation of detector	$\pm 9\%$	$\pm 5\%$	$\pm 9\%$	$\pm 6\%$	$\pm 3\%$
$b \to c\ell\nu$ composition	$\pm 2\%$	$\pm 1\%$	$\pm 2\%$	$\pm 6\%$	$\pm 3\%$
$b \to u\ell\nu$ composition	$\pm 6\%$	$\pm 3\%$	$\pm 4\%$	$\pm 9\%$	$\pm 7\%$
Integrated luminosity	$\pm 2\%$	$\pm 1\%$	$\pm 2\%$	$\pm 2\%$	$\pm 2\%$
Lepton identification	$\pm 2\%$	$\pm 1\%$	$\pm 2\%$	$\pm 2\%$	$\pm 2\%$
Fake lepton rate	$\pm 1\%$	$\pm 1\%$	$\pm 1\%$	$\pm 3\%$	$\pm 2\%$
Fit technique	$\pm 5\%$	$\pm 3\%$	$\pm 5\%$	$\pm 5\%$	$\pm 5\%$
f_{+-}/f_{00}	$\pm 2\%$	$\pm 1\%$	$\pm 3\%$	$\pm 3\%$	$\pm 3\%$
$B \to \pi\pi\ell\nu$ nonresonant	-8%	-4%	-10%	-10%	-10%
τ_B	$\pm 1\%$	$\pm 2\%$	$\pm 3\%$	$\pm 3\%$	$\pm 3\%$
Total systematic error (excluding model dep.)	${}^{+13\%}_{-15\%}$	${}^{+7\%}_{-8\%}$	${}^{+12\%}_{-16\%}$	${}^{+14\%}_{-17\%}$	${}^{+13\%}_{-16\%}$

Table 10.1: Summary of systematic errors.

Systematic change	$\Delta\mathcal{B}(B \to \rho\ell\nu)$
Fake rate 2× nominal	−0.4%
Fake rate down 1/2× nominal	+0.3%
$B \to D\ell\nu$ up 10%	−0.3%
$B \to D\ell\nu$ down 10%	+0.3%
$B \to D^*\ell\nu$ up 10%	+0.5%
$B \to D^*\ell\nu$ down 10%	−0.6%
$B \to D^{**}\ell\nu$ up 40%	−1.0%
$B \to D^{**}\ell\nu$ down 40%	+1.5%
$b \to c\ell$ other up 40%	−0.1%
$b \to c\ell$ other down 40%	+0.1%
$B \to \eta^{(\prime)}\ell\nu$ up 50%	+4.0%
$B \to \eta^{(\prime)}\ell\nu$ down 50%	−3.3%
$B \to b_1\ell\nu$ up 50%	−1.5%
$B \to b_1\ell\nu$ down 50%	+3.0%
$B \to a_i\ell\nu$ up 50%	−0.5%
$B \to a_i\ell\nu$ down 50%	+2.5%
$B \to \rho(2S)\ell\nu$ up 50%	−0.5%
$B \to \rho(2S)\ell\nu$ down 50%	+1.2%
MC track finding eff. down 1%	+3.0%
MC cluster finding eff. down 2%	−4.0%
Tracks/clusters with $\cos\theta \geq 0.93$	+2.0%
MC charged track momentum smearing	−3.0%
MC cluster energy smearing	−2.0%
Increase fraction of events with a K_L	−1.0%
Increase K_L energy deposit in MC	−3.3%

Table 10.2: Systematic pulls around the nominal fit for the branching fraction measurement. In each case, $\delta|V_{ub}|/|V_{ub}| = 1/2\delta\mathcal{B}/\mathcal{B}$.

Systematic change q^2 range (GeV^2/c^4)	$\delta\Delta\Gamma/\Delta\Gamma$ ($0 < q^2$)	$\delta\Delta\Gamma/\Delta\Gamma$ ($7 < q^2 < 14$)	$\delta\Delta\Gamma/\Delta\Gamma$ ($q^2 > 14$)
Fake rate 2× nominal	+0.5%	+2.5%	+1.4%
Fake rate down 1/2× nominal	−0.9%	−3.0%	−1.3%
$B \to D\ell\nu$ up 20%	+0.5%	+1.9%	0%
$B \to D\ell\nu$ down 20%	−0.6%	−2.0%	+0.4%
$B \to D^*\ell\nu$ up 20%	+1.9%	+6.2%	+2.4%
$B \to D^*\ell\nu$ down 20%	−2.4%	−6.0%	−2.1%
$B \to D^{**}\ell\nu$ up 40%	−0.1%	−0.6%	−0.4%
$B \to D^{**}\ell\nu$ down 40%	+0.1%	+0.8%	+0.4%
$b \to c\ell$ other up 40%	−0.4%	+1.5%	+0.5%
$b \to c\ell$ other down 40%	+0.4%	−1.4%	−0.5%
$B \to \eta^{(\prime)}\ell\nu$ up 50%	+0.7%	+6.8%	+4.7%
$B \to \eta^{(\prime)}\ell\nu$ down 50%	−1.3%	−7.1%	−5.0%
$B \to b_1\ell\nu$ up 50%	+0.2%	+1.6%	+0.8%
$B \to b_1\ell\nu$ down 50%	−0.4%	−1.5%	−0.7%
$B \to a_i\ell\nu$ up 50%	+1.0%	5.0%	+3.0%
$B \to a_i\ell\nu$ down 50%	−1.2%	−4.7%	−3.2%
$B \to \rho(2S)\ell\nu$ up 50%	+0.1%	+0.6%	+0.2%
$B \to \rho(2S)\ell\nu$ down 50%	−0.1%	−0.5%	−0.1%
MC track finding eff. down 1%	+3.0%	−2.0%	+2.7%
MC cluster finding eff. down 2%	+1.0%	−0.2%	+2.5%
Tracks/clusters with $\cos\theta \geq 0.93$	+7.0%	+4.0%	+5.0%
MC charged track mom. smearing	−4.0%	−1.5%	−1.8%
MC neutral cluster E smearing	−1.8%	−2.5%	−2.1%
Increase fraction of events with a K_L	−1.3%	−2.1%	−1.7%
Increase K_L energy deposit in MC	−2.3%	−2.4%	−2.6%

Table 10.3: Systematic pulls around the nominal fit for the $\Delta\Gamma$ measurements.

48% (76%) for $B \to D^*\ell\nu$, 23% (1%) for $B \to J/\psi X$, and 5% (5%) for $B \to D^{**}\ell\nu$.

The $b \to c\ell\nu$ systematic error reflects the fit sensitivity to the shape of the ΔE vs. $M(\pi\pi)$ distribution determined from the $b \to c\ell\nu$ Monte Carlo simulation. (Recall that the fitting method already allows the data to determine the overall normalization of the $b \to c\ell\nu$ background as well as the shape of its lepton-energy distribution.) To evaluate this systematic error, we vary the relative sizes of the background sources. For $B \to D\ell\nu$ and $B \to D^*\ell\nu$ variations are $\pm 20\%$, well beyond the current experimental uncertainties in their branching fractions. For $B \to D^{**}\ell\nu$ and $B \to J/\psi X$ we make variations of $\pm 40\%$. These uncertainties produce only a small effect in the signal branching fraction, about 2%.

10.2 $b \to u\ell\nu$ background uncertainty

The same method is used to evaluate the uncertainty due to the $b \to u\ell\nu$ simulation. (The fit method allows the data to determine the normalization of this background component in each lepton-energy bin.) We vary the relative contribution of each mode predicted by the ISGW2 model by $\pm 50\%$. The systematic error assigned is the sum in quadrature of these variations.

We also examine the sensitivity of the fit to the $B \to \pi\ell\nu$ decay distributions. In contrast to $b \to u\ell\nu$, where the normalization is allowed to vary in each lepton-energy bin of the fit, the shape of the $B \to \pi\ell\nu$ lepton-energy distribution is fixed by the Monte Carlo prediction. We therefore vary the lepton-energy spectrum of the $B \to \pi\ell\nu$ Monte Carlo and use form factors for $B \to \pi\ell\nu$ determined using several different methods (much as we have done for the $B \to \rho\ell\nu$ component of the fit). In both cases, the $B \to \rho\ell\nu$ results are robust against changes to the $B \to \pi\ell\nu$ Monte Carlo. We include this uncertainty in the systematic error due to the $b \to u\ell\nu$ simulation.

10.3 Detector simulation uncertainty

The computation of $|\mathbf{p}_{\rm miss}|$ relies on the Monte Carlo simulation to adequately simulate the detector response for all charged tracks and clusters in the event, not just those used to form the $\rho + \ell$ candidate. To evaluate our sensitivity to the details of our detector Monte Carlo simulation, we vary the input parameters of the Monte Carlo. These variations include conservative variations of the tracking efficiency, charged-track momentum resolution, CsI cluster identification efficiency, cluster energy resolution, and the simulation of the detector endcaps. In addition, we examine our sensitivity to the number of K_L^0 mesons produced and the accompanying detector response.

In particular,

- We lower the charged track finding efficiency by 1(5)% for tracks above (below) 250 MeV. Estimates based on track embedding studies (that is, to add a Monte Carlo simulated track of known momentum to events and compare the efficiency for reconstructing this track in data and Monte Carlo simulation) show that the Monte Carlo correctly models the tracking efficiency seen in the data to better than 0.5% except at low momentum.
- We lower the cluster finding efficiency by 2%.
- We increase the charged track momentum smearing in the the Monte Carlo according to

$$\vec{p}_{\rm track} \to \vec{p}_{\rm qq} + 1.1(\vec{p}_{\rm track} - \vec{p}_{\rm qq}) \tag{10.3.1}$$

- We increase the cluster energy smearing in the the Monte Carlo according to

$$E_{\rm cluster} \to E_{\rm qq} + 1.1(E_{\rm cluster} - E_{\rm qq}) \tag{10.3.2}$$

- We ignore any track or cluster in the endcap ($\cos\theta \geq 0.93$). This is a rather extreme variation; however we see only a small effect on the branching ratio.

- We increase the fraction of events generated with a K_L. We assign a weight according to $1.1^{N_{K_L}}$.
- We increase the energy of showers attributed to a K_L by 20%.

Considering these pulls, we assign a conservative ±9% systematic error on the branching fraction due to changing the Monte Carlo efficiency and smearing input parameters.

10.4 N($B\bar{B}$) and lepton ID uncertainty

The uncertainty of the number of $B\bar{B}$ events lepton ID efficienies have been each evaluated to be ±2%. Chapter 5 describes how the number of $\Upsilon(4S) \to B\bar{B}$ events and the ±2% error are determined.

The lepton identification systematic error is due to the uncertainty in the Monte Carlo simulation of the identification efficiency. For electron identification, electrons from bhabha events are embedded into hadronic events and studied in order to determine the absolute efficiency. The results of this embedding are then directly used in the Monte Carlo simulation to mock up the efficiency of electron identification as a function of track momentum and dip angle. For muon identification, $e^+e^- \to \mu^+\mu^-\gamma$ events are used to measure the efficiency in data and Monte Carlo simulation. The agreement between them is quite good. We assign a ±2% uncertainty due to the simulation of lepton identification.

10.5 Fake lepton uncertainty

Events where a hadron has satisfied each of the lepton identification requirements are a small source of background events. The shapes of the kinematic distributions for these events are determined using the data. We examine events that pass all analysis requirements except the lepton identification requirements. Therefore, we reconstruct $\rho - h^\pm$ instead of $\rho - \ell^\pm$ events. Because we use data to determine these shapes, we do not evaluate a systematic error due to their uncertainty.

To determine the normalization of this background contribution, we examine samples of tagged hadrons to compute the rate at which hadrons satisfy our lepton identification requirements. In particular, hadron samples from $D^0 \to K^-\pi^+$, $D^0 \to K^-\pi^+\pi^0$ and $K_s \to \pi^+\pi^-$ are used. For high-momentum leptons, this normalization has been determined to better than $\pm 10\%$ [77]. We have taken a more conservative uncertainty of $\pm 50\%$. Because the fake lepton background contribution is small, this variation is has only a very small effect on our results ($\pm 1\%$ on the branching fraction).

10.6 f_{+-}/f_{00} uncertainty

Our nominal result assumes that f_{+-}/f_{00} is 1.0 ± 0.1. We assign f_{+-}/f_{00} within its error. When given different values of f_{+-}/f_{00}, the fit results change as to conserve the yield of ρ^+ plus ρ^0 events, rather than the yield of ρ^+ or ρ^0 events individually remaining constant. In this way, the branching ratio for $B \to \rho^+\ell\nu$ changes less than linearly with the value of f_{+-}/f_{00}. We observe a $\pm 2\%$ effect on the branching fraction.

10.7 Fit method uncertainty

Among the checks of the method which have been performed are checks that the fitter does indeed give the correct results (both for the central value and the error) for $\mathcal{B}(B \to \rho\ell\nu)$. These checks were performed using Monte Carlo simulation to make up "mock" data samples. In this way, various types of fits could be performed to fairly (that is without using the data) determine which fit method gives the best results. The method used in this thesis gives the correct result (on average) for $\mathcal{B}(B \to \rho\ell\nu)$, and gives compariable errors to other fitting methods considered. Among the fit techniques examined was the addition of $\cos\theta_\ell$ to the fit of the $\pi^\pm$ and π^0 modes. That is, we performed a 2D fit to ΔE and $\cos\theta_\ell$, where θ_ℓ is the angle between the lepton momentum direction in the W rest frame and the W momentum direction in the B-meson rest frame. We observe a 5% shift in $\mathcal{B}(B \to \rho\ell\nu)$ between our nominal fit and the fit including $\cos\theta_\ell$. Although the Monte Carlo "mock" data sample studies indicate that this is expected to be the case in approximately 25% of data sets, we assign this 5% as a systematic error due to our fitting method.

10.8 B-meson lifetime uncertainty

As described in Chapter 8, we rely on the B-meson lifetime in two ways. First, the ratio of B^0 to B^+ lifetimes is used to determine the relative number of $B^0 \to \rho^-\ell^+\nu$, $B^+ \to \rho^0\ell^+\nu$, and $B^+ \to \omega\ell^+\nu$ events. Second, to extract $|V_{ub}|$ and $\Delta\Gamma$ from the measured yields, $\Gamma(B) = 1/\tau_B$ is needed, as shown in Eq. 8.9.1. To evaluate our sensitivity we vary the lifetime and the ratio of lifetimes within their errors. The systematic uncertainty due to the B-meson lifetime is small, $1-3\%$, for each measurement.

10.9 Nonresonant $B \to \pi\pi\ell\nu$ uncertainty

Finally, we assign a systematic error associated with a nonresonant $B \to \pi\pi\ell\nu$ contribution. Like signal events, nonresonant events would have a ΔE distribution centered around zero. The $\pi\pi$ invariant-mass distribution, however, would be somewhat different. Although we do not know how to describe the $M(\pi\pi)$ distribution of such a contribution, other properties help us to distinguish resonant $B \to \rho\ell\nu$ from nonresonant $B \to \pi\pi\ell\nu$. The isospin (I) of the hadronic system in a $B \to \pi\pi\ell\nu$ decay must be either $I = 0$ or $I = 1$. For $I = 1$, where the relative production of $\pi^\pm\pi^0$:$\pi^+\pi^-$:$\pi^0\pi^0$ is 2:1:0, the relative orbital angular momentum (L) must be odd. The $L = 1$ contribution is dominated by the ρ resonance [13]. Contributions from $L = 3,\ 5,\ ....$ are suppressed. For $I = 0$, the relative production of $\pi^\pm\pi^0$:$\pi^+\pi^-$:$\pi^0\pi^0$ is 0:2:1, distinct from $I = 1$. An $I = 0$ contribution will consist primarily of $L = 0$. In addition, the

$\pi^0\pi^0$ mode, which has no resonant contribution, is useful for constraining the size of any nonresonant $B \to \pi\pi\ell\nu$ contribution.

Nonresonant events should also differ from $B \to \rho\ell\nu$ events in their q^2 distribution. We expect nonresonant events to occur mainly at low q^2, where the daughter u quark has a large momentum relative to the spectator quark. As shown in Table 3.4, the efficiency of the $E_\ell > 2.3$ GeV requirement is highest at large q^2. Thus, we expect to preferentially select resonant $B \to \rho\ell\nu$ events.

To assign a systematic error, we include a possible nonresonant contribution in our fit, using two sets of assumptions for the $M(\pi\pi)$ and q^2 distribution. First, we consider a $M(\pi\pi)$ distribution with a broad Breit-Wigner shape having $M = 0.8$ GeV$/c^2$ and $\Gamma = 1.0$ GeV$/c^2$. To simulate a q^2 distribution that is peaked at low q^2, we use $B \to \pi\ell\nu$ form factors from the ISGW2 model. The second set of parameters is designed such that the nonresonant contribution is very similar to resonant $B \to \rho\ell\nu$ events. We use $B \to \rho\ell\nu$ form factors (again from ISGW2) and a ρ Breit-Wigner for the parent $M(\pi\pi)$ distribution.

Using these two sets of assumptions, we repeat our likelihood fit with the additional freedom of a possible nonresonant $B \to \pi\pi\ell\nu$ contribution. As described above, we assume that this contribution is primarily $I = 0$. A 20% $I = 1$ contribution accounts for a possible $L = 3$ component. Additionally, we perform the fit with and without the $\pi^0\pi^0$ mode.

In all fits, we find a nonresonant component consistent with zero. The systematic error is assigned from the increase in the statistical uncertainty on the $B \to \rho\ell\nu$ yield due to the correlation with the nonresonant fit component. This systematic error is one-sided, as our nominal fit assumes no nonresonant contribution. The associated uncertainty is 8%, which we regard as conservative.

In addition to these fits, we have performed a fit where the signal contribution is reweighted to have the kinematics of a semileptonic decay to a scalar meson. The daughter hadron has a ρ line shape just as is the case for the nominal fit. This fit is performed to test if the data better agrees with a $B \to \rho\ell\nu$ hypothesis or with decay to a scalar meson, were the θ_ℓ distribution will be $\sin^2\theta_\ell$. The difference in likelihood between this fit and the nominal fit is 2.5σ, favoring the $B \to \rho\ell\nu$ hypothesis. This result and the systematic error study above indicate that our result is almost completely due to $B \to \rho\ell\nu$ events, as opposed to $B \to \pi\pi\ell\nu$ nonresonant events.

Chapter 11

$\mathcal{B}(B \to \rho\ell\nu)$, $|V_{ub}|$, and $\Delta\Gamma$ results

In this chapter we extract our final results using the fit results described in Chapter 9 and the systematic error studies in Chapter 10. We first discuss the branching fraction and $|V_{ub}|$ results from the analysis described in this thesis. Then our results for $\Delta\Gamma$ in bins of q^2 are discussed. Finally, we summarize an average for the branching fraction and $|V_{ub}|$ results with the previously published CLEO analysis.

11.1 Branching fraction and $|V_{ub}|$ results

To extract the $B \to \rho\ell\nu$ branching fraction from our measured yields, we must extrapolate to the full lepton-energy range. We use form-factor models, as described in Section 3, to determine the signal efficiency. The fitted yields themselves depend only slightly on the set of form factors used. The signal efficiency and yield for each form-factor model are presented in Tables 9.4, 9.5, and 9.6. In addition, to extract $|V_{ub}|$, we use the value of $\tilde{\Gamma}_{\text{thy}}$ for each form-factor model, along with τ_B, to relate the branching fraction result to $|V_{ub}|$, as given by Eq. 8.9.1. Results for $\mathcal{B}(B \to \rho\ell\nu)$ and $|V_{ub}|$ are presented in Figs. 11.1 and 11.2.

The final values for $\mathcal{B}(B \to \rho\ell\nu)$ and $|V_{ub}|$ are the averages of the results obtained using the five form-factor models. We assign a systematic error to

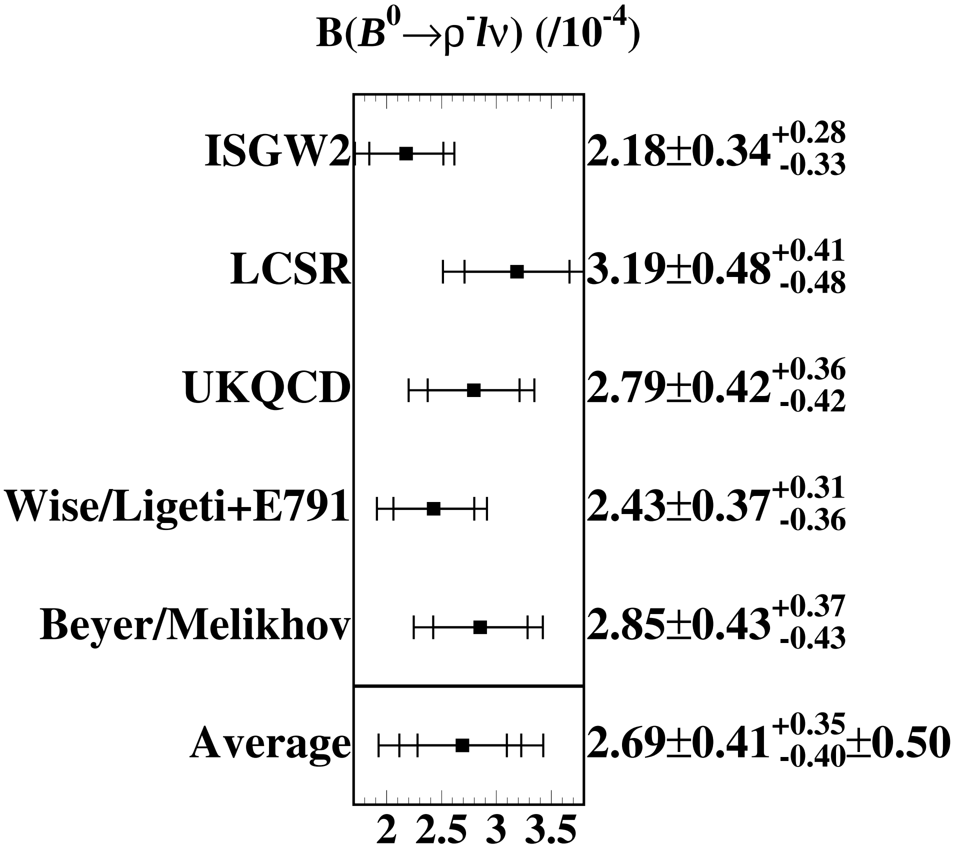

Figure 11.1: $\mathcal{B}(B^0 \to \rho^-\ell^+\nu)$ results. The errors are statistical, systematic, and theoretical (on the averages), successively combined in quadrature. The theoretical error is taken to be 1/2 of the full spread of results.

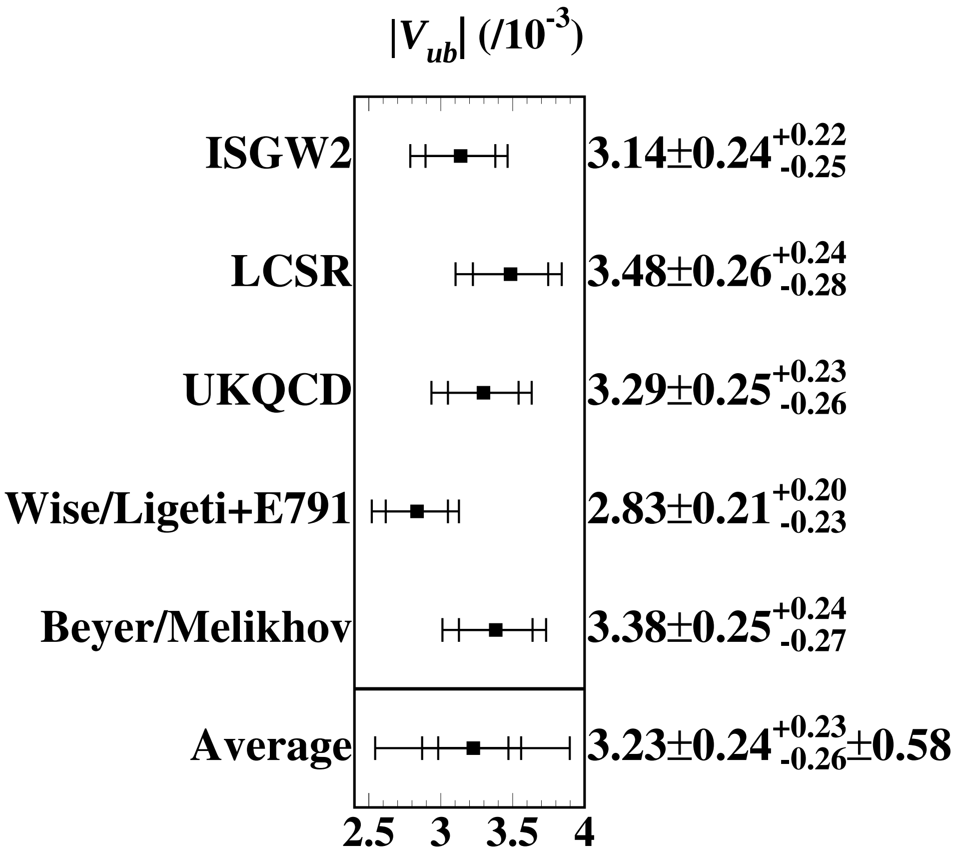

Figure 11.2: $|V_{ub}|$ results. The errors are statistical, systematic, and theoretical (on the averages), successively combined in quadrature. The theoretical error is taken to be 1/2 of the full spread of results in quadrature with the additional uncertainty due to the determination of $\tilde{\Gamma}_{\text{thy}}$.

account for the substantial spread in results among the form-factor models. For the measurement of $\mathcal{B}(B \to \rho\ell\nu)$ this error is assigned to be 1/2 the full spread among the five form-factor model results. This uncertainty reflects our sensitivity to the different *shapes* of kinematic distributions predicted by the models, (mostly due to the $E_\ell > 2.3$ GeV acceptance. For $|V_{ub}|$, we must also include an error due to the uncertainty on the computation of $\tilde{\Gamma}_{\rm thy}$, relecting the different *normalizations* of the form-factor models. The models quote errors on $\tilde{\Gamma}_{\rm thy}$ between 17% and 50%. We have therefore assigned a 30% error on $\tilde{\Gamma}_{\rm thy}$ (corresponding to a 15% error on $|V_{ub}|$), rather than 15%, which is the spread in predictions among models. We find

$$\begin{aligned} \mathcal{B}(B^0 \to \rho^-\ell^+\nu) &= (2.69 \pm 0.41^{+0.35}_{-0.40} \pm 0.50) \times 10^{-4}, \\ |V_{ub}| &= (3.23 \pm 0.24^{+0.23}_{-0.26} \pm 0.58) \times 10^{-3}. \end{aligned} \qquad (11.1.1)$$

The errors are statistical, systematic, and theoretical. The dominant uncertainty on $|V_{ub}|$ arises from the theoretical error on the normalization, $\tilde{\Gamma}_{\rm thy}$. This 30% uncertainty (corresponding to a 15% error on $|V_{ub}|$) is independent of the method used to measure $\mathcal{B}(B \to \rho\ell\nu)$, and it is larger than the statistical error on $|V_{ub}|$ (6%) or the model dependence of the detection efficiency (19% on ϵ or 9% on $|V_{ub}|$).

11.2 $\Delta\Gamma$ results

Our results for $\Delta\Gamma$ in bins of q^2 are shown in Figs. 11.3, 11.4, and 11.5. As for the branching fraction and $|V_{ub}|$ results, we compute an average over form-factor models and assign the theoretical uncertainty to be one-half the full spread in results. For these measurements, the model dependence comes primarily from the variation in the efficiency of the HILEP lepton-energy requirement. We find

$$\begin{aligned}
\Delta\Gamma(0 < q^2 < 7\ \mathrm{GeV}^2/c^4) &= (7.6 \pm 3.0^{+0.9}_{-1.2} \pm 3.0)\ \mathrm{ns}^{-1}, \\
\Delta\Gamma(7 < q^2 < 14\ \mathrm{GeV}^2/c^4) &= (4.8 \pm 2.9^{+0.7}_{-0.8} \pm 0.7) \times 10^{-2}\ \mathrm{ns}^{-1}, \\
\Delta\Gamma(14 < q^2 < 21\ \mathrm{GeV}^2/c^4) &= (7.1 \pm 2.1^{+0.9}_{-1.1} \pm 0.6) \times 10^{-2}\ \mathrm{ns}^{-1} \quad (11.2.1)
\end{aligned}$$

where the errors are statistical, systematic, and theoretical. The statistic errors are presently quite large on these measurements. We can, however, draw several conclusions. Because the form-factor models predict nearly the same q^2 distribution at large lepton energy, we cannot distinguish among them, as shown in Fig. 11.6. The models do, however, agree well with the q^2 distribution seen in the data. Figure 11.7 shows the $\Delta\Gamma$ results after the extrapolation to the full q^2 range. At high q^2, our lepton-energy requirement covers a large fraction of the allowed lepton-energy range (as shown in Fig. 3.6), and we are able to measure a partial rate with a relatively small theoretical error. In contrast, at low q^2, the theoretical error associated with the extrapolation to low lepton-energy is similar to the large statistical uncertainty.

11.3 Average with previous results on $B \to \rho\ell\nu$

We have formed an average for $\mathcal{B}(B \to \rho\ell\nu)$ and $|V_{ub}|$ with the previously published CLEO exclusive $b \to u\ell\nu$ result [9] (denoted as the neutrino reconstruction analysis in this section).

As summarized in Table 11.1 the two methods share only a small fraction of events and are therefore essentially statistically independent. To draw this conclusion, we examined the data samples, and not on the various Monte Carlo samples, in each analysis for common events. The neutrino reconstruction events considered include events in the ρ modes with signal-like M_B, ΔE, and $M(\pi\pi)$. To evaluate the statistical overlap, we exclude these events from our data to see if our branching ratio significance is affected.

Looking at our HILEP sample in the ρ modes, there are 20 events in common out of approximately 800 in our sample and 200 events in the neutrino

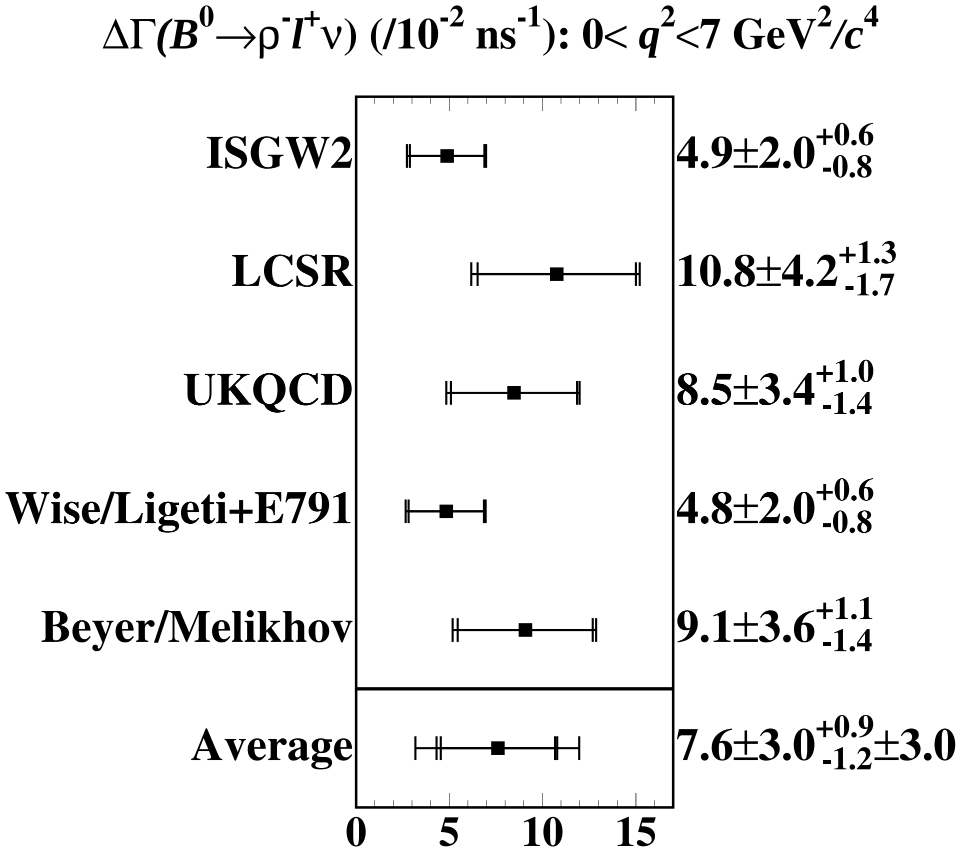

Figure 11.3: The partial width ($\Delta\Gamma$) for $0 < q^2 < 7$ GeV$^2/c^4$. The errors are statistical, systematic, and theoretical (on the averages), successively combined in quadrature. The theoretical error on each measurement is taken to be 1/2 of the full spread of results for the form-factor models.

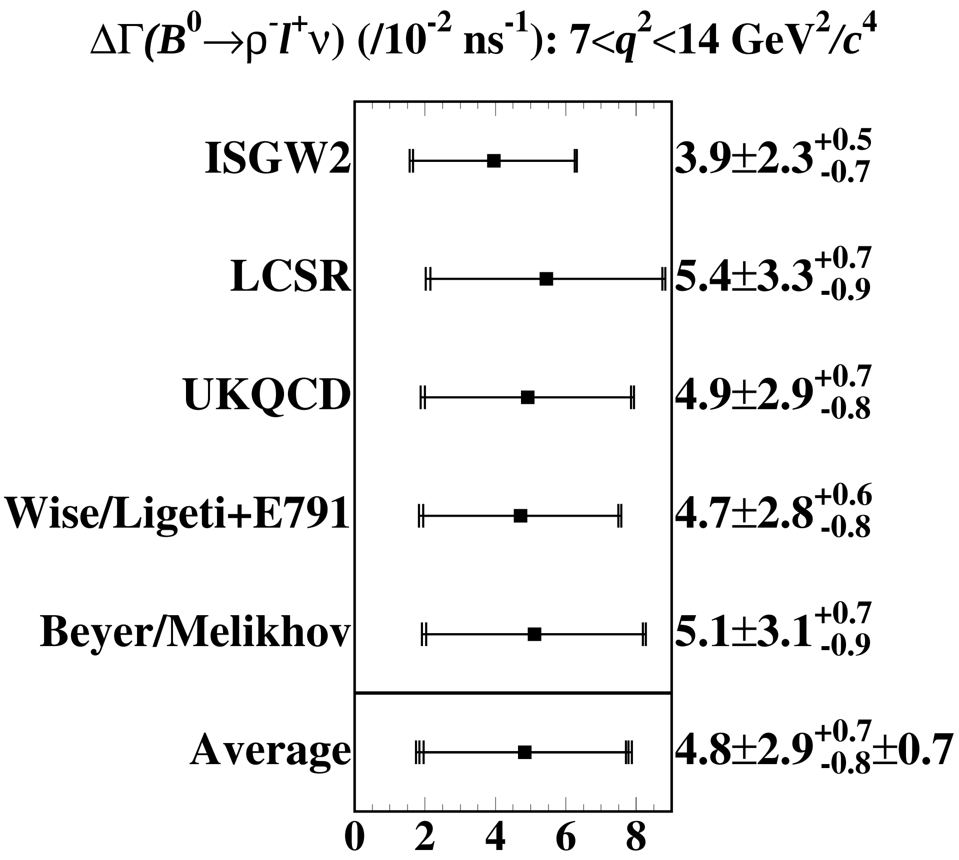

Figure 11.4: The partial width ($\Delta\Gamma$) for $7 < q^2 < 14\ \mathrm{GeV}^2/c^4$. The errors are statistical, systematic, and theoretical (on the averages), successively combined in quadrature. The theoretical error on each measurement is taken to be 1/2 of the full spread of results for the form-factor models.

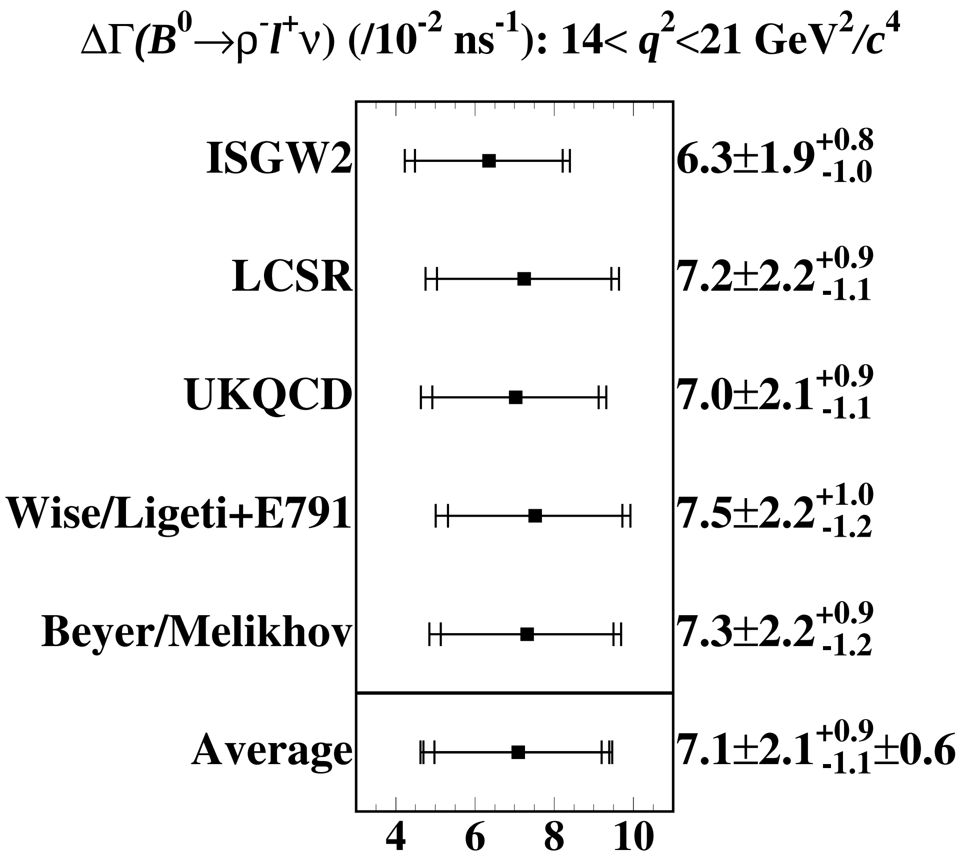

Figure 11.5: The partial width ($\Delta\Gamma$) for $14 < q^2 < 21$ GeV$^2/c^4$. The errors are statistical, systematic, and theoretical (on the averages), successively combined in quadrature. The theoretical error on each measurement is taken to be 1/2 of the full spread of results for the form-factor models.

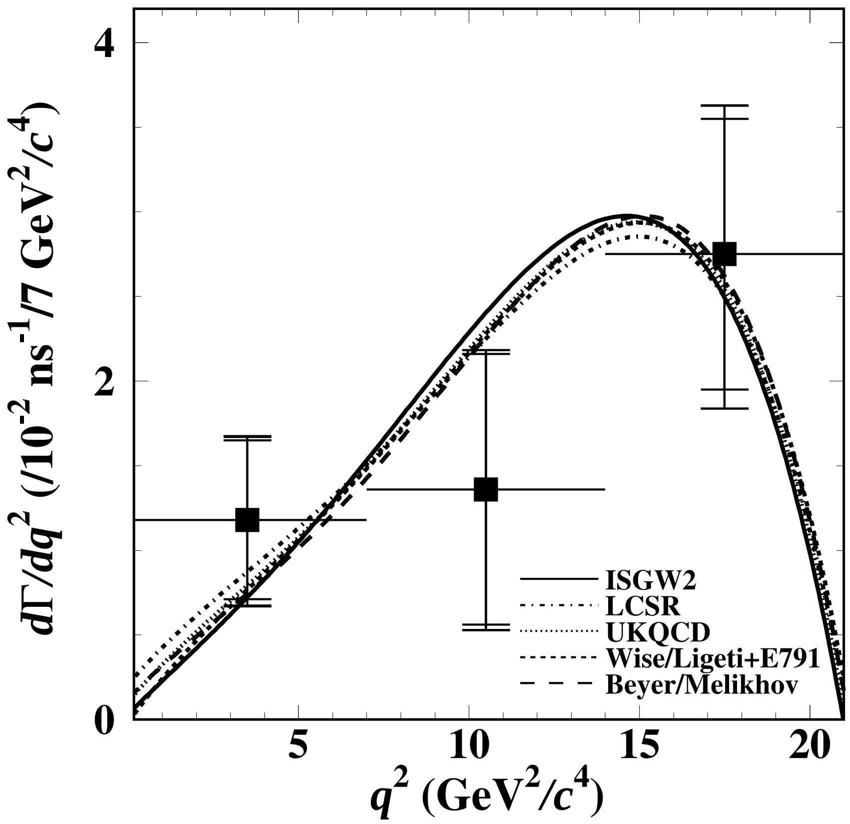

Figure 11.6: Comparison of measured $\Delta\Gamma$ distribution (points with error bars) with expectations from the form-factor models (curves) for the $E_\ell > 2.3$ GeV region. The errors on the points are statistical, systematic, and theoretical, successively combined in quadrature. Because the form-factor models predict nearly the same q^2 distribution at large lepton energy, we cannot distinguish between them.

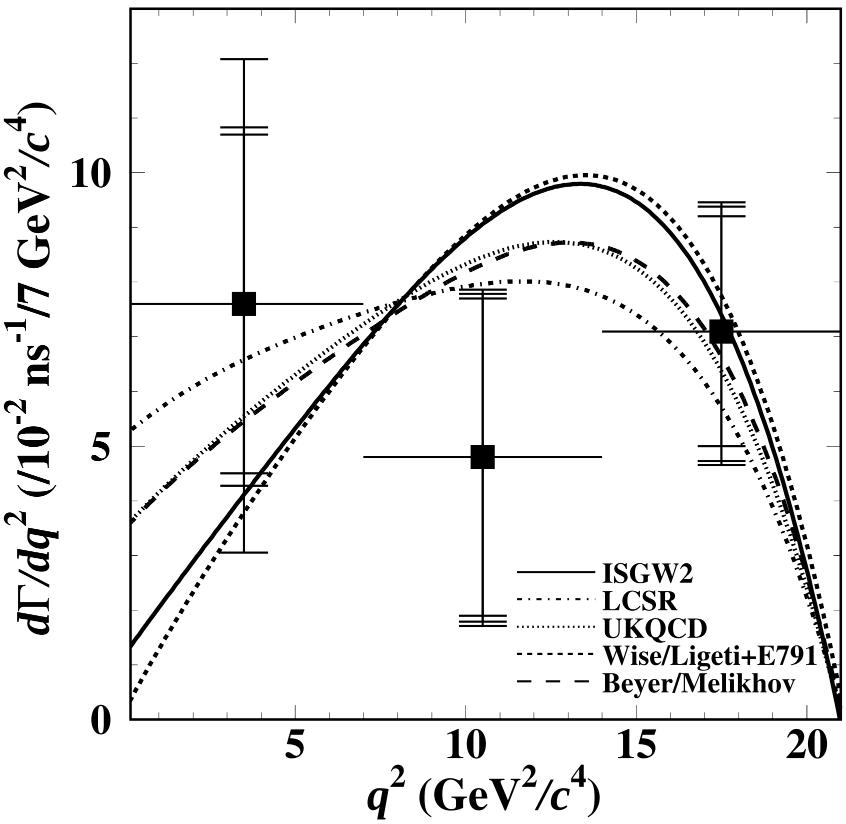

Figure 11.7: Comparison of measured $\Delta\Gamma$ distribution (points with error bars) with expectations from the form-factor models (curves) after the data have been extrapolated over the full E_ℓ range. The errors on the points are statistical, systematic, and theoretical, successively combined in quadrature. Because the form-factor models predict nearly the same q^2 distribution at large lepton energy, we cannot distinguish between them.

# of entries from ν-recon.	226
HILEP events in ρ modes	619
Shared events in HILEP ρ modes	20
HILEP events in ρ modes and ρ-like $M(\pi\pi)$	199
Shared events in HILEP ρ modes with ρ-like $M(\pi\pi)$	12
Significance of BR result WITH shared events	6.5 σ
Significance of BR result WITHOUT shared events	6.6 σ

Table 11.1: Summary of event overlap between this analysis and the ν-reconstruction analysis.

reconstruction sample. Additionally requiring that these events are close to the ρ mass in $M(\pi\pi)$, we have only 12 out of 199 events in common. Running the fit without these common events shows that the significance remains fairly constant, changing from 6.5σ to 6.6σ. We conclude that we do not need to worry about statistical overlap when combining results. Simple $\sqrt{n}$ arguements lead to the same conclusion.

The overlap in systematic error is large. The neutrino reconstruction systematic error is $\pm 18.4\%$ with a -20% error due to nonresonant $B \to \pi\pi\ell\nu$. Our systematic errors are $\pm 12.6\%$ and -8%. The majority of the systematic error is due to the same uncertainties. For the branching fraction measurements, we compute the correlation coefficient to be 0.67 for the systematic errors other than the nonresonant error and the model dependence error.

The statistical and systematic correlations in hand, a weight has been assigned to each analysis such as to minimize the total error (statistical, systematic, and theoretical) on the average. Because Ref. [9] extracts $|V_{ub}|$ using both $B \to \rho\ell\nu$ and $B \to \pi\ell\nu$ results, we perform the average separately for the branching fraction and $|V_{ub}|$ measurements. The average is performed as follows:

1. Assign a weight, w_i, to each analysis ($\Sigma w_i = 1$).

2. Given these weights, evaluate the average $\mathcal{B}(B \to \rho\ell\nu)$ and $|V_{ub}|$ for each form factor model. The published result has been updated to consider the same set of form-factor models as used in this paper. (These results are described in Chapter 4.)
3. Given the result for each form factor model, determine the average (an average of averages) and model dependence error using the method described above.
4. Return to step #1 in order to step through the possible w_i.
5. Select the set of w_i that minimizes σ_{tot}, which is defined as

$$\sigma_{\text{tot}} = \sigma_{\text{stat}} \oplus \frac{1}{2}(\sigma_{\text{sys, upper}} + \sigma_{\text{sys, lower}}) \oplus \sigma_{\text{model dep}} \qquad (11.3.1)$$

   where $\sigma_{\text{sys, upper}}$ and $\sigma_{\text{sys, lower}}$ are the upper and lower systematic errors including the nonresonant error.

Figure 11.8 shows σ_{tot} for the branching fraction and $|V_{ub}|$ measurements as a function of the weight placed on each measurement. We have tried several other averaging methods, and obtain similar results for w_i. Figures 11.9 and 11.10 show the resulting averages accounting for correlated systematic errors between the two methods. Averaging these results over form-factor models, as described above, we obtain

$$\begin{aligned}\mathcal{B}(B^0 \to \rho^- \ell^+ \nu) &= (2.57 \pm 0.29^{+0.33}_{-0.46} \pm 0.41) \times 10^{-4}, \\ |V_{ub}| &= (3.25 \pm 0.14^{+0.21}_{-0.29} \pm 0.55) \times 10^{-3}, \qquad (11.3.2)\end{aligned}$$

where the errors are statistical, systematic, and theoretical.

11.4 Testing the isospin constraints

Each of our results depends on the isospin and quark model relationships in Eqs. 8.2.1 and 8.2.2:

$$\begin{aligned}\Gamma(B^0 \to \rho^- \ell^+ \nu) &= 2\Gamma(B^+ \to \rho^0 \ell^+ \nu), \\ \Gamma(B^+ \to \rho^0 \ell^+ \nu) &= \Gamma(B^+ \to \omega \ell^+ \nu). \qquad (11.4.1)\end{aligned}$$

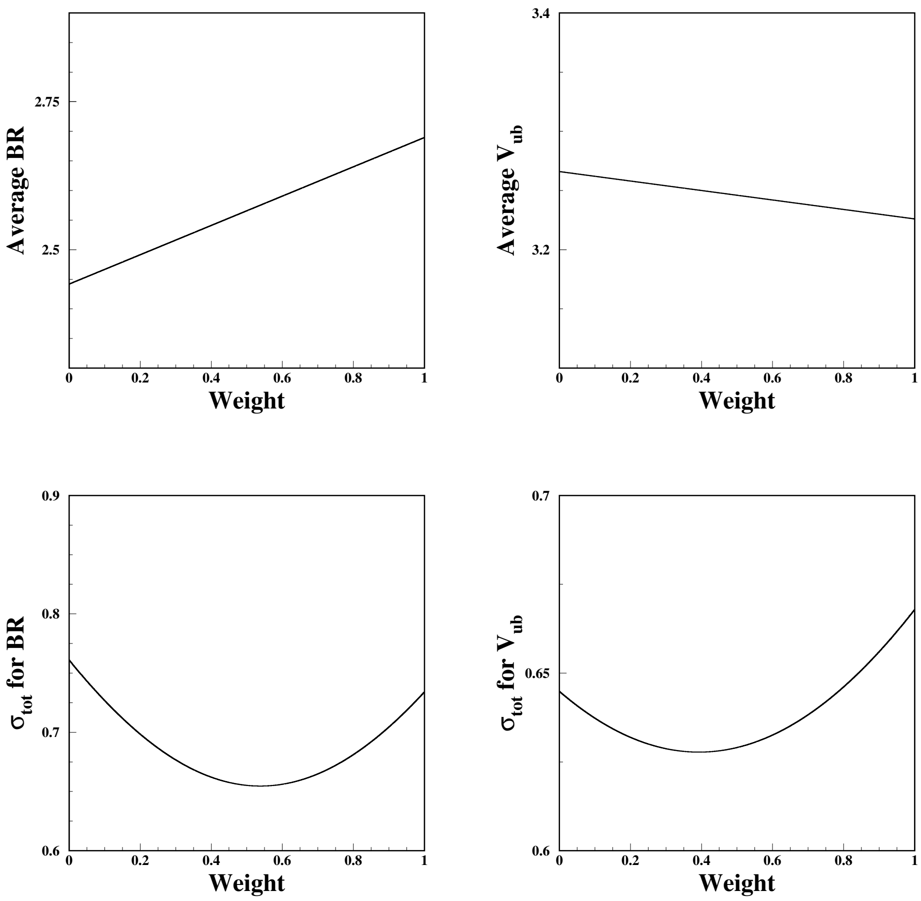

Figure 11.8: Average branching ratio and $|V_{ub}|$ results as a function of the weight placed on this analysis in the average. The left (right) hand plots show branching ratio ($|V_{ub}|$) results. The upper (lower) plots show the central value ($\sigma_{\rm tot}$) determined.

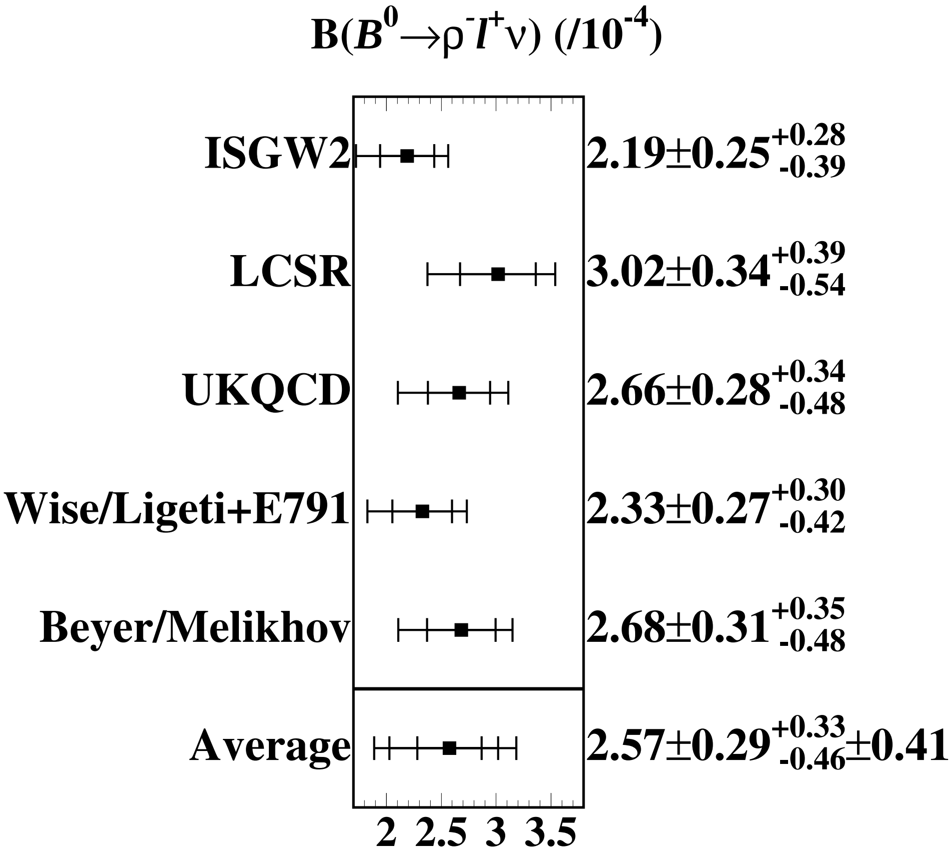

Figure 11.9: Branching fraction results averaged with the previous CLEO analysis. The errors are statistical, systematic, and theoretical (on the averages), successively combined in quadrature. The theoretical error is taken to be 1/2 of the full spread of results.

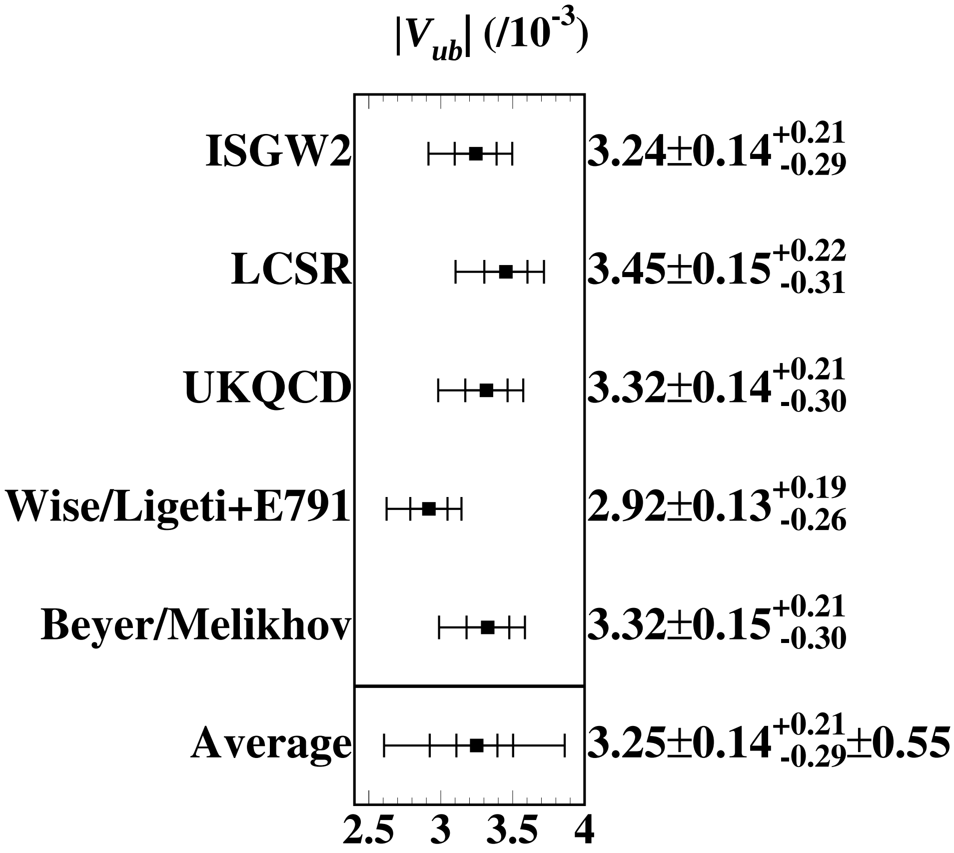

Figure 11.10: $|V_{ub}|$ results averaged with the previous CLEO analysis. The errors are statistical, systematic, and theoretical (on the averages), successively combined in quadrature. The theoretical error is taken to be 1/2 of the full spread of results in quadrature with the additional uncertainty due to the determination of $\tilde{\Gamma}_{\rm thy}$.

In this chapter we present results without these constraints. In addition, we discuss possible large isospin breaking due to $\rho - \omega$ mixing, as described in Ref. [76].

11.4.1 Branching fraction results

Figure 11.11 shows the branching fraction for $B^0 \to \rho^- \ell^+ \nu$ as a function of $\Gamma(B^+ \to \rho^0 \ell^+ \nu)/\Gamma(B^0 \to \rho^- \ell^+ \nu)$ and $\Gamma(B^+ \to \omega \ell^+ \nu)/\Gamma(B^0 \to \rho^- \ell^+ \nu)$. Violations in the relations of Eq. 11.4.1 of 20% result in changes to our branching fraction result of at most 5%.

In addition, we can evaluate the log likelihood as a function of $\Gamma(B^+ \to \rho^0 \ell^+ \nu)/\Gamma(B^0 \to \rho^- \ell^+ \nu)$ and $\Gamma(B^+ \to \omega \ell^+ \nu)/\Gamma(B^0 \to \rho^- \ell^+ \nu)$. These results are shown in Figs. 11.12 and 11.13. The minima in these distributions occur at $\Gamma(B^+ \to \rho^0 \ell^+ \nu)/\Gamma(B^0 \to \rho^- \ell^+ \nu) = 1.7^{+1.0}_{-0.6}$ and $\Gamma(B^+ \to \omega \ell^+ \nu)/\Gamma(B^0 \to \rho^- \ell^+ \nu) = 1.1^{+0.6}_{-0.3}$, where the errors is statistical only. These relations are in reasonable agreement, with large errors, with Eq. 11.4.1.

11.4.2 $\rho - \omega$ mixing

In several papers, G. López Castro *et al.* predict a large isospin breaking effects in $B \to \rho \ell \nu$ due to ρ-ω mixing [76]. They predict that

$$\begin{aligned} \frac{d\Gamma(B^+ \to 2\pi \ell \nu)}{ds} &= \frac{\sqrt{s}}{\pi} \frac{\Gamma(B^+ \to \rho^I(s) \ell^+ \nu) \Gamma(\rho^I(s) \to \pi^+ \pi^-)}{(s - m_\rho^2)^2 + m_\rho^2 \Gamma_\rho^2} \\ &\times \left| 1 + \frac{m_{\rho\omega}^2}{s - m_\omega^2 + i m_\omega \Gamma_\omega} \right|^2 \end{aligned} \tag{11.4.2}$$

where the last term is due to $\rho - \omega$ mixing. Here, $m_{\rho\omega}^2$ is the mixing stength ($\approx -4 \times 10^{-3}$ GeV^2), and ρ^I, along with ω^I in the equivalent expression for $B \to 3\pi \ell \nu$, are the isospin conserving eigenstates. To evaluate the effect of $\rho - \omega$ mixing on the full rate of $B^+ \to 2\pi \ell \nu$ and $B^+ \to 3\pi \ell \nu$, López Castro *et*

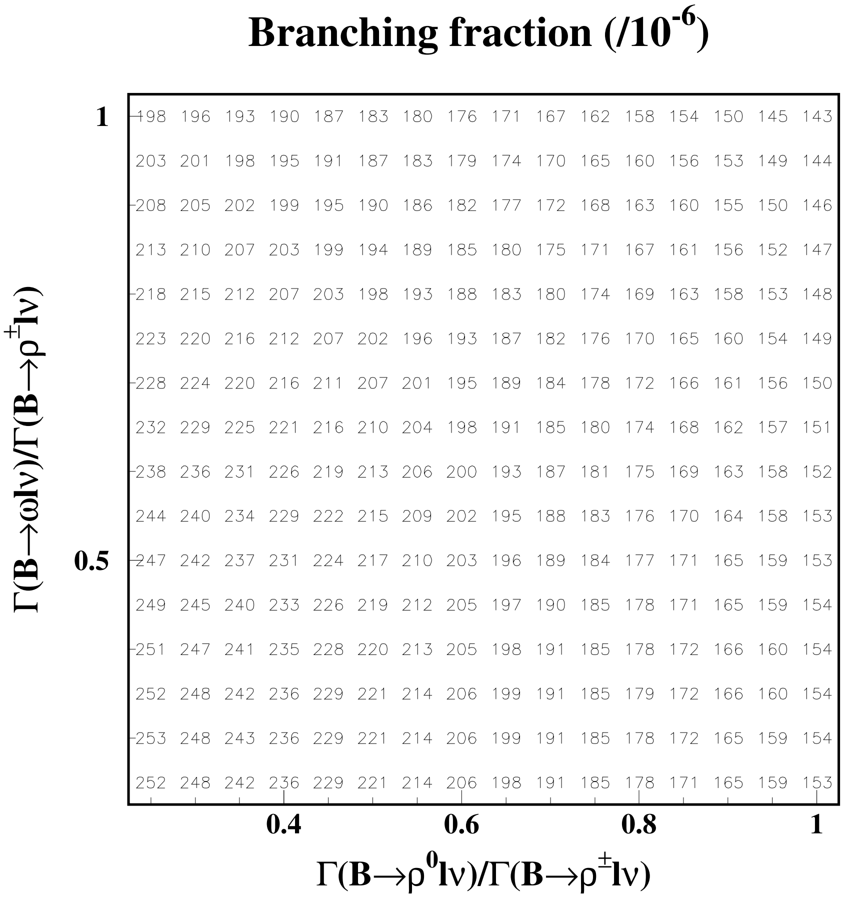

Figure 11.11: Branching fraction results for $B^0 \to \rho^- \ell^+ \nu$ using the ISGW2 model as a function of $\Gamma(B^+ \to \rho^0 \ell^+ \nu)/\Gamma(B^0 \to \rho^- \ell^+ \nu)$ and $\Gamma(B^+ \to \omega \ell^+ \nu)/\Gamma(B^0 \to \rho^- \ell^+ \nu)$. The nominal fit is performed at $\Gamma(B^+ \to \rho^0 \ell^+ \nu)/\Gamma(B^0 \to \rho^- \ell^+ \nu) = \Gamma(B^+ \to \omega \ell^+ \nu)/\Gamma(B^0 \to \rho^- \ell^+ \nu) = 0.5$. For 20% variations around this point, the branching fraction is stable to within 5%. The branching fraction is significantly more sensitive to the value of $\Gamma(B^+ \to \rho^0 \ell^+ \nu)/\Gamma(B^0 \to \rho^- \ell^+ \nu)$ than $\Gamma(B^+ \to \omega \ell^+ \nu)/\Gamma(B^0 \to \rho^- \ell^+ \nu)$.

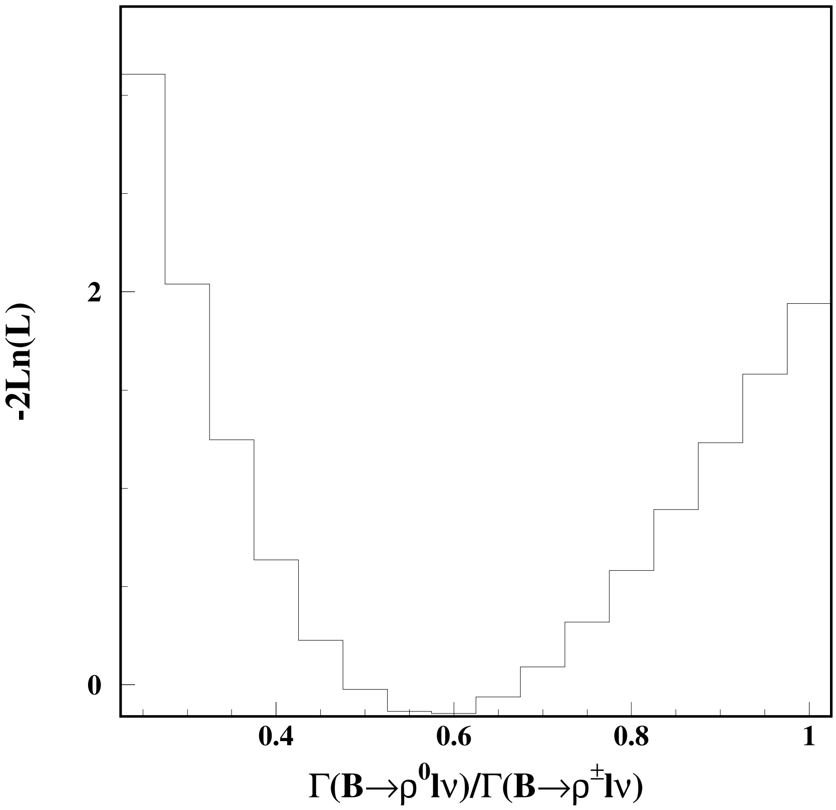

Figure 11.12: $-2ln\mathcal{L}$ vs. $\Gamma(B^+ \to \rho^0\ell^+\nu)/\Gamma(B^0 \to \rho^-\ell^+\nu)$. Our nominal results are for $\Gamma(B^+ \to \rho^0\ell^+\nu)/\Gamma(B^0 \to \rho^-\ell^+\nu) = 0.5$.

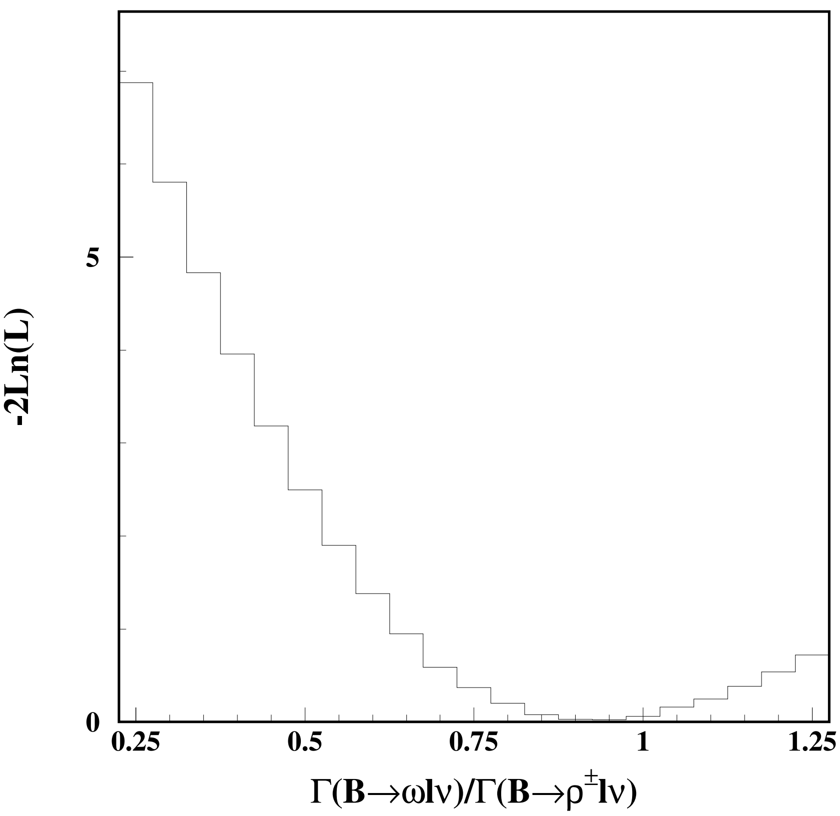

Figure 11.13: $-2ln\mathcal{L}$ vs. $\Gamma(B^+ \to \omega\ell^+\nu)/\Gamma(B^0 \to \rho^-\ell^+\nu)$. Our nominal results are for $\Gamma(B^+ \to \omega\ell^+\nu)/\Gamma(B^0 \to \rho^-\ell^+\nu) = 0.5$.

al. then evaluate this integrals at $s = m_\rho^2$ and $s = m_\omega^2$, respectively, and find

$$\begin{aligned}
\left.\frac{d\Gamma(B^+ \to 2\pi\ell\nu)}{ds}\right|_{s=m_\rho^2} &= \frac{1}{\pi m_\rho \Gamma_\rho}\Gamma(B^+ \to \rho^I \ell\nu) \\
&\times \mathcal{B}(\rho^I \to \pi\pi)\left|1+\epsilon\right|^2 \\
\left.\frac{d\Gamma(B^+ \to 3\pi\ell\nu)}{ds}\right|_{s=m_\omega^2} &= \frac{1}{\pi m_\omega \Gamma_\omega}\Gamma(B^+ \to \omega^I \ell\nu) \\
&\times \mathcal{B}(\omega^I \to \pi\pi\pi)\left|1+\epsilon\right|^2 \qquad (11.4.3)
\end{aligned}$$

where ϵ is

$$\epsilon = \frac{m_{\rho\omega}^2}{m_\rho^2 - m_\omega^2 + i m_\omega \Gamma_\omega} \qquad (11.4.4)$$

for the $\pi\pi$ mode and

$$\epsilon = \frac{m_{\rho\omega}^2}{m_\omega^2 - m_\rho^2 + i m_\rho \Gamma_\rho} \qquad (11.4.5)$$

for the $\pi\pi\pi$ mode. Plugging in standard values for the masses and widths, one finds that $|1+\epsilon|^2 = 1.34$ for the 2π mode, or more than a 30% isospin breaking effect. They also predict a 1% effect on $B^+ \to \omega\ell^+\nu$. As the $B^0 \to \rho^-\ell^+\nu$ channel is not subject to these effects, these results would imply

$$\begin{aligned}
\Gamma(B^0 \to \rho^-\ell^+\nu) &= (2/1.34)\Gamma(B^+ \to \rho^0\ell^+\nu), \\
\Gamma(B^0 \to \rho^-\ell^+\nu) &= (2/1.01)\Gamma(B^+ \to \omega\ell^+\nu). \qquad (11.4.6)
\end{aligned}$$

Given these, our result for $\mathcal{B}(B^0 \to \rho^-\ell^+\nu)$ would be 9% lower.

However, doing the the integral over s in Eq. 11.4.2 gives very different results. Doing this integral should properly take into account the finite ρ and ω width. In Figs. 11.14 and 11.15 we show $|1+\epsilon|^2$ for the $\pi\pi$ and $\pi\pi\pi$ modes as functions of s. In particular, it is clear that for the $\pi\pi$ mode, $|1+\epsilon|^2$ is sharply peaked near the nominal ρ mass. Integrating over s is both of these distributions, weighted by the proper Breit-Wigner function, results in a small effect due to $\rho-\omega$ mixing. Ignoring any s dependence of $\Gamma(B^+ \to \rho^I(\omega_I)\ell\nu)$ and $\Gamma(\rho^I(\omega_I) \to \pi\pi))$, we find that $|1+\epsilon| \approx 1.03$ for the $\pi\pi$ mode and $|1+\epsilon| \approx 0.99$ for the $\pi\pi\pi$ mode.

These results are insensitive to the exact range of s integrated over once the $\pm\Gamma(\rho)$ or $\pm\Gamma(\omega)$ region is included. When the integration is performed, $\rho - \omega$ mixing has a negligible effect on our results. We believe that integrating over s is more reliable than the procedure used by López Castro et al..

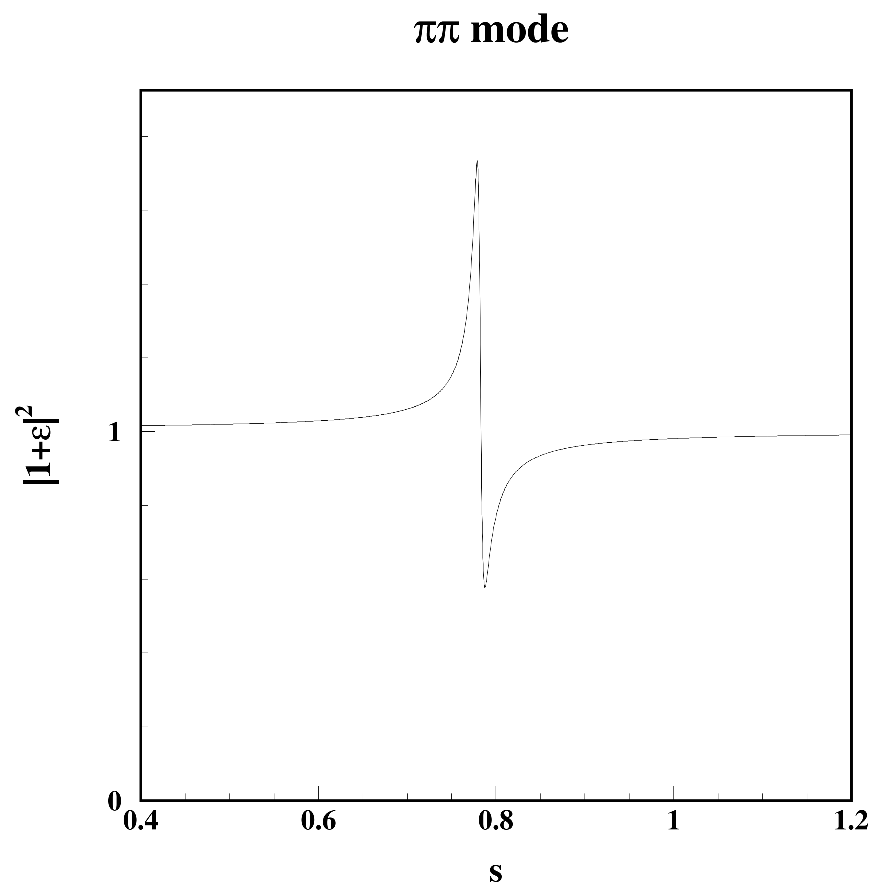

Figure 11.14: $|1+\epsilon|^2$ for the $\pi\pi$ mode as a function of s. This function is sharply peaked in the region close to the nominal ρ-meson mass.

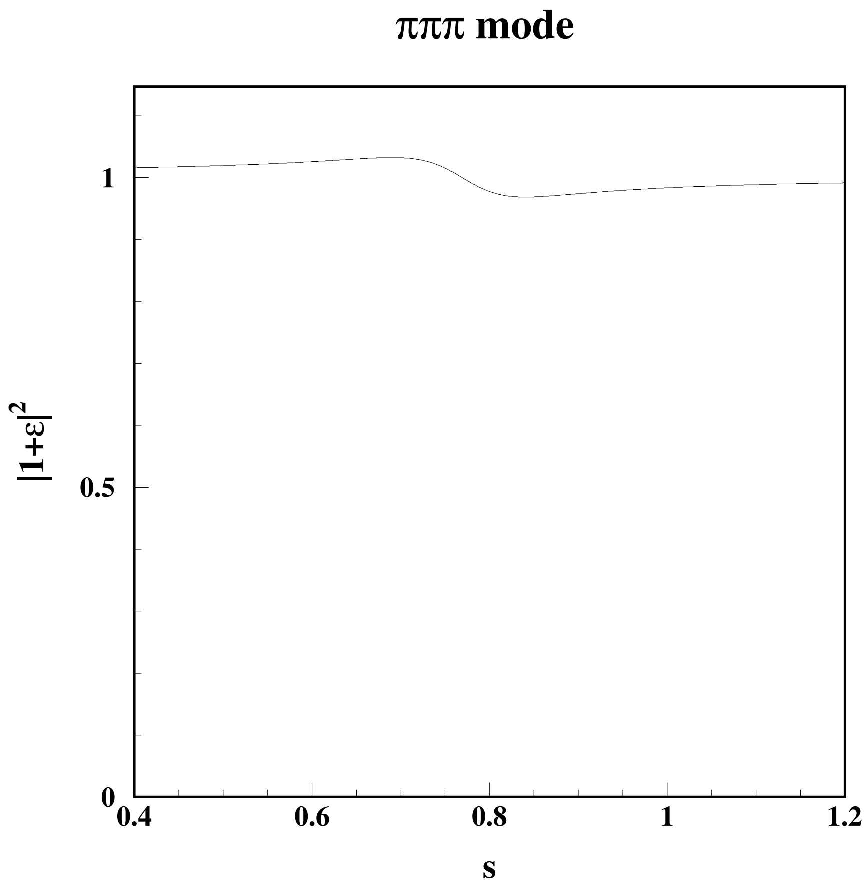

Figure 11.15: $|1+\epsilon|^2$ for the $\pi\pi\pi$ mode as a function of s. Due to the large ρ width, this fuction is broadly peaked and does not lead to a large isospin breaking effect.

Chapter 12

Conclusion and outlook

12.1 Branching fraction and $|V_{ub}|$

We have performed a measurement of $\mathcal{B}(B \to \rho\ell\nu)$, $|V_{ub}|$, and the q^2 distribution in $B \to \rho\ell\nu$ decay using a data sample of approximately 3.3×10^6 $B\bar{B}$ pairs. Using leptons near the $b \to c\ell\nu$ lepton-energy endpoint, we find

$$\begin{aligned} \mathcal{B}(B^0 \to \rho^- \ell^+ \nu) &= (2.69 \pm 0.41^{+0.35}_{-0.40} \pm 0.50) \times 10^{-4}, \\ |V_{ub}| &= (3.23 \pm 0.24^{+0.23}_{-0.26} \pm 0.58) \times 10^{-3}, \end{aligned} \tag{12.1.1}$$

where the errors are statistical, systematic, and model dependence. The $\mathcal{B}(B \to \rho\ell\nu)$ result confirms the previous CLEO result, and has a comparable statistical precision. Additionally, this result is statistically independent from the previous CLEO results and has a somewhat smaller systematic error. Averaging these results, we find

$$\begin{aligned} \mathcal{B}(B^0 \to \rho^- \ell^+ \nu) &= (2.57 \pm 0.29^{+0.33}_{-0.46} \pm 0.41) \times 10^{-4}, \\ |V_{ub}| &= (3.25 \pm 0.14^{+0.21}_{-0.29} \pm 0.55) \times 10^{-3}. \end{aligned} \tag{12.1.2}$$

These values represent the current best CLEO results based on exclusive $b \to u\ell\nu$ measurements. For the branching fraction, the experimental and theoretical uncertainties are comparable. On the other hand, the experimental errors are less than the theoretical uncertainties in the determination of $|V_{ub}|$. Figure 12.1 shows the unitarity triangle constraints using Eq. 12.1.2 for the $|V_{ub}|$

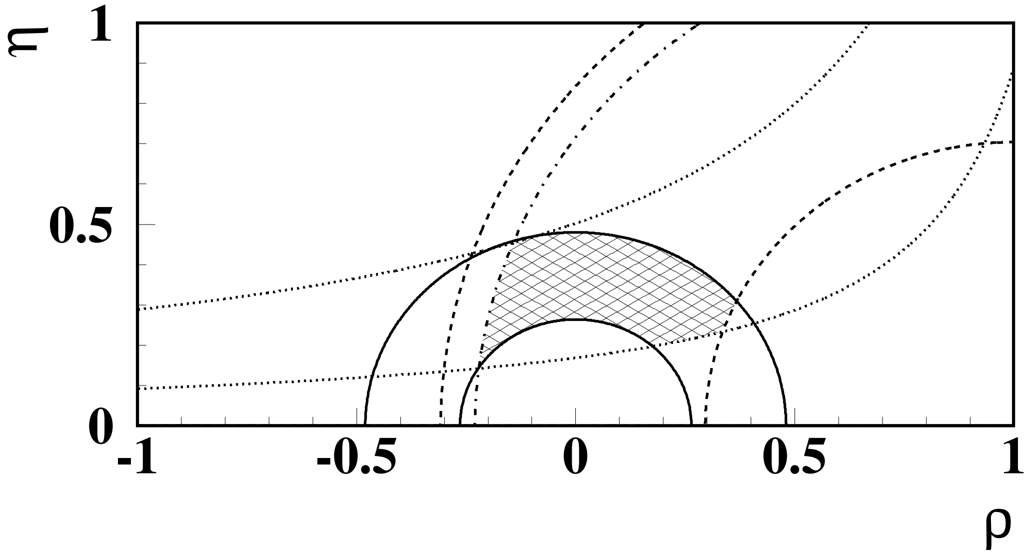

Figure 12.1: Unitarity triangle constraints with the $|V_{ub}|$ in Eq. 12.1.2 (solid lines). Other constraints are from B_d mixing (dashed lines), B_s mixing (dot-dashed lines), and ϵ_K (dotted lines). The hatched band corresponds to a 1.5σ allowed region.

constraint. A small improvement is observed compared with that from the inclusive CLEO and ARGUS measurements (see Fig. 2.6). More important is the agreement observed between the exclusive and inclusive measurements. Additionally, Fig. 12.2 shows what the constraint on the unitarity triangle would be if the uncertainy on $\tilde{\Gamma}_{\mathrm{thy.}}$ were small compared to the experimental errors. This constraint includes all experimental errors, including that due to the uncertainty in the kinematics of $B \to \rho\ell\nu$ decay. With only theoretical improvements, the constraint from $|V_{ub}|$ can improve considerably.

Figure 12.3 compares the value of $|V_{ub}|$ with those determined by other methods. The five measurements are in good agreement. The average CLEO result from $B \to \rho\ell\nu$ decay is the most precise of these measurements.

It is reasonable to question if this is a fair comparison. In particular, the

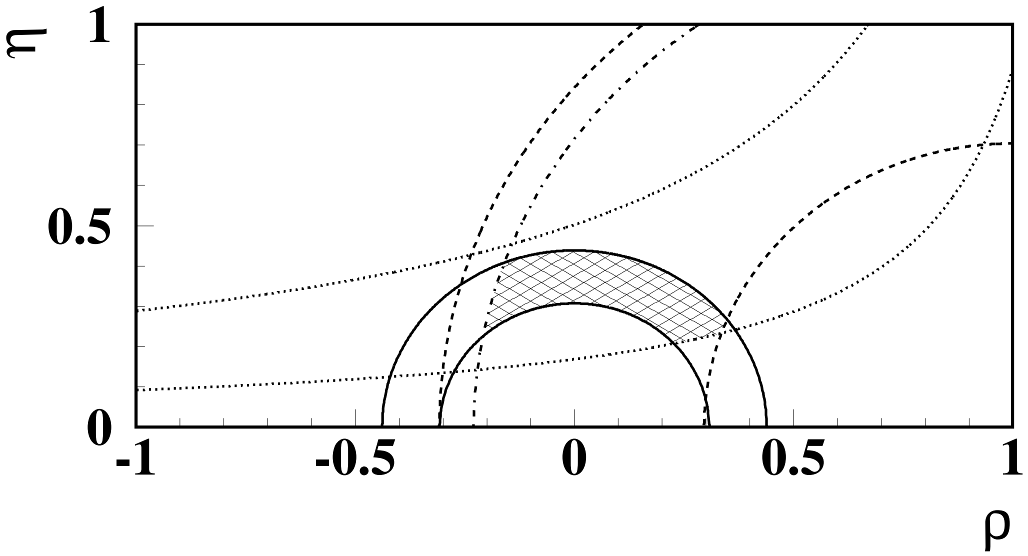

Figure 12.2: Unitarity triangle constraints with the $|V_{ub}|$ in Eq. 12.1.2 (solid lines), where we have not included the uncertainty due to the determination of $\tilde{\Gamma}_{\rm thy.}$. A substantial improvement in the constraint is observed. Other constraints are from B_d mixing (dashed lines), B_s mixing (dot-dashed lines), and ϵ_K (dotted lines). The hatched band corresponds to a 1.5σ allowed region.

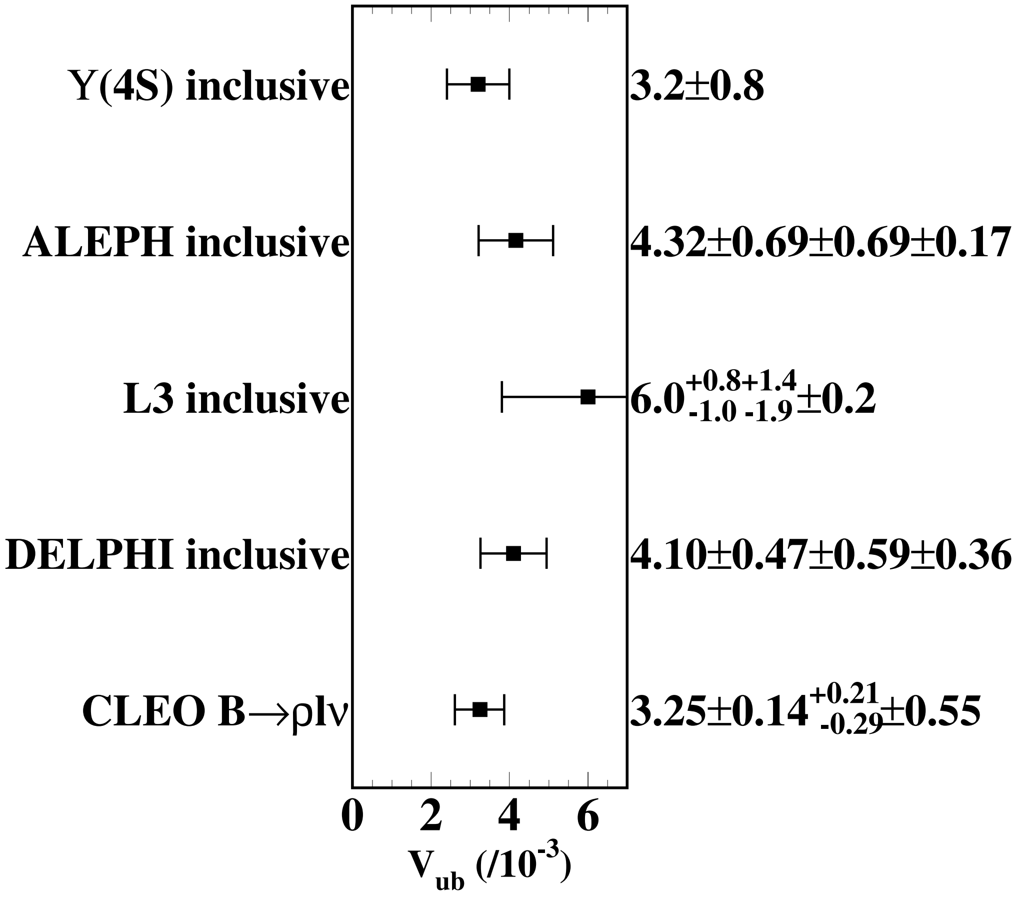

Figure 12.3: Comparison of $|V_{ub}|$ results. The error bars represent all experimental and theoretical errors taken in quadrature.

theoretical error may be accounted for differently among the different measurements. To address this, we consider the measurement presented in this thesis and the DELPHI inclusive measurement. There are two pieces to the theoretical error. The first is due to the kinematics of $b \to u\ell\nu$ decay. The $B \to \rho\ell\nu$ measurement is limited to the large lepton-energy region, and thus is dependent on form-factor models to provide the efficiency for the extrapolation to the full lepton-energy range. The DELPHI measurement is sensitive over a somewhat larger lepton-energy range, however uncertainties enter due to the reconstruction of the hadronic mass. In both cases this uncertainty is evaluated by varying the inputs of the decay matrix element. At CLEO, different models are used to predict the form factors. For the DELPHI measurement the parameters of the model are varied. We assert that this uncertainty is treated in a similar manner in each measurement and is 8% on $|V_{ub}|$ for both measurements. (For the DELPHI measurement, we have included the uncertainty in the $b \to u\ell\nu$ kinematics but not that in Eq. 4.2.4 due to the error on m_b.) It is a common misconception in the literature that this uncertainty is significantly larger for high-lepton energy $B \to \rho\ell\nu$ analyses of data samples collected at the $\Upsilon(4S)$.

The other source of theoretical uncertainty is due to the determination of $|V_{ub}|$ from a measured branching fraction. For $B \to \rho\ell\nu$, this is expressed as a 30% uncertainty on $\tilde{\Gamma}_{\text{thy.}}$, which cooresponds to a 15% error on $|V_{ub}|$. For the DELPHI measurement, the value of $|V_{ub}|$ is determined from the number of events using Eq. 4.2.4. The only uncertainty on this relative that has been evaluated is that due to the uncertainty on m_b. Refs. [42, 43, 44] indicate that the uncertainty on Eq. 4.2.4 is of order $\pm 5\%$. The total theoretical error, from both signal kinematics and the normalization factor between branching fractions and $|V_{ub}|$, is somewhat smaller for the inclusvie measurements as compared to measurements of $B \to \rho\ell\nu$ at CLEO. On the other hand, the quoted statistical and systematic are considerably larger. Thus, the average result given in Eq. 12.1.2 for $|V_{ub}|$ using $B \to \rho\ell\nu$ and $B \to \pi\ell\nu$ decay at CLEO is the most precise measurement of $|V_{ub}|$.

12.2 Measurement of q^2 distribution

We have also measured the q^2 distribution in $B \to \rho\ell\nu$ decay in three q^2 bins. We find

$$\begin{aligned}
\Delta\Gamma(q^2 < 7\ \mathrm{GeV}^2/c^4) &= (7.6 \pm 3.0^{+0.9}_{-1.2} \pm 3.0) \times 10^{-2}\ \mathrm{ns}^{-1}, \\
\Delta\Gamma(7 < q^2 < 14\ \mathrm{GeV}^2/c^4) &= (4.8 \pm 2.9^{+0.7}_{-0.8} \pm 0.7) \times 10^{-2}\ \mathrm{ns}^{-1}, \\
\Delta\Gamma(q^2 > 14\ \mathrm{GeV}^2/c^4) &= (7.1 \pm 2.1^{+0.9}_{-1.1} \pm 0.6) \times 10^{-2}\ \mathrm{ns}^{-1} \quad (12.2.1)
\end{aligned}$$

where the errors are statistical, systematic, and theoretical.

Because we are sensitive to a large fraction of the allowed lepton-energy region at high q^2, we measure the partial rate for $q^2 > 14\ \mathrm{GeV}^2/c^4$ with relatively little model dependence.

12.3 Outlook

The results presented here, in particular $\Delta\Gamma$, are promising for future analyses of $B \to \rho\ell\nu$ that utilize the high lepton-energy region to determine $|V_{ub}|$. If the full q^2 range is to be used, then theoretical predictions for $\tilde{\Gamma}_{\mathrm{thy}}$ made with good precision are needed in order to improve upon the current value of $|V_{ub}|$. For this to occur, experimental measurements of the q^2 distribution would be helpful. For high lepton-energies, the predicted shapes of the q^2 distributions are virtually identical for the different form-factor models. The models, therefore, cannot be distinguished on the basis of measurements in this lepton-energy region alone. Thus, it is important to include leptons whose energy is below the lepton-energy endpoint region ($E_\ell < 2.0$ GeV) in order to constrain the form-factor model predictions.

On the other hand, measurements of the high q^2 region are currently statistically limited. The uncertainty due to the decay kinematics in this region are considerably smaller than those over the full q^2 range. Indeed, the theoretical error on the $\Delta\Gamma$ measurement in the highest q^2 bin is less than 10%, to be compared with 16% on the average branching fraction measurement. The question we have not addressed is with what precision can $\tilde{\Gamma}_{\rm thy}$ predictions be made for only the high q^2 region. We expect that the error on these predictions should be smaller than those over the full q^2 range for those models that make an extrapolation to the low q^2 region (lattice QCD in particular).

Experimentally, new measurements of $B \to \rho\ell\nu$ and the inclusive $b \to u\ell\nu$ branching fractions at the $\Upsilon(4S)$ will soon be made. As discussed in Chapter 5, CLEO has already collected approximately nine million $B\bar{B}$ events. This is roughtly three times the data sample examined in this thesis and should allow for the measurement of the q^2 distribution with significantly better precision. In the slightly longer term, the BABAR, BELLE, and CLEO III experiments are either just beginning to collect data, or soon will be. The measurements performed at the Z resonance are not likely to be improved beyond the current results.

More experimental data, however, does not lead directly to an improved measurement of $|V_{ub}|$ using $B \to \rho\ell\nu$ decay. Experimental techniques that are sensitive below the lepton-energy endpoint region, where form-factor models can be distinguished, are needed to provide meaningful results on the q^2 distribution.

Measuring $|V_{ub}|$ using only part of the allowed q^2 range lead to greater precision than those over the full q^2 range. With more data (which will be provided first by the full CLEO II dataset and then by the B factories), such a measurememt should become competitive. In either case, it will remain important to understand the error on the extraction of $|V_{ub}|$ from an measurement of the (partial) branching fraction for $B \to \rho\ell\nu$.

Bibliography

[1] M. Kobayashi and T. Maskawa, Prog. Theor. Phys. **49**, 652 (1973).

[2] J. H. Christenson *et al.*, Phys. Rev. Lett. **13**, 138 (1964).

[3] S. W. Herb *et al.*, Phys. Rev. Lett. **39**, 252 (1977).

[4] Ch. Berger *et al.*, Phys. Lett. B **76**, 243 (1978).

[5] C. W. Darden *et al.*, Phys. Lett. B **76**, 246 (1978).

[6] D. Andrews *et al.*, Phys. Rev. Lett. **45**, 219 (1980).

[7] G. Finocchiaro *et al.*, Phys. Rev. Lett. **45**, 222 (1980).

[8] S. Behrends *et al.*, Phys. Rev. Lett. **50**, 881 (1983).

[9] J. P. Alexander *et al.*, Phys. Rev. Lett. **77**, 5000 (1996).

[10] J. Bartelt *et al.*, Phys. Rev. Lett. **71**, 4111 (1993).

[11] M. Acciarri *et al.*, Phys. Lett. B **436**, 174 (1998).

[12] R. Barate *et al.*, Eur. Phys. J. **C6**, 555 (1999).

[13] L. K. Gibbons, Annu. Rev. Nucl. Part. Sci. **48**, 121 (1998).

[14] M. Wirbel, B. Stech, and M. Bauer, Z. Phys. **C29**, 637 (1985).

[15] J. G. Körner and G. A. Schuler, Z. Phys. **C38**, 511 (1988).

[16] N. Isgur, D. Scora, B. Grinstein, and M. B. Wise, Phys. Rev. **D39**, 799 (1989).

[17] N. Isgur and D. Scora, Phys. Rev. **D52**, 2783 (1995).

[18] M. Beyer and D. Melikhov, Phys. Lett. **B436**, 344 (1998).

[19] R. N. Faustov, V. O. Galkin, and A. Yu. Mishurov, Phys. Rev. **D53**, 6302 (1996).

[20] N. B. Demchuk *et al.*, Phys. Atom. Nucl. **60**, 1292 (1997).

[21] A. Abada *et al.*, Nucl. Phys. **B416**, 675 (1994).

[22] C. R. Allton *et al.*, Phys. Lett. **B345**, 513 (1995).

[23] L. Del. Debbio *et al.*, Phys. Lett. **B416**, 392 (1998).

[24] S. Narison, Phys. Lett **B283**, 384 (1992).

[25] P. Ball and V. M. Braun, Phys. Rev. **D58**, 094016 (1998).

[26] A. Khodjamirian *et al.*, Phys. Lett. **B410**, 275 (1997).

[27] Z. Ligeti and M. B. Wise, Phys. Rev. **D53**, 4937 (1996). E. M. Aitala *et al.*, Phys. Rev. Lett. **80**, 1393 (1998).

[28] B. Stech, Phys. Lett. **B354**, 447 (1995).

[29] B. Stech, Z. Phys. **C75**, 245 (1997).

[30] J. M. Soares, Phys. Rev. **D54** 6837 (1996).

[31] C. G. Boyd and I. Z. Rothstein, Phys. Lett. **B420**, 350 (1998).

[32] C. Caso *et al.* (Particle Data Group), Eur. Phys. J. **C3**, 1 (1998).

[33] C. Campagnari and M Franklin, Rev. Mod. Phys. **69**, 137 (1997).

[34] Y. Fukuda *et al.*, Phys. Rev. Lett. **81**, 1562 (1998).

[35] I. S. Towner, J. C. Hardy, nucl-th/9809087.

[36] H. Leutwyler and M. Roos, Z. Phys. C **25**, 91 (1984).

[37] P. Abreu *et al.*, Phys.Lett. B **439**, 209 (1998).

[38] R. Fulton *et al.*, Phys. Rev. Lett. **64**, 16 (1990).

[39] J. Bartelt *et al.*, Phys. Rev. Lett. **71**, 4111 (1993).

[40] H. Albrecht *et al.*, Phys. Lett. B **234**, 409 (1990).

[41] M. Battaglia *et al.*, submitted to the ICHEP'98 Conference, ICHEP98 #241, (1998).

[42] A. Falk, Z. Ligeti, and M. B. Wise, Phys. Lett. B **406**, 225 (1997).

[43] I. Bigi, R. D. Dikeman, and N. Uraltsev, Eur. Phys. J. C **4**, 453 (1998).

[44] N. G. Uraltsev, Int. J. Mod. Phys. A **11**, 515 (1996).

[45] L. Wolfenstein, Phys. Rev. Lett. **51**, 1945 (1983).

[46] J. Flynn, Plenary talk given at the 28th International Conference on High Energy Physics, July 1996, Warsaw, Poland.

[47] A. J. Buras and R. Fleischer, in *Heavy Flavours II* (World Scientific, Singapore, 1997), edited by A. J. Buras and M. Linder; Preprint hep-ph/9704376.

[48] T. Inami and C. S. Lim, Prog. Theor. Phys. **65**, 297 (1981).

[49] J. D. Richman, "*Heavy-quark physics and CP violation*", in *Les Houches 1997 summer school proceedings* (Elsevier Science B. V., 1998).

[50] J. D. Richman and P. R. Burchat, Rev. Mod. Phys. **67**, 893 (1995).

[51] This notation applies to the decay of a charge -1/3 quark. If Q is a +2/3 charge quark, $V_{q'Q}$ should be replaced by $V^*_{Qq'}$.

[52] BABAR Collab., *The BABAR Physics Book*, SLAC-R-0504 (1998).

[53] H. Albrecht *et al.*, Phys. Lett. B **318**, 397 (1993).

[54] B. Barish *et al.*, Phys. Rev. Lett. **76**, 1570 (1996).

[55] ALEPH Collab., EPS-0404, contribution to the Int'l. Europhysics Conference on High Energy Physics, Brussels, Belgium (1995).

[56] P. Abreu *et al.*, Z. Phys. C **66**, 323 (1995).

[57] R. Akers *et al*, Z. Phys. C **60**, 199 (1993).

[58] M. Acciarri *et al.*, Z Phys. C **71**, 379 (1996).

[59] J. L. Rosner, in *B Decays*, edited by S. Stone (World Scientific, Singapore, 1992), p. 312.

[60] K. Ackerstaff *et al.*, Phys. Lett B **395**, 128 (1997).

[61] D. Buskulic *et al.*, Phys. Lett. B **395**, 373 (1997).

[62] P. Abreu *et al.*, Z. Phys. C **71**, 539 (1996).

[63] B. Barish *et al.*, Phys. Rev. D **51**, 1014 (1995).

[64] H. Albrecht *et al.*, Phys. Lett. B **324**, 249 (1994).

[65] H. Albrecht *et al.*, Phys. Lett. B **275**, 195 (1992).

[66] J. E. Dubosq *et al.*, Phys. Rev. Lett. **76**, 3898 (1996).

[67] R. Akers *et al.*, Z. Phys. C **67**, 57 (1995).

[68] A. Anastassov *et al.*, Phys. Rev. Lett. **80**, 4127 (1998).

[69] D. Buskulic *et al.*, Phys. Lett. B **345**, 103 (1995).

[70] Y. Kubota *et al.* (CLEO Collaboration), Nucl. Instr. Methods Phys. Res. **A320**, 66 (1992).

[71] D. Lange and A. Ryd, *The EvtGen Event Generator Package*, Presented at the International Conference on Computing in High-Energy Physics. Chicago, 1998. See also http://charm.physics.ucsb.edu/people/lange/EvtGen/index.html.

[72] R. Brun *et al.*, GEANT v. 3.15, CERN DD/EE/84-1.

[73] G. C. Fox and S. Wolfram, Phys. Rev. Lett. **41**, 1581 (1978).

[74] R. A. Fisher, Annals of Eugenics **7**, 179 (1936).

[75] F. James, CERN Program Library Long Writeup, Mar. 1994.

[76] J. L. Díaz-Cruz *et al.*, Phys. Rev. **D54**, 2388 (1996).

[77] M. Chadha *et al.*, Phys. Rev. D **58**, 32002 (1998).